Structure and Electronics of Donor-Acceptor Blends

eman ta zabal zazu

Universidad
del País Vasco

Euskal Herriko
Unibertsitatea

Elizabeth Goiri Little

Supervisors:

Dimas G. de Oteyza
J. Enrique Ortega

A thesis submitted for the degree of

Ph.D.

February 2014

Resumen

El estudio de películas orgánicas se ha disparado en las últimas décadas, y hoy en día es un área de investigación extremadamente relevante. Ello se debe a que los materiales orgánicos han demostrado ser una alternativa viable a los semiconductores inorgánicos de los que tradicionalmente se han fabricado dispositivos electrónicos como los LED, los transistores o las células fotovoltaicas. Aun sufriendo generalmente de una menor eficiencia en comparación con los materiales inorgánicos, los orgánicos tienen la gran ventaja de tener un coste de fabricación mucho menor, y ofrecen además características interesantes como bajo peso y flexibilidad.

Simplificando, podemos imaginar que estos dispositivos están formados por una película orgánica conectada por dos electrodos. En algunos dispositivos optoelectrónicos conviene utilizar una mezcla de moléculas dadoras y aceptoras. Tanto la interfaz entre ambos tipos de moléculas como la interfaz metalorgánica son determinantes en procesos que definen la funcionalidad del dispositivo.

Los sistemas estudiados en esta tesis pueden considerarse modelos de estas interfaces. En este trabajo se estudian la estructura y el alineamiento energético de monocapas moleculares que son mezclas de dos moléculas conjugadas de pequeño tamaño, una dadora y otra aceptora. Las moléculas utilizadas son la ftalocianina de cobre (CuPc) y el pentaceno (PEN)—moléculas dadoras bien conocidas por su uso en dispositivos—y sus respectivas homólogas fluoradas, FCuPc y PFP, que son moléculas aceptoras. Las combinaciones dador-aceptor estudiadas son CuPc+PFP y PEN+FCuPc, y los substratos utilizados, las superficies (111) de los metales nobles Au, Ag y Cu.

Además de las mencionadas capas binarias, se estudió la estructura del sistema PFP/Ag(111), el cual presenta una transición estructural a baja temperatura, pasando de una capa inconmensurada y modulada por una estructura de moiré a una dotada de dislocaciones lineales periódicas. Con ayuda de cálculos teóricos se hace posible entender y racionalizar la aparición de dichas dislocaciones.

Se han utilizado varias técnicas, siempre en ultra alto vacío. La microscopía de efecto túnel (STM) permite caracterizar la estructura lateral de las capas moleculares con resolución molecular, mientras que la técnica de ondas estacionarias de rayos X (XSW) determina la distancia substrato-molécula. En cuanto a la estructura electrónica, ésta se puede estudiar con las técnicas de espectroscopía de fotoelectrones y absorción de rayos X. En espectroscopía diferenciamos entre la de rayos X (XPS), que sondea los niveles ocupados profundos, y la ultravioleta (UPS), que sondea los menos profundos. Por último, la técnica de absorción de rayos X (NEXAFS) proporciona información acerca de los niveles desocupados.

Red de Dislocaciones del PFP/Ag(111) La monocapa de PFP sobre Ag(111) forma una capa ordenada en la que las moléculas se disponen en filas, con una celda unidad oblicua. A baja temperatura presenta una transición estructural, formándose una de red de dislocaciones lineales que occurren cada seis filas de moléculas. Ésta se ha caracterizado por STM a una temperatura de 100 K. Combinando los parámetros obtenidos experimentalmente con cálculos teóricos de DFT podemos lograr entender su aparición. La estructura de una monocapa molecular depende del delicado equilibrio entre las interacciones que rigen el proceso de ensamblado. Al aplicar los cálculos, distinguimos entre interacciones intermoleculares, interacciones intermoleculares mediadas por el substrato e interacciones molécula-substrato. Comparamos la energía de tres situaciones. En primer lugar, la estructura conmensurada propuesta en la literatura; en segundo lugar, la estructura inconmensurada sin dislocaciones que resulta de los parámetros obtenidos por STM; y por último, se estudia la estructura con dislocaciones. Se da por hecho que éstas son un mecanismo para relajar tensión acumulada en las filas anteriores por poco a poco ir alejándose del lugar de adsorción más favorable: la dislocación por tanto, devuelve las siguientes filas a posiciones de adsorción más favorables, a costa de reducir la densidad de moléculas y las interacciones intermoleculares.

Los resultados de los cálculos muestran que la estructura conmensurada es considerablemente menos favorable energéticamente que la inconmensurada, debido a una distancia intermolecular demasiado pequeña. En cuanto a las dislocaciones, se calculó la energía de una capa molecular con dislocaciones cada $N = 3, 4, 5, ...10$ filas moleculares. En todos los casos se encuentra una situación más favorable que la conmensurada y en concreto cuando $N = 5, 6, 7$ la introducción de dislocaciones es favorable frente a el caso de una capa sin dislocaciones (la capa inconmensurada), demostrándose así que éstas son una estrategia de liberación de tensión acumulada.

Mezclas Moleculares Dador-Aceptor Pasamos ahora a las mezclas moleculares. Al depositar aproximadamente la misma cantidad de dos moléculas diferentes sobre la superficie (111) de Au, Ag o Cu—sea el par de moléculas PEN+FCuPc o CuPc+PFP—éstas forman por autoensamblaje una capa ordenada con un patrón característico y con estequiometría 1:1, de forma que cada molécula queda rodeada por moléculas de la especie contraria, maximizando así el contacto entre dadores y aceptores. La fuerza impulsora de la formación de esas capas cristalinas son las interacciones intermoleculares vía puentes de hidrógeno, los cuales se establecen entre los átomos de hidrógeno de la molécula dadora y los de fluoro de la molécula aceptora. La estructura que se forma es la que logra maximizar estas interacciones. El hecho de que la estructura formada sobre los diferentes substratos es prácticamente idéntica lleva a la conclusión de que las fuerzas intermoleculares dominan sobre las interacciones molécula-substrato. Sin embargo, el efecto del substrato se ve tanto en la orientación de las moléculas como en la clara relación epitaxial que las capas moleculares tienen con la superficie metálica. (Variando la cantidad relativa de moléculas dadoras y aceptoras es posible formar una gran variedad de estructuras cristalinas de estequiometría diferente a la 1:1.)

Una vez estudiada la estructura de estas capas, podemos preguntarnos, cómo influye el nuevo entorno de las moléculas en su estructura eléctronica? Para contestar esta pregunta, nos centramos en la estequiometría 1:1, y llevamos a cabo medidas de espectroscopía, de adsorción y de ondas estacionarias sobre las capas mixtas, y sobre capas puras, éstas últimas sirvendo de referencia. La primera observación que hacemos por XPS y UPS es un desplazamiento de los niveles energéticos hacia menores energías de ligadura en el caso de la molécula dadora y un desplazamiento a mayores energías de ligadura en el caso de la molécula aceptora. Típicamente, los desplazamientos de niveles electrónicos se pueden asociar con una carga o descarga de la molécula. En este caso podríamos esperar que la molécula aceptora recibe carga de la molécula dadora. Sin embargo, la dirección de los desplazamientos es la contraria a la que esperaríamos de esa situación, por tanto debemos concluir que éstos tienen otro origen. La propuesta que aquí hacemos es que los desplazamientos son la consecuencia de un anclaje de los niveles moleculares a su nivel de vacío.

La deposición de moléculas sobre un substrato metálico produce un cambio en la función de trabajo del sistema, debido a la modificación del dipolo superficial del substrato (por efecto “push back”, la transferencia de carga o el dipolo molecular intrínseco). Aunque todas nuestras moléculas (CuPc, PEN, FCuPc, PFP) bajan el nivel de vacío (reducen la función de trabajo) al depositarse una capa pura de ellas, los dadores CuPc y PEN provocan una bajada mucho mayor que PFP y FCuPc, respectivamente. Por esta razón, al mezclar PEN con FCuPc, o CuPc con PFP, el nivel de vacío de la muestra mezclada se encontrará entre el de la molécula dadora y la molécula aceptora. Si los niveles moleculares están anclados al nivel de vacío, al comparar capas puras y mixtas, veremos un desplazamiento de los niveles hacia menores energías de ligadura en el caso de la molécula dadora, y hacia mayores energías de ligadura en el caso de la molécula aceptora.

El anclaje al nivel de vacío es de esperar en sistemas poco interactivos, en los que no existe transferencia de carga. Por eso las mezclas sobre Au(111) siguen de cerca los desplazamientos arriba mencionados. Sin embargo, cuando utilizamos substratos más reactivos, como Ag(111) y Cu(111), existirán efectos adicionales que debemos tener en cuenta y observaremos que los desplazamientos de los niveles moleculares divergen de aquéllos predichos por el modelo de anclaje al nivel de vacío. Este trabajo busca entender estas discrepancias y explicarlas con efectos como la transferencia de carga y los cambios en la distancia de adsorción.

Abstract

The growing potential of organic layers as the main component in electronic devices has led to a boom in the study of organic metal interfaces. Both the structure of organic overlayer and its electronic energy level alignment with the metal are defining characteristics of the system. In this thesis we explore both structural and electronic properties of organic monolayers on single crystal surfaces. Copper phthalocyanine (CuPc) and pentacene (PEN) are organic semiconductors well known for their successful integration into optoelectronic devices. These, along with their fluorinated counterparts fluorinated copper phthalocyanine (FCuPc) and perfluoropentacene (PFP) are molecules employed in this work.

In Chapter 3 a purely structural study of the dislocation network formed at low temperature in the PFP/Ag(111) system is made. Theoretical calculations based on the experimental structural parameters obtained by scanning tunneling microscopy (STM) rationalize the generation of dislocations by taking into account the effects of intermolecular, molecule-substrate and substrate mediated interactions.

The remaining two chapters deal with the main focus of this dissertation, this being the structure (Chapter 4) and electronics (Chapter 5) of monolayer donor-acceptor blends made up of CuPc and PEN (donors) and their fluorinated counterparts FCuPc and PFP (acceptors) on noble metal (111) substrates. STM measurements show that, regardless of the substrate, the molecular blends—CuPc+PFP and FCuPc+PEN—share a common structure that tends to maximize donor-acceptor contact, due to the leading role of hydrogen bonding in the self-assembly process. The new environment of the molecules is found to produce changes in the electronic levels of the molecules, thereby affecting the energy level alignment between the

organic layer and the metal. Photoelectron spectroscopy using X-ray and UV radiation allows probing the molecules' occupied levels, whereas X-ray absorption allows probing the unoccupied levels. For weakly interacting systems a simple vacuum level pinning scenario suffices to explain the changes in the molecular levels. For more strongly interacting systems the effects of charge transfer and of conformational changes (assessed by X-ray standing wave measurements) must be taken into account in order to understand the changes taking place in these mixed layers and provide a complete picture of the energy level alignment in such systems.

Acknowledgements

The completion of this thesis would not have been possible without the help and support of many people.

First I would like to thank **Enrique Ortega** for the opportunity to work in his research group, for reading through the manuscript and for his unquenchable optimism.

I'm especially grateful to **Dimas G. de Oteyza** for his guidance during my PhD and in the writing of my thesis; for his patience and good-humor, which he surely needed to get through these last pages full of CuPc, PFP, PEN and FCuPc.

Many people contributed to the measurements presented in this work: **Celia Rogero** provided her brand new STM and UPS equipment and also her help getting them going, making it possible for me to add valence bands, work functions and surface dipoles to my thesis.

Dimas G. de Oteyza, Afaf El-Sayed, Celia Rogero and Patrizia Borghetti were present in our numerous XPS and NEXAFS beamtimes at the Elettra synchrotron. Thanks also to the beamline scientists there—**Luca Floreano**, **Albano Cossaro** and **Alberto Verdini**—for their great assistance at the five-star beamline ALOISA.

The XSW measurements at the ESRF ID32 beamline were possible thanks to the guidance and participation of Manfred Matena and **Jorge Lobo-Checa**.

The PFP/Ag(111) dislocations could be modeled and explained with the help of the theoretical calculations and ideas of **Juanma García Lastra**.

My PhD included a three month research stay at the National Institute for Materials Science in Tsukuba, Japan. I am grateful to **Wakayama-san** not only for hosting my stay and for his guidance in the lab but also for his eagerness to introduce me to the Japanese culture.

Thanks go also to **Patrizia Borghetti** for her heroic work helping us stitch together all our mixed data (and for providing vital sustenance in the form of *Nackis*®), to office mates **Rubén González**—for a fruitful collaboration (leading to publications in prestigious journals such as *J. Procr.*) and for his poky encouragement—and **Zakaria El-Degwy**, whom I hope to meet again soon.

Extra thanks go to **Manfred Matena**, for all his help with the XSW data analysis inside the lab, but for a lot more besides outside it; to **Afaf El-Sayed**, my inversely fluorinated friend, for discussions, arabic lessons and her friendship (and for that final kick I needed to get my thesis submitted); and finally to **Pinkitxo**, my counterpart, for these five years under the same roof, for sharing with me music, morcilla & much more.

Lastly, to **my famerly** for their encouragement (and even for some science talk `<skuik>pohiaps???<\skuik>`)!

A more mundane but important note on money: it makes the world go round, and without it, I would not have been able to go ahead with my PhD. Thanks to the **Donostia International Physics Center** for a generous grant.

This document was created using the LaTeX thesis template made available by OpenWetWare.org.

Contents

1

Metal-Organic Interfaces

1.1 Introduction

Organic films have attracted tremendous interest over the last few decades due to their potential use as components in organic electronic devices such as light emitting diodes (OLED), field-effect transistors (OFET) and photovoltaics (OPV). In this field previously dominated by inorganic materials, organics offer a wide range of new possibilities such as device flexibility, light weight, and most importantly, a much lower production cost. [1]

Some of these devices can already be found on the market, such as OLED televisions from the well-known companies LG (2012) and Samsung (2013), while many more are still being developed: the first prototype of a flexible OLED display based on organic transistors was recently unveiled by SONY (2010), and flexible OPVs are slowly entering the market, with record efficiencies of up to 12% achieved in the laboratory [2].

Organic electronic devices are composed of a thin organic layer sandwiched between two electrodes. Focusing on the example of a photovoltaic cell, the organic layer is made up of two components, donor and acceptor molecules. The contact area between donor and acceptor is called a heterojunction. When light strikes the organic layer, photons are absorbed, exciting electrons in the material and thereby forming excitons. These then migrate towards the donor-acceptor interface, where they separate and flow as free charge carriers to the electrodes. One of the crucial aspects of this process is the charge extraction at the organic/metal interfaces, which of course depends on the nature of the interface.

Both the crystalline structure and the electronic properties of the organic layer and the metal will affect the charge extraction process at their interface. For this reason, a large part of the research in this field is devoted to the study of organic monolayers deposited on conducting substrates, and seeks to understand the basic workings of these interfaces.

On the other hand, there is still much to learn about the basic properties of matter. Working with small molecules on atomically flat metal substrates in ultra high vacuum provides the simplest setting in which to learn about these. At the most basic level is the study of single molecules [3], which aims to understand their intrinsic properties, the effect of the environment (e.g. substrate, defects, or neighboring molecules), and even single molecule chemistry, by imaging reactions in real space [4]. Advances in scanning tunneling microscopy (as well as spectroscopy) and atomic force microscopy have opened up this new field of research by enabling submolecular imaging.

Other studies focus on full monolayers, which often arrange into ordered patterns, driven by what is called self-assembly. In such systems, the balance of molecule-molecule and molecule-substrate interactions determines the final structure of the overlayer. The incredible variety of molecules, and the ability to very specifically functionalize them, has allowed the detailed study of the interactions that drive their assembly. Today our understanding of these enables us to control and tailor the structure of the layers, and has givien birth to the concept of supramolecular engineering [5].

1.2 Self-Assembly of Organic Layers

When deposited onto a substrate, molecules will very often spontaneously assemble into a compact ordered layer. This process is referred to as self-assembly [6]. The driving forces behind this phenomenon are weak non-covalent interactions between the system's components. In nature self-assembly occurs on a grand scale, building up life from matter: we find it in DNA, whose curious helix structure stems from hydrogen bonding between both strands, in the folding of proteins, whose form is essential for their proper function, or in the double lipid layer surrounding each of our cells. The same interactions are at work in our more primitive systems consisting of molecules deposited on a metal surface, and are the cause of the formation of ordered overlayers.

In order to understand the basic physics involved in the self-assembly process, the interactions in these systems can be divided into molecule-substrate and molecule-molecule interactions. It is the balance and optimization of these interactions, as well as the kinetics of the system, that ultimately determine the structure of the molecular overlayer. In this section, we try to give a brief overview of the interactions governing the assembly, mainly based on Refs. 7 (molecule-substrate interactions) and 8 (intermolecular interactions).

1.2.1 Molecule-Substrate Interactions

The first step in the self-assembly of a molecular overlayer is the adsorption of the molecule on the metal substrate. All atoms and molecules experience attractive long-range van der Waals forces. This means that anything will "stick" (adsorb) on a surface, if the temperature is low enough. Depending on the interaction strength, adsorption can be physisorptive or chemisorptive.

Physisorption can be described in terms of a short range repulsive potential $V_{\text{rep}}(z)$, and a long range attractive potential $V_{\text{attr}}(z)$, z being the atom-surface separation along the surface normal. The $V_{\text{rep}}(z)$ term describes the so-called Pauli repulsion experienced by the approaching adsorbate as orbitals of the surface and the molecule begin to overlap. It represents the cost of keeping the overlapping states orthogonal (orthogonalization energy), as dictated by Pauli's exclusion principle. On the other hand, the attractive van der Waals term can be described by

$$V_{\text{attr}}(z) = \frac{C}{(z - z_0)^3} + O(z^{-5}).$$

Van der Waals interactions arise from the interaction of an instantaneous dipole in the molecule (or atom) with an induced charge fluctuation in the metal. Therefore, the constant C is related to the polarizability of the atom and the dielectric function of the metal[1].

In physisorption the adsorbate's energy levels experience little or no change. However, when stronger interactions are present, actual chemical bonds between adsorbate and surface can be formed, and the adsorbate's levels can be substantially modified. In such cases we talk of chemisorption.

---

[1] The van der Waals interaction between two atoms decreases as z^{-6}, however due to many-body effects, the physisorption interaction between surface and adsorbate decays more slowly, as z^{-3}.

In **chemisorption**, as the molecule approaches the surface, its electronic states interact with those of the metal. As a consequence, the energy of the molecular orbitals' changes. Though the energetic ordering of the orbitals generally does not change, the spacing between them may. Also, interaction with the surface may split levels that were degenerate in the gas phase. If there are no substrate electrons at the energy of a molecular orbital, it will remain sharp. This is the case of adsorption on insulators or semiconductors, in which molecular frontier orbitals (typically dominating the adsorbate/substrate chemistry) fall in the band gap, limiting the interaction to a weak physisorption .

The interaction with broad bands, such as s- or p-bands, gives rise to a weak coupling that causes a lowering and broadening of the molecular orbitals, whereas the interaction of a molecular level with a narrow, more localized metal band, such as a d-band, has a much more pronounced effect. The strong coupling gives rise to distinct new levels: bonding and anti-bonding orbitals are created, below and above the metal band, respectively. These two contrasting cases are shown schematically in Fig. 1.1.

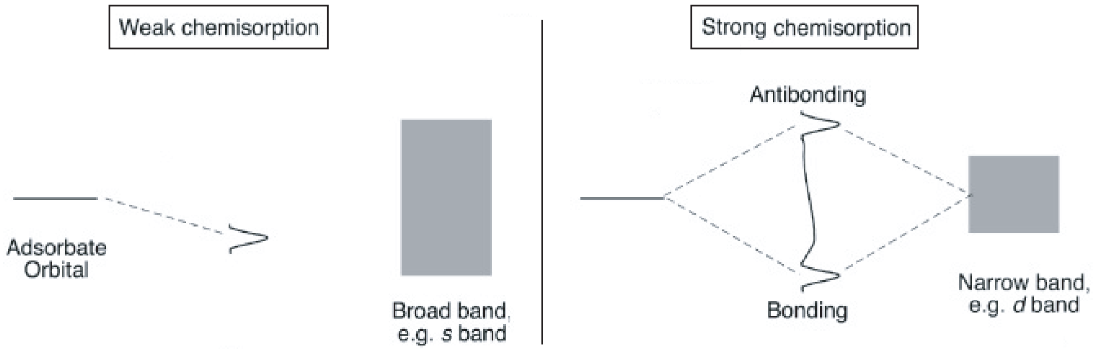

Figure 1.1: Weak chemisorption: interaction of an adsorbate orbital with a broad band (e.g. s-band) results in a broadening and lowering of the adsorbate level. Strong chemisorption: the adsorbate level interacts strongly with a narrow band (e.g. d-band) and is split into a bonding and an anti-bonding combination, one below and one above the metal band. Adapted from Ref. 7.

Typically, the interaction with a d-band metal is considered as a two step process. In the first step (1) the molecule interacts with the sp-band, causing a lowering of the molecular orbitals. In a second step (2) the levels overlapping with the d-band split into the bonding/antibonding combination. The interaction strength between molecule and substrate is determined by the relative occupancy of these two orbitals: if only the bonding states are filled, the bond will be a strong one; however, filled or partially filled anti-bonding states will weaken the bond. The filling of states depends on the position of the d-states relative to the Fermi level, which varies from metal to metal. Moving from left to right across the row of transition metals the d-bands shift downwards relative to E_F. Therefore, for early transition metals the anti-bonding state lies above the Fermi level and is empty, making both steps (1) and (2) attractive. On the other hand, in Cu, Ag and Au the anti-bonding state has dipped below the Fermi level and is full, resulting in a repulsion that tends to cancel out the attraction from step (1).

In order to explain the different reactivities of Cu, Ag and Au (i.e. across a column of the period table), the coupling strength in step (2) must be considered. The orthogonalization energy associated with the interaction between molecular and metal states increases as the d-orbitals become more extended. Au's 5d orbitals are more extended than Cu's 3d orbitals, making the interaction with Au more repulsive.

Summarizing, there are two factors determining the strength of the chemisorption interaction:

- the degree of filling of the antibonding adsorbate-metal d-states, which is related to the position of the d-band with respect to the Fermi level, and increases left to right across a row of transition metals in the periodic table
- the coupling strength, which is related to the expanse of the d-bands and increases down a column in the periodic table.

The frontier orbitals in organic semiconductor molecules normally have π-character (oriented perpendicular to the molecular plane) and their interaction with the metal's d-band determines the strength of the adsorbate-substrate interaction. The optimization of these π-d interactions often results in a flat-lying adsorption geometry. By contrast, in cases where interaction with the substrate is weaker, molecules tend to adopt a standing position in order to optimize intermolecular interactions by maximizing contact.

1.2.2 Intermolecular Interactions

Though certainly the weakest, **van der Waals interactions** are also the most ubiquitous of the intermolecular interactions. They are long range interactions and lack directionality and selectivity. As mentioned earlier, they are an attractive force arising from the interaction of an instantaneous dipole in the molecule with an induced charge fluctuation in the metal or other molecule. In systems where stronger competing forces are absent, van der Waals interactions have been found to determine the structure of the overlayer (see Fig. 1.2a) [9]. (Van der Waals interactions are also believed to be responsible for the gecko's ability to "stick" to virtually any surface [10].)

Substrate mediated interactions are interactions that arise from the effect of adsorption on the substrate. Adsorbates (or surface defects) on a metal act as scattering centers for the substrate's electrons, creating so-called Friedel oscillations in the surface charge density [11]. This change in the surface potential can have an effect on the adsorption of other molecules, creating more or less favorable adsorption sites. The perturbation of the substrate's electronic structure due to hybridization with an adsorbate can also affect the adsorption of further molecules, as was verified experimentally for benzene on Pt(111) [12]. Another form of substrate mediated interaction can involve the perturbation of the crystal structure by adsorption, though this is limited to strongly chemisorptive interactions [13].

Dipole-dipole interactions refer to interactions among permanent molecular dipoles (and even higher multipoles) and have a $\sim r^{-3}$ dependence. Both in-plane electric dipoles [14] and out-of-plane dipoles [15; 16] have been found to have an effect on molecular ordering. The latter can also arise from the interface dipole due to molecular adsorption. Theoretical modeling shows that interaction between phases made up of dipoles of two different magnitudes can lead to phase separation into a well-defined pattern [17], which has served to explain several experimental results [15; 16]. An example of a molecular layer in which dipole-dipole interactions play a dominant role is shown in Fig. 1.2b

Metal coordination was first studied in solution, and proved to be an excellent technique to form highly ordered and stable porous molecular networks, offering a high degree of control. Today, the possibility to form analogous networks on surfaces has been demonstrated. Adsorbed molecules can form coordination molecules with metal adatoms from the substrate itself [18], or with metallic atoms deposited onto the surface [19; 20]. Coordination bonds are selective, directional, and relatively strong, as compared with hydrogen bonds for example. An example of a coordination network is shown in Fig. 1.2c.

Hydrogen-bonds are perhaps the most "famous" interactions, and are of particular importance to the work presented in this thesis. In a hydrogen bond a hydrogen atom H is covalently bound to a more electronegative atom X, creating partial positive and negative charges in H and X, respectively. An electrostatic attraction between the partially positive H and additional atom A can then arise. The more electronegative the X atom, the more intense the attraction. The situation is commonly represented as X-H $\cdots$ A. The most typical example is that of a water molecule: H-O-H $\cdots$ O-H_2.

Though all hydrogen bonds are electrostatic, the degree of their electrostatic character can vary widely, from a partly covalent H $\cdots$ A link in strong hydrogen bonds to weak interactions such as C-H $\cdots$ O. The interaction strength of hydrogen bonds therefore spans a large range of energies, from around 40 kcal/mol to 0.25 kcal/mol [21; 22]. Stronger H-bonds tend to show shorter bond lengths and a stronger directionality that favors linearity (180°, angle between X-H and H $\cdots$ A). Examples of hydrogen bonds and their interaction strengths are shown in Fig. 1.3, and Table 1.1 summarizes the most relevant features of hydrogen bonds.

The literature is filled with examples of monolayers—both single component [23] or more commonly multi-component [24; 25]—whose structure is determined by hydrogen bonding. An example of one if these is shown in Fig. 1.2d.

A well known family of H-bonded network is that of blends of fluorinated and non-fluorinated molecules, such as those studied in this thesis. The CH $\cdots$ FC hydrogen bonds in these systems are among the weakest (see Fig. 1.3), in spite of the large electronegativity of F. This is due to the lack of polarizability of fluorine [21]. Fluorination (the exchange of a molecule's hydrogen atoms for fluorine atoms) increases the the molecule's ionization potential and electron affinity, and is a way to create an n-type semiconductor from a p-type semiconductor. These molecular blends can therefore be considered donor-acceptor blends, which are relevant in optoelectronics applications.

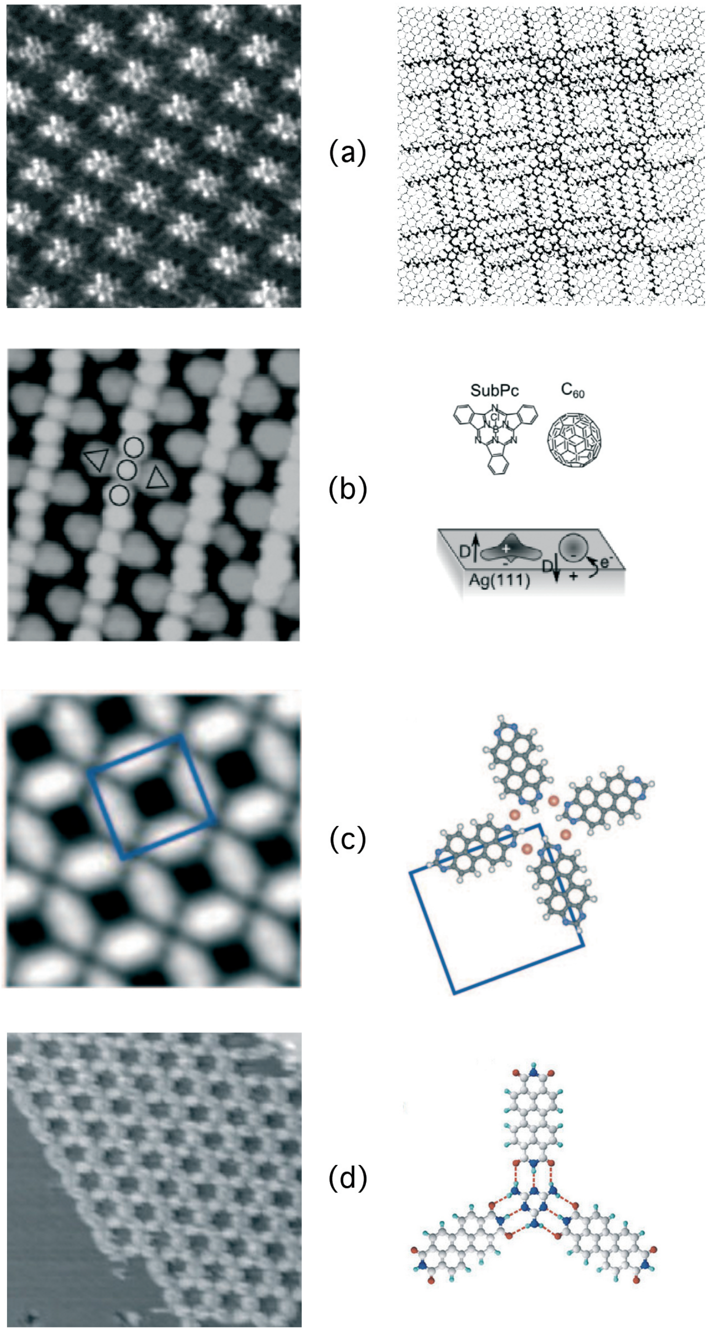

Figure 1.2: Molecular monolayers with different dominating intemolecular interactions. (a) van der Waals interactions stabilize the monolayer of alkylated metal $PcOC_8$ on HOPG. Adapted from Ref. 9. (b) Dipole-dipole interactions phase separates molecules with different dipolar moments, SubPC and C_{60}, into a striped pattern. Adapted from Refs. 15 and 8. (c) Metal coordination arises in the TAPP/Cu(111) system. Adapted from Ref. 18. (d) Hydrogen bonding drives the assembly of this ordered PTCDI-melamine network. Adapted from Ref. 26.

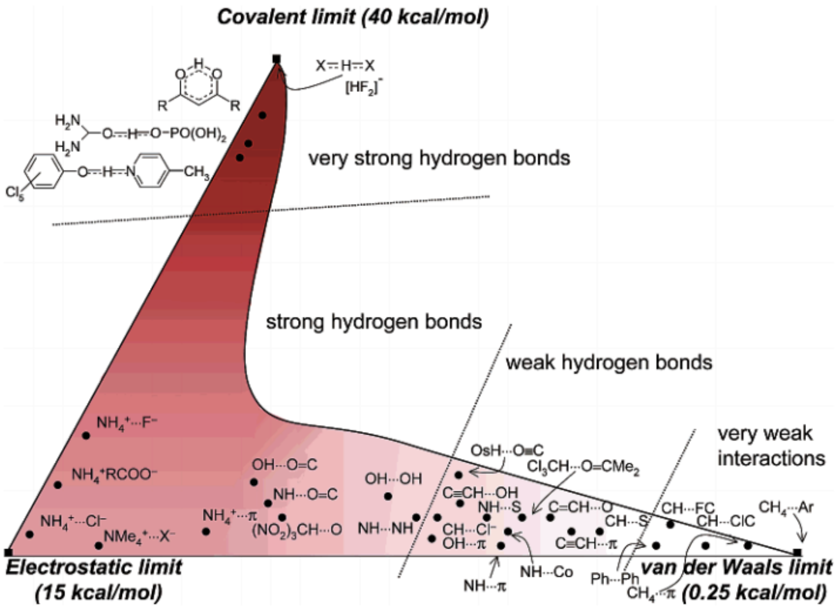

Figure 1.3: Diagram of H-bond strength. Three extreme situations of widely differing energies are shown. The figure serves as a rough guide to the balance of electrostatics, van der Waals nature, and covalency in an H-bond. Taken from Ref. 21.

	Strong	Moderate	Weak
interaction type	strongly covalent	mostly electrostatic	electrostatic/ dispersive
bond lengths (Å)			
H · · · A	1.2 – 1.5	1.5 – 2.2	> 2.2
lengthening of X-H (Å)	0.08 – 0.25	0.02 – 0.08	< 0.02
X-H vs H · · · A	X-H $\simeq$ H · · · A	X-H $<$ H · · · A	X-H $\ll$ H · · · A
X· · ·A (Å)	2.2 – 2.5	2.5 – 3.2	> 3.2
directionality	strong	moderate	weak
bond angles (°)	170 – 180	> 130	> 90
bond energy (kcal/mol)	15 – 40	4 – 15	< 4

Table 1.1: Strong, moderate and weak hydrogen bonds following the classification of G. A. Jeffrey, *An Introduction to Hydrogen Bonding*, Oxford University Press, 1997. The numerical values are meant to be guiding values. Adapted from Ref. 22

1.2.3 Epitaxy

As a consequence of interactions between the substrate and the self-assembled overlayer, a geometric relationship may arise between the two lattices. This geometric relation between substrate and overlayer is referred to as epitaxy.

Before addressing the different types of epitaxy, we will introduce the concept of *domains*. The molecules in a crystalline overlayer and the associated unit cell normally adopt a very specific orientation with respect to the underlying substrate. As a result of the symmetry of the substrate, the overlayer can grow on the substrate in different, equivalent, orientations. For example, a FCC (111) surface, such as those this work concentrates on, has a C3 symmetry and three mirror planes[1]. This means that there will be six different domains: three are related by 120° rotations, and the other three are the corresponding mirror domains, related to the former by reflection, as shown in Fig. 1.4. The symmetry of the overlayer can make some of these coincide, reducing the number of different domains.

As described in Hook's epitaxy review [27], an expitaxial interface can be fully characterized by seven parameters: $\mathbf{a}$, $\mathbf{b}$ and α, the lattice parameters of the overlayer; $\mathbf{A}$, $\mathbf{B}$ and β, the lattice parameters of the substrate, and θ the azimuthal angle between the lattice vectors $\mathbf{a}$ and $\mathbf{A}$. The overlayer and substrate lattices can be related in the following way:

$$\begin{pmatrix} \mathbf{a} \\ \mathbf{b} \end{pmatrix} = C \begin{pmatrix} \mathbf{A} \\ \mathbf{B} \end{pmatrix} = \begin{pmatrix} c_{11} & c_{12} \\ c_{21} & c_{22} \end{pmatrix} \begin{pmatrix} \mathbf{A} \\ \mathbf{B} \end{pmatrix}$$

where

$$c_{11} = \frac{b\sin(\alpha-\theta)}{a\sin(\alpha)} \qquad c_{12} = \frac{b\sin(\theta)}{A\sin(\alpha)}$$

$$c_{21} = \frac{B\sin(\alpha-\theta-\beta)}{a\sin(\alpha)} \qquad c_{22} = \frac{B\sin(\theta+\beta)}{A\sin(\alpha)}$$

The transformation matrix C describes the relative geometries of overlayer and substrate. Matrices corresponding to different domains of the same overlayer structure

---

[1] The FCC (111) surface appears to have six-fold symmetry if only the first atomic layer is considered, however, if the stacking of the first few layers is taken into account, the symmetry is reduced to three-fold. Curiously however, the symmetry of the molecules makes the domains generated by the six-fold symmetry indistinguishable from those that would be generated by a three-fold symmetry.

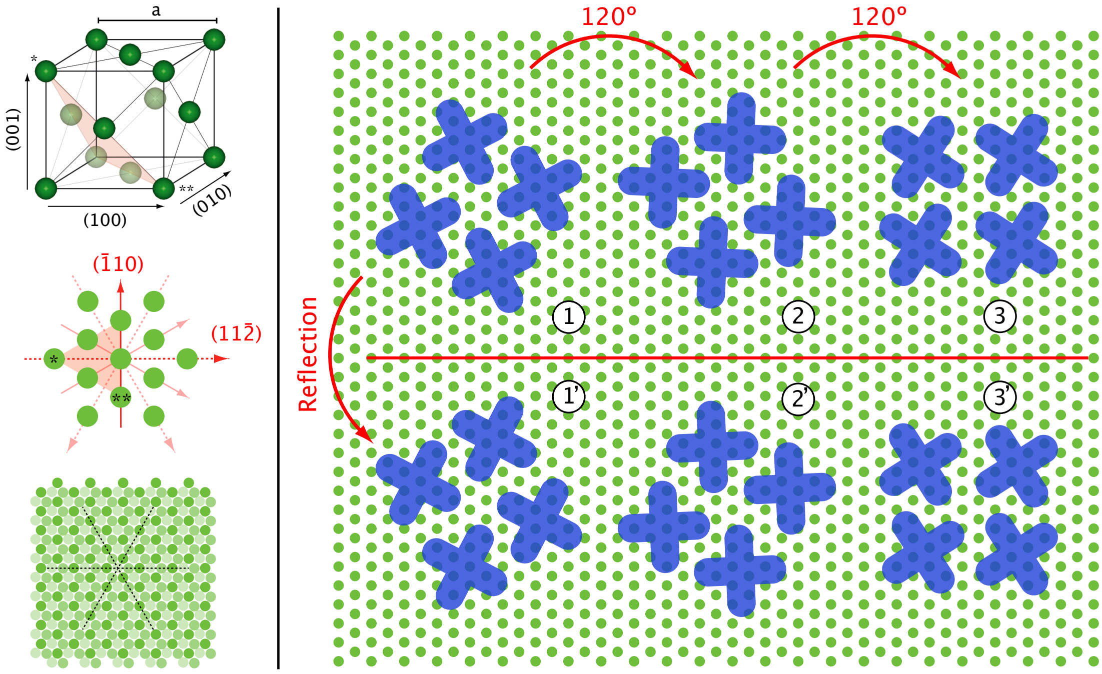

Figure 1.4: Substrate symmetry and domains. Left: face centered cubic structure with (111) plane marked pink. Below, the principal directions of the (111) surface are marked in red. The C3 symmetry and three mirror planes of the fcc (111) surface is shown at the bottom, with different shades of green indicating the different atomic layers. Right: The three-fold symmetry of the fcc (111) substrate gives rise to six equivalent domains. Blue crosses represent molecules.

are related to one another by rotation and reflection matrices. Using this matrix C, the different types of epitaxy can be classified in the following manner:

- Commensurism: The matrix elements c_{ij} are all integers and the overlayer lattice points lie simultaneously on two primitive substrate lines and coincide with symmetry equivalent substrate points (Fig. 1.5a). Each primitive overlayer lattice vector is an integer multiple of an identically oriented substrate lattice vector. Commensurism is also known as "point on point" (POP) coincidence.

- Coincidence-I: Among the c_{ij} at least two integers are confined to a single column of the matrix, and every lattice point of the overlayer lies at least on one primitive lattice line of the substrate. For this reason, this type of epitaxy is also called "point on line" (POL) coincidence. POL coincidence can be subdivided into two types:

  - Coincidence-IA: all the matrix elements are rational numbers, as shown in Fig. 1.5b for two alternative unit cells.

  - Coincidence-IB: At least one of the non-integer elements in the matrix is an irrational number. This produces an incommensurate relation between the overlayer and substrate along the coincideing primitive lattice vector. A coincidence-IA cell may appear to be a coincidence-IB cell if its supercell size exceeds the bounds of the experimental measurements.

- Coincidence-II: The c_{ij} are rational, but no column consists of integers. Only some of the overlayer lattice points lie on primitive substrate lattice lines, as shown in Fig. 1.5c.

- Incommensurism: At least one of the matrix elements are irrational numbers and neither column of the traslationa matrix consists of integers. Under this condition, no distinctive registry between the substrate lattice and the overlayer exists.

The types of epitaxy that have just been described roughly reflect a descending order of overlayer-substrate energies. In practice, the energies will depend upon the ratio of coinciding to non-coinciding lattice points, which is a measure of the degree of fit between the two lattices. Commensurism therefore represents the most favorable

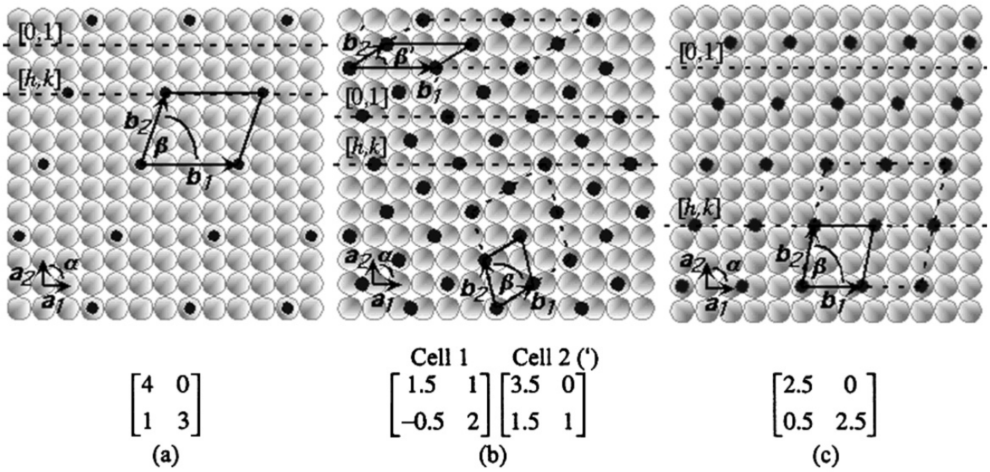

Figure 1.5: Different types of epitaxy. Overlayer lattice points are depicted as small filled circles and substrate lattice points are depicted as larger shaded circles. Overlayer primitive cells are indicated by solid lines and lattice lines are depicted by dashed lines. (a) Commensurate overlayer, (b) Coincidence-IA POL, (c) Coincidence-II. (Image from Ref. 27).

condition with respect to the overlayer-substrate energy. The reason for this is that the surface potentials of the two opposing lattices are phase coherent, optimizing the attractive interactions that drive the formation of the overlayer. [27]

1.3 Energy Level Alignment

Understanding and controlling the energy level alignment in organic-metal systems is of great interest, since it is what determines the charge injection barriers that are so important in device performance. Early on, it was assumed that the energy level alignment of weakly interacting adsorbates and the substrate would be determined by the alignment of their respective vacuum levels. In such a scenario, the electron injection barrier Φ_{Be} on different substrates is perfectly predictable, being directly related to the substrate's work function by $\Phi_{\mathrm{Bh}} = \mathrm{IE} - \Phi_{\mathrm{m}}$ (see Fig. 1.6a).[1] This is referred to as the **Schottky-Mott model**. The Schottky-Mott model is generally applicable to interfaces formed by spin-coating polymer films on metal electrodes or evaporation of molecules onto contaminated metal surfaces. However, the situation is

---

[1] Or, equivalently, $\Phi_{\mathrm{Be}} = \Phi_{\mathrm{m}} - \mathrm{EA}$

somewhat more complicated for interfaces formed in an ultra-high vacuum environment, such as those we are concerned with: experimentally it is observed that the adsorption of molecules on a surface causes a change in the metal's work function. This change is due to the modification of the interface dipole and is brought about firstly by the so-called **pillow-effect**, i.e. Pauli repulsion between the molecule's electrons and the metal's electron tail pushing the latter back into the metal, and also by other factors like charge transfer, surface rearrangement, mirror forces, chemical interactions and the molecule's permanent dipole [28]. The result is a dipole Δ across the molecule-metal interface that breaks the vacuum level alignment, as shown in Fig. 1.6b. (Though in the figure the most typical situation of a downward shift of the vacuum level is shown, many examples of upward shifts also exist.)

In the following we will discuss the interface dipole in more detail.

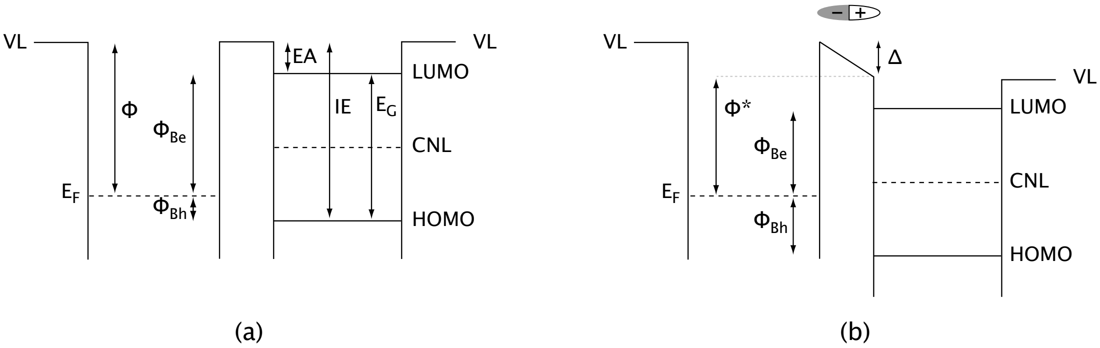

Figure 1.6: Energy level alignment diagrams neglecting (a) and accounting for (b) the interface dipole. Notice the different charge injection barriers Φ_{Be} (electron) Φ_{Bh} (hole). VL = vacuum level, E_F = substrate's Fermi level, Φ = substrate's work function, HOMO and LUMO = frontier orbitals, EA = electron affinity, IE = ionization energy, E_G = energy gap, CNL = charge neutrality level.

1.3.1 The Interface Dipole

We begin by reviewing the concept of vacuum level of clean metal surfaces, basing ourselves on the review paper of Ishii et al. [28].

Strictly speaking, the vacuum level VL(∞) is the energy of an isolated electron at rest in a vacuum. However, in practical terms, and in experiments, the vacuum level of a solid refers to the energy of an electron at rest just outside the solid. In spite of being outside, it is still affected by the solid's potential, and this "surface vacuum level" VL(s) is therefore different from VL(∞) (see Fig. 1.7a). The effect of the solid on VL(s) is clearly demonstrated by the dependence of the work-function on the surface of a single crystal: the different faces of a W crystal have substantially different work functions ($\phi_{W_{100}} = 4.63\,\mathrm{eV}$, $\phi_{W_{110}} = 5.25\,\mathrm{eV}$, $\phi_{W_{111}} = 4.47\,\mathrm{eV}$). This difference in work-function is mostly due to the surface dipole layer formed by the tailing of the metal's electron cloud into the vacuum, which is different at the different crystal surfaces. As illustrated in Fig. 1.7b, this tailing makes the vacuum side of the surface negative, and the inner bulk side positive (and the larger this dipole, the larger the work function). The potential created by the dipole layer as a function of distance is shown Fig. 1.7c and d. We consider an electron at a distance x from a dipole layer of finite extension with a representative length L. At very small distances $x \ll L$, the dipole layer can be considered to be infinitely extended. In this case, the potential energy is simply a step function across the dipole layer and $V(x)$ is independent of x. Far away from the dipole, $x \gg L$, the dipole layer can be regarded as a point dipole, so the potential decreases as x^{-2}, eventually converging to V(∞).

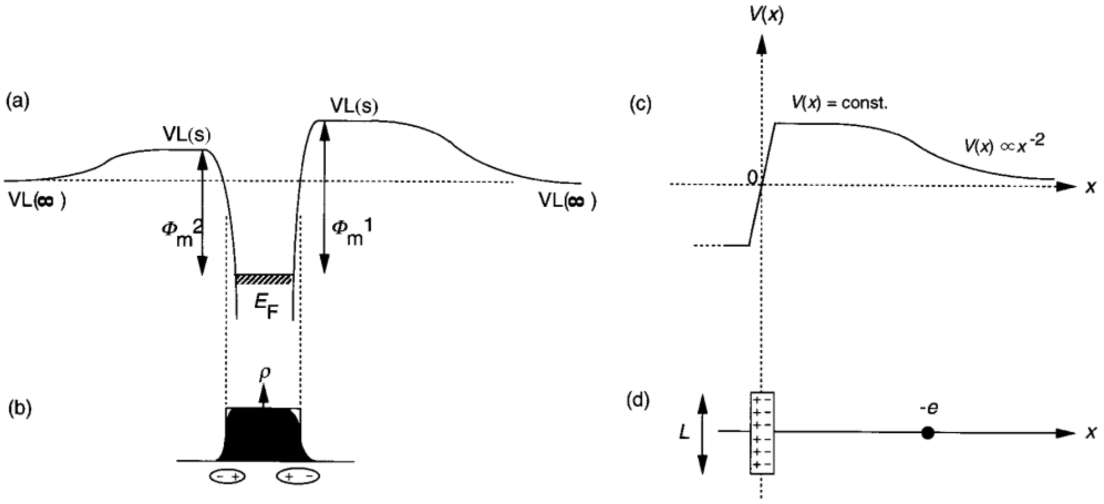

Figure 1.7: (a) Potential surface for an electron in and out of a metal crystal for two different crystal faces. (b) Electron density in the metal. Tailing at the surface forms a dipole layer. Note that the different crystal faces have different degrees of tailing, and therefore different work functions. (c) Potential at distance x from a dipole layer of extension L. (d) Dipole layer and electron at distance x, referred to in (c). Taken from Ref. 28.

Let us now consider the adsorption of a molecule on the surface of the metal. We follow the approach of Vazquez et al. [29], which breaks up the energy level alignment into two steps, (1) the pillow effect and (2) charge transfer.[1]

As the molecule approaches the surface, the repulsion between the molecule's electrons and the metal's electron tail causes the latter to be pushed back into the metal. This "push-back" or "pillow" effect modifies the metal's original surface dipole, as shown in Fig. 1.8, and causes a reduction in the metal's work function:

$$\phi^* = \phi - \Delta^{\mathrm{P}}$$

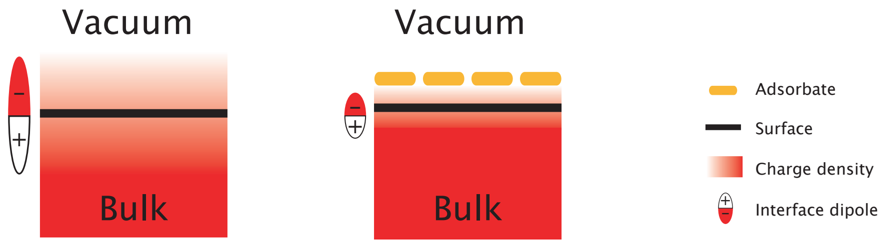

Figure 1.8: Left: Surface dipole of a clean surface due to electron cloud spilling into the vacuum. Right: Compression of the electron tail due to the presence of an adsorbate.

Next, the interface relaxes by transferring charge between the metal and the organic molecule. Before going any further we must introduce the concept of **metal-induced gap states**: due to the proximity between the organic molecule and the metal, the continuum of metal states overlaps with the molecular states, broadening them and inducing a density of states in the gap, known as metal induced gap states (MIGS) or induced density of interface states (IDIS) [31]. The energy up to which the density of states must be integrated in order to obtain the amount of charge in the neutral molecule is called the charge neutrality level (CNL). A misalignment of CNL and the Fermi level E_{F} when molecule and metal come into contact will cause a charge to flow to or from the IDIS. The dipole created by this charge flow will tend to align CNL and E_{F}. Once in equilibrium, the total charge in the IDIS will be zero if the Fermi level precisely aligns with the CNL, and positive or negative, respectively, if it is below or above it [31].

---

[1] In case of an intrinsic molecular dipole, this would simply be added directly to the dipole Δ in step (1) [30].

Therefore, when the molecule and the metal come into contact charge can flow to and from the IDIS, and this charge flow will tend to align the metal's Fermi level and the molecule's CNL.

Fig. 1.9 shows two examples of this two step process. To the left the pillow-effect (1) is represented; it creates a downward dipole barrier $\Delta^{\mathrm{P}} < 0$. If there is an IDIS in the molecule, the metal-molecule system will now relax through charge transfer (2), creating the additional dipole Δ^{IDIS} and resulting in a total dipole $\Delta^{\mathrm{TOT}} = \Delta^{\mathrm{P}} + \Delta^{\mathrm{IDIS}}$. In the first example, the molecule's CNL falls above the Fermi level, $E_{\mathrm{F}} > E_{\mathrm{CNL}}$, so charge flows from the molecule's gap states to the metal and Δ^{IDIS} has the same sign as Δ^{P}. In the second, $E_{\mathrm{F}} < E_{\mathrm{CNL}}$, so charge from the metal flows into the molecule's the gap states and Δ^{IDIS} and Δ^{P} have opposite signs. In both cases the charge flow and the resulting barrier Δ^{IDIS} tend to align E_{F} and E_{CNL}.

How closely they are actually able to align depends on the IDIS available to give or receive charge in the molecule (in Fig. 1.9 above, they are not able to completely align). The screening parameter S is a measure of this, and can be defined as $S = d\Phi_{\mathrm{Be}}/d\Phi_{\mathrm{m}}$

The additional dipole created due to charge transfer to or from the IDIS is

$$\begin{aligned}\Delta^{\mathrm{IDIS}} &= (1-S)(\Phi_{\mathrm{m}}^{*} - \mathrm{CNL}) \\ &= (1-S)(\Phi_{\mathrm{m}} - \Delta^{\mathrm{P}} - \mathrm{CNL}).\end{aligned}$$

Combining the pillow and IDIS contributions we obtain a total dipole [29]

$$\Delta^{\mathrm{TOT}} = \Delta^{\mathrm{IDIS}} + \Delta^{\mathrm{P}} = (1-S)(\Phi_{\mathrm{m}} - \mathrm{CNL}) + S\Delta^{\mathrm{P}}.$$

At one extreme, we can imagine a situation in which $S = 0$. This means that the IDIS is large enough to provide/accept all the charge necessary to completely align E_{F} and CNL, for any value of Φ_{m}. In such a case the electron injection barrier is fixed, and what varies with Φ_{m} is the magnitude of the dipole set up at the interface (related to the amount of charge transferred). This situation is called **Fermi level pinning**.

At the other extreme is the situation where no IDIS is available to give or take charge to or from the metal, and $S = 1$. In such a case E_{F} and CNL are unable to align and the interface dipole, and therefore the Φ_{Be}, is determined solely by the push back effect (only step (1) takes place in Fig. 1.9).

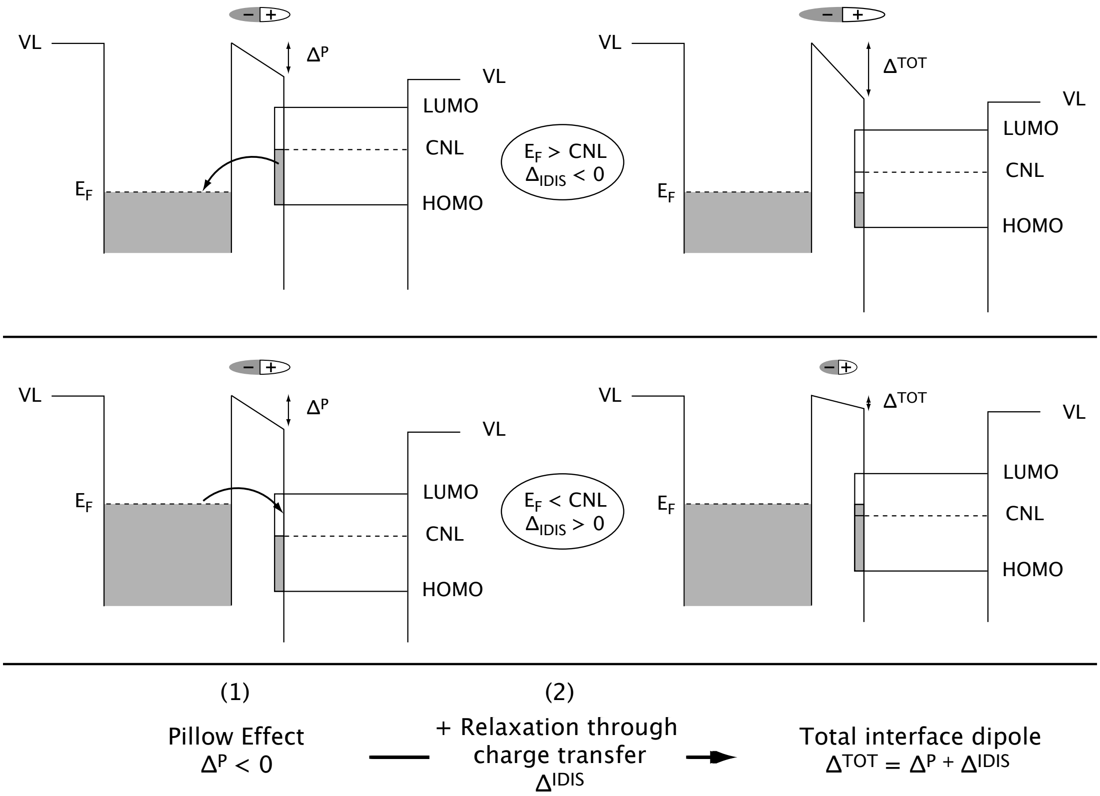

Figure 1.9: Contribution of (1) the pillow effect (Δ^{P}) and (2) charge transfer (Δ^{IDIS}) to the interface dipole. Above: $E_{\mathrm{F}} > E_{\mathrm{CNL}}$, charge flows from the molecule to the metal substrate. Below: $E_{\mathrm{F}} < E_{\mathrm{CNL}}$, charge flows from the metal to the molecule. In both cases the charge flow creates an additional surface dipole Δ^{IDIS} that tends to align E_{F} and E_{CNL}. The partially filled grey bar represents the IDIS, and arrows indicate the direction of charge transfer.

The most typical situation is one between these two extremes, with $0 < S < 1$: charge transfer brings E_{F} and CNL closer together, contributing to the interface dipole, but is not able to completely align them due to a limited IDIS.

The vacuum level alignment of the Schottky-Mott model (Fig. 1.6a) corresponds to a case with no IDIS and no pillow-effect ($\Delta^{\mathrm{P}} = \Delta^{\mathrm{IDIS}} = 0$), and we find $S = 1$ when E_{F} falls anywhere within the gap, since $\Phi_{\mathrm{Be}} = \Phi_{\mathrm{m}} - \mathrm{EA}$. However, for values of Φ_{m} that have E_{F} fall outside the gap, a charge transfer will be possible between the frontier orbitals and the metal, and a dipole layer will be set up at the interface, breaking the vacuum level alignment.

Fig. 1.10 shows some experimental examples by Hill et al. [32] for films of PTCDA, $\mathrm{Alq_3}$ and CBE on various metal substrates. The Shottky-Mott limit is represented by a dashed line. For PTCDA, the position of E_{F} within the gap does not vary for different values of the work function, indicating Fermi level pinning ($S \simeq 0$); $\mathrm{Alq_3}$ on the other hand shows nearly the $S = 1$ limit. The offset between the experimental results and the dashed line representing the Schottky-Mott limit represents the interface dipole (in this case nearly exclusively due to the pillow effect). The last example, CBP, is an intermediate case, with $S = 0.6$ and contributions from both the pillow effect and charge transfer to the interface dipole.

1.4 Phthalocyanine and Pentacene

The molecules used in this work are copper phthalocyanine (CuPc) and pentacene (PEN), as well as their respective perfluorinated compounds, fluorinated copper phthalocyanine (FCuPc) and perfluoropentacene (PFP). These are flat, π-conjugated organic semiconducting molecules, widely studied due to their promising performance in organic electronic devices.

Perfluorination is a process that replaces a molecule's peripheral hydrogen atoms with fluorine atoms. This tends to increase the molecule's ionization potential and electron affinity, making it favor electron- rather than hole-transport (i.e. p-type semiconductors can be made into n-type semiconductors) [33]. Its size however, remains practically unchanged. The chemical structure of the (non-fluorinated) molecules is shown in Fig. 1.11.

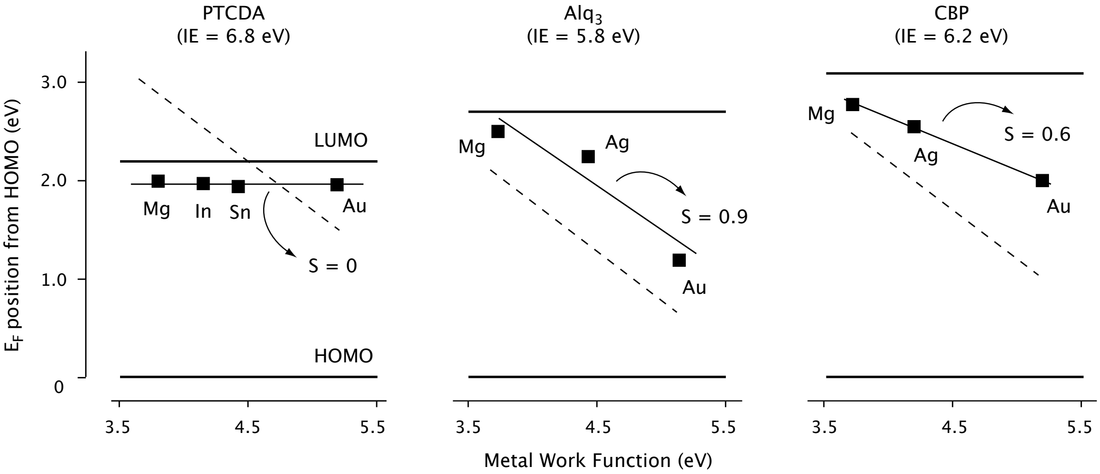

Figure 1.10: Position of Fermi level in the gap for three organic molecules (PTCDA, Alq$_3$ and CBP) as a function of metal work function. The HOMO of the three organics are aligned and each LUMO is positioned according to the optical band gap. The slope of the lines represent the screening parameter S. The oblique dashed lines correspond to the Schottky-Mott limit ($S = 1$). Adapted from Ref. 32.

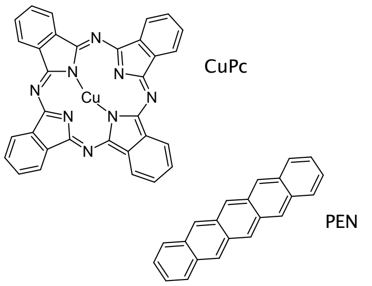

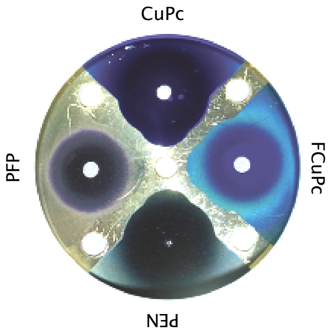

Figure 1.11: Left: Chemical structure of Copper Phthalocyanine (CuPc) and Pentacene (PEN). Right: The color of each molecule can be seen from the residual molecular powder on this evaporator.

Phthalocyanines are dyes closely related to natural occurring porphyrins, such as hemoglobin, chlorophyll a, vitamin B12 and turacin (a red pigment found only in the wings of the African turaco birds). Like porphyrins, they are excellent ligands that can coordinate with nearly any metal.[1] Phtalocyanines, however, do not occur in nature, but are synthetic molecules. Their color ranges from reddish blue to yellowish green and they have been widely used as dyes in ink, paint, plastics and textiles since the 1930s. The most widely used phthalocyanine in the industry is Copper phthalocyanine or CuPc, which is produced worldwide; it has a blue shade (see Fig. 1.11) and is most widely used in printing inks, while its chloro and bromo derivatives are important green organic pigments. Phthalocyanines have extremely poor solubility in organic solvents and a high thermal stability [34]. Today, CuPc has found new application in the field of nanotechnology thanks to its high thermal stability and semiconducting properties. It has been successfully integrated in organic devices such as field-effect transistors [35], light emitting diodes [36] and solar cells [37], and and is widely studied for this reason.

Pentacene is another synthetic semiconducting molecule, first synthesized in 1912 [38]. Interest in PEN as a promising p-type organic semiconductor has grown in recent years due to its remarkable performance in devices. Indeed, PEN thin film transistors have produced one of the highest charge carrier mobilities of any organic field effect transistor, even matching that of amorphous silicon [39]. Perfluorination of PEN leads to an increase of about 1 eV in its ionization potential and electron affinity [40]. PEN and PFP can be combined to obtain high-performance p-n junctions and complementary circuits [41].

---

[1] The porphyrin in hemoglobin is coordinated with Fe, chlorophyll with Mg, vitamin B12 with Co, turacin with Cu. Porphyrins are ring-shaped and the metallic atom is held in the center of the ring.

2

Experimental Techniques

2.1 UHV Basics

All the experiments performed for this thesis took place in ultra high vacuum (UHV) conditions. Ultra high vacuum is usually defined as the region below 10^{-9} mbar and is essential for many surface science experiments because it is the only way to procure atomically clean surfaces and maintain them contamination-free long enough to perform the experiment. Techniques relying on beams of particles or higher energy radiation additionally require UHV because it allows the beams to travel undisturbed until striking the surface or detector. [42]

Using kinetic theory of gases, it is possible to estimate the contamination time, i.e. the time taken for a perfectly clean surface to acquire a monolayer of contaminant. This time depends on molecular weight, temperature, pressure and the reactivity of the system (expressed as a sticking coefficient s—the probability that an incident molecule will remain on the surface, $0 \leq s \leq 1$). However, as a rule of thumb at a pressure of 10^{-6} mbar a surface will remain clean for around 10^{1} s, at 10^{-7} mbar it will remain clean for around 10^{2} s and so on. This means that at typical UHV pressures (10^{-10} mbar) the sample surface will be free of contaminants for $10^{5}\,\mathrm{s} \sim 1\,\mathrm{day}$, long enough to perform an experiment. Figure 2.1 shows the relationship between pressure, contamination time and mean free path lengths (the average distance travelled by a particle before undergoing a collision with another).

In order to reach the UHV regime multiple pumps are used. First, the chamber will be pumped down to around 10^{-2} mbar using a roughing pump. When this pre-vacuum

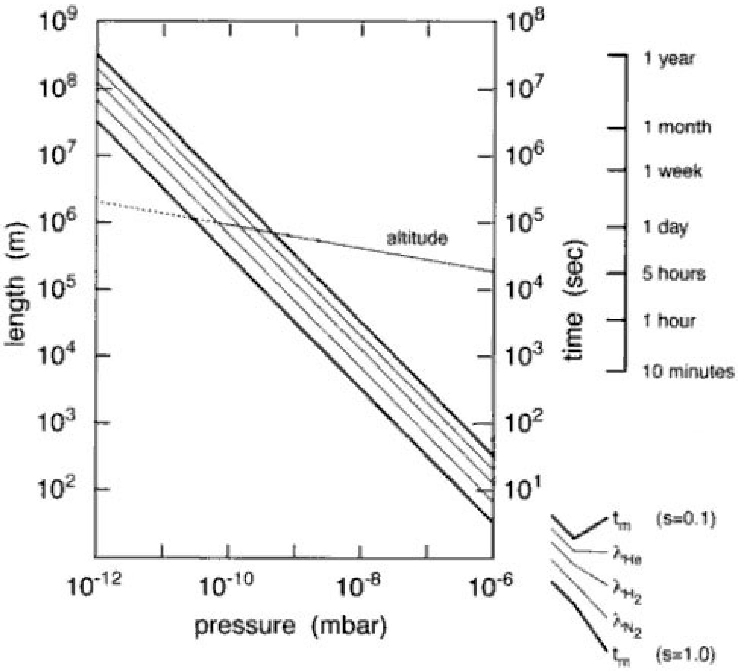

Figure 2.1: Relationship between gas pressure, surface contamination times and mean free path lengths. t_m is time contamination time of nitrogen, calculated using $s = 0.1$ and 1.0, λ_X is the mean free path of a molecule of X in X. The variation of Earth's atmospheric pressure with altitude is shown for comparison. UHV is attained at an altitude of about 900 km. Adapted from Ref. 42

pressure is obtained, the chamber can be further pumped down to about 10^{-6} mbar by a turbomolecular pump. At this stage, further pumping will not improve the pressure, as molecules from the air adsorbed on chamber walls will readily replace those being pumped out; this is called outgassing. At room temperature the adsorbed gases slowly desorb constituting a large virtual leak which would continue for years. To eliminate this problem a so-called bake-out is done. This involves heating the system to 150-200° C. In this way the adsorbed molecules, water in particular, desorb from the walls and can be removed from the chamber by the pumps. A large system is typically baked for at least 24 hours, after which it is left to cool again. At this point, the many filaments that are part of other components of the system (e.g. pressure gauges, evaporators, titanium sublimation pumps) must also be degassed by heating. By the time the system reaches room-temperature, the pressure inside will be classifiable as UHV. The chamber still needs to be pumped continuously in order to maintain UHV conditions, as there will always be some outgassing in spite of the bake-out. The dominant residual gases making up the low pressure in the chamber are usually H_2, H_2O, CO, CO_2 and a variety of hydrocarbons.

It is of course also essential that the chamber be leak free. To ensure that flanges are air tight, these are attached with bolts, which serve to compress steel knife edges within the flanges into softer copper gaskets, thus creating an all-metal leak proof seal.

UHV chambers are most commonly constructed from non-magnetic stainless steel, though other low-outgassing materials such as glass or aluminum can be used. Ceramics are used where electrical insulation is required. [42]

2.2 Scanning Tunneling Microscopy

2.2.1 Overview

An STM's principle of operation is as follows: a metallic probe tip is brought within several ångströms of the sample, close enough for the wavefunctions of the tip and the sample to overlap and generate a finite tunneling conductance. When a voltage is then applied between the tip and the sample a tunneling current I flows from one to the other. This current depends strongly on the tip's distance z from the sample, increasing by about a factor 10 per ångström. The tip is then made to scan over the surface, using a feedback loop to keep the tunneling current constant (constant current mode). Another possibility is to keep the height of the tip constant and measure the variations in the tunneling current (constant height mode). In both cases a signal is obtained (z or I) that is directly related to the topography of the sample surface, or more precisely, to its local density of states. Fig. 2.2 shows a schematic drawing of the STM's principle of operation.

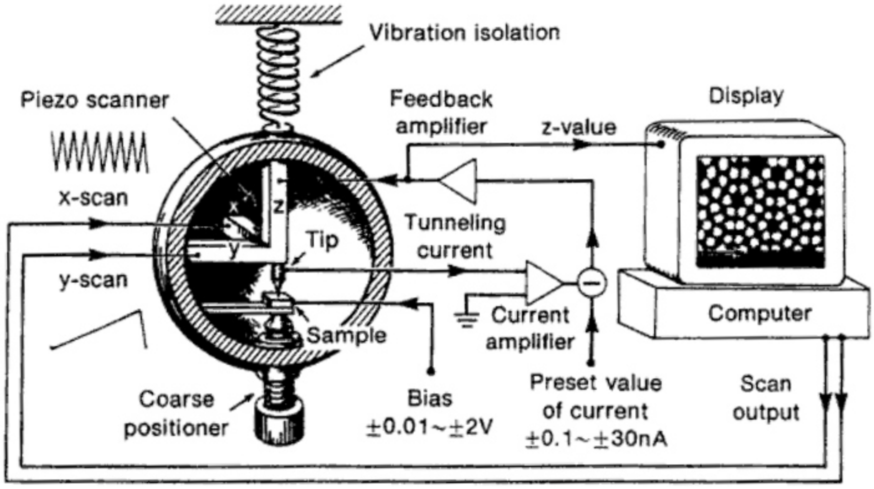

Figure 2.2: This schematic diagram of an STM shows the feedback controlled piezo scanning the tip over the sample. A potential difference is applied between tip and sample and the system is isolated from vibrations. The z values obtained during the scan are represented on the computer as a topographical image. Taken from Ref. 43.

It is clear that if the tip is to be in such close proximity to the surface a good vibration isolation system is imperative, since any vibration, caused by anything from wind to footsteps is sure to disrupt the system. Two approaches are commonly used to minimize this mechanical noise. The first is to make the STM unit as rigid as possible . The second is to reduce the transmission of vibrations from the environment. The first practical STM prototype (which according to its creators made use of a considerable amount of Scotch tape) used a primitive version of superconducting levitation, which used up 20 l of liquid Helium per hour. Today's STMs, such as the one used in the research presented here, achieve vibration isolation by a set of suspension springs and a damping mechanism, such as an eddy current damping mechanism.

Another challenge the STM presented was how to control the position of the tip with an accuracy in the ångström range. A high-performance STM requires a resolution of about 0.1 Å normal to the surface (z direction) and about 1 Å laterally (x and y

directions). Such requirements can be satisfied by using piezoelectric ceramics, i.e. materials which undergo a dimensional change when an electric voltage is applied to them. Potential differences of 1 mV to 1000 V result in mechanical motion in the range from less than one ångström to a few micrometers. Single crystals of many compounds behave in this way, for example quartz, and more recently, polycrystalline ceramic materials have been developed for this purpose.

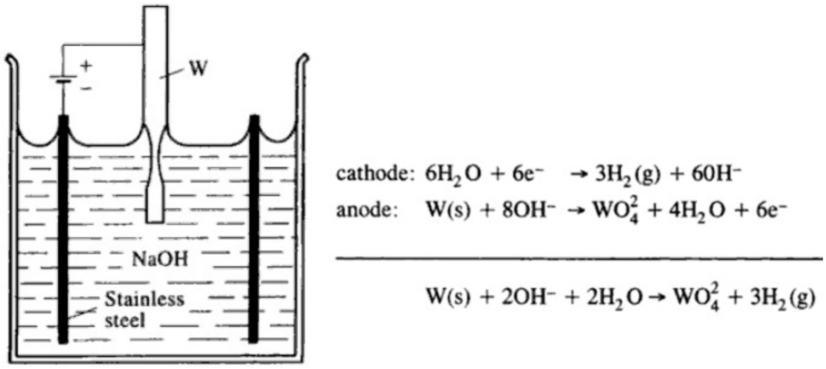

Figure 2.3: A tungsten wire (anode) being etched in NaOH. The cathode consists of a stainless-steel cylinder which surrounds the anode. The overall electrochemical reaction is $W(s) + 2OH^- \rightarrow WO_4^2 + 3H_2(g)$, i.e. the anode is etched away via oxidative dissolution of W to soluble tungstate WO_4^{2-}. Image from J. P. Ibe et al., *J. Vac. Sci. Technol. A*, **8**(4), 3570 (1990).

Finally, the subtlety of the STM lies in the tip. Its size, shape and material will influence the resolution as well as the measured electronic structure. The microstructure of the tip is the key to image resolution: it is necessary to have a single site of closest atomic approach, i.e. an atomically sharp tip. The purity of the metallic tip is important to avoid an additional tunneling barrier, for example due to an oxide layer: the effective resistance of an oxide layer on a tip could easily be much higher than the tunneling gap resistance, meaning that contact between tip and sample would have to occur before the required tunneling current could be obtained.

STM tips are typically made of tungsten (W), platinum-iridium (Pt-Ir), or less frequently gold (Au). The advantage of W is that it is a stiff metal, the disadvantage that it oxidizes easily. The opposite is true of Pt: it is a soft metal but inert to oxidation. Adding Ir to form an alloy adds stiffness while maintaining a chemically inert material. W and Pt-Ir are both widely used, the latter particularly in atmospheric and electrochemical environments. Tips can be fabricated from metal wires in a variety of ways. The preferred method for W tips is electrochemichal etching. A possible set-up is shown in figure 2.3, in which the tungsten wire serves as the anode in a NaOH or KOH solution and a stainless steel cylinder surrounding the anode as a cathode. Pt-Ir tips on the other hand, are commonly made by mechanical shearing, but can also be etched. Figure 2.4 shows SEM micrographs of a sheared tip and an etched tip.

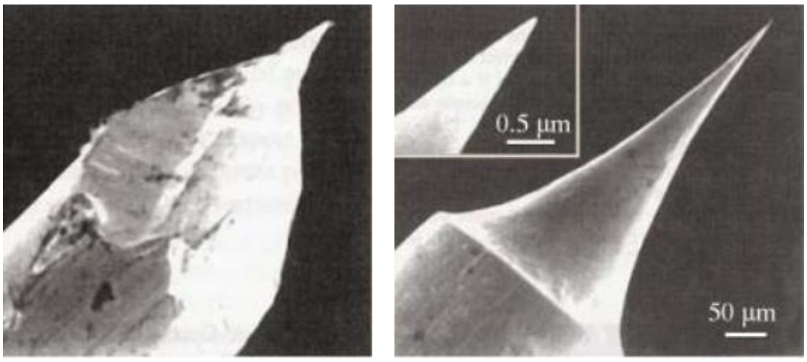

Figure 2.4: A mechanically cut STM tip (left) and an electrochemically etched tip (right). Taken from A. Stemmer *et al.* Ultramicroscopy **30**(3), 263 (1989).

The tip also inevitably undergoes changes at the atomic scale when it interacts with the sample surface. A bias of just a few volts means very local, high fields in the vecinity of the tip which will reshape it at the atomic level, influencing the imaging. Controlled crashing with the sample can also help obtain a sharp atomic tip. Figure 2.5 shows a very nice example of the spontaneous tip changes that inevitably occur and their influence on imaging.

STM measurements can be performed in air, in inert gas, in ultrahigh vacuum and even in liquids, and the operating temperature ranges from close to absolute zero to a few hundred degrees centigrade. [44]

2.2.2 A Model for STM

STM is based on the tunneling effect: a particle incident upon a potential barrier higher than the particle's kinetic energy has non-zero probability of traversing the forbidden region and reappearing on the other side. This effect is a consequence of the wavelike properties of particles and is therefore quantum mechanical in nature. The tunneling

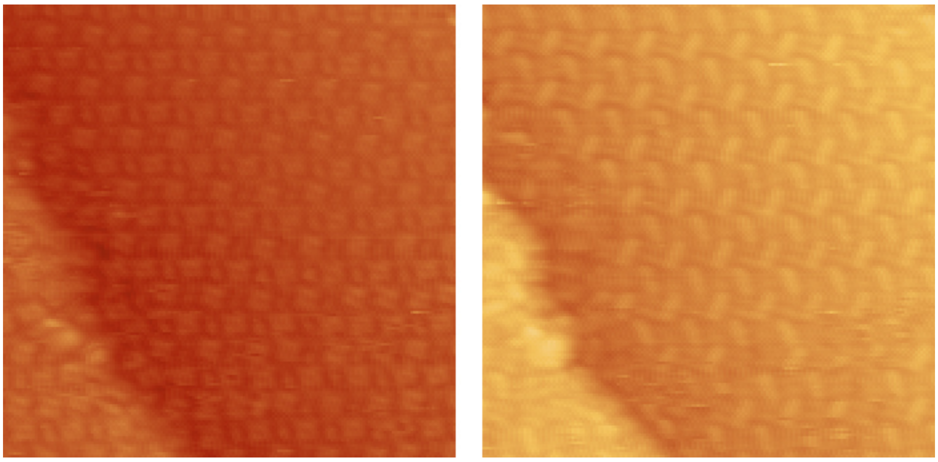

Figure 2.5: Both these images were taken at the same bias voltage and tunneling current, but a spontaneous change in the tip altered the measured electronic structure. In the image to the left the CuPc molecules (flower shape) are clearly visible, whereas in the image to right it is the PFP molecules (peg shape) which show an enhanced contrast.

effect successfully explains many physical phenomena. It was first applied by Gamow in 1928 to explain nuclear α-decay.

A first approach to STM theory can be made using a simple one dimensional model, as done in C. Julian Chen's textbook [43]. We consider an electron of energy E moving in a potential $U(z)$. In classical mechanics the electron would be described by

$$\frac{p_z^2}{2m} + U(z) = E \tag{2.1}$$

where m is the electron mass. The electron's momentum p_z is not defined in areas with $E < U(z)$; the electron cannot penetrate into these regions, so called potential barriers. In quantum mechanics the electron is described by a wavefunction $\psi(z)$ which satisfies the Schrödinger equation

$$-\frac{\hbar^2}{2m}\frac{d^2\psi(z)}{dz^2} + U(z)\psi(z) = E\psi(z). \tag{2.2}$$

Considering the case of a piecewise-constant potential U, the solution to this equation in the classically allowed region, $E > U$ is

$$\psi(z) = \psi(0)e^{\pm ikz} \qquad \text{with} \qquad k = \frac{\sqrt{2m(E-U)}}{\hbar}, \tag{2.3}$$

where k is the wave vector. The electron is moving with a constant momentum $p_z = \hbar k = \sqrt{2m(E-U)}$. as in the classical case. However, unlike in the classical case, there exists a solution to eq. 2.2 in the $E < U$ region:

$$\psi(z) = \psi(0)e^{-\kappa z} \qquad \text{with} \qquad \kappa = \frac{\sqrt{2m(U-E)}}{\hbar}. \tag{2.4}$$

This describes a state of the electron decaying in the $+z$ direction (into the barrier). The probability of observing the electron at a point z is proportional to $|\psi(0)|^2 e^{-2\kappa z}$ and is nonzero throughout the barrier. This means the electron has a finite probability of penetrating the barrier.

How do we apply this model to STM? The barrier shown in red in figure 2.6 can represent the metal-vacuum-metal junction formed by the metal sample and tip and the space between them. The minimum energy required to remove an electron from a metallic surface is called the work function ϕ. This quantity depends on the material and also on the crystallographic orientation of the surface and is typically between 2 and 5 eV. The work function represents the height of the barrier keeping the (most energetic) electrons from reaching the tip and the width of this barrier represents the distance to the tip. Neglecting thermal excitations, the Fermi level E_F is the upper limit of the occupied states in a metal. If the vacuum level (E_{vac}) is taken as the reference point of energy, $E_F = -\phi$. We take the work functions of sample and tip to be equal for simplicity's sake. Electrons can tunnel from sample to tip and vice versa, so the net tunneling current is zero. When a voltage V is applied between the tip and the sample a net tunneling current is established. The situation is shown in Figure 2.6. Depending on the sign of the bias, electrons can tunnel from sample to tip or vice versa.

An electron in the state ψ_n of energy E_n lying between $E_F - eV$ and E_F has a finite probability of tunneling to the tip. If we assume $eV \ll \phi$ then the energy levels of all the sample states of interest are very close to E_F, i.e. $E_n \simeq -\phi$. The probability w of an electron in the nth sample state to tunnel to the tip surface ($z = W$) is

$$w \propto |\psi_n(0)|^2 e^{-2\kappa W} \qquad \text{with} \qquad \kappa = \sqrt{\frac{2m\phi}{\hbar}} \tag{2.5}$$

$\psi_n(0)$ being the wavefunction of the nth sample state at the sample surface ($z = 0$) and κ the decay constant applied to the case of a sample state near the Fermi level in the barrier region (i.e. in eq. 2.4 $U = E_{\text{vac}} = 0$ and $E = -\phi$).

As long as the condition of the tip does not vary, the electrons tunneling to the tip surface have a constant velocity. The electrons contributing to the tunneling current

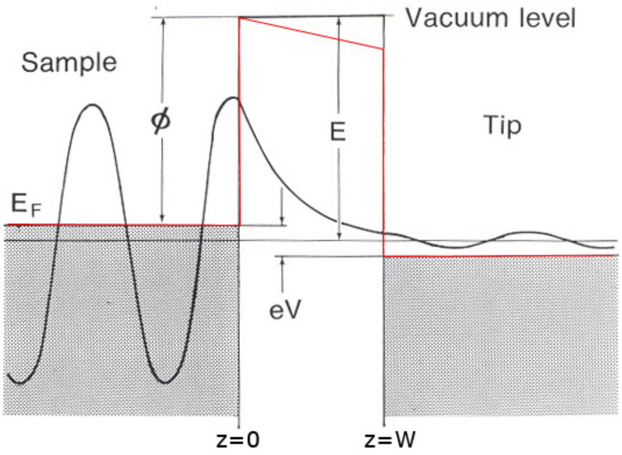

Figure 2.6: The sample (left) and the tip (right) are modeled as semi-infinite pieces of free-electron metal. The work function ϕ is the height of the barrier the electron must tunnel through to reach the tip and the width of the barrier W represents the distance to the tip. Adapted from Ref. 43.

I are those within the energy interval eV below the Fermi energy and the current is directly proportional to the number of states in this energy interval. (This number depends on the sample material: for metals it is a finite number; for semiconductors and insulators it is a very small number or zero.) We can write

$$I \propto \sum_{E_n=E_F-eV}^{E_F} |\psi(0)|^2 e^{-2\kappa W}. \tag{2.6}$$

If V is small enough, the density of electronic states does not vary significantly within the interval we are considering, and eq. 2.6 can be written in terms of the local density of states (LDOS) at the Fermi level. The LDOS of the sample at a location z and an energy E is defined as

$$\rho_S(z,E) \equiv \frac{1}{\epsilon} \sum_{E_n=E-\epsilon}^{E} |\psi_n(z)|^2. \tag{2.7}$$

for a sufficiently small ϵ. The LDOS is the number of electrons per unit volume per unit energy, at a given point in space and at a given energy. The value of the surface LDOS near the Fermi level is an indicator of whether the surface is metallic or insulating.

We now rewrite eq. 2.6 as

$$I \propto V \rho_S(0,E_F) e^{-2\kappa W} \tag{2.8}$$

Inserting a typical value for the work function of 4 eV we obtain (approximately) $I \propto e^{-2W}$, meaning that the current decays about $e^2 \simeq 7.4$ times per Å.

According to eq. 2.7 and using eq. 2.4

$$\begin{aligned} \rho_S(W, E_F) &= \frac{1}{eV} \sum_{E_n = E_F - eV}^{E_F} |\psi_n(W)|^2 \\ &= \frac{1}{eV} \sum_{E_n = E_F - eV}^{E_F} |\psi_n(0) e^{-\kappa W}|^2 \\ &= \frac{1}{eV} \sum_{E_n = E_F - eV}^{E_F} |\psi_n(0)|^2 e^{-2\kappa W} \qquad (2.9) \end{aligned}$$

With this, we see that the the tunneling current is proportional to the Fermi-level LDOS *of the sample at the tip surface*:

$$I \propto \rho_S(W, E_F) V, \qquad (2.10)$$

Thus, by scanning the tip over the sample surface at constant tunneling current, a topographic image is generated. According to this simple model this topographic image is a constant Fermi-level LDOS map of the sample surface, and doesn't depend on the electronic structure of the tip.

A more in-depth treatment of a tunneling junction was given by Bardeen in 1961 [45], while working in the field of superconductivity.[1] In his theory, Bardeen starts from two free subsystems (tip and sample in our case) and calculates the tunneling current from the overlap of the wavefunctions of the free systems using time-dependent first-order perturbation theory.[2] Central to the application of Bardeen's tunneling theory is the evaluation of the so-called tunneling matrix elements:

$$M = -\frac{\hbar^2}{2m} \int_{\Sigma} (\chi^* \nabla \psi - \psi \nabla \chi^*)$$

This is a surface integral of the tip and sample wavefunctions (χ and ψ) on a separation surface Σ, shown in figure 2.7. The tunneling current can be obtained by summing over all relevant states, i.e. those in the interval eV involved in the tunneling process. At

---

[1] Measurements of the tunneling current through a superconductor-insulator-superconductor junction (Giaever, 1960) had revealed the energy gap in the superconductors's density of states, which was critical evidence in favor of the Bardeen-Cooper-Schrieffer theory of superconductivity.

[2] For a comprehensive tutorial on the application of Bardeen's theory to STM see [46].

finite temperature the electrons in both electrodes follow the Fermi distribution $f(E)$, and for bias voltage V the tunneling current I can be written as:

$$\begin{aligned} I &= \frac{4\pi e}{\hbar}\int_{-\infty}^{+\infty}[f(E_F+\frac{1}{2}eV+\epsilon)-f(E_F-\frac{1}{2}eV+\epsilon)] \\ &\quad \times\rho_S(E_F+\frac{1}{2}eV+\epsilon)\rho_T(E_F-\frac{1}{2}eV+\epsilon)|M(\epsilon)|^2d\epsilon \end{aligned}$$

At low temperature, or when k_BT is smaller than the energy resolution required in the measurement, the Fermi distribution f can be approximated by a step function, obtaining:

$$I=\frac{4\pi e}{\hbar}\int_{-\frac{1}{2}eV}^{+\frac{1}{2}eV}\rho_S(E_F+\frac{1}{2}eV+\epsilon)\rho_T(E_F-\frac{1}{2}eV+\epsilon)|M(\epsilon)|^2d\epsilon$$

From this expression it is clear that in Bardeen's theory both sample and tip play equally important roles: an STM image is a convolution of sample and tip DOS ρ_S and ρ_T. In fact, a direct consequence of Bardeen's theory is the so-called reciprocity principle: if the electronic state of the tip and the sample state under observation are interchanged, the image should remain the same (see figure 2.8). This principle truly shows the equal importance, and indeed, interchangeability, of the roles of sample and tip.

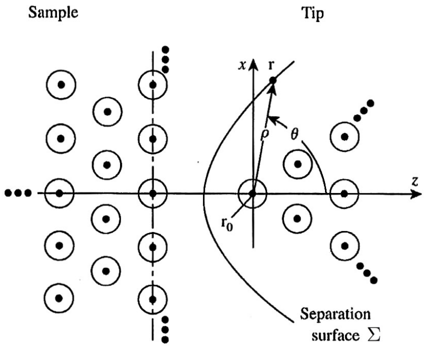

Figure 2.7: Derivation of Bardeen's matrix elements - The separation surface between tip and sample, used to calculate the tunneling matrix elements. Its exact position and shape is not important. (Image from Chen, *Phys. Rev. B* **42**, 8841-8857 (1990))

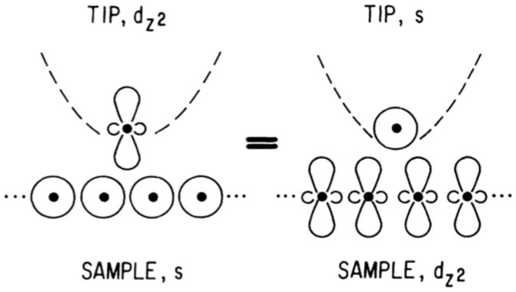

Figure 2.8: Reciprocity Principle - An image of microscopic scale may be interpreted either by probing the sample state with a tip state or by probing the tip state with a sample state (Image from Ref. 47)

Understandably, it is difficult to know the exact form of the tip states. A particular model was therefore proposed, in which the tip properties could be taken out of the problem: in 1986 Tersoff and Hamann applied Bardeen's theory to STM in their *s*-wave-tip model [48], in which the STM tip was modeled as a spherical potential well and only the s-wave solution taken into account. The result at low bias is a tunneling current of a very simple form

$$\begin{aligned} I &\propto \sum_{E_\mu=E_F-eV}^{E_F} |\psi_\mu(\mathbf{r}_0)|^2 \\ &= eV\rho_S(\mathbf{r}_0, E_F), \end{aligned} \tag{2.11}$$

proportional to the Fermi-level LDOS *of the sample at the center of curvature of the tip* $\mathbf{r}_0$. Thus, in Tersoff and Hamann's approximate model the STM image is independent of tip electronic states and reflects the property of the sample only. The Tersoff-Hamann approximation is valid for nanometer-scale imaging, but is unable to account for atomic resolution: atomically resolved images can have corrugation amplitudes of 30 pm, whereas the Tersoff-Hamann approximation predicts just 3 pm.

This shows that tip electronic states can have dramatic effects on STM images of atomic-size features. The *s*-wave tip function is clearly not accurate enough to describe these. Using Bardeen's matrix-elements, we can find that a p_z-state will lead to an increased corrugation, and therefore an enhanced resolution. In the same way, d_{z^2} state can have an even larger effect on the measured corrugation (see figure 2.9).[1]

It was proposed early on that atomic resolution could be due to a single dangling bond from the tip [49]. All metals commonly used in STM tips (W, Pt, Ir) are *d*-band metals. Calculations of the electronic states for a number of W clusters showed that there is a d_{z^2} state protruding from the apex atom of many W clusters, energetically very close to the Fermi energy, and that the tunneling current is predominately contributed by this *d* state [50].

In conclusion, the STM imaging mechanism can be described in terms of localized surface states on the tip, such as p_z or d_{z^2} dangling bond states (see Fig. 2.10). With these tip states, the nucleus of the apex atom of the tip follows a contour determined

---

[1] Another curious phenomenon encountered in STM imaging, corrugation inversion, is due to the effect of $m \neq 0$ states such as d_{xz} and d_{x^2} states. When corrugation is inverted, atom sites appear as depressions instead of protrusions.

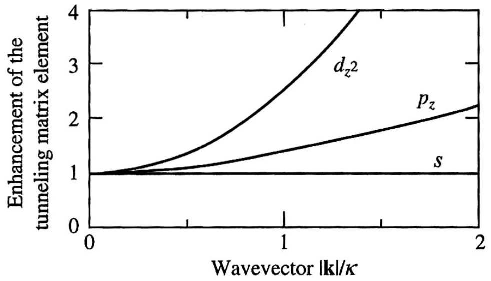

Figure 2.9: Corrugation enhancement - p_z and d_{z^2} orbitals in the tip contribute to an enhancement of the corrugation that can be measured by an s orbital. (Image from [47])

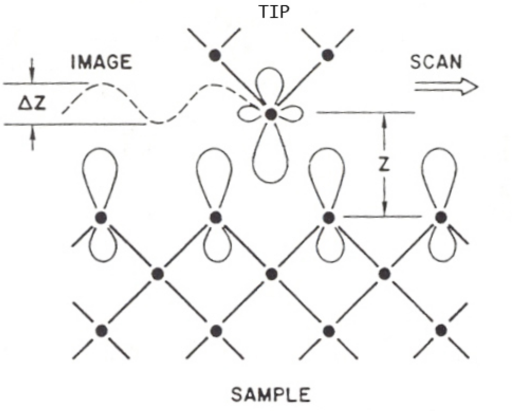

Figure 2.10: STM imaging mechanism - A d_{z^2} state protruding from the apex of a W tip interacts with an array of sp^3 states on a Si surface, resulting in a highly corrugated tunneling current distribution. (from Chen, *J. Vac. Sci. Technol. A* **9**, 44-50 (1991))

by the derivatives of surface wave functions of the sample, which exhibit much stronger atomic corrugation than the Fermi-level LDOS [47]. This mechanism is thus able to explain atomic resolution.

Another factor to consider in STM imaging is tip-sample interactions. At tip-sample distances of just a few ångström interactions are very strong. One consequence of these interactions is that the potential barrier the electrons must tunnel through becomes much lower than the vacuum level, and as a result the wavefunctions are modified. [43]

2.2.3 STM Imaging

As we have seen in the previous section, the interpretation of STM images is not always straightforward. STM images are not simply topographical; rather, they are a view of the electronic structure of the sample, and also greatly influenced by the tip.

Clean Surfaces

Due to the nature of the tunneling process, STM must be limited to samples which are conducting, i.e. metals or semiconductors. Since its inception in 1981, STM has been able to map semiconducting and metallic surfaces and their reconstructions with atomic resolution. In semiconductors, relatively large voltages are required, due to the energy gap at the Fermi level. They also generally show a pronounced voltage dependence. By changing the sign of the voltage, the tunneling direction is reversed. A positive sample bias means electrons from the tip will tunnel to the sample's unoccupied states; a negative sample bias means electrons from the sample's occupied states tunnel to the tip. The bias polarity thus determines whether unoccupied or occupied electronic states of the sample are probed. The atoms in a semiconductor form covalent, directional bonds. Semiconductor surfaces often show empty dangling bonds. When scanning such a surface by STM, these occupied bonds or empty dangling bonds are imaged, depending on the voltage. An example of this can be seen in Fig. 2.11, which shows the Si(100) surface imaged at positive and negative bias.

In the case of metals the bias dependence is not so great, and the bias voltage can be of the order of mV as there is no energy gap. An example of the (for some) routinely obtained atomic resolution is shown in figure 2.12 for the Cu(111) surface.

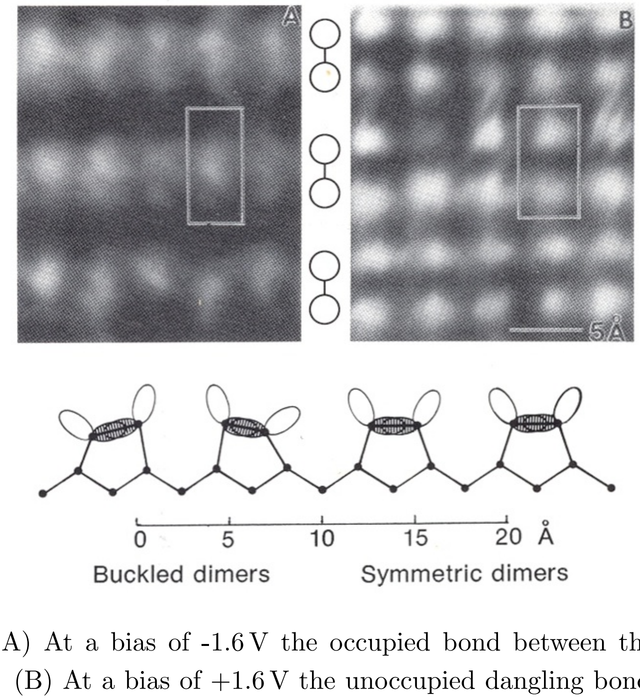

Figure 2.11: (A) At a bias of -1.6 V the occupied bond between the two atoms in a dimer is imaged. (B) At a bias of +1.6 V the unoccupied dangling bond on each Si atom is imaged. Image from Hamers, *Ann. Rev. Phys. Chem* **40**, 531-559 (1989).

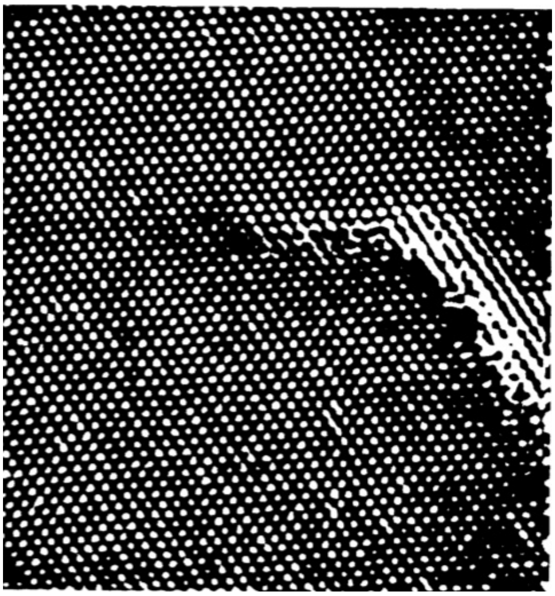

Figure 2.12: An atomically resolved STM image of the Cu(111) surface. Image from Samsavar et al., *Phys. Rev. Lett.* **65**, 1607-1610, (1990).

Covered Surfaces

Interpreting images of individual adsorbates on a substrate can be difficult as well. One of the first theoretical studies to try to understand images of adsorbates was done by Lang [51] and showed that adatoms of different chemical species show characteristically different profiles: they can be imaged as bumps of different heights or as depressions, depending on the density of states near the Fermi energy, and the influence of the adsorbate on the DOS of the sample surface. This influence, and therefore STM corrugation, can be related to the elemental electronegativity and especially polarizability of the adatom [52]. Examples of adsorbed atoms that are imaged as depressions are O on Pt(111) [53] or N on Fe(100) [54].

The adsorbates studied in this thesis are organic molecules.

In practice, the first difficulty to be overcome when imaging molecules is eliminating their mobility on the substrate. This can be done in several ways, for example by

- strong chemisorption on appropriate substrates offering a high binding strength,
- co-adsorption with other molecules, thereby stabilizing particular surface structures,

- working at low temperatures,
- self-assembly of stable molecular structures [55].

Thin layers of molecules deposited and immobilized on a conductive single crystal substrate with atomically flat terraces can be imaged by STM to obtain information about

- binding sites on and orientation of molecules with respect to the substrate lattice,
- the periodicity of self-assembled surface structures, as well as
- defects and domains appearing in these structures [55].

When the first organic molecules were imaged in the eighties, it was debated whether STM was imaging the actual molecules or simply the their effect on the metal substrate, as organic molecules typically have a large HOMO-LUMO gap compared with the voltages used in STM.

However, it was later found that when a molecule is directly adsorbed on a conductive surface, the discrete molecular levels are broadened, shifted and mixed because of the interaction with the electronic continuum of the substrate. As a consequence, many molecular orbitals contribute to the tunneling current through the molecule, even when their energies are far away from the Fermi level of the substrate [56]. The interaction of the substrate with the molecular orbitals makes it possible to image molecules, but also means that the images may not represent the electronic structure of the isolated molecule.

2.3 Photoelectron Spectroscopy

If energetic enough, light incident on matter will eject electrons from it. This phenomenon is known as the photoelectric effect: an electron initially in a state with binding energy E_{i} absorbs a photon of energy $h\nu$, allowing it to overcome the material's work function ϕ and to escape from the material with a kinetic energy E_{Kin}. This can be expressed in the following manner:

$$E_{\mathrm{Kin}} = h\nu - E_{\mathrm{i}} - \phi \tag{2.12}$$

In photoelectron spectroscopy (PES), the ejected electrons, called photoelectrons, are detected. Light incident on a material penetrates several hundred nanometers. However, the photoelectrons that are actually able to exit the material (and reach the detector) originate only in the first few atomic layers of the surface.[1] The electrons that make it out without losing their initial kinetic energy are the ones described by Eq. 2.12. Plotting their number as a function of their kinetic energy provides a kind of "map" of the density of occupied states of the probed material, showing peaks corresponding to the electrons' energy level of origin, as illustrated in Fig. 2.13. [57]

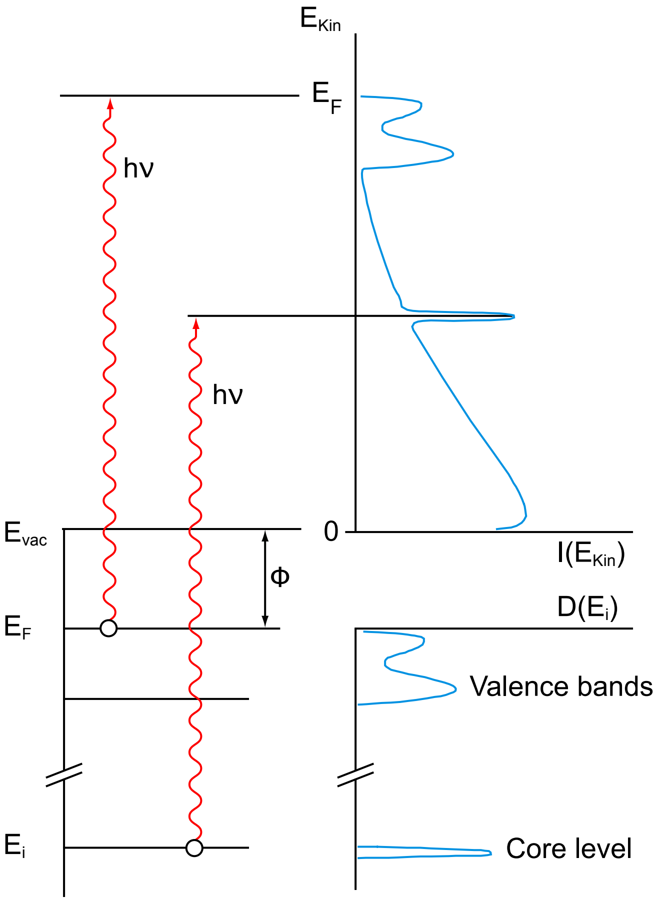

Figure 2.13: The photoemission spectrum $I(E_{\mathrm{Kin}})$ is to first order a fingerprint of the density of states $D(E_{\mathrm{i}})$ of the probed material. Adapted from Ref. 57.

---

[1] For the kinetic energy range typical of x-ray excitation (a few hundred eV up to 1.5 keV) the mean free paths are of the order of 1 nm; below 100 eV they can be as short as one or two atomic layers. This is what makes PES a surface sensitive technique.

Of course, experimentally, the actual correspondence to the density of states is not so direct: besides the elastic photoemission process described by Eq. 2.12, in which electrons are able to exit the material without losing kinetic energy on their way out, there are a number of other effects and processes the electrons can undergo, and these also contribute to the photoemission spectrum:

- The photoelectrons that do lose energy on their way out of the material, mainly through collisions, make up a **continuous inelastic background** that is observed as a steadily increasing intensity for decreasing kinetic energies
- An ejected electron leaves behind a hole that will be filled in order to relax the system. When an electron from a higher energy level fills this hole either a photon or another electron will be emitted. The latter process is called **Auger emission**, and produces features in the photoemission spectrum that have a fixed kinetic energy. (This is applicable when using x-rays to excite the material.)
- The **cross-section** of the excitation process varies considerably between energy levels, and this will determine the relative intensity of the elastic peaks of the spectrum. As shown in Fig. 2.14, the cross-section is also dependent on the photon energy and an appropriate choice of photon energy is therefore necessary.

Fig. 2.14 shows a photoemission spectrum of sodium, taken using 100 eV radiation for excitation. The relative intensities of the core-levels can be understood from their different cross sections, shown on the right hand side of the figure.

Depending on the energy of the photons used to irradiate the material, photoelectron spectroscopy is divided into x-ray photoelectron spectroscopy (XPS), and ultraviolet photoelectron spectroscopy (UPS). In the following sections we will explore these two techniques in more detail. The more energetic the light we use is, the deeper into the atom we can probe.

2.3.1 X-Ray Photoelectron Spectroscopy

In XPS, x-ray photons ($h\nu = 100\,\mathrm{eV} - 10\,\mathrm{keV}$, or $\lambda = 100 - 1\,\mathrm{\AA}$) are used to probe the material. Light of this energy is able to eject electrons from the innermost (most tightly bound) electrons, i.e. from the core-levels. These show up in the XPS spectra as sharp peaks whose locations are defined by the electron binding energies. The

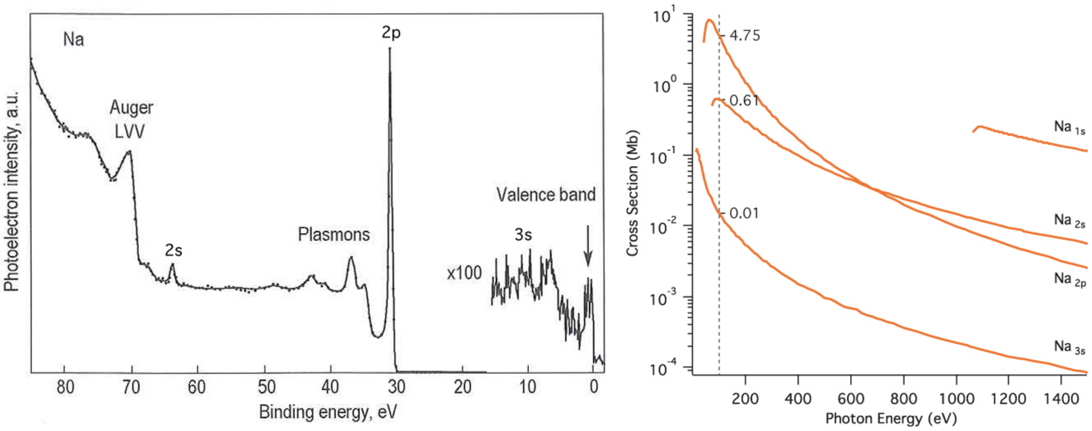

Figure 2.14: XPS spectrum of Na with a photon energy of 100 eV. Core level, Auger and plasmon features are indicated. Note the weak intensity of the valence band features (adapted from Ref. 57). To the right, cross sections of all Na's energy levels are shown (data from Ref. 58). The 2p level has the highest cross section and dominates the XPS spectrum at 100 eV; the 2s level has a cross section that an order of magnitude lower, but can still be identified at this excitation energy. 3s is lost in the ill-defined valence region, and 1s needs at least 1070.8 eV for photoemission to take place.

binding energies are characteristic of each atomic species, so each element has an XPS fingerprint that can be used to identify its presence in the sample. The XPS spectrum therefore contains information on the surface composition.

The binding energy of the electron at a given level is defined by the interplay between the Coulomb attraction to the nucleus and the screening of this attraction by other electrons in the atom. Changes in the chemical environment can therefore lead to variations in the position of core level, called *chemical shifts*. The origin of these shifts could be [57]

- Formation of chemical bonds involves electron transfer, and therefore changes in the charge density of the atom. This in turn affects the binding energy of the electrons, as can be seen in Fig. 2.15b and c. In this case, the chemical shifts can be related to electronegativity differences, and in the examples, the electrons from C atoms bound to more electronegative atoms will have higher binding energies.
- Electron charge transfer to a given atom will enhance the electron screening of the nucleus, weakening the electron binding energy. Conversely, electron charge transfer from a given atom weakens the screening and will increase electron binding

energies. For instance, in the sodium azide complex of Fig. 2.15a the negatively charged nitrogen has a better screened nucleus, and so it is easier to extract an electron from it, resulting in a lower binding energy.

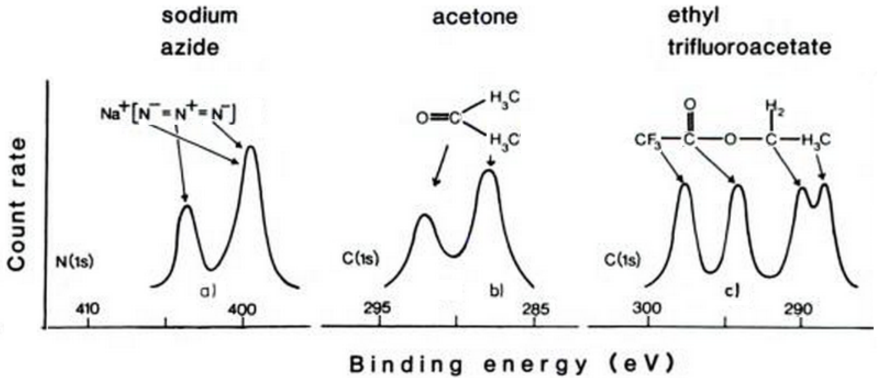

Figure 2.15: Some typical examples of molecules containing carbon atoms in different chemical environments, showing the chemical sensitivity of the core levels. Adapted from Ref. 59.

The *line shape* of the core-levels gives us further information on the physics of the system. The intrinsic (irreducible) width of a core-level line in XPS is due to the lifetime τ of the core hole state created in the photoemission process[1] and given by $\Gamma = 2\hbar/\tau$. This finite lifetime results in a Lorentzian line-profile (also known as the natural line-profile). However, the core-level line is further broadened by the resolution limit of the analyzer, which produces a Gaussian line-shape. For this reason, a combination of these two lineshapes, called a Voigt profile, is most often used to fit the core-levels.

Let us now explore the production of x-rays. Synchrotron radiation is dealt with in the Appendix and here only a brief overview of x-ray tubes as laboratory sources is given. These produce x-rays by bombarding a target with high energy electrons. The electrons, produced by a hot filament, are accelerated toward a metal target anode by a high voltage. When the electrons strike the target, radiation is produced due to two distinct processes, and the resulting x-ray spectrum is a superposition of both contributions:

---

[1] The lifetime τ of the core hole state, i.e. the time before the system relaxes by filling the core hole, is in the femto- or subfemtosecond range [60] , giving an intrinsic line with of 0.1-1 eV

- **Bremsstrahlung**, or braking radiation, is produced by the deceleration of the electrons as they strike the target. It is a continuous distribution that grows in intensity and shifts toward higher energy with increasing acceleration potential.

- **Characteristic peaks** appear in the spectrum as a consequence of the excitation of the target material by the electrons colliding with it. These can eject core-electrons (as in XPS) from the target material, leaving vacancies that will be filled by electrons from higher energy levels, leading to the emission of x-rays. Logically, the characteristic peaks depend on the anode material. Common materials are Mg and Al, for which the emission spectrum is dominated by unresolved $K_{\alpha 1}$ and $K_{\alpha 2}$ lines ($2p_{1/2} \rightarrow 1s$ and $2p_{3/2} \rightarrow 1s$ transitions) at 1253.6 eV for Mg and 1486.6 eV for Al.

Only about 1% of the bombarding electrons' energy is radiated, the rest being converted into heat, making a water cooling an essential part of any x-ray source.

2.3.2 Ultraviolet Photoelectron Spectroscopy

UPS uses ultraviolet light ($h\nu = 10 - 50\,\mathrm{keV}$, or $\lambda = 1000 - 250\,\text{Å}$) to eject electrons. This relatively low photon energy serves to probe states near the Fermi energy, such as the substrate's valence band and surface states, and the low energy occupied molecular orbitals of adsorbates, in particular the HOMO.

Another useful application of UPS is that it allows determining the sample work function. Fig. 2.16 shows a complete UPS spectrum, with the fastest electrons defining the Fermi cut-off at high kinetic energies and the so-called secondary electron cut-off (SECO) on the low kinetic energy end. The SECO results from the large number of secondary electrons emitted with low kinetic energies as a consequence of the multiple scattering processes undergone while exiting the material. It defines the position of the vacuum energy at the sample surface. The work function is simply the difference between the photon energy and the full width of the spectrum, as is illustrated in the figure. In practice, an external bias should be applied to the sample in order to shift the whole spectrum to higher kinetic energy, since stray electric or magnetic fields may degrade the transmission function of the analyzer at low energies. [61]

As laboratory sources for UPS, gas discharge lamps are used, most commonly He gas. A high ignition voltage ($\sim 7000\,\mathrm{V}$) is initially used to partly ionize He gas in

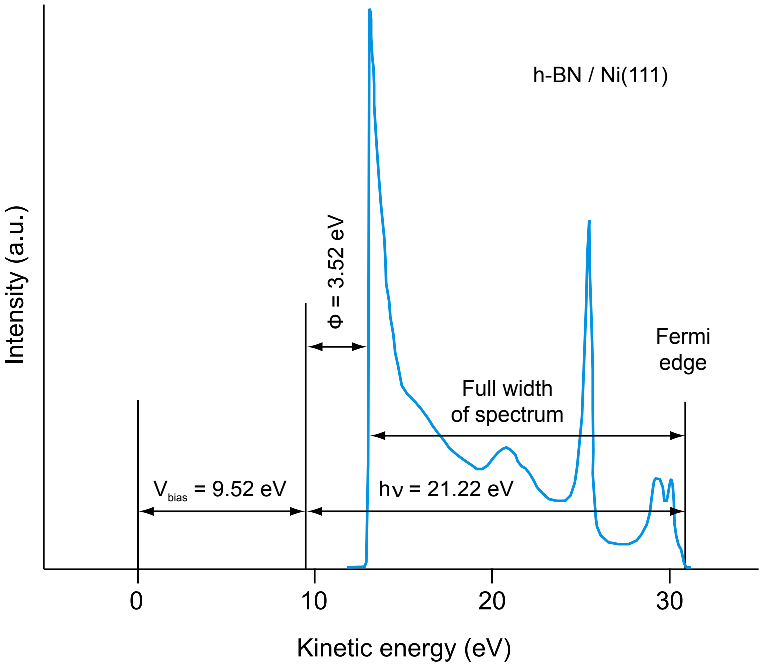

Figure 2.16: UPS spectrum. Secondary electron cut-off allows the determination of the work-function. Adapted from Ref. 61.

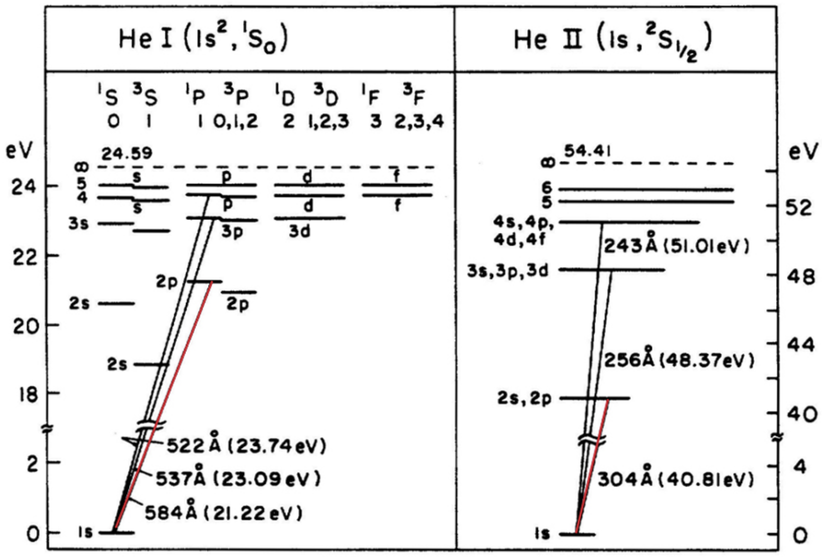

Figure 2.17: Transitions responsible for the ultraviolet light produced in a He gas discharge lamp. He-I transitions correspond to those taking place in the neutral He atom, while He-II refers to those of the singly ionized atom. Taken from *Principles of Ultraviolet Photoelectron Spectroscopy* by J. Wayne Rabalais, John Wiley & Sons Inc. (1977).

a cavity, and once this is achieved, a lower operating voltage ($\sim$ 1500 V) is able to maintain a discharge: electrons (accelerated from cathode to anode) collide with He atoms and ions, exciting their electrons to higher energy levels. When these decay, photons of characteristic energy are emitted. Helium's only two electrons are in the lowermost 1s level. Most of the intensity of the emitted light comes from the He-I_α transition (2p → 1s, 21.22 eV); other lines present in the He discharge are He-I_β (3p → 1s, 23.09 eV), He-I_γ (4p → 1s, 23.74 eV) and He-II_α (2p → 1s, 40.81 eV), though these have an intensity of about 2% with respect to the main He-I_α. These and other possible transitions are shown in Fig. 2.17.

2.4 Near-Edge X-Ray Absorption Fine Structure

We will only give a brief introduction to this technique, abbreviated as NEXAFS. For a more in depth treatment refer to Ref. 62.

In the previous section we described photoelectron spectroscopy, which serves to probe the occupied states of matter. The NEXAFS technique, by contrast, is used to probe *unoccupied* states. The sample is irradiated with monochromatic x-rays, the energy of which is varied around an ionization edge. The absorption of a photon excites an electron to an unoccupied level, leaving behind a hole. The system subsequently relaxes, filling the hole, and leading to the emission of an Auger photoelectron or fluorescent photon. Both of these channels are a direct measure of the existence of the hole created by the x-ray absorption, and consequently a measure of the absorption cross-section. Though either channel can be detected, electron detection is more common, as it provides a higher surface sensitivity. Furthermore, for low-Z molecules the Auger electron yield is much higher than the fluorescent yield.

The origin of NEXAFS features is shown schematically in Fig. 2.18 for a π-bonded diatomic unit. In general, the energy dependence of the atomic photoabsorption cross sections resembles a step function. At high energies it is identical with the ionization cross section (proportional to $E^{7/2}$). The step represents the excitation of the core electron to the continuum (or quasicontinuum) of final states. Around the ionization threshold, resonant transitions are superimposed on the step-like shape. These transitions occur when the energy of the incoming photons exactly matches the energy

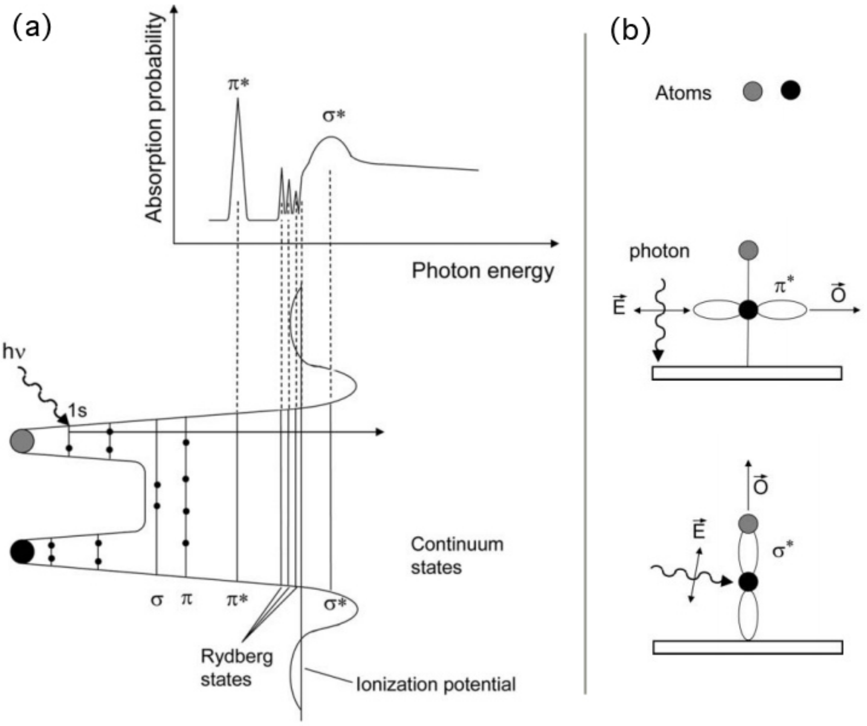

Figure 2.18: (a) Electrons are promoted from core levels into different unoccupied levels by sweeping through a range of excitation energies around the ionization edge. The subsequent detection of the electrons or photons resulting from the relaxation processes yields a NEXAFS spectrum. (b) Angular dependence of NEXAFS resonances for a π-bonded diatomic molecule adsorbed with its molecular axis normal to the surface. The π^*-resonance is maximized at normal incidence (above), while the σ^*-resonance is maximized at grazing incidence (below). Adapted from Ref. 62.

difference between the initial state and an unoccupied molecular state, as shown in Fig. 2.18.

In a π-bonded diatomic subunit (extendable to π-conjugated molecules) the lowest unoccupied molecular orbital is usually a π^*-orbital, the σ^*-orbitals being at higher energies. σ^*-orbitals are most often found above the vacuum level for the neutral molecule, however the π^*-state is pulled below the ionization potential by the electron-hole Coulomb interaction. Contrary to the XPS technique, a NEXAFS excitation does not ionize the atom or molecule, but promotes an electron to an unoccupied state. The hole created during this process and the excited electron will therefore interact.

The measured width of a resonance is determined by the instrumental resolution (Gaussian line-shape), the lifetime of the excited state (Lorentzian line-shape), and the vibrational motion of the molecule (unsymmetrical broadening). Lifetime broadening of π-resonances is generally much smaller than that of σ-resonances due to the fact that the latter are found at higher energies where σ states can overlap with the continuum, which provides a larger number of decay channels.

NEXAFS can also be used to investigate the orientation of molecules on a surface. The spatial orientation of an orbital can be obtained by taking NEXAFS measurements at more than one angle of incidence. For linearly polarized light (such as that produced in a synchrotron), it follows from Fermi's Golden Rule that the transition probability from a 1s initial state to a directional final state is proportional to $\cos^2 \delta$, where δ is the angle between the electric field vector $\mathbf{E}$ and the direction of the final state orbital $\mathbf{O}$. Therefore, the intensity of a resonance is largest when the electric field vector $\mathbf{E}$ lies along the direction of the orbital and vanishes when it is perpendicular to it. This is illustrated in Fig. 2.18b. The polarization dependence of the intensity of the different resonances allows for the determination the molecular orientation.

2.5 X-Ray Standing Waves

The x-ray standing waves (XSW) technique provides a way to obtain the height above the substrate of molecular adsorbates. Being not so well known and very interesting, a relatively detailed description is given. The information on the development of diffraction theory of the first section is based on the book *Dynamical Theory of X-Ray Diffraction* by A. Authier [63], whereas the rest of the information, which pertains more directly to the XSW technique was taken from the reviews of J. Zegenhagen [64] and D. P. Woodruff [65].

2.5.1 All about Bragg's Law

A crystalline solid is made up of periodically arranged atoms that can be visualized as forming atomic planes separated by a fixed distance. When x-rays are incident on the crystal, the atoms' electronic clouds are brought into oscillation, causing them to re-radiate with the same frequency. In general, these reradiated or scattered waves cancel out, but for very specific conditions the scattered waves are in phase and build up in constructive interference. The conditions under which this occurs are summed up by Bragg's law

$$d \sin\phi = n\lambda, \qquad n \in \mathbb{N} \tag{2.13}$$

where d is the distance separating a set of atomic planes, ϕ is the angle of incidence of the x-rays with respect to the atomic planes and λ is their wavelength. In the following, we will assume $n = 1$.

When the Bragg condition is met, the incident x-rays appear to be reflected off the atomic planes of the crystal. If we consider a fixed angle of incidence (and $n = 1$), we will observe the reflection for incident x-rays with a wavelength $\lambda_{\text{Bragg}} = d \sin\phi$, or equivalently, an energy $E_{\text{Bragg}} = \frac{hc}{d \sin\phi}$.

The simplest treatment of x-ray diffraction, Laue's *geometrical theory*, adds the amplitudes of the waves diffracted by each atom taking into account the path differences between them, but neglecting any interaction of the x-rays with matter. For a given angle of incidence, this results in a discrete energy value at which reflection takes place, E_{Bragg}[1] as shown in Fig. 2.19a.

A more realistic view is given by Darwin's *dynamical theory* of diffraction. Instead of assuming that the incident wave keeps the same intensity as it propagates through the crystal (as in the geometrical theory, clearly violating conservation of energy), the dynamical theory considers a reflected and a transmitted wave at each atomic plane, which in turn generate reflected and transmitted waves each time they cross an atomic plane and so on. This leads to a set of recurrent equations from which it is possible

---

[1] For an infinite and perfectly periodic crystal the reflection domain is reduced to a Delta distribution and would be represented by a single point in reciprocal space.

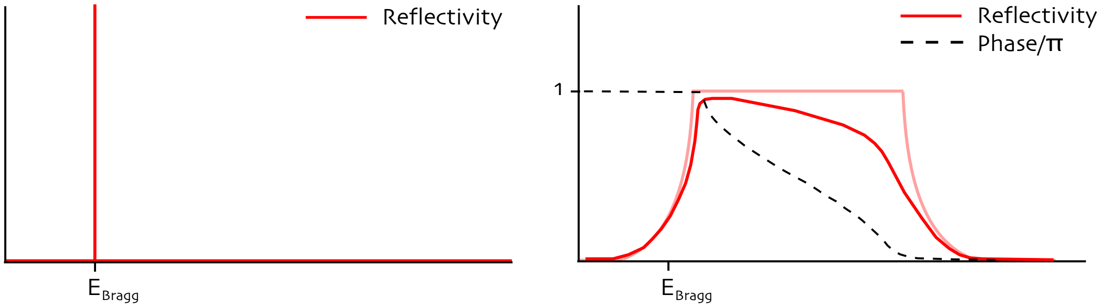

Figure 2.19: Reflectivity at the Bragg condition according to the geometrical theory and the dynamical theory. (a) The geometrical theory predicts an infinite reflected x-ray intensity at the Bragg energy, clearly violation conservation of energy. (b) The dynamical theory takes into account the attenuation of the x-rays as they penetrate the crystal, and predicts a domain of unit reflectivity (flat topped curve, faded out) and a phase change of π of the standing wave field within this energy range. Taking absorption into account, the reflectivity is no longer unity away from the Bragg condition and the curve becomes more rounded. Adapted from Ref. 63.

to obtain the amplitude reflected at the crystal surface. The result is that in a certain range of energies around the Bragg energy, the reflected intensity is equal to one, as shown in Fig. 2.19b. Within this energy range of unit reflectivity, x-rays incident on a crystal will set up a standing wave field in it, due to the superposition of incident and reflected waves. The phase of this standing wave field with respect to the atomic planes varies by π within the reflectivity range.

Summarizing, the crucial results of the dynamical theory that are the basis of the XSW technique are

- the existence of a total reflection *domain* (unit reflectivity), as opposed to a single peak at E_{Bragg} (infinite reflectivity) (and the possibility to set up a standing wave field in the crystal using x-rays within this domain)
- the existence of a phase change of the standing wave field with respect to the atomic planes occurring within the total reflection domain.

These results are shown in Fig. 2.19b. The flat-topped reflectivity curve is known as the Darwin curve; its width is of the order of a few seconds of arc, and its onset is slightly shifted with respect to the Bragg angle.

This unit-reflectivity plateau is valid only for the (unrealistic) case of a non-absorbing crystal. Prins extended Darwin's theory to the case of absorbing crystals, showing that due to absorption there is no longer a *total* reflectivity domain: absorption reduces the reflectivity away from the onset of the curve and gives it a more rounded appearance,[1] as shown in Fig. 2.19.

When first comparing his theory to experimental results, Darwin found profound disagreement in the value of the reflected intensity and in width of the experimental reflectivity curve—also called a rocking curve[2]—, which was much larger than the predicted reflectivity domain. In order to explain these discrepancies, the concept of crystal mosaicity was introduced: the crystal can be seen as being composed of a mosaic of small crystalline blocks more or less misoriented with respect to one another, with each block contributing its own slightly shifted rocking curve. The width of the rocking curve is therefore a measure of the mosaicity of the crystal.

2.5.2 Interference of X-rays

When two coherently related traveling waves interfere, an x-ray standing wave is generated. This is precisely what happens when, in that certain range around the Bragg energy, x–rays incident on a crystal are reflected.

The incident and scattered (electromagnetic) waves can be characterized by the complex amplitudes $\mathcal{E}_0$ and $\mathcal{E}_{\mathcal{H}}$ of their electric fields

$$\mathcal{E}_0 = E_0 e^{2\pi i(\nu_0 t - \mathbf{K_0}\cdot\mathbf{r})}; \qquad \mathcal{E}_{\mathcal{H}} = E_H e^{2\pi i(\nu_H t - \mathbf{K_H}\cdot\mathbf{r})}$$

where ν is the frequency of both waves, $\mathbf{K}$ is their propagation vector ($|\mathbf{K}| = \lambda^{-1}$) and $\mathbf{r}$ is the position vector from an arbitrary origin. We assume $\nu_0 = \nu_H$, which leads to $|\mathbf{K_0}| = |\mathbf{K_H}|$. The amplitudes E_0 and E_H are complex numbers, i.e. they contain a phase factor. [64]

---

[1] The reason for the asymmetry of the curve is that at its onset, the nodes of the standing wave field coincide with the atomic planes, minimizing absorption. The absorption then gradually increases throughout the reflection domain, as the standing wave maxima move toward the atomic positions.

[2] Though we have been dealing reflectivity as a function of x-ray energy, with a fixed angle of incidence, from Eq. 2.13 we see that an alternative approach could be to use a fixed energy, and vary the angle of incidence. The reflectivity curve is then obtained by "rocking" the sample, hence "rocking curve".

Since $\mathcal{E}_0$ and $\mathcal{E}_{\mathcal{H}}$ are coherent, we can write

$$E_H = \sqrt{R}E_0 e^{i\phi}$$

where ϕ is independent of t and $\mathbf{r}$. In this way, R represents the reflectivity, since the intensities of the two waves are related via

$$R = \frac{I_H}{I_0} = \frac{|E_H^2|}{|E_0^2|}.$$

The superposition of the incident and reflected x-rays give

$$\mathcal{E} = \mathcal{E}_0 + \mathcal{E}_{\mathcal{H}} = \sqrt{R}E_0 e^{i\phi} e^{2\pi i(\nu t - \mathbf{K_H}\cdot\mathbf{r})} + E_0 e^{2\pi i(\nu t - \mathbf{K_H}\cdot\mathbf{r})}$$

A proper choice of origin makes the phase of E$_0$ disappear, so we can substitute E_0 by $|E_0|$. Defining $\mathbf{H} = \mathbf{K_H} - \mathbf{K_0}$[1] leaves us with

$$\begin{aligned} \mathcal{E} &= \sqrt{R}|E_0|e^{i\phi}e^{2\pi i(\nu t - \mathbf{K_0}\cdot\mathbf{r})}e^{-2\pi i\mathbf{H}\cdot\mathbf{r}} + |E_0|e^{2\pi i(\nu t - \mathbf{K_0}\cdot\mathbf{r})} \\ &= \sqrt{R}|E_0|e^{2\pi i(\nu t - \mathbf{K_0}\cdot\mathbf{r})}(1 + \sqrt{R}e^{i(\phi - 2\pi\mathbf{H}\cdot\mathbf{r})}) \end{aligned}$$

(this is the x-ray standing wave field at position $\mathbf{r}$ that forms when two plane waves interfere.) The normalized intensity I is given by $\mathcal{E}\mathcal{E}^*/|E_0|^2$:

$$I = |1 + \sqrt{R}e^{i(\phi - 2\pi\mathbf{H}\cdot\mathbf{r})}|^2 = 1 + R + 2\sqrt{R}\cos(\phi - 2\pi\mathbf{H}\cdot\mathbf{r})$$

In the above expression for the intensity the time dependence vanishes, indicating that the field is stationary. There is a *modulation* of the x-ray intensity in the direction of $\mathbf{H}$, and no modulation in the direction perpendicular to $\mathbf{H}$, i.e. the nodes and antinodes of the wavefield intensity lie on planes.

The scalar product $\mathbf{H}\cdot\mathbf{r}$ can be written in terms of the perpendicular distance to the crystal planes z and the interplanar distance d_H:

$$I = 1 + R + 2\sqrt{R}\cos(\phi - 2\pi\frac{z}{d_H}) \qquad (2.14)$$

---

[1] When $\mathbf{K_0}$ and $\mathbf{K_H}$ correspond to an incident and diffracted beam respectively, the two wavevectors are related via Bragg's law, which can in fact be written as $\mathbf{K_H} = \mathbf{K_0} + \mathbf{H}$, where $\mathbf{H}$ is now related to the reciprocal lattice vector $\mathbf{G}$ via $\mathbf{H} = \mathbf{G}/(2\pi)$.

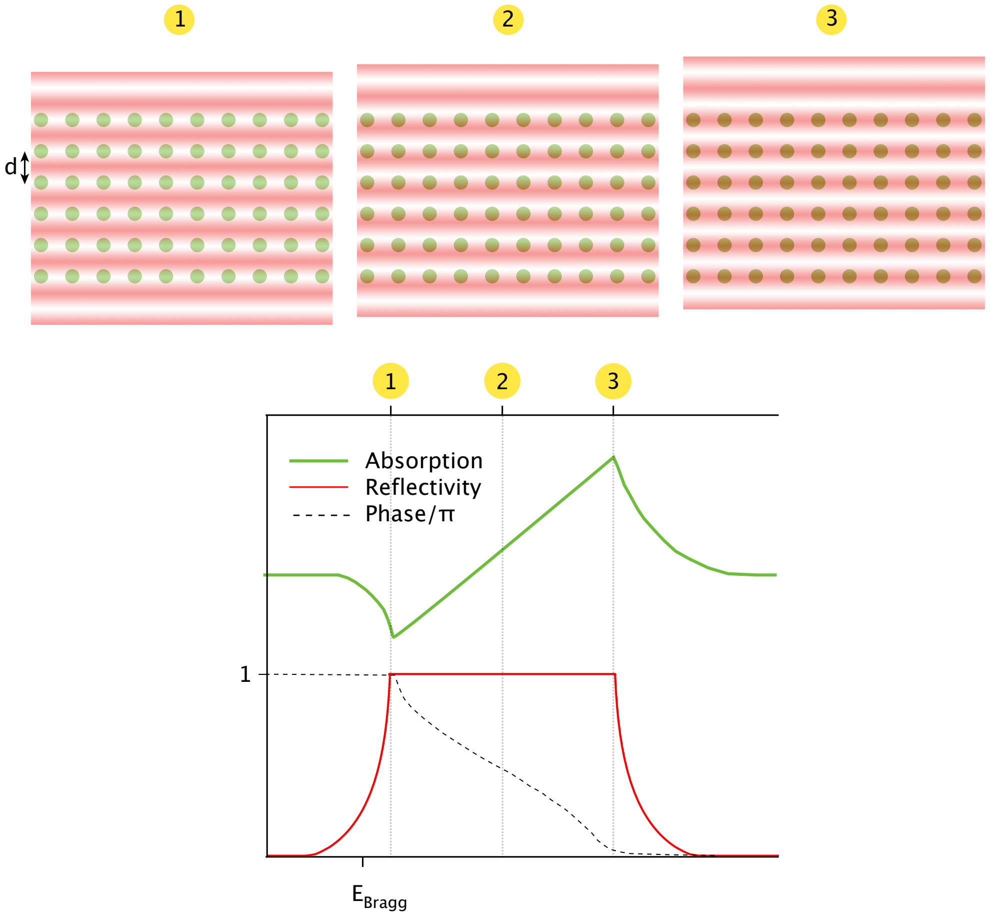

Figure 2.20: Standing wave field within the crystal for x-ray energies at the beginning (1), in the middle (2) and at the end (3) of the total reflectivity domain. Below, the reflectivity and the phase of the standing wave with respect to the atomic planes is shown, as well as the crystal absorption.

2.5.3 Obtaining adsorption heights from XSW

Let us now explore the consequences of these results. We consider irradiating our crystal with x-rays and varying their energy so as to sweep through the total reflection domain of the Darwin curve. Away from the Bragg condition ($E \ll E_{\text{Bragg}}$) nothing out of the ordinary happens, the incident x-ray wave enters the crystal and is partially absorbed by it (as in the XPS technique). As we increase the energy past $E \sim E_{\text{Bragg}}$ we enter in the unit reflectivity domain, and the incident and reflected waves form a standing wave field within the crystal. Importantly, the nodes of this standing wave field fall precisely on the atomic planes of the crystal, i.e. the intensity on the atomic planes of the crystal is zero at this point. Further increasing the energy will change the phase of the standing wave with respect to the atomic planes, and thus the intensity falling on the atomic planes. When the energy of the x-rays reaches the end of the total reflection domain, the phase will have shifted by π and the maxima of the standing wave field will be falling on the atomic planes. This process is illustrated in figure 2.20.

If we now imagine the crystal has impurities midway between the atomic planes (or equivalently, adsorbed at a distance $d_H/2$ on the crystal surface)[1], at the Bragg energy, the nodes of the standing wave field will lie on the atomic planes (as usual), whereas the impurities will be receiving the full intensity of the field. As the x-ray energy sweeps through the rocking curve, the crystal planes and the impurities will receive different (approximately inverse) intensities. It now becomes clear that to each position in (or on) the crystal there corresponds a characteristic intensity profile as the x-ray energy is swept through the Bragg energy. Some examples are shown in Fig. 2.21. The intensity profile associated with a specific atomic species, in combination with the spatial intensity distribution of the x-ray standing wave as a function of the x-ray energy, would allow us to obtain the position of this atomic species relative to the atomic planes.

The intensity distribution of the x-ray standing wave is known (Eq. 2.14), but how can we experimentally determine the intensity profiles of a given atom? This is done taking advantage of photoemission, and of the fact that to first order the photoelectron yield is proportional to the x-ray intensity on the atom: by recording the photoelectron

---

[1] XSW first developed as a technique for studying the position of impurities in a crystal matrix [66; 67], but is now widely used as a means to determine the adsorption height of molecular adsorbates, as it will be in this work.

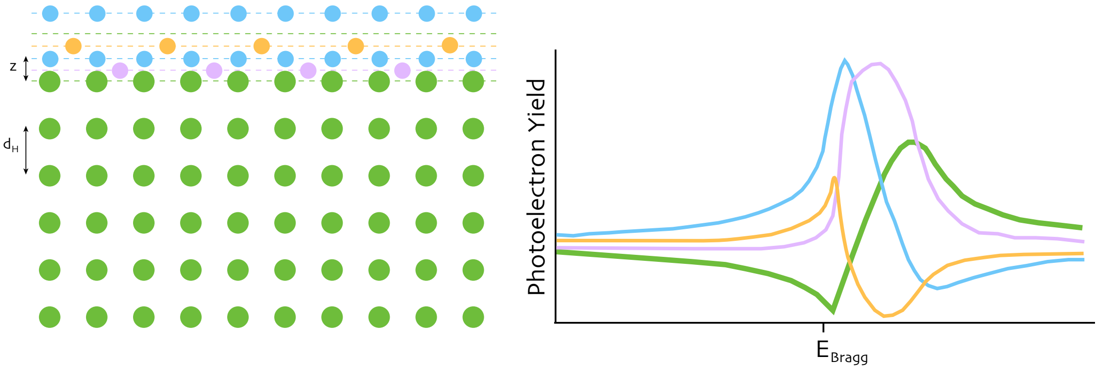

Figure 2.21: Photoelectron yield curves (proportional to x-ray intensity) for a crystal (green) and atoms adsorbed at different heights (pruple, blue, orange). Note that both adsorption heights of the blue atoms—differing by d_H, the distance between atomic planes and the standing wave periodicity—give rise to the same curve. Figure adapted from Ref. 68

yield[1] of a given atomic species at different energies around the Bragg energy and noting the variation in intensity of each core-level, we can obtain the photoelectron yield $Y(E)$.

This experimentally obtained photoelectron yield curve could now be fit using Eq. 2.14 to find z, the perpendicular distance from the crystal planes. However, it is unrealistic to assume that all absorber atoms contributing to the photoelectron yield have the very same z value. Thermal vibration or static disorder, co-occupation of two or more sites by the same atomic species are all factors that should be accounted for. It is therefore assumed that there is a distribution of z positions, the fraction of absorbers at a spacing z within a range dz being given by $f(z)dz$, defined such that $\int_0^{d_H} f(z)dz = 1$. [65]

The photoelectron yield can be expressed from 2.14 as

$$Y(E) = 1 + R + 2\sqrt{R}\int_0^{d_H} f(z)\cos{(\phi - 2\pi\frac{z}{d_H})}.$$

(Recall the energy dependence of the reflectivity $R(E)$ and the phase $\phi(E)$, shown in Fig. 2.21.) It can be shown that this is equivalent to

$$Y(E) = 1 + R + 2F^H\sqrt{R}\cos{(\phi - 2\pi P^H)}, \tag{2.15}$$

---

[1] The photoelectron yield is determined from a series of XPS spectra in an excitation energy range ±2 eV around the Bragg energy.

with two free parameters called the coherent fraction F^H (ranging from 0 to 1), related to the distribution of positions, and the coherent position P^H, related to the position by $z = d_H(n + P^H)$, with $n \in \mathbb{N}$.

The small width of the rocking curve means that a highly collimated x-ray beam and high crystalline perfection are necessary to apply the XSW technique. As previously mentioned, the crystal's mosaicity causes a broadening of the reflectivity curve. This broadening much be much smaller than the rocking curve's width. Normal incidence XSW (NIXSW)[1] minimizes the demands on crystal perfection, since at this angle of incidence the rocking curve's width is at its maximum. It is therefore the most widely used geometry, since only covalent semiconductor crystals like Si or Ge fulfill the demands of off-normal XSW.

2.5.4 Multipole Correction Parameters

It has been shown that depending on the experimental conditions, the dipole approximation is not generally applicable to the XSW analysis. That is, the photoelectron yield does not depend linearly on the x-ray intensity, as assumed above. For low Z elements (such as those found in organic adsorbates) and photon energies in the keV range, higher order terms contribute non-negligibly to the photoelectron yield and must be taken into account [69]:

$$Y = 1 + S_R R + |S_L|\sqrt{R} F_H \cos\left(\phi - 2\pi P^H + \psi\right) \tag{2.16}$$

S_R, S_L and ψ are called the multipole correction parameters, and they depend on the atomic species, the substrate and the geometry of the experiment.

---

[1] NIXSW refers to normal incidence of the x-rays with respect to the d planes one is exploiting, and not necessarily to the sample surface.

3

A Molecular Dislocation Network: PFP/Ag(111)

Dislocation networks and moiré patterns are both structures that form at heterointerfaces as a way to relieve strain caused by a lattice mismatch. In dislocation networks the strain is relieved laterally, while in moiré patterns it is relieved vertically. Both structures are attractive due to their great potential as nanoscale growth templates. Most examples of dislocation networks and moirés up to date occur in inorganic materials. Though moirés have been observed in organic layers for decades now [70; 71; 72; 73], only a few recent reports on organic dislocation networks exist [74; 75; 76; 77]. The additional internal degrees of freedom of molecules and the weakness of the non-covalent interactions present in organic layers make these inherently more complex than their inorganic analogues. For this reason, a basic understanding of the formation of these structures is still lacking. Here, we use the PFP/Ag(111) dislocation network as a model system and attempt to disentangle the different interactions present at the interface. Combining STM measurements with first-principle theoretical calculations we put forward a model that takes into account these different interactions and that is able to rationalize the formation of the dislocations in this system.

3.1 STM Results

Our low temperature STM measurements show that PFP monolayers (MLs) on Ag(111) arrange into a highly crystalline structure with large faultless domains exceeding 100 nm (see Fig. 3.1). The molecules are in a flat-lying configuration with an oblique unit cell of dimensions $a = 8.8 \pm 0.9\,\text{Å}$, $b = 17 \pm 1\,\text{Å}$, $\phi = 62 \pm 2°$. The long unit cell vector b is oriented along the close-packed direction of the substrate, though the long molecule axis very slightly deviates (approx. 3°) from this direction. Given the hexagonal symmetry of the Ag(111) surface, six discrete domains are observed, these being three rotational domains and their corresponding mirror-domains.

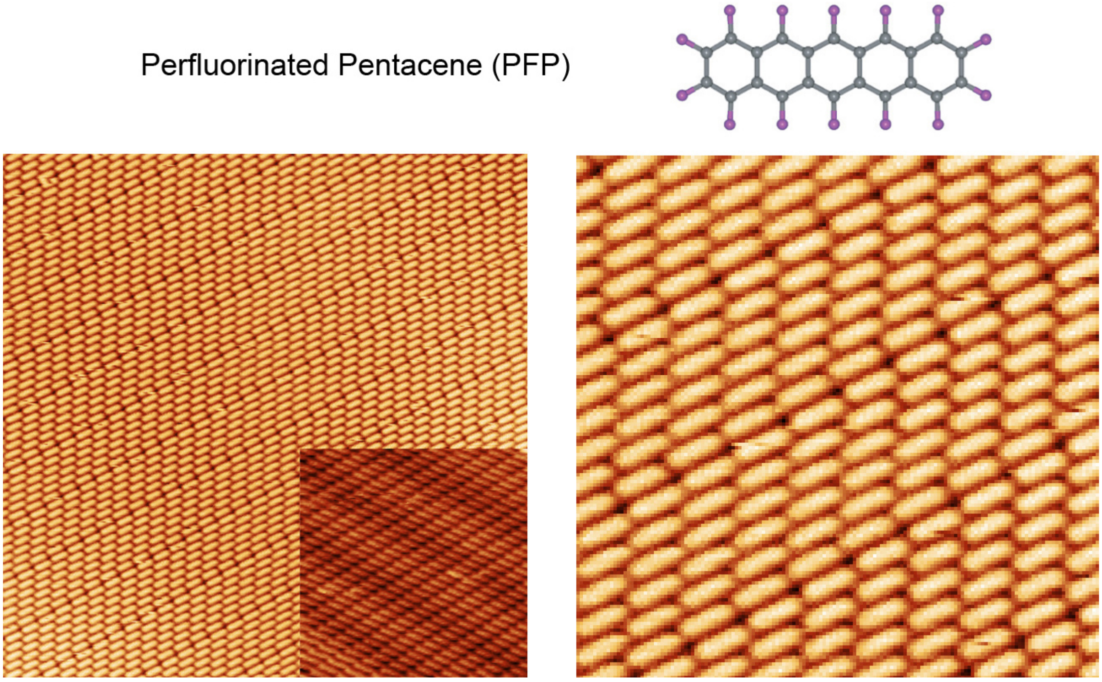

Figure 3.1: Above: Chemical structure of PFP molecule. Left: 50 nm x 50 nm image (-1.37 V, 9.08 pA) of PFP/Ag(111) showing the high crystallinity of the monolayer and periodic dislocations. Right: 15 nm x 15 nm image shows a close-up of the dislocation lines appearing every six molecule rows. PFP molecules appear as single peg-shaped features. Inset: The moiré structure found at room temperature, which is free of lateral dislocations. Taken from Ref. 78.

Additionally, a superstructure consisting of periodic dislocation lines in the direction of the long unit cell axis appears, usually every six molecules, as can be seen in Fig. 3.1. Along these dislocation lines, the molecules end up side by side in a nearly rectangular cell, as opposed to laterally shifted like in their oblique unit cell (unit cells marked in red in Fig. 3.2a). This side-by-side arrangement is expected to be energetically less favorable: the fluorine atoms are directly across from each other, enhancing electrostatic repulsion. This leads to an increased lateral distance between molecules (by 7 ± 4% as measured by STM—significantly lower than the 33% dilation associated with the recently proposed commensurate model [77; 79]) that lowers the packing density of the layer, thereby decreasing the energy gain associated with the molecule-substrate interactions.

3.2 Theoretical Calculations

Quantification of the molecule-substrate and intermolecular interactions, the balance of which lead to this specific arrangement, is obtained from Density Functional Theory (DFT) calculations, all of which have been carried out through the GPAW code [80]. The study of layers of aromatic molecules deposited on a metallic surface through DFT calculations brings up the question, which exchange-correlation functional is most appropriate for the particular system in question. The performance of Local Density Approximation (LDA) [81], General Gradient Approximation (GGA) [82], ab initio van der Waals (vdW-DFT) [83] and semi-empirical van der Waals (DFT-D) [84] functionals for different systems has been extensively investigated in the literature. One of the main conclusions of these studies is that GGA functionals have a general tendency to underestimate adsorption energies and overestimate distances between the aromatic molecule and the metal [85; 86; 87; 88]. Another general trend is that LDA functionals yield shorter distances and stronger adsorption energies than DFT-D and vdW-DFT. However, it is not possible to know a priori which of them will give results closer to the experimental ones for a particular system and thus, it is necessary to check this. In the case of PFP on Au(111) the calculated Au-PFP distances can be compared with the experimental one ($Z = 3.14\,\text{Å}$) measured recently by Duhm et al. [89]. Unfortunately, there is no experimental data for the PFP/Au(111) adsorption energy. However, it is possible to compare the calculated and experimental adsorption energies for a similar system to PFP/Au(111) such as pentacene (PEN) on Au(111) [90]. Toyoda et al. have studied the performance of GGA, DFT-D and vdW-DFT functionals for these two systems. In the present work we have completed the study, including the LDA results (see Table 1). Regarding the distance in the PFP/Au(111) system, the closest result to the experimental one is given by LDA. DFT-D shows a very good performance as well. Concerning the energetics in the PEN/Au(111) system, the LDA value is again the closest to the experimental one, whereas DFT-D gives the worst result. In view of these results, the LDA functional was chosen for the remainder of the calculations.

Table 3.1: Calculated equilibrium distances (Z) and adsorption energies (E_a) for PFP and PEN on Au(111) using LDA, GGA, vdW-DFT and DFT-D functionals. The experimental distance for PFP/Au(111) the experimental adsorption energy for PEN/Au(111) are also shown.

	LDA (PZ)		GGA (PBE)		vdW-DFT		DFT-D		Experimental	
	Z(Å)	E_a(eV)	Z(Å)	E_a(eV)	Z(Å)	E_a(eV)	Z(Å)	E_a(eV)	Z(Å)	E_a(eV)
PEN	3.0^e	1.55^e	3.7^a	0.14^a	3.7^a	1.66^a	3.2^a	2.51^a	–	1.1^b
PFP	3.16^e	1.30^e	4.2^c	0.08^c	3.7^c	1.94^c	3.2^c	2.68^c	3.14^d	–

[a] Ref. 85; [b] Ref. 90; [c] Ref. 86; [d] Ref. 89; [e] Present work.

The calculations can be divided in two parts. First, the molecule substrate interactions were quantified: maintaining the molecular orientation observed in the experiment, the adsorption energy of a PFP molecule on the Ag(111) surface was calculated as a function of its displacement over the surface (see Fig. 3.2a). The calculations yield a large adsorption energy ranging from 1.34 to 1.12 eV, depending on the molecule's adsorption site. As can be seen in the figure, there is a large variation in adsorption energy as the molecule is displaced in the Y direction, whereas the adsorption energy remains practically constant in the X direction. The reason for this lies in the size and shape of the molecule: its long axis—oriented in the X direction—is several times larger than the lattice spacing, making the displacement in this direction less perceptible. The calculations show that the adsorption of a molecule on the silver substrate is always favorable for the system. As a consequence, the more compact the arrangement of the layer is, the higher the energy gain will be. A dislocation reduces the compactness by increasing the width of the unit cell by about 7%, thus effectively reducing the energy gain associated with the molecular adsorption by this amount, which is of the order of 0.08 eV.

In the second part of the calculations we focus on the intermolecular interactions. We consider two contributions: intermolecular interactions neglecting the substrate, and those mediated by it (see appendix A.1 for details). Calculations yielded 0.06 eV and 0.03 eV respectively, giving a total attractive intermolecular interaction energy of

0.09 eV for both the oblique or rectangular unit cells. Substrate mediated interactions (SMI), are discussed in the literature [12; 91], but to our knowledge up till now there have been few attempts to quantify them. Sykes et al. were able to experimentally determine the SMI of benzene on Au(111), finding it to be approximately 0.005 eV per molecule [91], compared with a molecule-substrate interaction of 0.64 eV [92]. In view of these values, a substrate mediated interaction energy of 0.03 eV compared to a molecule-substrate interaction of around 1.2 eV as found in our PFP/Ag(111) system seem reasonable results, considering the larger size, and number of atoms in PFP compared to benzene.

3.3 A Model

The structural model obtained from our experiments is shown in Fig. 3.2a. According to this model, the molecules arrange around the adsorption minimum (blue area) in their oblique configuration so as to maximize the energy gained from adsorption and optimize the packing density. As the molecules get farther from the equilibrium position (dark blue), the adsorption energy continuously decreases from molecule to molecule, until reaching a threshold value for which it becomes more favorable to form a dislocation in spite of the loss of compactness, instead of maintaining the oblique configuration. (The situation should of course be symmetrical, as is shown in the figure: dislocations occur after molecule 6 and before molecule 1.) The molecules therefore shift to remain on a more favorable position on the substrate, adopting a rectangular cell.

We have performed theoretical calculations using the unit cell parameters obtained by STM in order to show that the formation of dislocations reduces the system's energy density. First we consider a dislocation-free system. Given the incommensurability of the overlayer in the direction of a, molecules will occupy all positions on the substrate, i.e. the molecule-substrate interaction energy per molecule will simply be the average value, 1.23 eV. The energy density in this case comes out to be 9.97 meV/Å^2. Next, we consider the different possible dislocations that could occur (after $N = 3, 4, 5, 6, 7, 8, 9$ or 10 molecules). As these are naturally a way to increase the energy gain of the system, we assume that the dislocation lines must minimize the overall system energy by keeping the molecules in a certain range of adsorption energies. In order to do so it is necessary for the dislocation to bring the next group of N molecules to a position

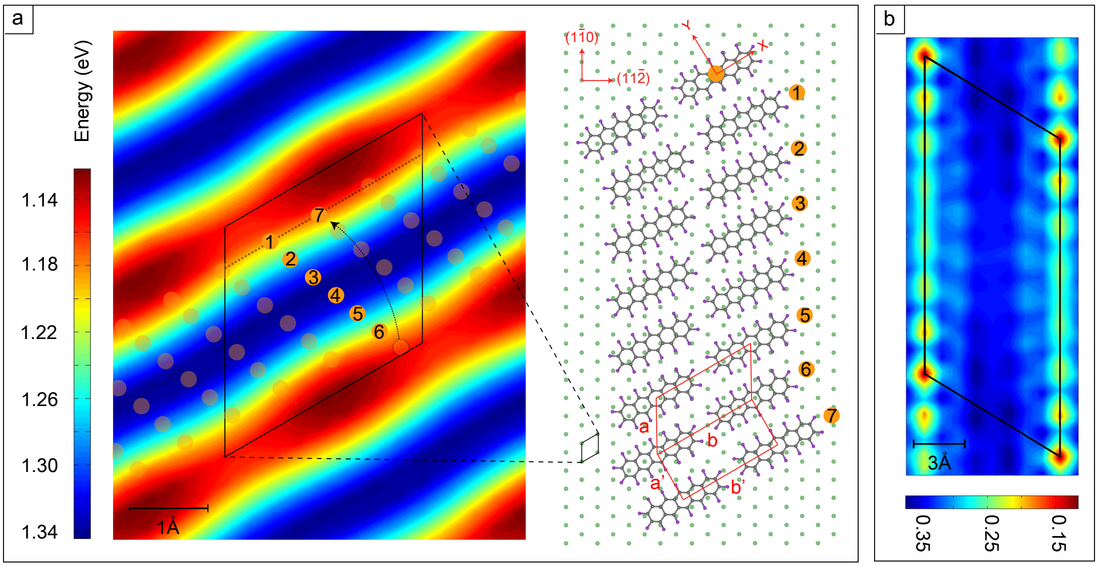

Figure 3.2: (a) Model for dislocations. Structure is commensurate in the direction of b, but not in that of a. Oblique and rectangular cells are marked in red. On the left the adsorption energy of PFP molecule as a function of its position on the substrate is shown. Numbers indicate the positions of molecules as in the schematic to the right, projected onto a single unit cell. It is essential for the model that the next group of molecules (7 and on) be aligned in Y with the first group (1-6) (b) Adsorption energy for a molecule on the first PFP layer. Oblique unit cell of first layer is marked, with the vertices corresponding to molecular centers of the first layer molecules. Adapted from Ref. 78.

equivalent to that of the first group, i.e. there must be no displacement in Y with respect to the previous group (alignment in Y). This guarantees that successive groups will remain in the region of minimum adsorption energy and not stray into less favorable areas. This is made clear in Fig. 3.2a: the dotted line joining positions 1 and 7 marks the direction of constant Y. Taking the rectangular lattice angle as $\phi' = 90°$ and the experimental oblique-cell parameters [1], we calculate the cell dilation necessary to keep the successive groups of molecules aligned in Y for each N. All that is left now is to calculate the energy density in each case. The results are plotted in Fig. 3.3 and show that for $4 < N < 8$, dislocations are an effective way to reduce the total energy of the system. The maximum energy gain is achieved for $N = 6$, the experimentally observed case, with an energy density of $10.03\,\mathrm{meV/Å^2}$. The difference with $N = 5$ and 7 is small, explaining why these are sometimes observed.

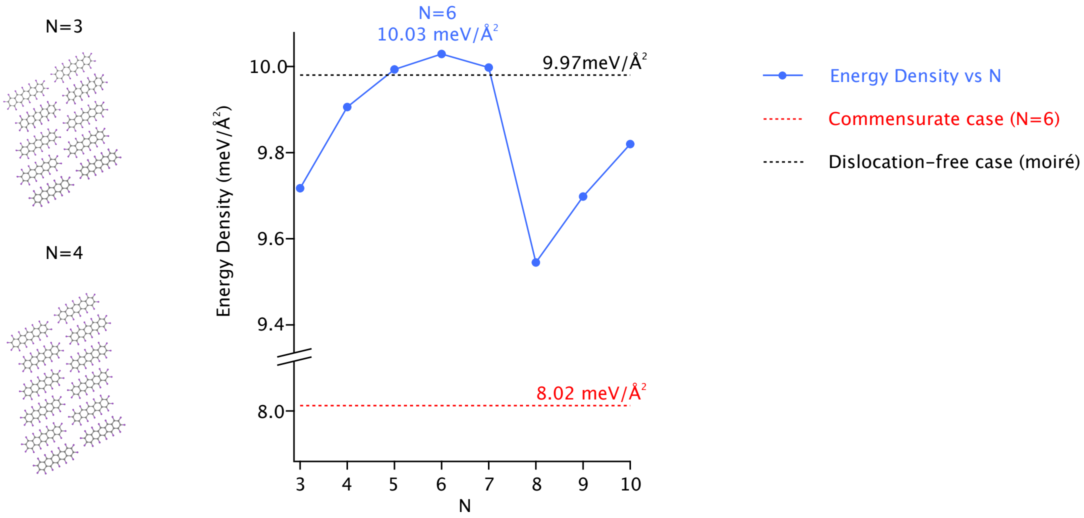

Figure 3.3: Energy densities for the system with dislocations every N molecules (blue), the dislocation-free case (black) and the commensurate case (red). The approximate structure of the $N = 3$ and $N = 4$ cases are shown. Adapted from Ref. 78.

By comparing the energy densities of the $N = 6$ case and the dislocation-free layer we can obtain an estimate of the threshold energy associated with the formation of the dislocations. This difference is $0.06\,\mathrm{meV/Å^2}$. Such a small value is typically within DFT error margins. Therefore, while the energy variation with N is significant and

---

[1] Parameter a was fixed to $a = 8.87\,Å$ in agreement with the 7% dilation of the rectangular unit cell resulting from the model with $N = 6$.

unambiguously favors periodicities around $N = 6$, the reliability of the $0.06\,\mathrm{meV/Å^2}$ difference with respect to the dislocation-free layer may be doubted.

Interestingly, additional STM measurements at room temperature (RT) prove the correct order of magnitude of our DFT results and the subtlety of the energy balance responsible for such dislocation networks. RT PFP/Ag(111) measurements show ordered layers with an oblique cell practically identical to that found at low temperature (LT). However, instead of the dislocation lines, a voltage-independent modulation of contrast is observed along the same direction. This modulation is interpreted as a linear moiré pattern generated by the lattice mismatch between overlayer and substrate (see Fig. 3.1, inset), in which molecules on areas of same contrast are located on crystallographically equivalent substrate sites. This occurs with a longer periodicity as compared to the dislocations, after around 8 molecules in the direction of the short axis. An explanation for the differences between LT and RT monolayers may be that the strain associated with the mismatch in PFP-substrate positions responsible for the dislocations at LT is compensated at RT by substrate phonons and molecular vibrations. Multiplying the area of the unit cell times 0.06 meV, yields about 8 meV per molecule,[1] which is of the order of the thermal energy at LT ($kT \sim 8\,\mathrm{meV}$) and far below that of RT ($kT \sim 26\,\mathrm{meV}$), as would be expected from the presence of the dislocations at LT and their disappearance at RT. The most recent publication dealing with the PFP/Ag(111) interface, by Marks et al. [93] observes a structural transition occurring at 130 K by two photon photoemission (2PPE) and low energy electron diffraction (LEED). From their LEED results, they conclude that the system passes from an ordered phase at low temperature (dislocation network) to a disordered phase above 130 K. Our findings of an ordered (moiré) phase at room temperature are not in agreement with the claim of a disordered phase, however, different preparation methods may be able to explain this discrepancy, since our RT layers were freshly deposited, and not obtained from heating the LT phase.

Note that the model proposed (Fig. 3.2) is essentially different from that proposed in previous work [77; 79], where the structure is proposed to be commensurate throughout the layer. We discard a commensurate structure because it fails to explain the

---

[1] The exact value should be taken with care not only because of DFT error margins, but also because differences in the thermal expansion coefficients between the organic layer and the Ag substrate may additionally modify the interaction potential landscape.

periodic dislocation lines: upon commensuration, all molecules are energetically alike; intermolecular interaction energy is indeed accumulated throughout the layer at the expense of an optimized molecule substrate matching, but that energy is always the same. Thus, if the oblique arrangement is energetically favorable for one molecule, it should be the same for all the next ones and a dislocation would not be favored at any time. We performed calculations for the commensurate case, and found the intermolecular interactions of the commensurate oblique cell to be strongly repulsive (-0.29 eV per molecule) due to the proximity of the fluorine atoms of neighboring molecules. Considering each molecule to be on the most favorable adsorption site (1.34 eV), the energy density of the commensurate layer comes out to be 8.02 meV/Å^2, well below the 10.03 meV/Å^2 of the non-commensurate structure we propose. (See Fig. 3.3 for a comparison of all calculated energy densities.)

We also discard a bistability of relatively similar energy configurations (oblique vs. rectangular unit cells) as source for the dislocation formation. This was proposed e.g. for the linear dislocation patterns at the TCNQ/Cu(100) interface [76]. However, that should lead to a random distribution of the dislocation lines. Instead, the well defined periodicity we observe suggests there is an additional elastic stress contribution that leads to periodic accumulation and release of stress throughout the layer, as suggested above.

3.4 Second Layer Growth

Upon increasing coverage, it becomes clear that the dislocation lines arising from the interactions at the molecule-substrate interface are transferred to the second layer (Fig. 3.4 b), contrasting with previous reports [77; 79]. While this might be ascribed to the different preparation conditions, DFT calculations support the convenience of dislocation transfer to the second layer. The adsorption energy of a PFP molecule azimuthally oriented as those in the first monolayer has been calculated by DFT as function of its lateral displacement (Fig. 3.2b). The maximum adsorption energy (0.35 eV) is significantly lower than that of PFP on Ag(111) and explains the absence of second layer islands until the first layer is complete. As in the case of PFP on the silver surface, there is a strong variation in the direction of a and only a minor modulation along b. However, given that at the dislocation lines the molecules are not only shifted along b, but are also subject to an increased distance along a, the dislocations are transferred to the second layer to avoid an accumulated mismatch along a and its associated energy loss.

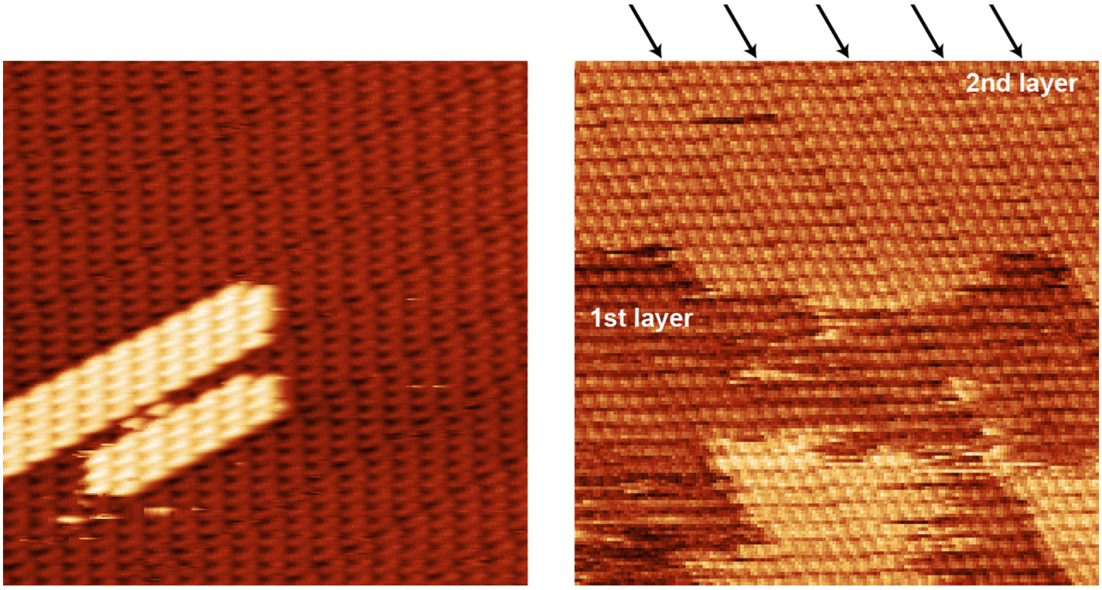

Figure 3.4: 30 nm × 30 nm images of initial (a) and more advanced (b) stages of second layer growth. In (b) it becomes clear that the dislocation pattern is transferred to the second layer. Arrows mark second-layer dislocation lines. Taken from Ref. 78.

4

Self-Assembly and the Role of H-Bonding

This chapter exclusively presents STM data. The measurements were taken on a variety of machines: the CuPc+PFP systems were measured on a VT-Omicron STM and a SPECS Århus STM at the NanoLab in San Sebastián, Spain, while the PEN+FCuPc and CuPc+PEN systems were measured on a JEOL STM at the MANA Nano-Electronics Materials Unit at NIMS[1] in Tsukuba, Japan.

The Ag(111) and Cu(111) were prepared by cycles of sputtering (800 eV) and annealing (300-400°), and molecules were evaporated from Knudsen cells, at temperatures of about 350°C for the phthalocyanines and 180°C for the pentacenes. The deposition rate could be controlled using a quartz crystal microbalance[2].

Images were analyzed using the free software *WSxM* by Nanotec [94] and the open source program *Gwyddion* [95].

This chapter examines the lateral structure of molecular monolayers (MLs) made up of different pair combinations of CuPc, PFP, FCuPc, and PEN by STM. There are two sections: the first focuses on the donor-acceptor pair CuPc+PFP, which is characterized on Ag(111) and Cu(111), and addresses the effect of the substrate. The structure of the single component layers is analyzed, followed by that of their 1:1 stoichiometric mixture. The CuPc+PFP mixture is found to assemble into a highly ordered layer that maximizes donor-acceptor contact, an indication of enhanced intermolecular

---

[1] National Institute for Materials Science

[2] The density of the molecules in their thick film structure is $\rho_{\mathrm{PFP}} = 2.1\,\mathrm{g/cm^3}$, $\rho_{\mathrm{CuPc}} = 1.6\,\mathrm{g/cm^3}$, $\rho_{\mathrm{PEN}} = 1.3\,\mathrm{g/cm^3}$, $\rho_{\mathrm{FCuPc}} = 2.0\,\mathrm{g/cm^3}$

interactions between the two different molecules, presumably by C-H$\cdots$F-C hydrogen bonding. In the second section, the substrate is fixed as Ag(111), and the role of hydrogen bonding is investigated by mixing the opposite donor-acceptor pair PEN+FCuPc, where hydrogen bonding is again expected, and the donor-donor pair CuPc+PEN, where hydrogen bonding cannot be present, and comparing their structures. Different arrangements for ratios other than 1:1 are also explored for the CuPc+PFP mixture.

Before beginning, the geometry of the substrate is briefly described as follows. The two substrates dealt with in this work, Ag(111) and Cu(111), are face centered cubic (111) surfaces, meaning they exhibit thee-fold rotational symmetry and three mirror planes (refer to Fig. 1.4). The topmost layer, illustrated in Fig. 4.1, presents six-fold symmetry and six mirror planes. The vectors defining these high symmetry directions are $(\bar{1}\,1\,0)$ (close-packed direction) and $(1\,1\,\bar{2})$ (next-nearest neighbor direction) and will be used to describe the epitaxial relationship between overlayer and substrate, and as the vector basis to define the epitaxial matrices. In the structural description of the layers, $(\bar{1}\,1\,0)$ and $(1\,1\,\bar{2})$ are used to refer to any of the six equivalent directions.

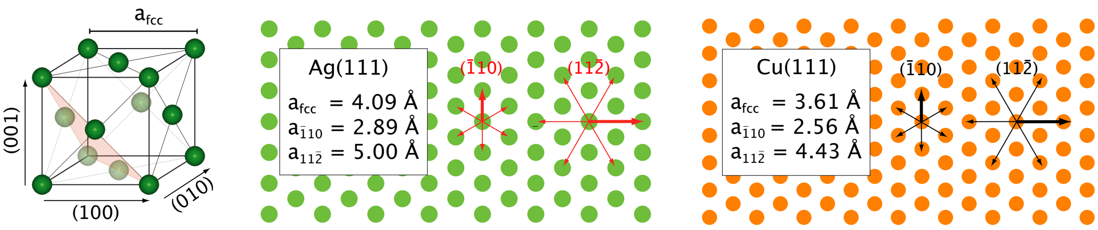

Figure 4.1: The fcc (111) surface has a nearest neighbor distance of $a_{\bar{1}10} = a_{\mathrm{fcc}}/\sqrt{2}$ and a next-nearest neighbor distance of $a_{11\bar{2}} = a_{\mathrm{fcc}} \cdot \sqrt{3/2}$.

4.1 The CuPc+PFP 1:1 Molecular Blend

In this first section the structure of monolayers of PFP and of CuPc, and their 1:1 molecular blend will be characterized for both the Ag(111) and Cu(111) substrates.

4.1.1 CuPc+PFP/Ag(111)

CuPc/Ag(111) - The structure of the CuPc/Ag(111) layer has already been reported on in two RT-STM studies by Manandhar et al. [96] and Grand et al. [97]. In both these studies monolayer coverages were obtained by thermal desorption of multilayers.

In the study by Manandhar et al. a square lattice (14 Å× 14 Å) was found. On the other hand, Grand et al. found three distinct molecular phases: two with a rectangular (12.5 Å× 14.5 Å and 11.6 Å× 15.0 Å) and one with an oblique (13.9 Å× 13.8 Å, 102°) unit cell. In their LEED study Kröger et al. [98] explored the coverage dependence of the unit cell (obtained by submonolayer deposition) in the 0.89ML-1.0ML range, finding a continuously expanding unit cell with increasing coverage.

In our study, samples were prepared by mono- or submonolayer deposition, in line with those of Kröger et al., however our STM measurements were conducted at liquid nitrogen temperatures. We find CuPc/Ag(111) forms a highly crystalline layer with large, faultless domains. The unit cell parameters were measured to be $a = 14.1 \pm 0.8$ Å, $b = 13.9 \pm 0.7$ Å, $\alpha = 88 \pm 4$° (see Fig. 4.2), in agreement with the unit cell obtained from thermal desorption by Manandhar et al. and within the ranges obtained in the study by Kröger et al.

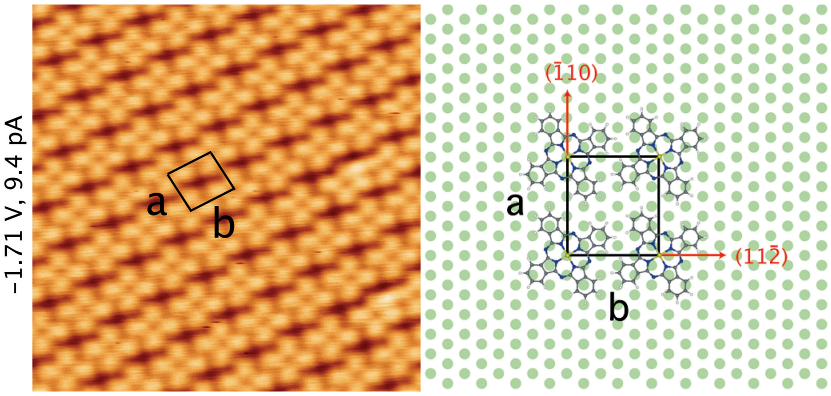

Figure 4.2: A 11.5 nm × 11.5 nm image of the CuPc/Ag(111) monolayer, with unit cell marked in black, and epitaxial model on the right.

As expected from the symmetry of the substrate and overlayer (refer to section 1.2.3), six discrete domains are observed, which show the influence of the substrate in the formation of the layer. An example of different domains is shown in Fig. 4.3. From analysis of domains, it is found that the unit cell vectors follow the $(\bar{1}\,1\,0)$ and $(1\,1\,\bar{2})$ directions, which in combination with the measured parameters allow us to describe the observed structure by a rectangular point-on-line commensurate unit cell with the epitaxial matrix

$$\frac{1}{3}\cdot\begin{pmatrix} 5 & 0 \\ 0 & 8 \end{pmatrix}.$$

The epitaxial model is shown in Fig. 4.2.

The diagonals of the CuPc molecule also follow the high symmetry directions, as has been previously reported in other Pc/Ag(111) studies [74; 96; 97; 99]. Fig. 4.3 additionally shows step edges lined with CuPc molecules. Surface defects and step edges are usually the first adsorption sites. The reason behind this has to do with the higher coordination at sites along the bottom of a step, as well as with the increased (at the bottom of the step) and decreased (at the top of the step) electron density at these sites [12]. However, in contrast to other systems such as CuPc/Au(111) [100] or FCuPc/Cu(111) [101], in this case the molecular rows forming at step edges do not seem to influence the domains extending into the terraces.

It was also possible to measure the second layer of CuPc, shown in Fig. 4.4. The inset profile shows two steps, indicated by arrows: one of about 2.3 Å, which corresponds to a monoatomic step on the Ag(111) surface ($d_{111} = 2.36$ Å), and a larger step of about 2.9 Å, which can be assigned to a step between the first and second layers. The molecules of the second layer, apparently lying flat like those of the first, follow the directions imposed by the layer underneath, as has been reported for other systems [78; 102]. However, the resolution of the image does not allow determining the molecular orientation of the CuPc molecules in the second layer.

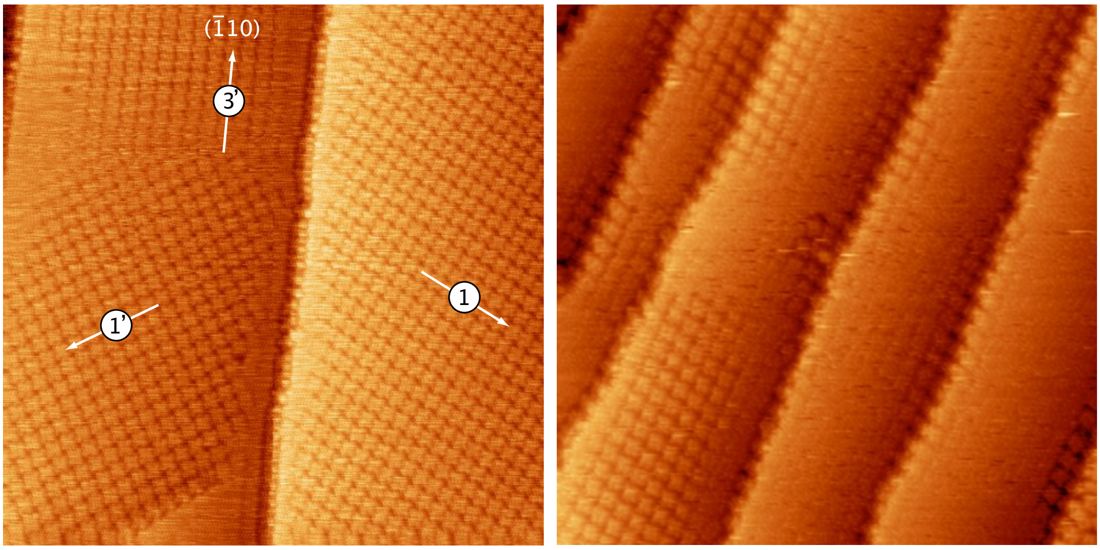

50 nm x 50 nm; –1.05 V, 11.4 pA

50 nm x 50 nm; –1.31 V, 9.9 pA

Figure 4.3: CuPc/Ag(111). Left: Three domains, labeled according to Fig. 1.4; Right: Image showing step decoration.

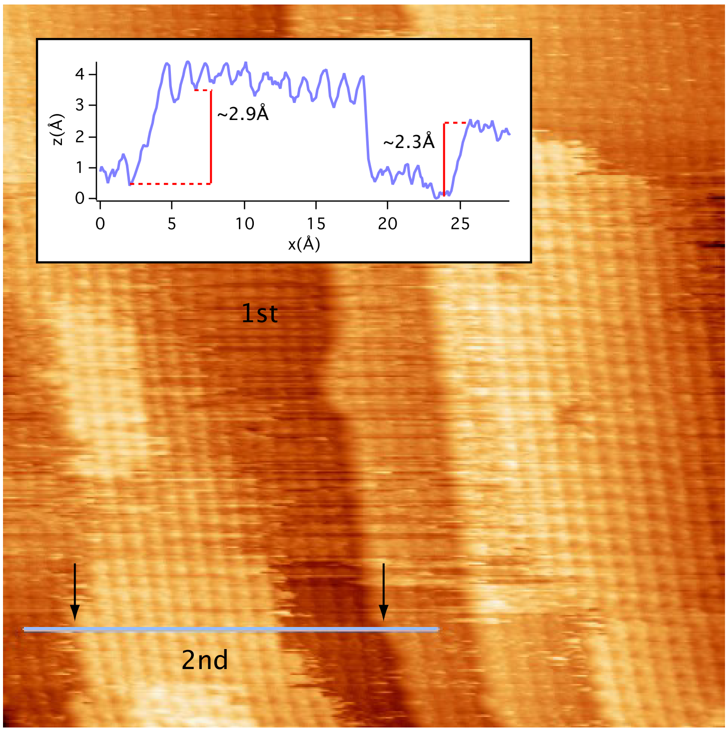

50 nm x 50 nm; -1.26 V, 8.8 pA

Figure 4.4: First and second layers of CuPc/Ag(111). Inset shows the profile of the steps marked by arrows in the main figure.

PFP/Ag(111) - As described in the previous chapter, PFP/Ag(111) forms very large faultless layers (both at low and room temperature) with a unit cell $a = 8.8 \pm 0.9$ Å, $b = 17 \pm 1$ Å, $\alpha = 62 \pm 2\,°$, shown in Fig. 4.5. The unit cell vectors follow the close-packed directions of the substrate, though PFP's long axis seems to deviate slightly from this direction (about 3°). The proposed structure has an oblique unit cell commensurate in the direction of the long unit cell vector **a**, but not so in the direction of the short unit cell vector **b** and is shown schematically in Fig. 4.5.

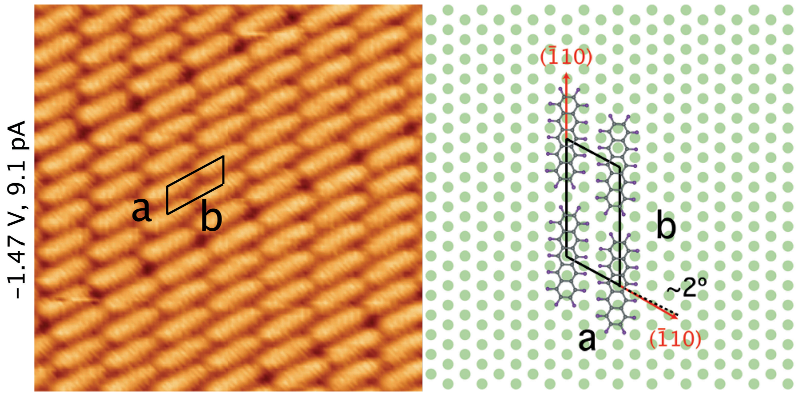

Figure 4.5: A 11.5 nm × 11.5 nm image of the PFP/Ag(111) monolayer, with unit cell marked in black, and epitaxial model on the right.

At low temperature a structural transition occurs, which has been described in detail in the previous chapter. Submonolayer PFP/Ag(111) (LT) is shown in Fig. 4.6 and is a nice example of the different domains that can occur on the surface. In this image a number of small domains have formed on narrow terraces. Additionally, the mobility of the PFP molecules in the submonolayer phase is revealed in the magnified image to the right, in which domains seem faded and streaky. In one area (third terrace from the left) two domains seem to be superimposed, criss-crossing. The reason for all this is that molecules are rapidly moving between different favored adsorption geometries faster than the tip is scanning. This sometimes gives molecules a faded or “phantom-like” [12] appearance. The mobility of the molecules in the submonolayer is likely enhanced by the scanning of the tip.

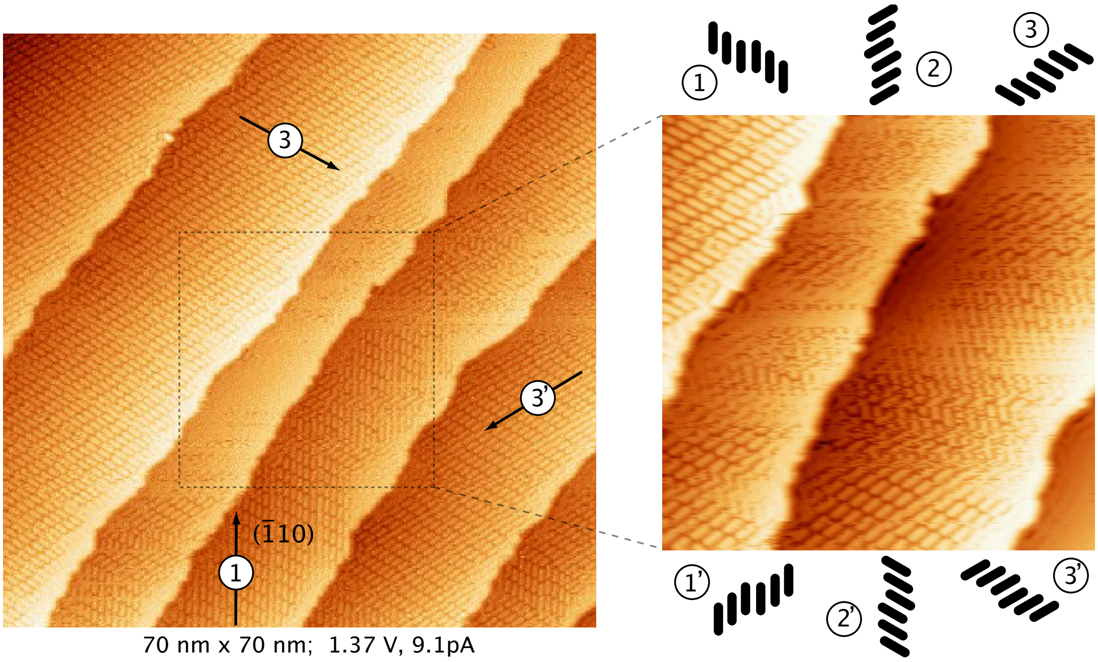

Figure 4.6: Different domains of PFP/Ag(111). Arrows point in the close packed directions, i.e. $(\bar{1}\,1\,0)$, and numbers identify each of the domains, represented to the right in analogy to Fig. 1.4. The enlarged area shows the mobility of submonolayer PFP.

CuPc+PFP/Ag(111) - Deposition of both molecules onto the Ag(111) substrate leads to an ordered molecular mixture, in which molecules of one type are surrounded by the other type. This strongly suggests that the assembly is driven by hydrogen bonding between PFP's fluorine atoms and CuPc's hydrogen atoms. The highly crystalline layers of the mixture can fill large terraces extending over 100 nm, as shown in Fig. 4.7. The unit cell of this 1:1 mixture has the parameters $a = 22 \pm 2$ Å, $b = 29.3 \pm 0.6$ Å, $\alpha = 89 \pm 6\,^{\circ}$, and unit cell vectors **a** and **b** that follow the high symmetry directions $(\bar{1}\,1\,0)$ and $(1\,1\,\bar{2})$, respectively. The mirror symmetry of the mixture reduces the number of distinguishable domains to just three. The observed structure fits nicely with a unit cell with the commensurate epitaxial relation (taking the substrate vectors $\mathbf{A}\|(\bar{1}\,1\,0)$ and $\mathbf{B}\|(1\,1\,\bar{2})$ as a basis)

$$\begin{pmatrix} 8 & 0 \\ 0 & 6 \end{pmatrix}.$$

An STM image of the mixture and its epitaxial model is shown in Fig. 4.8

This matrix describes the size and orientation of the unit cell on the substrate. However, it is interesting to look *into* the cell and examine the orientation of the individual molecules. A molecule normally has a preferred adsorption geometry on a given substrate, showing a preferential adsorption site (top, bridge, hollow) and orientation with respect to the underlying surface structure. This configuration corresponds to the energetically most favorable geometry. (In Chapter 3 the preferred adsorption site of PFP on Ag(111) was investigated with theoretical calculations; refer to Fig. 3.2.) Provided the molecules lack functional groups able to add significant intermolecular interactions, one may assume that the molecular arrangement in single-component monolayerswill be dominated by molecule-substrate interactions and that the molecules will therefore adopt their favored geometry. For this reason it is of interest to compare the molecular orientations of molecules in the 1:1 mix with those found in the single component layers.

We find that in the CuPc+PFP/Ag(111) system all the PFP molecules share the same (equivalent) orientation, with the long axis approximately following the $(\bar{1}\,1\,0)$ (close-packed) direction (see Fig. 4.8). This is the same orientation found in the PFP monolayer, which can be assumed to show the preferred geometry. The same is true for the CuPc molecule: in the mix, as well as the single component layer, the "arms" of the CuPc molecule point in the high-symmetry directions of the substrate, $(\bar{1}\,1\,0)$

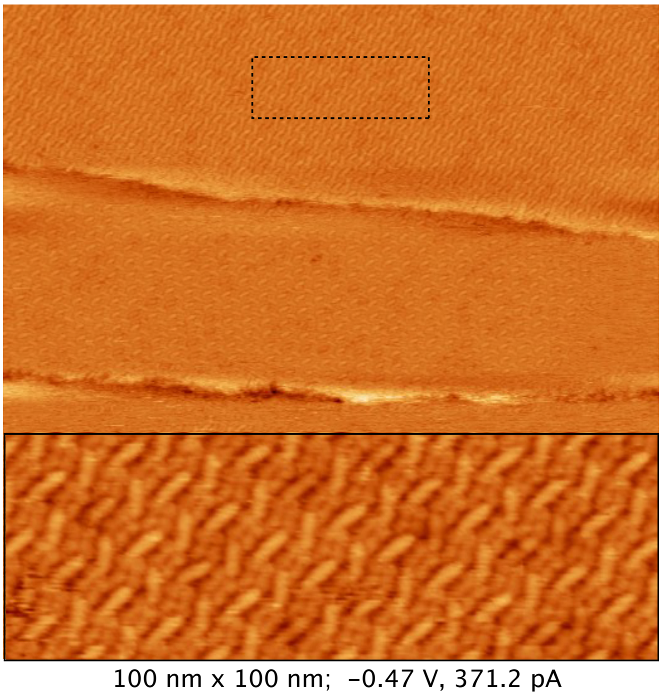

Figure 4.7: The CuPc+PFP/Ag(111) mixture is found to form very large stable layers, exceeding 100 nm. The image shows two large terraces covered with the mixture, which is shown in a close up below.

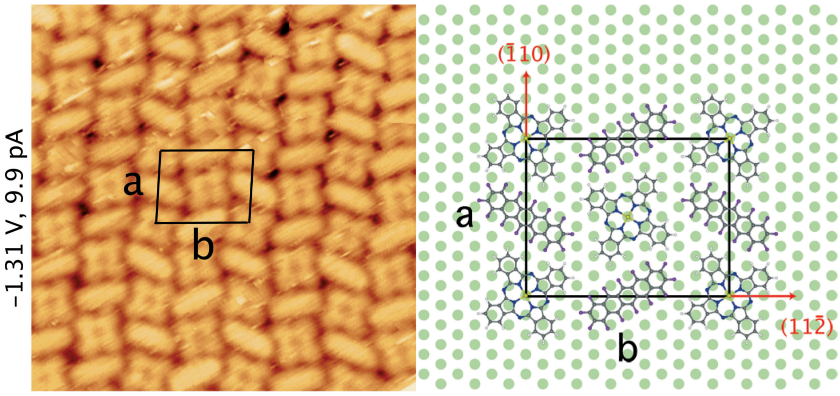

Figure 4.8: A 11.5 nm × 11.5 nm image of the CuPc+PFP/Ag(111) system, with unit cell marked in black, and epitaxial model on the right.

and $(1\,1\,\bar{2})$. From this analysis it becomes clear that the system has found a way to truly optimize the interactions: on the one hand, it preserves what we take to be the energetically most favorable molecular orientations, maximizing the energy gained from molecular adsorption, and on the other hand, it chooses to arrange the molecules in alternating rows in order to maximize contact between PFP and CuPc, and take full advantage of the enhanced intermolecular interactions that now exist between the molecules. Although nothing can be said about the actual *site* of adsorption, the proposed commensurability of the overlayer would additionally ensure a maximal energy gain on this front.

4.1.2 CuPc+PFP/Cu(111)

CuPc/Cu(111) - The CuPc/Cu(111) system was previously studied at low temperature for submonolayer coverages [103]. In this LT-STM study the adsorption geometry of individual CuPc molecules on the Cu(111) surface was determined: these are centered on top of a copper atom, and orient their diagonals in the high symmetry directions of the substrate. For submonolayer coverage a rectangular commensurate 15.5 Å × 17.6 Å cell is found, and the molecular orientation slightly deviates from that found for single molecules. In a study by Buchholz and Somorjai [104] based on LEED measurements, an oblique lattice 12.6 Å × 12.6 Å, 85° with an 8° angle between lattice vector and $(\bar{1}\,1\,0)$ direction is proposed. Fig. 4.9 shows an STM image of CuPc/Cu(111) along with an epitaxial model.

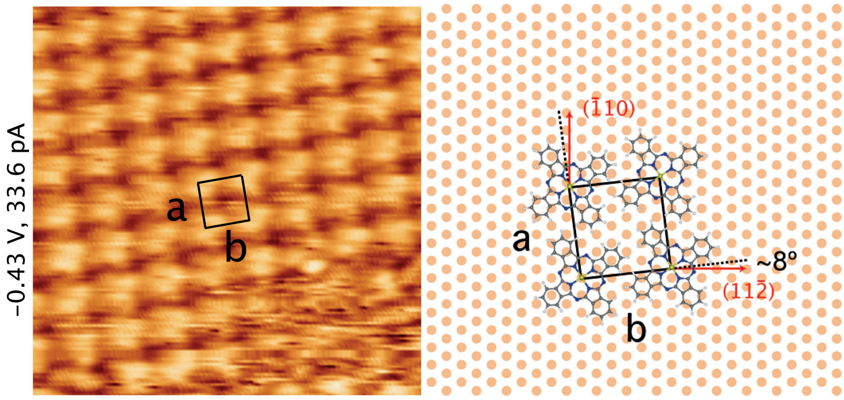

Figure 4.9: A 11.5 nm × 11.5 nm image of CuPc/Cu(111), with unit cell marked in black, and epitaxial model on the right.

In our room temperature study, we find a monolayer with parameters $a = 13.2 \pm 0.6$ Å, $b = 13.4 \pm 0.6$ Å, $\alpha = 89 \pm 3°$. Analysis of domain orientations shows that, in contrast to CuPc/Ag(111), the lattice vectors do not follow the high symmetry directions, but form an angle of $8 \pm 3°$ with them, in agreement the previous LEED study [104]. However, regarding the unit cell, our measurements reveal its size to be in between those proposed by Buchholz and Karacuban. In spite of the observation of six discrete domains, no clear epitaxial relation to the substrate was found.

On silver, large areas of high crystallinity were found, whereas on copper dislocations and domain boundaries are more common (see figure 4.10). This suggests a smaller diffusion length of CuPc on Cu(111), which is consistent with the commonly observed higher reactivity of Cu surfaces as compared to Ag. Additionally, the better registry of the CuPc molecules with the silver substrate may also favor an enhanced crystallinity on this substrate.

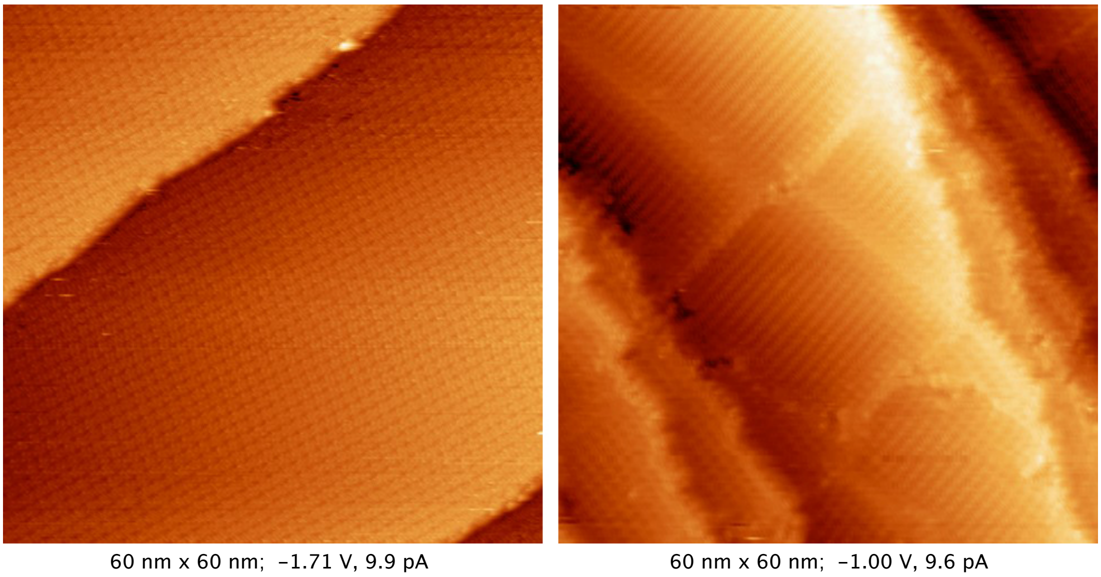

Figure 4.10: A higher crystallinity is found for CuPc on Ag(111) (left) than on Cu(111) (right).

PFP/Cu(111) - The PFP/Cu(111) system was first described by Koch et al. [105], who found a rectangular unit cell. The structure we were able to observe is somewhat different: it is oblique and more similar to that found on silver, with parameters $a = 9.2 \pm 0.9\,\text{Å}$, $b = 17 \pm 1\,\text{Å}$, $\alpha = 65 \pm 7\,^\circ$ and unit cell vectors pointing in the close-packed directions. It is quite possible that PFP/Cu(111) can form different structures, and that different preparation conditions may favor different polymorphs. In a more recent and detailed report [106] Glowatzki et al. describe the PFP layer in terms of a cell that is in better agreement with our data. Furthermore, they propose that the ordered PFP layer observed by STM by Koch et al. [105] is in fact a second layer of PFP, growing on an initially disordered monolayer. We cannot exclude the possibility that this be the case in our data as well.

Whether monolayer or bilayer, our PFP/Cu(111) images unambiguously showed discrete domains. This can be seen in Fig. 4.11, which shows three different domains, with rows following the $(\bar{1}\,1\,0)$ directions (marked with black arrows), indicating that an epitaxial relationship with the underlying substrate exists, or perhaps that the second

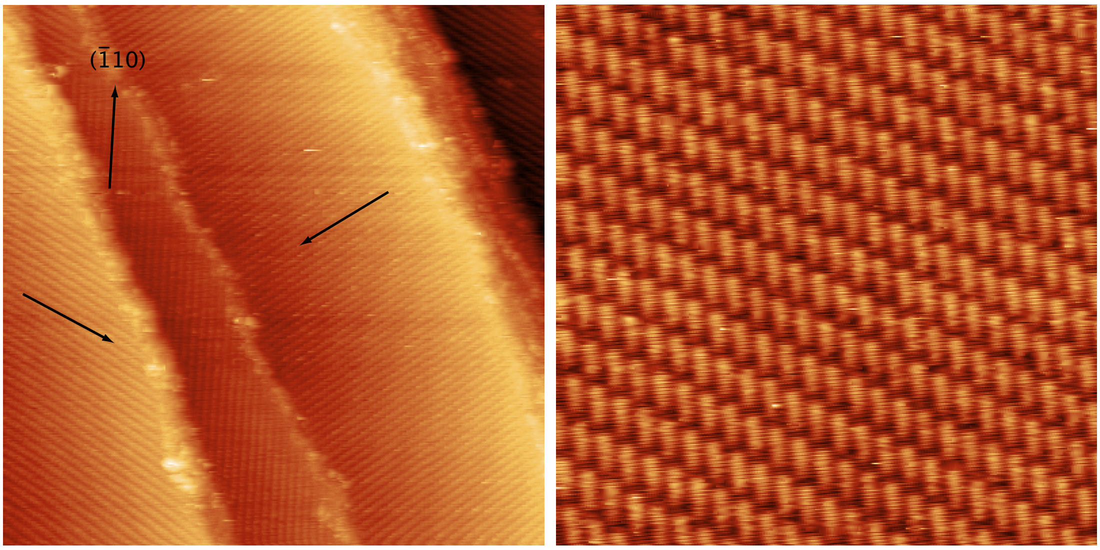

50 nm x 50 nm; −1.01 V, 9.1 pA

20 nm x 20 nm; −1.26 V, 7.6 pA

Figure 4.11: Left: Three domains of PFP/Cu(111), with arrows pointing in the close packed directions. Only the rows of PFP can be made out; Right: An image showing molecular resolution.

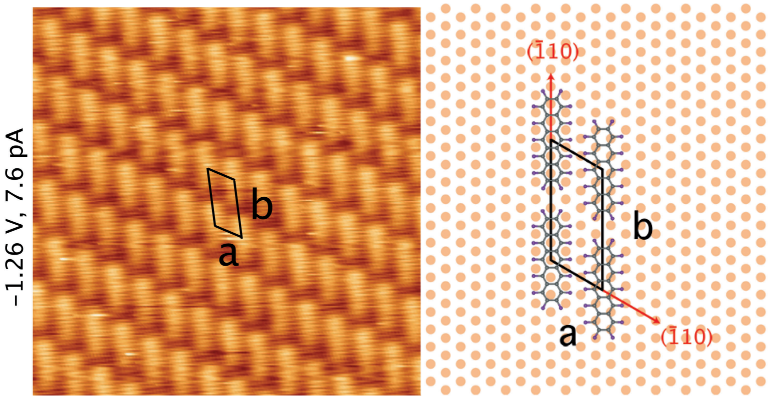

Figure 4.12: A 11.5 nm × 11.5 nm image of PFP/Cu(111), with unit cell marked in black, and epitaxial model on the right.

layer molecules follow the growth direction of those underneath, as was seen in the previous chapter for PFP/Ag(111). Fig. 4.12 shows an STM image of PFP/Cu(111) and it's relation to the substrate.

CuPc+PFP/Cu(111) - Mixing CuPc and PFP on the Cu(111) substrate leads to the same binary structure found on Ag(111), with parameters $a = 21 \pm 1$ Å, $b = 27 \pm 2$ Å, $\alpha = 89 \pm 5\,°$. As before, a rectangular cell commensurate with the substrate is proposed. In this case unit cell vectors **a** and **b** follow the high symmetry directions $(1\,1\,\bar{2})$ and $(\bar{1}\,1\,0)$ respectively, opposite to the case on Ag. The corresponding epitaxial matrix is

$$\begin{pmatrix} 0 & 5 \\ 11 & 0 \end{pmatrix}$$

Fig. 4.12 an STM image and epitaxial model of the mixture on Cu(111).

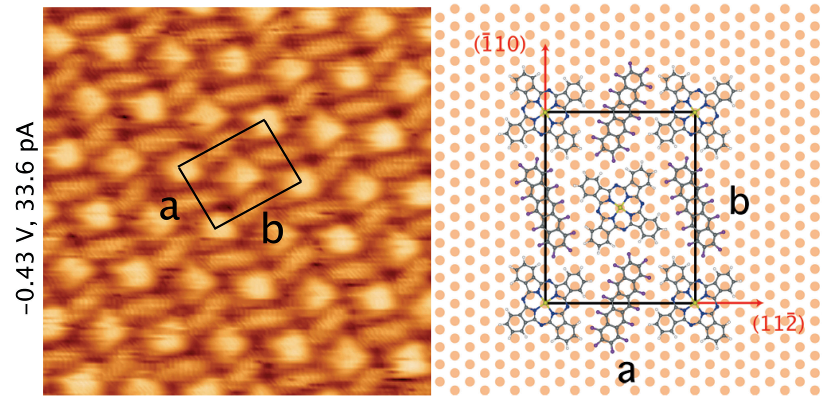

Figure 4.13: A 11.5 nm × 11.5 nm image of the CuPc+PFP/Cu(111) system, with unit cell marked in black, and epitaxial model on the right.

The orientation of the molecules is harder to make out on Cu(111) than on Ag(111), since the characteristic cross shape of CuPc is not clearly resolved in most images. However, from the available data, it does seem that CuPc has the same orientation in the mixture as it does in the single component monolayer, approximately following the substrates' high symmetry directions, as on Ag(111). As for the PFP molecules, their long axis is oriented approximately in the $(1\,1\,\bar{2})$ direction, opposite to the case on Ag(111). An unambiguous comparison with the monolayer is not possible, given the uncertainty of whether our images correspond to mono- or bilayer PFP. However, if we assume that the bilayer follows the growth of the monolayer as is found in other systems [78; 102], this means that the PFP molecule completely changes its geometry in the mixture, a possible argument for lower energy gain in this mixture on copper as compared to silver. Unfortunately, much less data was collected on copper than on silver, and no other indicators for this were observed.

So far CuPc and PFP have been shown to self-assemble into ordered blends on Ag(111) and Cu(111). Importantly, the layers that are formed on each substrate have a common overlayer structure, driven by the tendency to bring both molecular species into maximum contact in order to enhance the intermolecular interactions via C-F$\cdots$H-C hydrogen bonds. Furthermore, both systems have an epitaxial relationship with the underlying substrate, as evidenced by the existence of discrete domains. However, the details of the layers' epitaxy is unique to each substrate: on Ag(111) it is the unit cell vector **a** which follows the substrate's close-packed direction, whereas on Cu(111) it is **b**. As a consequence, the orientation of PFP with respect to the substrate is different in each case. This demonstrates the role of the substrate in the optimization of the overall interactions, which of course will depend on the substrate in consideration. It of interest to note that the same structure is found when these molecules are deposited on the Au(111) substrate [107]. This shows the dominating role the intermolecular interactions play in these systems. Related systems such as the inversely fluorinated pair PEN+FCuPc [108] or similarly shaped FCuPc+DIP [109] show the same effect and similar structures. A summary of the structures and their unit cell parameters can be found in the appendix.

4.2 The Role of H-bonding

In the previous section we saw that PFP and CuPc form virtually the same network on Au, Ag and Cu (111) surfaces. These layers are stabilized by hydrogen bonding between the peripheral fluorine and hydrogen atoms of the PFP and CuPc molecules, respectively. Focusing on the Ag(111) substrate, we will now explore the role of molecular fluorination by varying the overlayer's composition, and expect this to affect the intermolecular interactions. Three different molecular combinations have been studied on Ag(111): CuPc+PFP and PEN+FCuPc (fluorinated + non-fluorinated) and CuPc+PEN (non-fluorinated + non-fluorinated). The self-assembly of these layers gives us insight into the role of interactions between fluorinated and non-fluorinated molecules in the assembly process.

We first continue with the CuPc+PFP mixture on Ag(111), focusing now on the role of the H-bonds in the stabilization of the layer, and additionally present several other structures that the CuPc+PFP system can form when deposited in different molecular ratios. We then turn to the PEN+FCuPc system, characterizing first the monolayers and then the mixed phases, and finally, we present our findings on the mixture of the two non-fluorinated molecules, PEN and CuPc.

4.2.1 CuPc+PFP/Ag(111)

Fig. 4.14 shows a diagram of the unit cell of the 1:1 mix, based on the commensurate epitaxial model proposed for CuPc+PFP/Ag(111). Likely hydrogen bonds are drawn in blue between the pairs of H and F atoms whose H$\cdots$F distance is less or equal to 3 Å. From this crude modeling we can characterize the network as follows. The structure presents 24 hydrogen bonds per unit cell, and 12 hydrogen bonds per molecule. It becomes apparent from the diagram that hydrogen bonding is more present along the direction of the rows (close packed direction) than in the direction perpendicular to it: eight of the H-bonds per molecule pair are formed along the row, as compared to only four across rows. The H$\cdots$F distances range from 2.3 to 3.0 Å, the smaller H$\cdots$F distances occurring between molecules within the same rows and the larger ones between molecules in different rows (2.3 - 2.7 Å vs. 2.9 - 3.0 Å). The H-bond lengths can be an indicator for the strength of the hydrogen bond. Bond lengths larger than 2.2 Å such as those found in this CuPc+PFP network are classified as weak hydrogen bonds. [22; 110]. Their directionality (i.e. the angle between C-H and H$\cdots$F), which ranges from 140 to 160° is relatively high and is classified as "moderate" by Ref. 110 (see Table 1.1). The C-H$\cdots$F-C bond is known to be among the weakest hydrogen bonds [21; 22]. DFT calculations using the LDA functional on the CuPc+PFP layer in vacuum yield an energy of about 0.6 eV per unit cell. For an estimated 24 bonds per unit cell (Fig. 4.14) this corresponds to 0.03 eV per bond, well below the "weak" limit proposed by Jeffrey [110] (4 kcal/mol or 0.17 eV, see Table 1.1). In spite of their weakness, we find that, among the non-covalent interactions that drive the assembly of organic layers, the C-H$\cdots$F-C bond plays a very important role in the formation of this blend. We will see a dramatic confirmation of this at the end of this chapter.

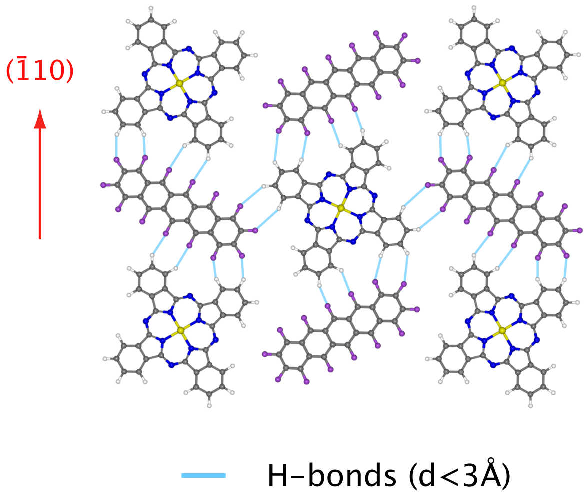

Figure 4.14: Likely H-bonds are marked for H$\cdots$F distances d smaller or equal to 3 Å.

Different Ratios

In the previous section, the 1:1 structure of the CuPc+PFP combination on Ag(111) was described. However, this is not the only structure that can form, though it is arguably the most stable [108]. More often than not, more than one structure will form on the sample.

The CuPc+PFP combination forms a variety of different phases, depending on the molecular ratio. Besides the 1:1 ratio, CuPc-rich phases in 6:3 and 9:6 ratios and PFP-rich phases in 2:4 and 3:6 ratios were found. It is certainly possible that more than these exist. Some of the observed structures have particularly complex patterns, with very large unit cells. All five blend structures are shown in Fig. 4.15. It is interesting to see that the three structures[1] 2:2, 6:3 and 9:6 strictly show the same molecular orientations. This is especially clear in the case of the less symmetric PFP. Furthermore, this orientation coincides with that of the monolayers, as we saw in the previous section for the 2:2. This provides some insight into how the system chooses the intricate patterns it arranges into. Clearly, one of the factors at play is the adsorption geometry on the substrate. These first three structures were obtained at low temperature. The remaining two (2:4 and 3:6) were obtained at room temperature, and do not follow the monolayers' molecular orientations so closely: while the 2:4 structure's CuPc molecules do seem to maintain the monolayer orientation, half of the PFP molecules do not. PFP exhibits two distinct orientations in this phase: one appears to be that of the monolayer—long axis (approximately) aligned with close packed direction—, while the other is perpendicular to it. The reduced stability of this latter geometry is neatly demonstrated by the streaks across the pairs of molecules exhibiting it. The same "flipping" phenomenon described in Chapter 3 (last section) is occurring in this system (this time at room temperature).

It is worth noting that in the opposite mix (PEN+FCuPc), FCuPc-rich phases have not been found on any of the substrates, PEN-rich phases being far easier to obtain [111]. The CuPc-rich phases shown in Fig. 4.15 were found by chance on a small portion of a sample on which a small amount of PFP was inadvertently evaporated. Attempts to reproduce them by controlled evaporation (at room temperature) were unsuccessful.

---

[1] All structures are classified according to the number of PFP/CuPc molecules per unit cell. Thus, the layer that up to now has been referred to as 1:1 will be called 2:2 in this section.

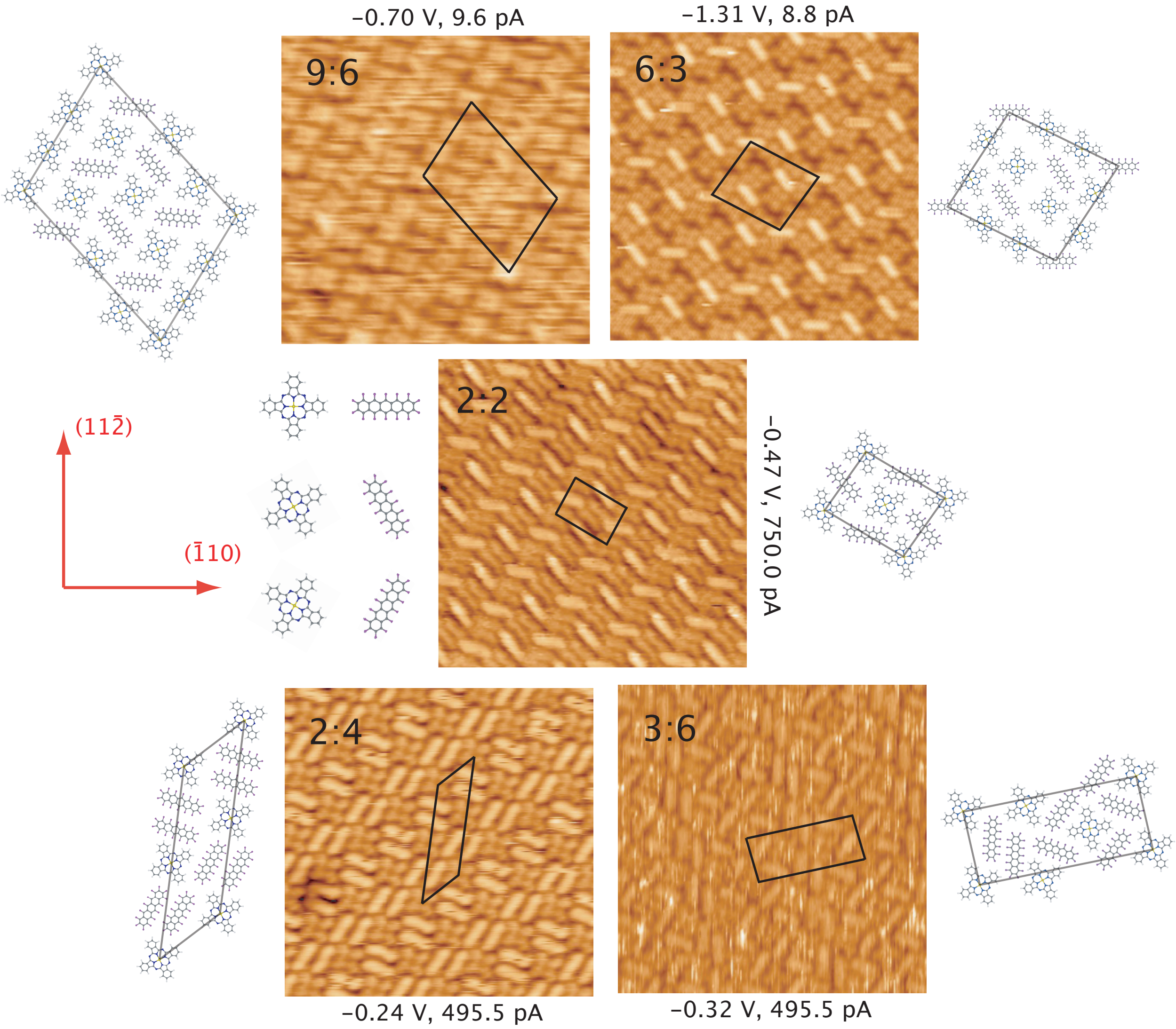

Figure 4.15: 20 nm×20 nm images of the different CuPc:PFP phases. Molecules to right show the orientations compatible with those in the monolayer.

4.2.2 PEN+FCuPc/Ag(111)

FCuPc - Depositing FCuPc Ag(111) is found to form an ordered layer. FCuPc forms pairs (sometimes triplets) of rows of different molecular orientations, which can present an oblique (A) or a nearly rectangular cell (B). The specular images of these rows (A' and B') also appear, mirrored across the direction of the rows, indicating that these grow following a high symmetry direction. From the known orientation of the crystal, we know this direction to be the high symmetry direction $(1\,1\,\bar{2})$, which is perpendicular to the crystal's close-packed direction. An image displaying all possible pairs of rows is shown in Fig. 4.16. The orientation of the molecules (represented by crosses) is shown above the image, and in all cases is found to have FCuPc's arms following the high symmetry directions. Some areas of FCuPc present a higher degree of order, in which a more regular A-A'-A-A' sequence is adopted, such as the area shown in Fig. 4.17. The intermolecular distance along the rows is found to be $a = a' = 15 \pm 1$ Å, and is equal to the inter-row distance in the direction perpendicular to the rows (the $(\bar{1}\,1\,0)$ direction), $b_\perp$. These parameters and the observation of the different configurations A and B of the rows are in agreement with a previous study at low temperature (77 K) by Huang et al. [102]. Oddly, however, this study states that the molecular rows follow the $(\bar{1}\,1\,0)$ direction, which is perpendicular to the direction we observe. It is very surprising that these two growth modes should be possible. We were able to observe several of the different domains, all unambiguously showing rows following the $(1\,1\,\bar{2})$ directions. Fig 4.18 shows three of these domains (related by 120° rotations).

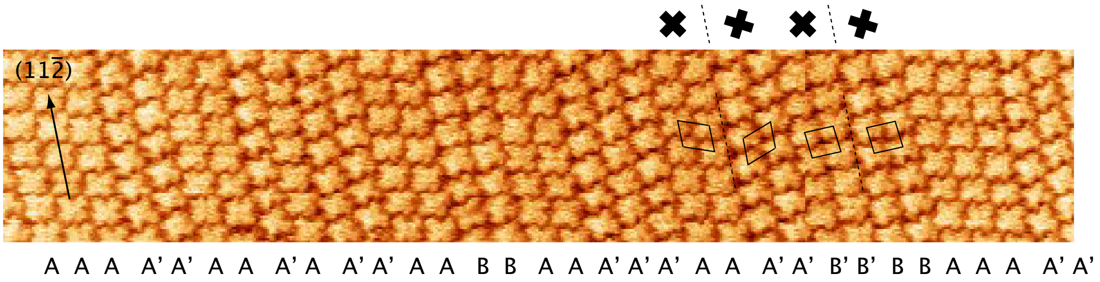

Figure 4.16: Alternating rows of the FCuPc/Ag(111) monolayer. A and A' (oblique cells) are mirror images of each other, with the high symmetry direction acting as the mirror plane.

A more detailed analysis of the unit cells yielded parameters $a = 15 \pm 1\,\text{Å}$, $b = 16 \pm 1\,\text{Å}$, $\alpha = 71 \pm 4°$ for the oblique structure A, and $a' = b' = 15 \pm 1\,\text{Å}$, $\alpha = 89 \pm 7°$ for the near-rectangular structure B. These parameters allow us to describe unit cells A and B, respectively, though the epitaxial matrices

$$\begin{pmatrix} 0 & 3 \\ 5 & 1 \end{pmatrix} \text{ and } \begin{pmatrix} 0 & 3 \\ 5 & 0 \end{pmatrix}.$$

The in-plane orientation of the FCuPc molecules seems to follow the trend of all the phthalocyanine systems described up to this point, the arms pointing in the high symmetry directions. Fig. 4.19 shows an STM image with FCuPc's unit cells, as well as a representation of this epitaxial model.

FCuPc presents a similar alteration of rows with different molecular orientation on Cu(111) [101; 107] and on HOPG [112], although in these cases single rows alternate, as opposed to pairs or triplets as is the case on Ag(111). This is in contrast to the FCuPc/Au(111) system, in which a single unit cell is seen, forming large highly crystalline domains [113]. The different, less homogeneous structures occurring on Ag(111) and Cu(111) (but not Au(111)) may be related to the additional dipole interactions that are be present in the layer: on Ag(111) and Cu(111), the FCuPc molecule distorts upon adsorption [69], raising its fluorine atoms above the carbon backbone, and creating an intramolecular dipole moment that is not present in FCuPc on Au(111) [114]. Interactions between the dipolar moments may affect the structure of the layer, especially in the case of Ag(111), where the periodicity of two or three rows suggests farther reaching interactions, as might be the r^{-3} dipole-dipole interaction.

FCuPc/Ag(111) additionally displays another structure, with a fixed molecular orientation, more in line with CuPc layers found on Ag(111) and Cu(111). Both structures are displayed side by side in Fig. 4.17. Unfortunately, the resolution does not allow determination of molecular orientation, however, by now it seems safe to assume that his phase will also present its phthalocyanines with arms stretching in the high symmetry directions. This additional structure was not mentioned in Ref. 102, and it is possible that FCuPc exhibits this polymorphism only at room temperature.

PEN - Previous studies of the PEN/Ag(111) system have established that the ordered layer of PEN observed at room temperature corresponds to a PEN bilayer [115; 116]. An ordered monolayer is observed only at low temperature [116] and is assumed to be disordered or highly mobile (2D gas) at room temperature. This contrasts with the

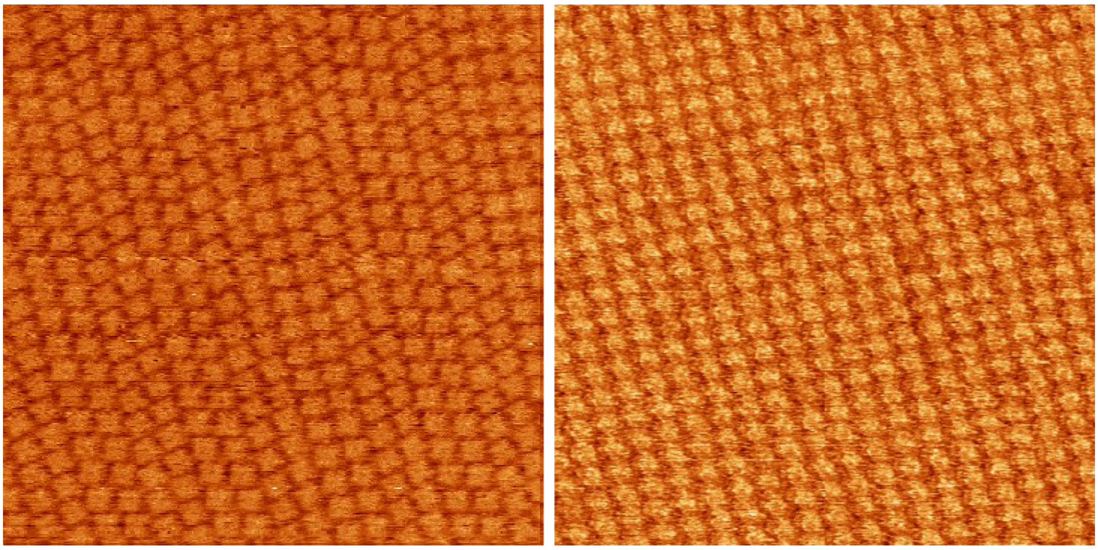
30 nm x 30 nm; 0.36 V, 78.3 pA

30 nm x 30 nm; −0.70 V, 500 pA

Figure 4.17: FCuPc/Ag(111) polymorphism. Left: a striped pattern of alternating FCuPc domains; Right: a simpler structure of FCuPc, with no domain alternation.

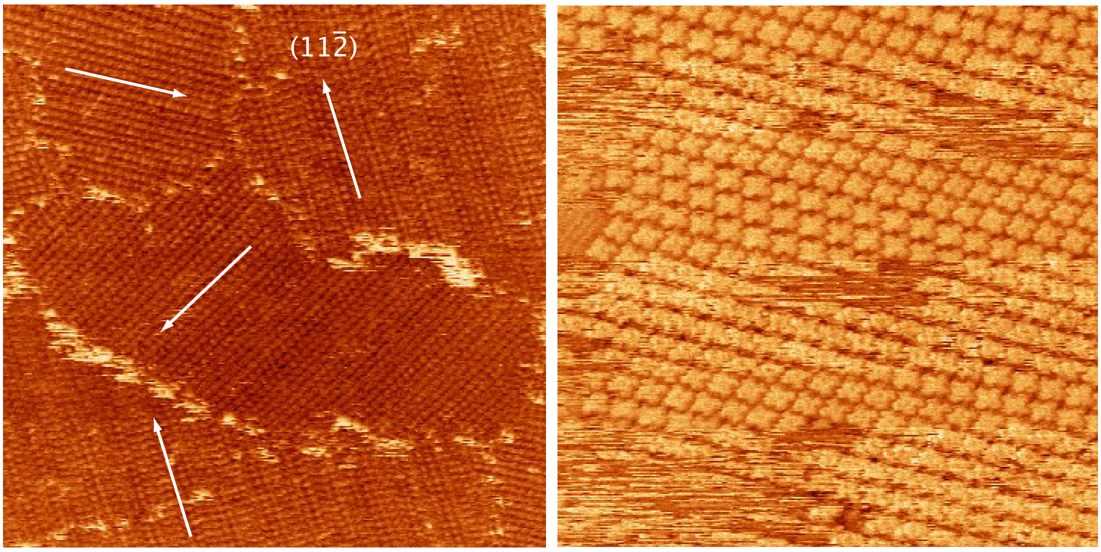

90 nm x 90 nm; 0.18 V, 108.3 pA

30 nm x 30 nm; 0.02 V, 308.3 pA

Figure 4.18: Left: Three different domains of FCuPc/Ag(111) related by 120° rotations. Higher mobility of molecules at domain boundaries is apparent. Right: Unstable tip during submonolayer imaging.

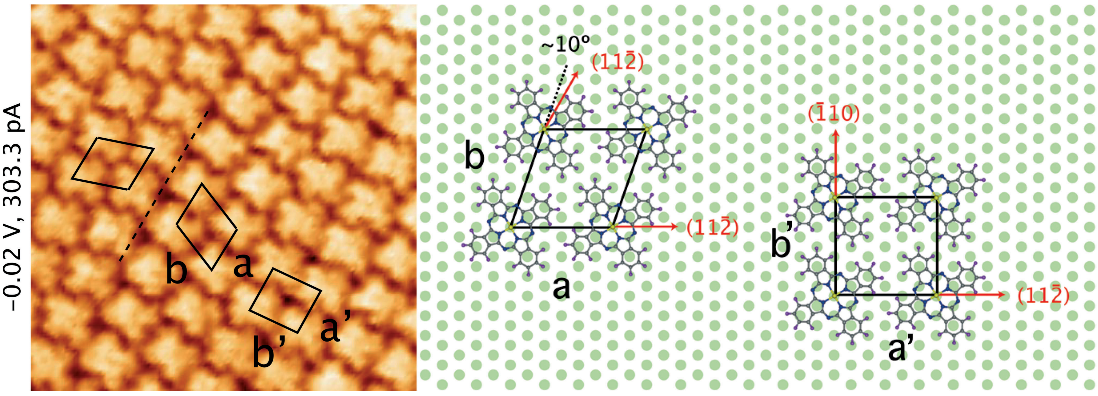

Figure 4.19: A 11.5 nm × 11.5 nm image of the FCuPc/Ag(111) system, with unit cell marked in black, and epitaxial model on the right.

ordered monolayers PEN forms on Cu(111) [117] and Au(111) [90], which are readily observable by STM at room temperature. As no option to cool down the system was available, we describe our observations of the bilayer. Though order is certainly still present in this layer, it is limited to a single direction: the PEN molecules form long rows, with molecules arranged side by side and an intermolecular distance of $a = 7.3 \pm 0.5$ Å. Often, ordered second layers keep an epitaxial relation with the layer underneath, or can still "feel" the substrate [78; 102], however, the rows of the PEN bilayer do not seem to have any preferred orientation, and the discrete domains expected from an epitaxial relation to the substrate lattice, or first layer, are not present. In fact, the rows are often seen to curve on the surface, as shown in Fig. 4.20. A similar 2 ML growth is found for PEN on the Au(100) [118].

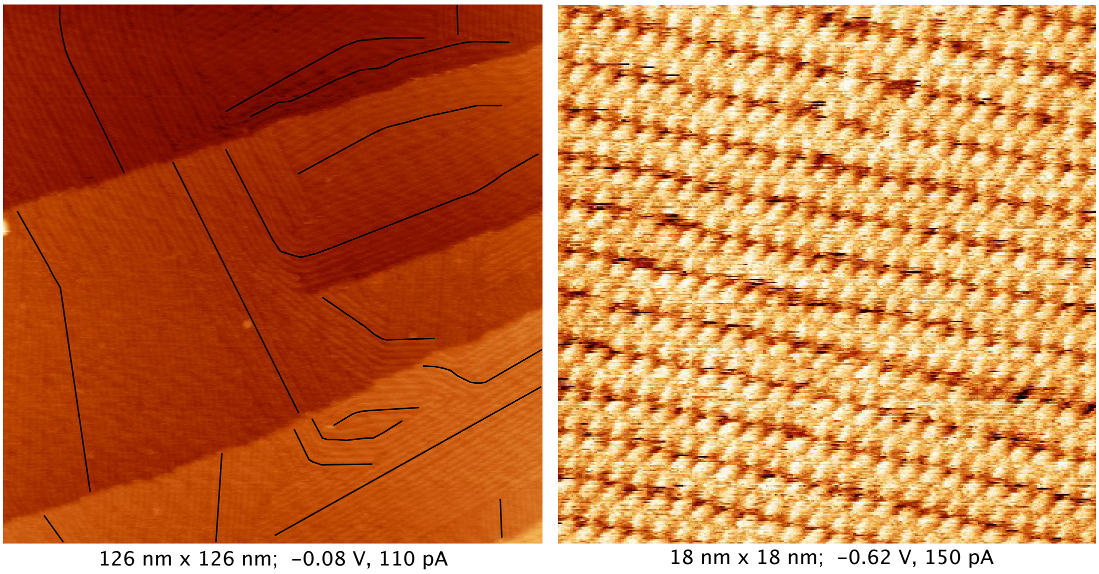

126 nm x 126 nm; −0.08 V, 110 pA

18 nm x 18 nm; −0.62 V, 150 pA

Figure 4.20: Left: An image of PEN/Ag(111). Some rows are marked with black lines to show the curving of the PEN rows. Right: Molecularly resolved image.

PEN+FCuPc - Mixing PEN and FCuPC on the Ag(111) substrate gives rise to the same 1:1 structure found for the opposite pair, showing PEN and FCuPc molecules maximizing contact with one another. The unit cell parameters were measured to be $a = 24 \pm 1\,\text{Å}$, $b = 27 \pm 2\,\text{Å}$, $\alpha = 92 \pm 5\,°$, with unit cell vectors **a** and **b** following the $(\bar{1}\,1\,0)$ and $(1\,1\,\bar{2})$ directions, respectively. The size of the cell as well as the orientation of its vectors are compatible with the commensurate epitaxial model put forth for the inversely fluorinated system CuPc+PFP/Ag(111). Thus, the proposed epitaxial relation is identical:

$$\begin{pmatrix} 8 & 0 \\ 0 & 6 \end{pmatrix}.$$

Fig. 4.21 shows an STM image and a scheme of the proposed expitaxial relation.

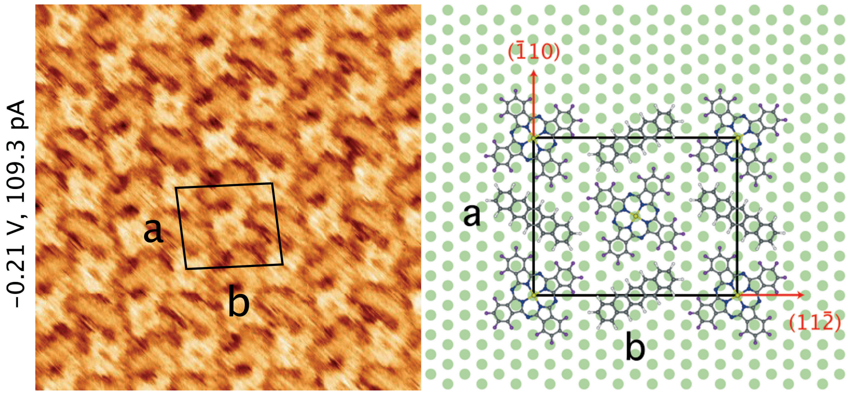

Figure 4.21: A 11.5 nm × 11.5 nm image of the PEN+FCuPc/Ag(111) sytem, with unit cell marked in black, and epitaxial model on the right.

The orientation of the molecules is also the same as that found for the CuPc+PFP/Ag(111) system, with FCuPc's arms pointing in high-symmetry directions and the long axis of PFP following the $(\bar{1}\,1\,0)$ directions.

No CuPc-rich phases were found, but a PEN-rich 2:1 structure was observed. Both mixes are presented in Fig. 4.22. The unit cell parameters of this second structure are $a = 32 \pm 2\,\text{Å}$, $b = 21 \pm 1\,\text{Å}$, $\alpha = 43 \pm 3\,°$. Analysis suggests that the short unit cell vector **a** follows the $(1\,1\,\bar{2})$ direction. The long axis of the PEN molecules also follows the close packed direction, as was the case in the 1:1 mix.

Interestingly, the imaging of the 2:1 phase is markedly different from that of the 1:1. As can be seen in Fig. 4.23 (right), the 1:1 phase is imaged much more clearly than the 2:1. The effect cannot be attributed to the STM tip, as it occurs systematically throughout the image. A likely explanation is that this effect is due to molecular motion in a structure that is less stable that the 1:1. The higher porosity of the 2:1 structure also helps explain the molecular motion.

In a small area, a third mixture was identified, corresponding to a 3:1 ratio, and with molecules oriented as in the other two mixtures. The structure is shown in Fig. 4.23. Unfortunately, only this one example was found for the 3:1 blend, however this suggests that this third mixture may also be able to form a stable structure on the Ag(111). The fact that the same structure has been shown to present excellent stability on Au(111) [108] further supports this scenario.

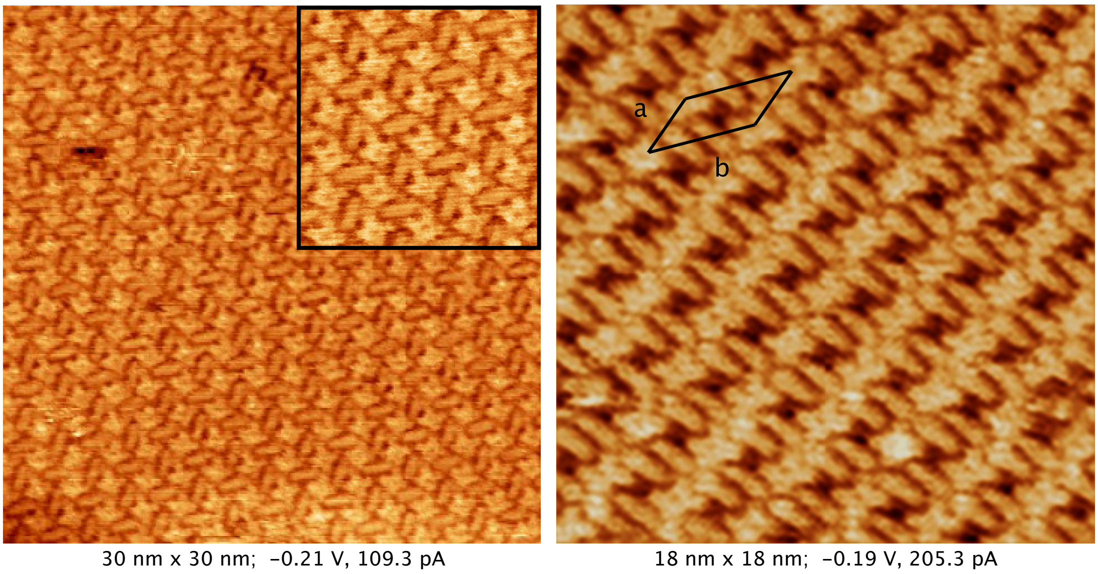

Figure 4.22: Left: The 1:1 PEN+FCuPc mixture (10 nm zoom in inset). Right: The more porous 2:1 mixture.

Comparing PEN+FCuPc and CuPc+PFP

Based on STM measurements we've proposed identical unit cells and epitaxial relations with the Ag(111) substrate for the PEN+FCuPc and CuPc+PFP layers. DFT calculations on free standing layers of both blends indeed results in equal unit cell parameters for the respective optimized structures. However, are these two layers equally stable? Calculations show the PEN+FCuPc layer to be about 0.3 eV more stable than the

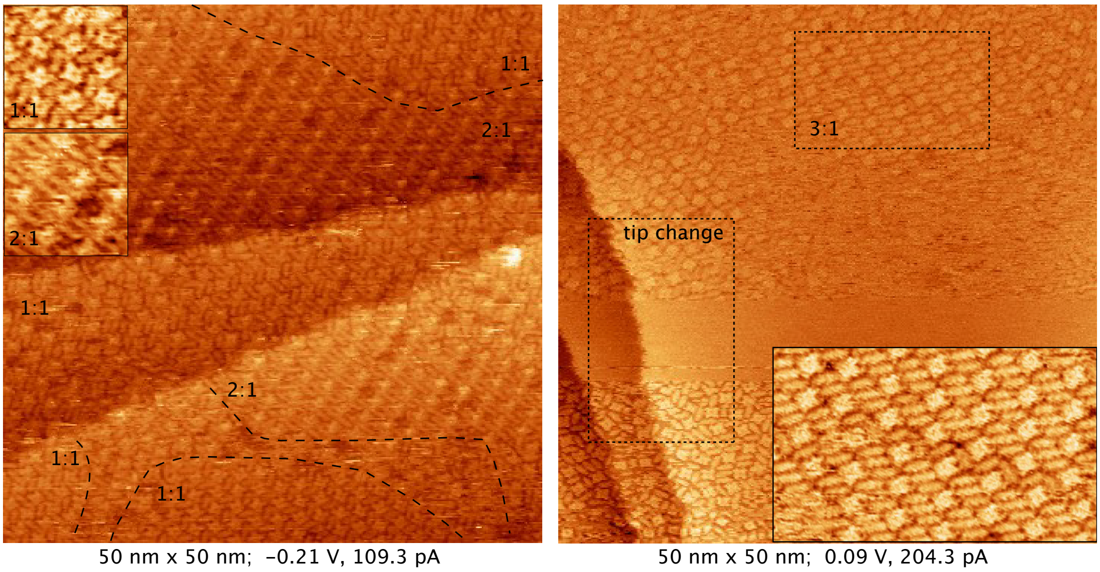

Figure 4.23: Left: Segregation between 1:1 and 2:1 phases of PEN+FCuPc/Ag(111). The 1:1 is imaged more clearly than the 2:1. Right: A small area of a 3:1 ordered mixture suggests it exists as a stable phase.

CuPc+PFP layer.[1] Though perhaps initially surprising, this difference is simply due to slightly different C-F/H bond lengths in the fluorinated and non-fluorinated molecules (C-F: 1.34 Å vs C-H: 1.09 Å). Assuming the $F \cdots H$ interactions to be purely electrostatic, the energy gain from each hydrogen bond in the layer is inversely proportional to the $F \cdots H$ distance. The sum of all the hydrogen bond $F \cdots H$ pairs $A = \sum_{i,j} 1/r_{ij}$ yields $\Delta A = A_{\mathrm{FCuPc+PEN}} - A_{\mathrm{CuPc+PFP}} = 0.13\,\text{Å}^{-1}$. Thus, on average the PEN+FCuPc layer has slightly shorter (and therefore stronger) $C\text{-}F \cdots H\text{-}C$ hydrogen bonds.

---

[1] LDA calculations yield a formation energy of 0.95 eV per unit cell for the PEN+FCuPc structure and 0.64 eV for CuPc+PFP. Though the energy values vary if different functional are used in the calculations (PBE, or vdW), the energy *difference* remains.

4.2.3 CuPc+PEN/Ag(111)

Up till now the two donor-acceptor pairs CuPc+PFP and PEN+FCuPc have been studied on different substrates. In all cases they have been found to self-assemble into an ordered layer that maximizes donor-acceptor contact. The driving force behind this arrangement is assumed to be the C-F$\cdots$H-C hydrogen bonding. This assumption can be supported by now mixing together CuPc+PEN and observing the structure of the layer. Since both PEN and CuPc are surrounded by hydrogen atoms, no hydrogen bonding can occur between the molecules, and intermolecular interactions are limited to weak van der Waals forces as in the monolayers.

We find that depositing these two molecules, which are virtually identical in shape in size to the previously described donor-acceptor pairs, leads to a complete change in the molecular layer's structure: instead of intermixing, the molecules segregate into distinct phases. Strips of PEN such as those observed in the single component samples appear embedded in an ordered CuPc matrix, as shown in Fig. 4.24. There being no selective interaction favoring a proximity of the different molecular species, there is no reason to intermix. This segregation is a clear demonstration of the role hydrogen bonding plays in the formation of the ordered phases of CuPc+PFP and PEN+FCuPc. Though C-F$\cdots$H-C bonds are classified as one of the weakest kinds of hydrogen bond [21; 22], it is clear that they play a crucial role in the ordering of our donor-acceptor blends.

Segregation has also been found for CuPc+PEN on the Au(111) and Cu(111) substrates [111], on which the donor-acceptor systems were found to order. Other donor-donor systems such as CuPc+DIP [16] do not segregate, but form ordered structures made up of alternating molecular rows. This structure, however, differs from that of the corresponding donor- acceptor network DIP+FCuPc [16]. This striped pattern has been interpreted as a series of domain boundaries between two phases, formed due to electrostatic interactions between dipoles (with an r^{-3} dependence) [16]: a striped pattern is found to be one of the energetically favored structures for phase segregation [17], which in this case between molecules associated with different dipolar moments. These dipoles can arise from an intrinsic dipolar moment of the molecules (e.g. FCuPc on Cu(111) or Ag(111)), but also simply from the interface dipoles created on the surface by the adsorbed molecules [119]. The related system CuPc+PEN/Cu(111) has also been found to form a striped pattern after a soft annealing, in our case however, though a striped pattern could also be expected from the arguments above, we were unable to observe any pattern after annealing, possibly due to molecular desorption.

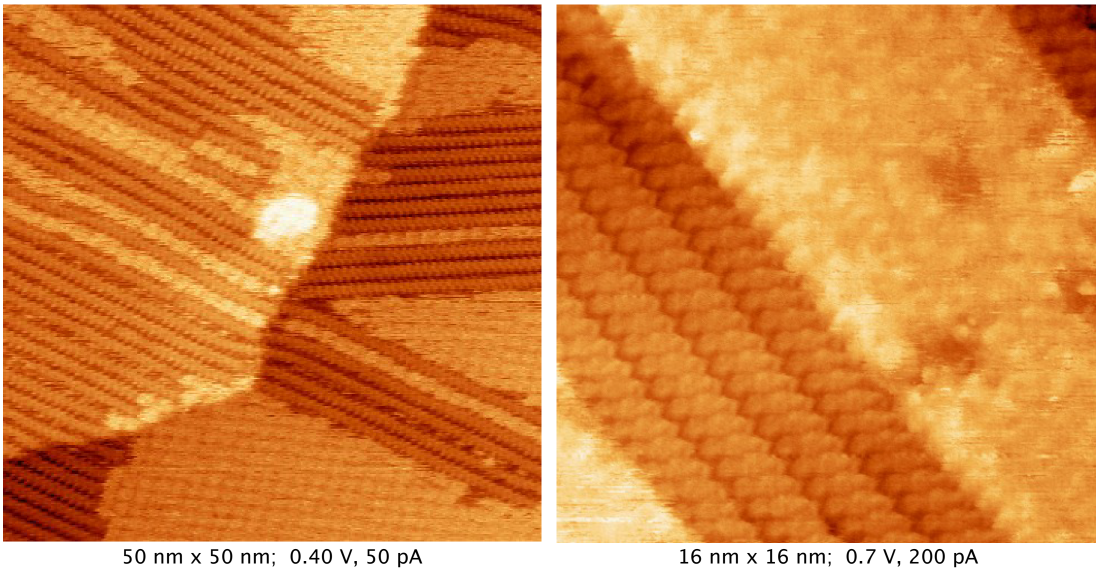

Figure 4.24: Two images showing the segregation of CuPc and PEN on Ag(111).

Summarizing, we find that mixing FCuPc and PEN on the Ag(111) substrate gives rise to the very same hydrogen bonded networks observed for the CuPc+PFP pair. Both the orientation of the molecules as well as the unit cell parameters and epitaxial relationship to the substrate are indistinguishable from the CuPc+PFP case. This shows that, while the substrate also plays a part in the assembly, the C-F $\cdots$ H-C bonds are the main driving force in the formation of these binary layers. Further proof of this is the dramatically different structure of the layer when hydrogen bonding is inhibited by replacing FCuPc by its non-fluorinated analogue CuPc, in which case CuPc and PEN segregate into distinct phases.

A summary of the structures and their unit cell parameters can be found in the appendix.

5

Energy Level Alignment in Molecular Blends

The previous chapter showed how hydrogen bonding between fluorinated and non-fluorinated molecules leads to ordered monolayer (ML) blends. The question that now arises is, how does this ordering and the presence of the two molecules on the substrate affect the electronics of the system? Already from STM images we can infer that

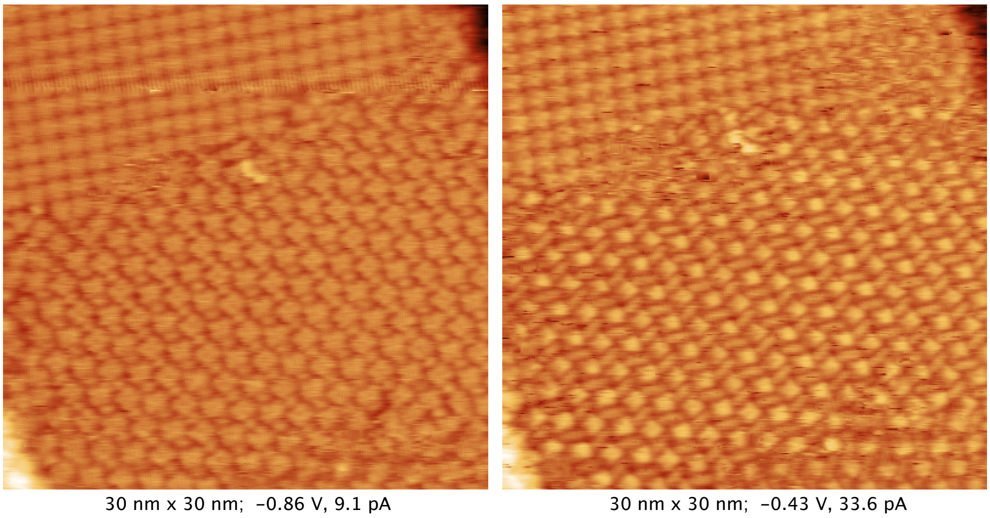

Figure 5.1: Two images of a domain boundary between pure CuPc and the 1:1 mixture, taken at different tunneling parameters. In the second image the CuPc molecules have a different contrast in the mixture than they do in the single component domain (upper part of the image), evidencing electronic changes.

some kind of electronic changes are taking place in the mixture, since depending on the tunneling conditions the molecules in the mix display a different contrast from those in the single component domains (see Fig. 5.1). These electronic changes will be explored in this last chapter.

First, we briefly present a previously studied blend, PEN+FCuPc/Au(111) [107; 111], which forms the same 1:1 structure presented in the previous chapter. This blend system has been characterized by PES and NEXAFS. Due to the absence of strong molecule-substrate interactions, the energy level alignment of this system can be explained quite well by a simple model based on vacuum level pinning (VLP). After examining this model system, we turn to our own (more interacting) systems—CuPc+PFP on Ag(111) and Cu(111), and PEN+FCuPc/Ag(111)—, which will be characterized by a number of experimental techniques (among them PES and NEXAFS). At the end, we assess the applicability of the previously mentioned model, and attempt to understand its limitations in terms of effects like charge transfer, conformational changes, etc.

5.1 The PEN+FCuPc/Au(111) Blend: A Model System

The FCuPc+PEN/Au(111) blend system has been studied by STM, XPS and NEXAFS [107; 108; 111; 113]. STM measurements showed FCuPc and PEN to assemble into an ordered structure optimizing C-F $\cdots$ H-C interactions, just like our systems, presented in the previous chapter. The low reactivity of the Au(111) substrate makes this a model system to investigate donor-acceptor interactions and their effect on both molecules' energy levels [107; 111]. The core-levels of this blend, as measured by XPS, show interesting changes with respect to those of single-component layers: acceptor core-levels in the mix are found to shift to higher binding energy, whereas donor core-levels are found to shift to lower binding energy. Moreover, if the donor-acceptor ratio is gradually varied, the core-levels shift accordingly. Valence band and NEXAFS measurements reveal the molecules' HOMO (highest occupied molecular orbital) and LUMO (lowest unoccupied molecular orbital) levels follow the same trend as the core-levels. All this data suggests a rigid shift of all levels. Fig. 5.2 presents these results, panel (a) showing the core-level spectra and panel (b) the valence-band spectra. It is important to note that the direction of the shifts is opposite to those expected from a scenario in which energy level shifts are driven by charge transfer from donors to acceptors. Clearly, a different mechanism is governing this behavior.

In previous work [107; 111] a model was put forward to explain the results described above. This model assumes **vacuum level pinning** (VLP) is taking place at these interfaces. As was discussed in section 1.3, the surface dipole of a metal substrate is modified by the presence of an adsorbate, which in most cases causes a reduction in the work function (or equivalently, a downward shift of the vacuum level) with increasing molecular coverage. As opposed to strongly interacting systems, in which electronic levels can become pinned to the Fermi level, in weakly interactive systems the molecule's electronic levels are found to shift with the vacuum level. It is said that the molecular electronic states are pinned to the local vacuum level.

The vacuum level pinning scenario can be extended to molecular blends. First, the vacuum level of such a system must be defined: assuming that each molecule contributes to the work function change according to the surface it occupies on the substrate, we can obtain the expected work function shift in the mix from the sum of that caused by FCuPc and that caused by PEN, i.e. from the sum of the effect of the *partial* layers of

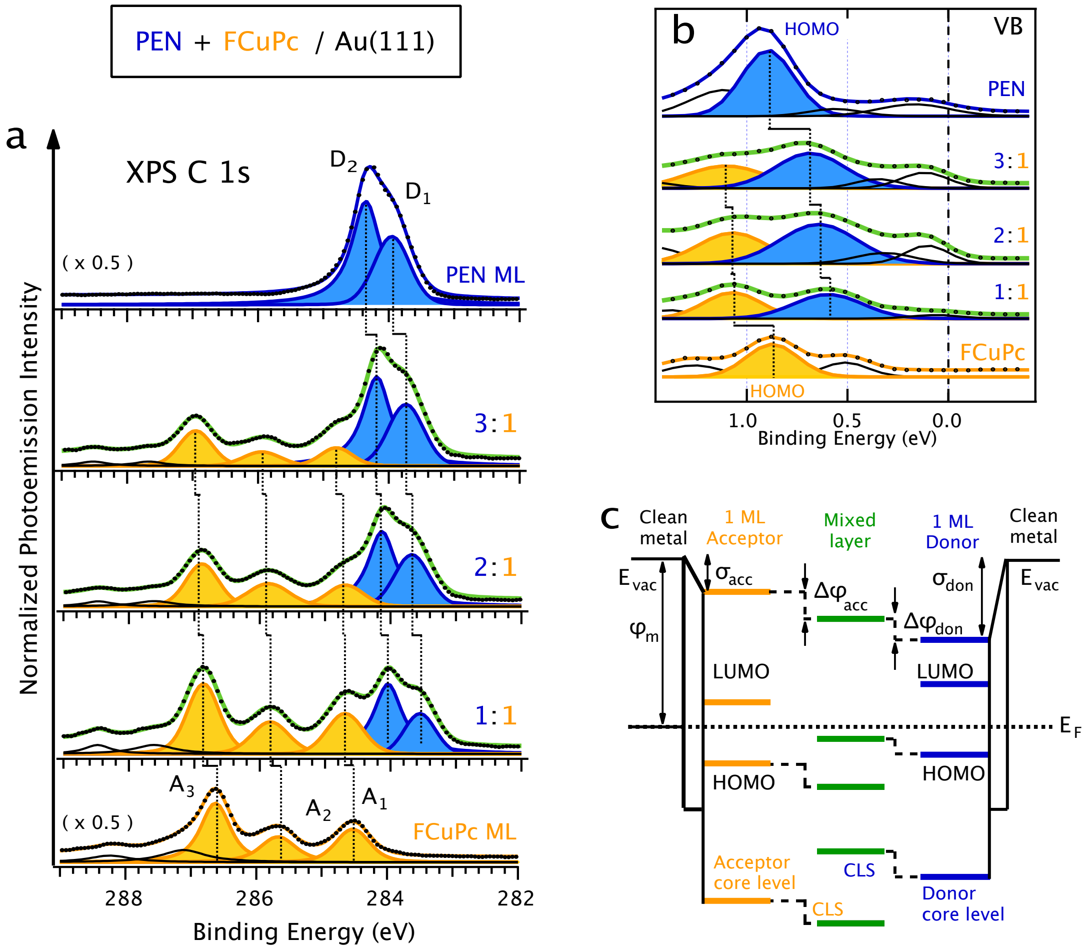

Figure 5.2: The PEN+FCuPc/Au(111) system - (a) C_{1s} core-level and (b) valence band spectra from donor-rich (top) to acceptor-rich (bottom) monolayer blends, measured by photoemission on the PEN+FCuPc/Au(111) system. (c) Schematic diagram of the energy-level alignment of single-component layers and donor-acceptor blends on metal surfaces. The varying vacuum level and the associated shift of molecular levels upon donor-acceptor blend formation in a vacuum-level pinning scenario are highlighted by dotted lines. Adapted from Ref. 111.

each molecule. In this way we arrive at a common vacuum level for the system [120] (Fig. 5.2c).

We know that depositing monolayers of PEN and FCuPc lower the work function of Au(111) by $\sigma_{\mathrm{PEN}} = 0.95\,\mathrm{eV}$ [121] and $\sigma_{\mathrm{FCuPc}} = 0.4\,\mathrm{eV}$ [111], respectively. We assume, as explained in detail in the next section, that the resulting interface dipole of the blend is the average of that of their components weighted by their respective partial surface coverages. Combining the σ values with the molecular sizes S [113] yields a shift in binding energies of about $\Delta\phi_{\mathrm{FCuPc}} \simeq 0.45\,\mathrm{eV}$ and $\Delta\phi_{\mathrm{PEN}} \simeq 0.20\,\mathrm{eV}$, which is in good agreement with experiment, both in the direction of the shifts (acceptor to higher, donor to lower binding energy) and in their magnitudes [111].

Theoretical calculations are able to reproduce these shifts by assuming that, in the absence of charge transfer, the shifts of the core-levels of the molecules are due to the change in their surroundings, which can be described in terms of an effective potential. Thus, in a monolayer of FCuPc, a FCuPc molecule feels the potential created by the surrounding FCuPc molecules. In the mixture it feels the potential created by the surrounding PEN molecules. This change in potential is, to first order, the shift experienced by the molecular levels [111; 122]. Though a small amount of charge is found to be transferred from donor to acceptor, the change in effective potential has a much stronger effect on the levels than the charge transfer, and is able to cancel out the effect of the latter.

The vacuum level pinning model is able to reproduce the shifts of the PEN+FCuPc system quite well, and can also account for the general behavior of other analogous systems on Au, Cu and Ag (111) substrates [111]. These are relevant findings for several reasons:

(i) the stoichiometry-dependent work function allows controlling the charge carrier injection barrier by varying the molecular ratios in the blend, while maintaining intimate molecule-substrate contact (i.e. no change of substrate or additional buffer layer are necessary to change the work function and energy level alignment);

(ii) the energy level alignment can be estimated from single-component film data;

(iii) interface energetics can be assessed by XPS.

However, deviations from the model can be ascribed to additional effects present in more interactive systems, in which molecular levels are not so strictly pinned to the local vacuum level. The aim of this chapter is to look into some of these more complex systems, in which the experimental and predicted shifts of the molecular levels do not agree so closely, and to attempt to understand the reasons behind the deviations.

5.2 The CuPc+PFP Blend on Ag(111) and Cu(111)

5.2.1 The Interface Dipole

As discussed in section 1.3, the deposition of molecules on a metal substrate affects the metal's work function, generally reducing it, due to the modification of the interface dipole. The work function change $\Delta\phi$ increases approximately linearly with molecular coverage, reflecting the dipole potential of the system averaged over the sample area [123].

The work function change was measured as a function of coverage for PEN, FCuPc, CuPc, PFP on the Ag(111) and Cu(111) surfaces (excepting the FCuPc/Cu(111) system, which could not be measured within the frame of this thesis due to experimental problems). The work function shifts for monolayer coverages—a quantity we refer to as σ—of the CuPc and PFP on the Ag and Cu (111) surfaces are summarized in Table 5.1. Those of FCuPc and PEN (presented in detail in section 5.3) and of the four molecules on Au(111) are included for comparison. Some of the systems measured for this work have already been reported on in the literature (PEN/Ag(111) [124], PFP/Ag(111) [79; 89], PEN/Cu(111) [105], PFP/Cu(111) [105]) and our measured values are in agreement with these previous studies (within 0.1 eV).

	FCuPc	CuPc	PFP	PEN
Au(111)	0.4 eV^a	0.8 eV^c	0.5 eV^b	0.95 eV^b
Ag(111)	0.2 eV	0.5 eV	0.4 eV	0.8 eV
Cu(111)	0.3 eV^d	0.7 eV	0.3 eV	1.0 eV

^{a} Ref. 111; ^{b} Ref. 121; ^{c} Ref. 125; ^{d} Ref. 126;

Table 5.1: Interface dipole values at monolayer coverage (σ) of FCuPc, CuPc, PFP and PEN on the Au, Ag and Cu (111) surfaces.

From Table 5.1 we see a trend when comparing the fluorinated molecules (acceptors) with their non-fluorinated analogues (donors): on a given substrate, the donor's shift is considerably larger than that of the corresponding acceptor. Let us recall the main contributions to the dipole barrier at the metal-organic interface. They are represented schematically in Fig. 5.3 and are (a) the push-back effect, (b) charge transfer and (c) the intrinsic dipole moment. Taking these factors into account, the difference between donors and acceptors can be understood as follows. A first factor may be the different electronic character of donors and acceptors: donors tend to lose charge to the metal substrate upon adsorption, whereas acceptors tend to gain charge. This behavior tends to add to the effect of the push back in the case of the donor (larger Δ), and to cancel the effect of the push back in the case of the acceptor (smaller Δ). Another contributing factor may be that, in general, acceptors tend to lie farther from the surface, so their push-back effect is smaller than in the case of the closer-lying donors. A last reason may come from the fact that, upon adsorption, many fluorinated molecules become distorted, with their (negatively charged) fluorine atoms lying above the carbon backbone [69; 105]. This results in a molecular dipole moment pointing into the surface, which reduces the work function change with respect to that of apolar non-fluorinated molecules. All these effects (whether independently or combined with one another) are able to account for the larger dipole barrier Δ found in the acceptors as compared to their respective donor molecules.

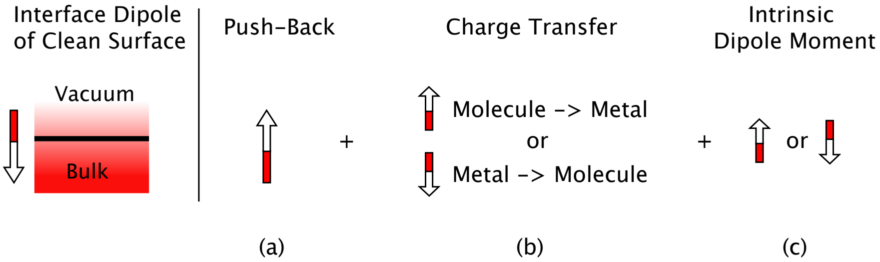

Figure 5.3: Schematic of the different phenomena contributing to the interface dipole: on the left the clean surface dipole is represented; on the right (a), (b) and (c) are factors that modify the metal's surface dipole.

We previously mentioned that the work function shift is a function of coverage. We now ask ourselves, what happens if the substrate is covered with two different molecules? How will the deposition of a donor and an acceptor affect the work function?

As indicated by the approximately linear coverage dependence of the work function, the effect of the molecular dipoles is additive. Taking the clean metal's vacuum level as reference, the position of the vacuum level of the blend system is therefore given by

$$\begin{aligned} \sigma_{\mathrm{Mix}} &= \frac{S_{\mathrm{acc}}}{S_{\mathrm{mix}}}\sigma_{\mathrm{acc}} + \frac{S_{\mathrm{don}}}{S_{\mathrm{mix}}}\sigma_{\mathrm{don}} \\ &= \frac{1}{S_{\mathrm{mix}}}(S_{\mathrm{acc}}\sigma_{\mathrm{acc}} + S_{\mathrm{don}}\sigma_{\mathrm{don}}), \end{aligned} \tag{5.1}$$

where $S_{\mathrm{don/acc}}$ is the area taken up by an individual donor/acceptor molecule and $S_{\mathrm{mix}} = S_{\mathrm{don}} + S_{\mathrm{acc}}$.[1] In essence, σ_{Mix} is the sum of the contribution of a partial donor layer and a partial acceptor layer, or equivalently the average of the σ_{don} and σ_{acc} contributions, weighted by the area each molecular species takes up on the surface. This is illustrated in Fig. 5.4.

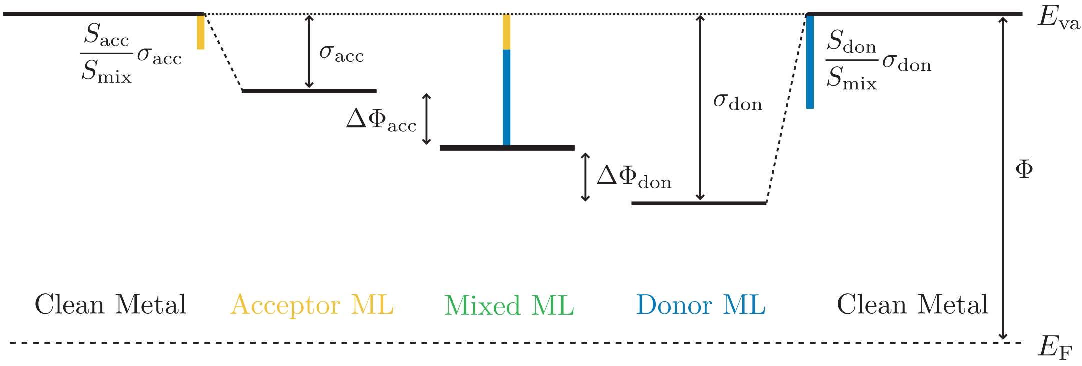

Figure 5.4: The Vacuum Level Pinning Model: $\sigma_{\mathrm{acc/don}}$ represents the vacuum level shift upon deposition of an acceptor/donor 1 ML. $S_{\mathrm{acc/don}}$ is the surface area occupied by the acceptor/donor molecule on the surface, and $\frac{S_{\mathrm{acc}}}{S_{\mathrm{mix}}} \cdot \sigma_{\mathrm{acc}}$ is the (smaller) shift due to a coverage equal to $\frac{S_{\mathrm{acc}}}{S_{\mathrm{mix}}}$ times the monolayer. A weighted average (based on surface area covered by each molecule) of the donor and acceptor vacuum level shifts yields the system's overall vacuum level. $\Delta\phi_{\mathrm{acc/don}}$ is the resulting work function (vacuum level) shift that is reflected as a shift to higher/lower binding energy in the donor/acceptor molecule's electronic levels.

---

[1] By taking $S_{\mathrm{mix}} = S_{\mathrm{don}} + S_{\mathrm{acc}}$ the mix is assumed to be a "closed packed" structure of the molecules, each of which occupy the same area in the mix as they do in their single component layers. This is found to be a very reasonable approximation.

We can express this as a shift with respect to the vacuum level of the full monolayers:

$$\Delta\phi_{\text{don}} = \frac{S_{\text{acc}}}{S_{\text{mix}}}(\sigma_{\text{acc}} - \sigma_{\text{don}}) \tag{5.2}$$

$$\Delta\phi_{\text{acc}} = \frac{S_{\text{don}}}{S_{\text{mix}}}(\sigma_{\text{don}} - \sigma_{\text{acc}}) \tag{5.3}$$

Since $\sigma_{\text{don}} - \sigma_{\text{acc}}$ is generally a positive number (recall Table 5.1), the result is a shift of the donor's vacuum level an amount $\Delta\phi_{\text{don}}$ to lower binding energy, and that of the acceptor an amount $\Delta\phi_{\text{acc}}$ to higher binding energy. These shifts are illustrated in Fig. 5.4. The PEN+FCuPc/Au(111) system presented in the previous section was said to be pinned to the vacuum level. The energy level shifts it presented were given by Eqs. 5.3 and 5.3.

We now go on to more closely examine how the molecules that are the focus of this section, CuPc and PFP, affect the Ag(111) and Cu(111) surfaces.

Experimental Details and Data Analysis

UPS work-function measurements were taken on a SPECS 10/35 UV source near normal emission. A negative bias of 24.22 V (in some cases 20 V) was applied to the sample in order to shift the entire spectrum to higher kinetic energies. This is routinely done for work function measurements in order to more clearly identify the spectrum's secondary electron cut-off, since at low kinetic energies the analyzer's transmission function is degraded by stray electric or magnetic fields. The work function change is obtained from the position of the cut-off (as is shown in Fig. 2.16 in section 2.3.2). The position was determined by fitting the cut-off to a sigmoid function

$$f(x) = a + \frac{b}{1 + e^{\frac{x_0 - x}{R}}},$$

where x_0, the center of the sigmoid, is taken as the position of the cut-off.

For the coverage dependent measurements, molecules were deposited sequentially, and a work function measurement was taken after each step.

The clean substrate was measured at the start of any experiment, and the position of the cut-off was found to be a good indicator for the cleanliness of the sample. From all the measurements of the clean samples we find an standard deviation of only ±0.03 eV associated with the measurement of the cut-off position (on Ag, the standard deviation was a mere ±0.01 eV). The work functions of the clean substrates were measured to be

4.73 eV for Ag(111) and 5.00 eV for Cu(111). This is in line with previously reported values, which vary between 4.74 and 4.90 eV for Ag(111) [127; 128; 129] and between 4.90 and 4.98 eV for Cu(111) [128; 130; 131].

CuPc and PFP single component layers

The coverage dependence of the work function of CuPc and PFP deposited on Ag(111) and Cu(111) is shown in Fig. 5.5. In all cases we observe a gradual decrease in the metal's work function as molecular coverage increases. The work function change eventually saturates and is constant or nearly constant for higher coverages. This saturation point corresponds to the monolayer coverage, at which the entire surface is covered with molecules. Further modification after this point is still possible in some cases, for example that of the TiOPc/HOPG system [123], in which the first layer of TiOPc adsorbs with its intrinsic dipole pointing into the surface, while in the the second it points away from the surface, compensating the dipole of the first layer. In our systems, PFP/Ag(111) shows a pronounced upward shift after 2 ML. This has been attributed to the switching from the flat lying configuration of PFP in the first two layers to the herringbone structure of the multilayer [105]. It is also interesting to note that for CuPc/Ag(111), $\Delta\phi$ decreases for coverages between one and two monolayers, indicating that the second layer contributes as a dipole pointing into the surface, though the reason for this is unclear.

The CuPc+PFP blend

Having measured the coverage dependence of the work function shift for PFP and CuPc layers on Ag(111) and Cu(111), we now turn to the work function shift of the mixture. We expect the total work function shift will be the sum of the shifts caused by the partial layers of CuPc and PFP making up the mixed layer, as was the case for the PEN+FCuPc/Au(111) system. We were able to measure the work function change in the CuPc+PFP molecular mixture on the Ag(111) and Cu(111) substrates and verify that, while the results approximately follow this idea, quantitative discrepancies are observed.

The experiment proceeded as follows. The metal surface (Ag(111) or Cu(111)) is first covered with a ca. half a monolayer of CuPc (the exact amount is not important), causing a measurable decrease in the work function. Subsequently somewhat less than

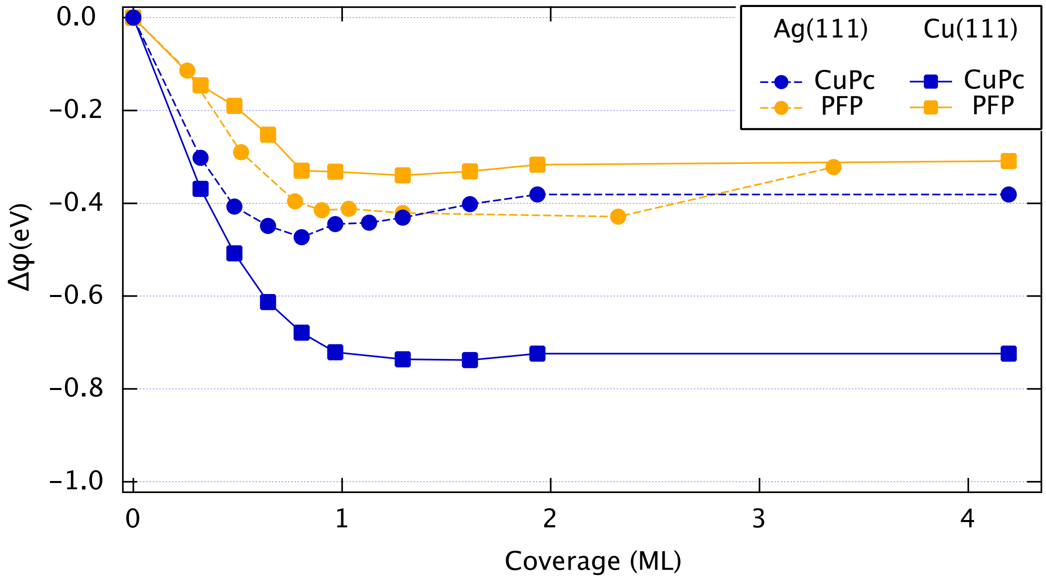

Figure 5.5: Work function shift as a function of coverage for CuPc and PFP on the Ag(111) and Cu(111) substrates.

half a monolayer of PFP is evaporated on the CuPc/Metal system (this is the coverage expected to form a 1:1 stoichiometric blend).[1] A further decrease in the work function is detected. This value is now compared with the value expected from the deposition of this (known) amount of PFP, which is known from the coverage dependence of the work function of PFP/Metal (Fig. 5.5). The experiment was performed on both Ag(111) and Cu(111).

On Ag(111) the evaporation of 0.32 ML of PFP on 0.32 ML CuPc/Ag(111) gave rise to a shift of −0.10 eV. This is a 40% reduction with respect to the $\Delta\phi^{\mathrm{Ag}}_{\mathrm{pure}} = -0.16\,\mathrm{eV}$ expected from the coverage dependence of PFP/Ag(111)'s work function. On Cu(111) we obtain similar results for deposition of 0.42 ML PFP onto 0.48 ML CuPc/Cu(111). We find a shift of $\Delta\phi^{\mathrm{Cu}}_{\mathrm{mix}} = -0.10\,\mathrm{eV}$, which is again a 40% reduction from the expected $\Delta\phi^{\mathrm{Cu}}_{\mathrm{pure}} = -0.17\,\mathrm{eV}$. Fig. 5.6 illustrates these shifts.

In both systems we find a smaller than expected shift of the work function. Due to the small absolute value of the discrepancies, $\delta = \Delta\phi_{\mathrm{mix}} - \Delta\phi_{\mathrm{pure}}$ ($\delta_{\mathrm{Ag}} = 0.06\,\mathrm{eV}$, $\delta_{\mathrm{Cu}} = 0.07\,\mathrm{eV}$), it is necessary to perform a careful error analysis to confirm the significance

---

[1] The mix on silver (0.32 ML PFP+0.48 ML CuPc) was checked by STM, and the statistical analysis of 14 large scale images revealed 72% of the surface to be covered with the 1:1 mixture, while the remaining area appeared to be empty (26%) or covered with patches of ordered PFP (2%).

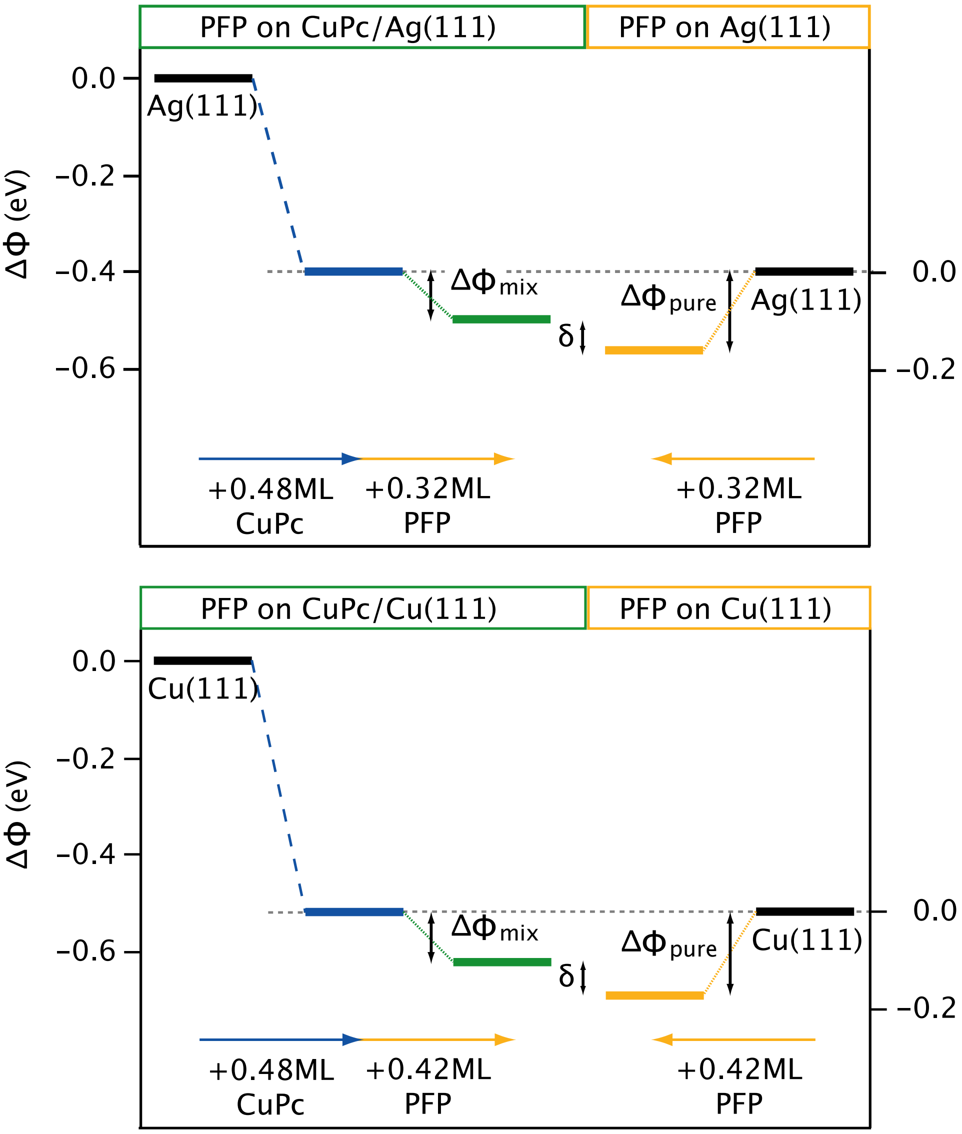

Figure 5.6: The work function (vacuum level) of the clean metal shifts upon deposition molecules. Depositing a certain amount of PFP onto the pre-covered CuPc/Metal system results in a further shift of $\Delta\phi_{\text{mix}}$. Deposition of the same amount of PFP onto the clean metal results in a shift $\Delta\phi_{\text{pure}}$. Experimentally, we find a difference δ between $\Delta\phi_{\text{pure}}$ and $\Delta\phi_{\text{mix}}$ ($\Delta\phi_{\text{pure}} > \Delta\phi_{\text{mix}}$). The blue bar on the left (CuPc/Metal) and the black bar on the right (clean metal) have been aligned in order to more easily compare $\Delta\phi_{\text{mix}}$ and $\Delta\phi_{\text{pure}}$. The errors in $\Delta\phi$ is represented by the shaded area. Adapted from Ref. 132.

of the results. There are two main contributions to the error. First, the uncertainty in the UPS measurements and in the cutoff determination by a sigmoid fit, which can be estimated from different measurements of the clean substrate. A standard deviation of 0.01 eV was found from nine measurements of the clean silver work function (4.73 eV), and of 0.03 eV from six measurements of that of clean copper (5.00 eV). The second, more important source of error comes from the evaporation procedure. This can be estimated by comparing the shift due to different submonolayer evaporations that were performed with those expected from Fig. 5.5. An error in coverage of $\frac{\Delta\Theta}{\Theta} = 0.2$ is found, which, for 0.48 ML PFP on Ag(111) and 0.32 ML PFP on Cu(111) translates into an error in energy of 0.03 eV and 0.04 eV, respectively. Combining both independent error sources, the maximum error reaches 0.03 eV for silver and 0.05 eV for copper, confirming the significance of the changes we observe. This is an important finding that affects the reliability of the predictions regarding interface energetics following the VLP model outlined in section 5.1.

To what can the changes be ascribed? The answer to this question is left for section 5.2.5, in which the discrepancies will be interpreted in terms of the different vertical geometries between single component and mixed phases.

5.2.2 Core-level Spectroscopy

Experimental Details and Data Analysis

All XPS measurements were performed at the ALOISA[1] beamline of the Elettra Synchrotron in Trieste, Italy [133]. The beamline uses a grating/crystal monochromator to cover a wide photon energy range spanning from 130 eV to 8 keV. It is equipped with a hemispherical electron energy analyzer characterized by a ±1° angular resolution. A grazing incidence angle (4°) was used and electrons were detected at normal emission.

All measurements were taken at room temperature. The C_{1s} and N_{1s} core-levels were probed with a photon energy of 500 eV, while for the F_{1s} an energy of 810 eV was used. The photoemission cross-sections of these core-levels are shown in Fig. 5.7 as a function of photon energy.

The molecular ratio of the mixed CuPc+PFP sample can be easily assessed by measuring a spectrum containing both N_{1s} and F_{1s} core-levels at the same energy (810 eV).

---

[1] Advanced Line for Overlayer, Interface and Surface Analysis

The intensity I of the N_{1s} and F_{1s} core-levels, respectively, are directly proportional to the number of CuPc and PFP molecules on the sample. By taking into account the different number N of nitrogen and fluorine atoms in CuPc and PFP—8 and 14, respectively—and the different photoemission cross-sections σ at 810 eV—ca. 0.13 and 0.29, respectively [58]—the molecular ratio R can be obtained from the relative intensities of the F_{1s} and N_{1s} core-levels:

$$R = \frac{N_{\mathrm{PFP}}}{N_{\mathrm{CuPc}}} = \frac{I_{\mathrm{F}} \cdot \sigma_{\mathrm{N}}(810\,\mathrm{eV}) \cdot N_{\mathrm{N}}}{I_{\mathrm{N}} \cdot \sigma_{\mathrm{F}}(810\,\mathrm{eV}) \cdot N_{\mathrm{F}}} = 0.26 \cdot \frac{I_{\mathrm{F}}}{I_{\mathrm{N}}}, \tag{5.4}$$

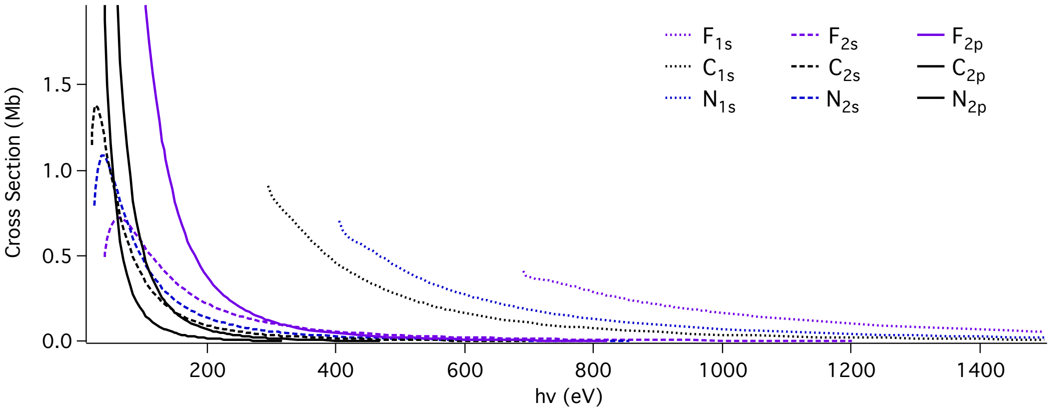

Figure 5.7: Cross-section of probed atoms C, N and F as a function of excitation energy. In our experiments, the 1s levels of C and N were measured at 500 eV, that of F at 810 eV. The curves show the typical behavior, having a sharp rise at the ionization threshold that leads to one or two maxima within the first couple of hundred electronvolts, followed by a monotonous falloff at higher energies [61]. Cross-section data from Ref. 58.

It is interesting to note that, due to the difference in size between both molecules, a 1:1 molecular ratio does not follow from depositing equal coverages of molecules (e.g. half a monolayer of each), but is closer to a 2:1 PFP:CuPc *coverage* ratio.

The spectra were aligned in energy using the substrate peaks as reference. The substrate peaks of a first spectrum were aligned to their theoretical values (see Table 5.2) and the remaining spectra were aligned by matching the substrate peaks to this first reference spectrum. This method allows for a very precise relative alignment between spectra that is better than 0.01 eV.

The Igor Pro macro *xpsmania*[1] was used to fit the spectra. Voigt line profiles, a convolution of Lorentzian and Gaussian line shapes, were used for each peak. When

---

[1] v. 3.2 3/4/2006; author: Francesco Bruno

	C_{1s}	N_{1s}	F_{1s}	Ag_{3d}	Cu_{3p}
B.E. (eV)	284.2	409.9	696.7	368.3 and 374.0	75.1 and 77.3

Table 5.2: Electron binding energies for the probed elements in their natural forms. (From the X-Ray Data Booklet, Section 1.1, by Gwyn. P. Williams.)

the full width at half maximum (FWHM) of a peak is stated hereon, it refers to the combined Lorentzian and Gaussian width [134]

$$f_V = 0.5346 \cdot f_L + \sqrt{0.2166 \cdot f_L^2 + f_G^2}.$$

A peak for each chemical environment was included in the fit, as well as shake-up satellites around 2 eV [31; 135; 136] from the main peaks to account for HOMO-LUMO excitations where necessary.

The fit of the mixture (the C_{1s} in particular) was based on an appropriately weighted sum of the fits for each molecule. Peak positions and widths were then adjusted accordingly, the latter being kept as similar as possible to those of the individual molecules' spectra.

PFP and CuPc single component layers

Fig. 5.8 shows the core-levels of (sub)monolayers of PFP (C_{1s} and F_{1s}) and CuPc (C_{1s} and N_{1s}) on Au, Ag and Cu (111) substrates, as well as those of a multilayer on Ag(111) (ca. 5 ML). It becomes apparent that in all four graphs the core-levels on Au, Ag and Cu are shifted with respect to one another. The trend is the same in all cases: the Au(111) spectrum is at lowest binding energy, followed by Cu(111), which is shfited ca. 0.5 eV with respect to Au(111), and finally Ag(111), shifted ca. 0.3 eV with respect to Cu(111). This shift reflects the different work functions of the three substrates.[1] Au has the largest work function ($\Phi_{Au(111)} = 5.3 - 5.5\,\text{eV}$ [137; 138]), followed by Cu ($\Phi_{Cu(111)} = 4.9 - 5.0\,\text{eV}$[128; 130; 131]), and Ag ($\Phi_{Ag(111)} = 4.7 - 4.9\,\text{eV}$[127; 128; 129]).

Let us turn to the multilayer spectra shown in Fig. 5.8. The inelastic mean free path of the photoemitted electrons within the sample amounts to just a few Ångström.

---

[1] In reality, this is only approximately true, since it neglects the fact that the effect of the molecule on the interface dipole of Au, Cu and Ag is not necessarily the same.

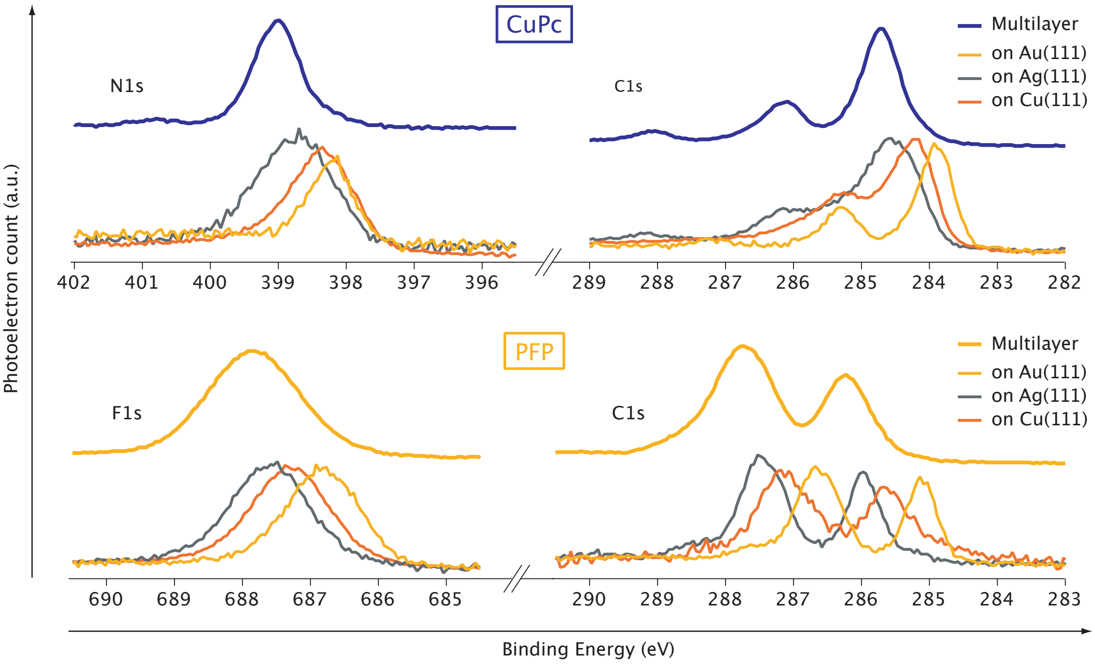

Figure 5.8: Comparison of CuPc and PFP core-levels for the molecules on the three substrates and in a multilayer on the Ag(111) substrate. Au(111) data from A. El-Sayed [111].

For this reason, multilayer spectra can provide information about the core-levels of the molecular film alone, with no influence from the underlying substrate. (Due to the relatively weak interaction among molecules, the multilayer spectrum is very similar to that of the gas phase [139].) Let us compare the multilayer spectra (both measured on Ag) with those of the monolayers. The first observation is that the multilayer spectra are shifted to to higher binding energies with respect to those of the molecular monolayers. The shift amounts to about 0.25 eV for both CuPc and PFP. This monolayer to multilayer shift is attributed to a less efficient screening of the photohole: when an electron is photoemitted from a molecule on the sample, it leaves behind a hole. As a consequence, the charge in the molecule and in the surroundings will rearrange in order to screen it. For a molecule adsorbed on a metal, the substrate can very effectively screen the hole, due to its large electron density. In the multilayer the screening effect of the metallic substrate is no longer present.

Besides a shift between them, the multilayer and Au(111) spectra are virtually identical in shape and in peak separations (especially evident in CuPc's C_{1s} spectrum). The fact that the spectra of CuPc and PFP are hardly affected upon adsorption of the molecules on Au(111) reflects a weak interaction with this substrate. This contrasts with the large changes found in the CuPc spectra on Cu(111) and especially Ag(111), in which lines are substantially broadened and shifted with respect to one another, indicating a stronger molecule-substrate interaction.

In the following we will describe the cases of PFP and CuPc on Ag(111) and Cu(111) more in detail, and compare them with the stoichiometric 1:1 mixture, first on Ag(111) and then on Cu(111).

PFP and CuPc single component layers on Ag(111)

The core-levels of approximately half a monolayer of CuPc on Ag(111) are represented in blue in Fig. 5.9. The most complicated spectrum is undoubtedly that of the C_{1s} level, which is a superposition of several peaks. This is due to the fact that CuPc's carbon atoms have different chemical environments that give rise to a chemical shift between the different peaks (see section 2.3.1). The carbon atoms with different chemical environments are, from lower to higher binding energy (right to left), those bound to hydrogen atoms (C_H), those bound solely to other carbon atoms (C_C) and those bound to nitrogen atoms (C_N). The stoichiometry of the chemically inequivalent carbon atoms dictates an intensity ratio of 2:1:1.

Besides these three main components, the feature at higher binding energy, at a distance of 2 eV from the C_N peak, is identified as a C_N shake-up satellite [135]. Some of the photoelectrons coming from the C_N carbons lose energy in a HOMO-LUMO excitation process before being detected. This lowers their kinetic energy (increases their apparent binding energy) by an amount equal to the HOMO-LUMO gap. The HOMO and LUMO have their strongest contribution around the central ring of the molecule, including on the C_N atoms [114; 139]. It is therefore expected that photoelectrons from C_N are the most likely to provoke HOMO-LUMO excitations.

The N_{1s} spectrum of CuPc is a lot simpler. Although theoretically there are two chemical environments for the N atoms (those bound to carbon and those bound to carbon and copper), the chemical shift between them is too small to resolve, and the core-level can be fit with a single peak.

It is worth commenting on the very large width of the core-levels of CuPc on Ag(111) (both C_{1s} and N_{1s}). The N_{1s} level can give an idea of this: its FWHM reaches 1.4 eV, compared to 0.8 eV in the CuPc multilayer or for CuPc/Au(111) [107] or to 1.1 eV for CuPc/Cu(111) (refer to Fig. 5.8). Typically, the broadening of core-levels of molecules adsorbed on metal surfaces can be ascribed to enhanced hybridization or metallicity, which results in a significantly reduced photo-hole lifetime. However, for the particular case of CuPc/Ag(111), we believe this is not the only cause of broadening.

A considerable amount of charge transfer from the substrate to the molecule is known to take place upon adsorption of CuPc on Ag(111) [98]. The effect of charge transfer to CuPc has been studied by potassium doping in a study by Calabrese et al. [140], who found it resulted in a broadening of the core-levels similar to that observed on Ag(111). The especially broad core levels of CuPc on Ag(111) indicate that important changes are taking place in the molecule upon adsorption on this substrate. The proposed scenario is one in which the charging of the molecule splits the degeneracy of the LUMO, as has been observed by STM [103; 141]. The LUMO, previously distributed throughout CuPc's cross-shape, becomes split in two equivalent orbitals making up the two "blades" of the cross. One of these two states lies lower in energy and becomes partly filled on the Ag substrate, the other remaining empty. It is proposed [125] that the broadening of the core-levels is due to the contribution from the charged atoms in one CuPc "blade" (where the new LUMO is located), and those in the uncharged CuPc "blade" (where the new LUMO is not located). The core-levels may therefore be fit using two peaks for each [125].

We now turn to PFP's spectra, which correspond to approximately half a monolayer. We find a C_{1s} spectrum with two clearly resolved peaks, separated ca. 1.5 eV. These two peaks can be readily assigned to the two different chemical environments found in the molecule, namely C_F and C_C: of the 22 carbon atoms in the molecule, 14 are bound to the outer fluorine atoms, while the remaining 8 are bound solely to other carbon atoms. This gives a theoretical peak ratio of 1.75:1, and also yields a good fit to the experimental data. However, two additional peaks, one at the high energy side of the main C_F peak and one at the low energy side of the C_C peak, are needed to completely reproduce the spectrum's shape. The one at higher energy is at a distance of 2.6 eV from the C_F peak, making it a likely candidate for a HOMO-LUMO shake-up peak. The origin of the peak at higher energy is not clear but could be associated to contamination, as for PFP/Cu(111) [105]. Finally, the F_{1s} peak of PFP can be fit with a single peak.

The CuPc+PFP blend on Ag(111)

The core-levels of the CuPc+PFP blend on Ag(111) are shown in green in Fig. 5.9. The molecular ratio (as defined in Eq. 5.4) was calculated to be $R \simeq 0.7$, indicating a larger number of CuPc molecules than PFP molecules. The effect of mixing is clearly seen in PFP's C_{1s} core-levels. Both of the acceptor's components, C_C and C_F, shift unambiguously to higher binding energies. The C_F component's shift of +0.36 eV is slightly larger than C_C's +0.25 eV shift, but it should be noted that the uncertainty in the determination of the latter peak's position is larger due to the overlap with the CuPc peaks. Furthermore, in the mix both peaks are broadened by about 30% with respect to their width in the single component layer.

Curiously, PFP's F_{1s} level does not shift along with the C_{1s} levels, as would be expected from a rigid shift of the levels. Instead it shows a shift of just +0.04 eV to higher binding energy, near the resolution limit. The peak is broadened by about 20% however.

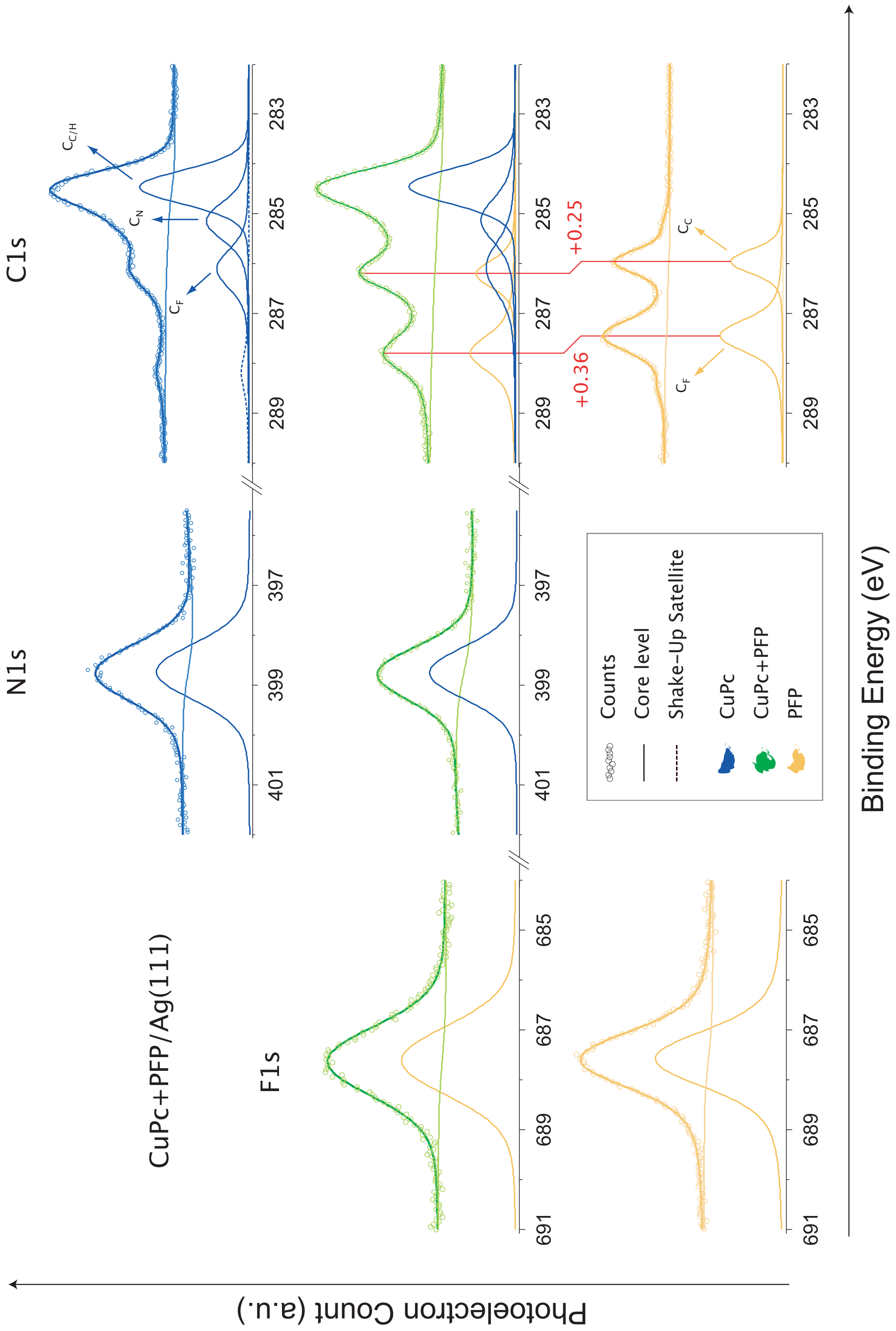

Figure 5.9: XPS spectra for single component and mixed layers of CuPc+PFP on Ag(111).

By contrast CuPc's C_{1s} components shift only negligibly in energy (a mere $-0.02\,\mathrm{eV}$ to lower binding energy) and show only small changes in width, or none at all. The same is true for the N_{1s} components.

PFP and CuPc single component layers on Cu(111)

We now examine the single component layer spectra of CuPc and PFP on Cu(111). These are shown in Fig. 5.10 in blue and yellow respectively.

Though not to the extent as on silver, CuPc's C_{1s} spectrum (ca. 0.5 ML CuPc) still shows considerable broadening with respect to the multilayer and CuPc/Au(111). This is evidence of a significant hybridization with the substrate, which has been shown to exist by measurements that further proved a significant charge transfer from Cu(111) to the CuPc LUMO. [142; 143] The spectrum shows two resolved peaks, one taller than the other, as we saw in the case of silver. These two distinguishable peaks correspond to the different chemical environments of the carbon atoms of the CuPc molecule. The more intense peak corresponds to the carbons bound to hydrogen and other carbon atoms ($C_{C/H}$), while the smaller one at higher binding energy corresponds to the pyrrole carbon atoms, i.e. those of the inner pyrrole ring of the molecule, bound to N (C_N).

Fitting the spectrum with three peaks corresponding to the three chemically different C atoms (C_H, C_C and C_N), with an intensity ratio of 2:1:1 (expected from the stoichiometry), takes care of the main part of the spectrum, but additional peaks are needed to obtain a smooth fit. The fourth peak (from the right) can be identified as the shake up of the C_H peak, being at a distance of 1.8 eV from it. The long trailing intensity at high binding energy is fit by a broad feature, and can be attributed to the combined effect of the shake ups of the remaining lines.

CuPc's N_{1s} level can be fit with a single peak.

The C_{1s} spectrum of the PFP half-monolayer, shown in yellow in Fig. 5.10, again shows its characteristic two-peak spectrum, as we saw on silver. The two peaks, separated 1.5 eV as on silver, correspond to the C_C and C_F (right to left) components and were fit accordingly in a 1:1.75 ratio. An additional peak at lower binding energy is present, which has been previously ascribed to residual carbon contamination [105].

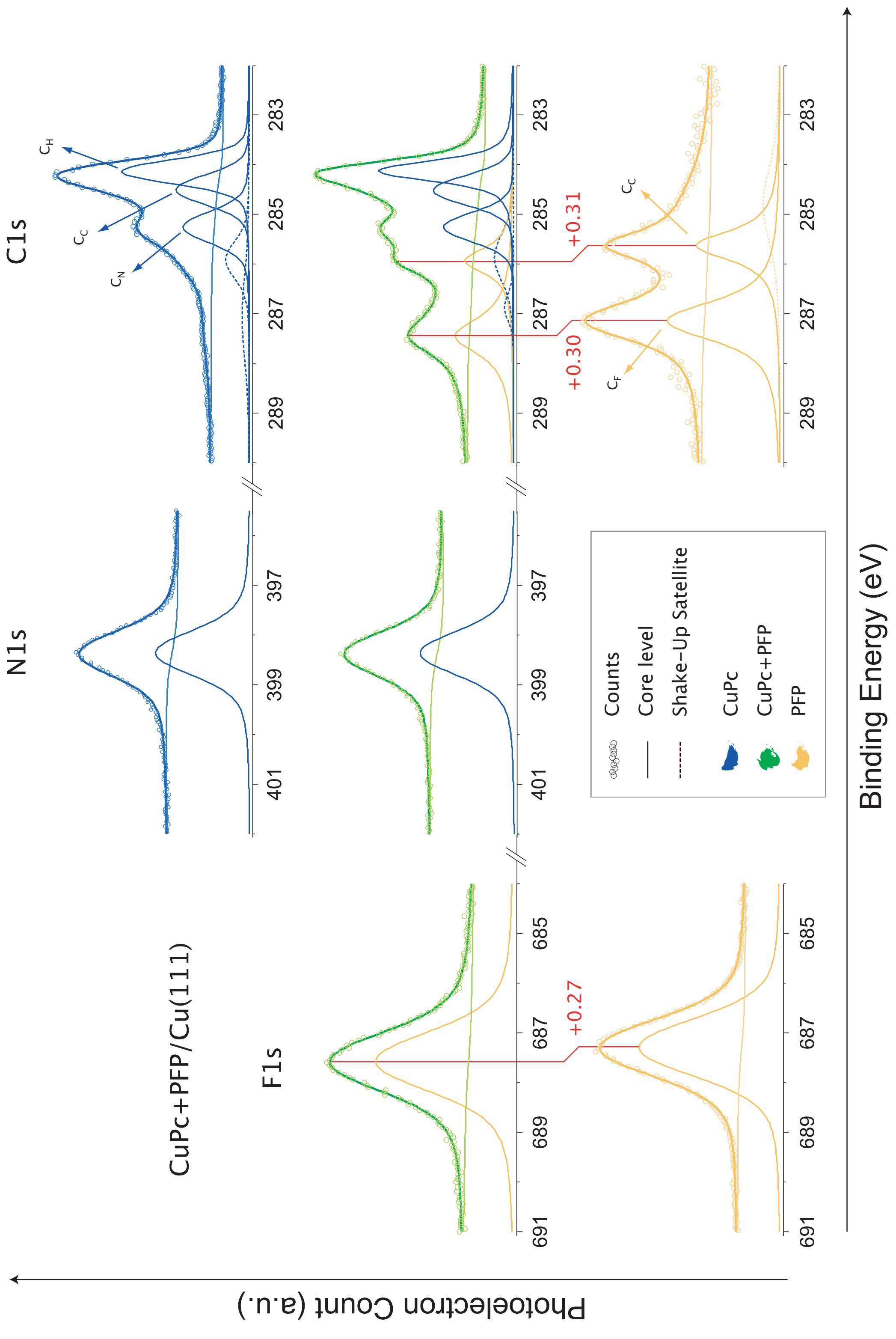

Figure 5.10: XPS spectra for single component and mixed layers of CuPc+PFP on Cu(111).

The CuPc+PFP blend on Cu(111)

We now turn to the fitting of the mixed system's core-levels on Cu(111), shown in green in Fig. 5.10. The molecular ratio in this system was very close to unity, being $R \simeq 1.1$ as defined by Eq. 5.4.

The daunting C_{1s} spectrum can be fit reasonably well based off a sum of the single component spectra of CuPc and PFP. It immediately becomes clear that a considerable shift of the PFP components is again necessary. This shift amounts to about +0.3 eV. The width of the peaks changes only slightly when going from the single component phase to the mix. The CuPc C_{1s} components remain practically unchanged both in peak position and in width. The same is true for the N_{1s} levels.

Contrary to the case on silver, PFP's F_{1s} component shifts by about the same amount as the C_{1s} components (+0.27 eV), suggesting that all PFP's levels are shifting together.

The observed changes on silver and on copper are quantitatively and qualitatively similar. In both cases we observe a shifting of the acceptor levels to higher binding energy upon mixing (with the exception of the F_{1s} level on Ag(111)), whereas the donor core-levels remain practically unchanged.

5.2.3 The Valence Band

Experimental Details

Measurements of the valence band were made using the SPECS 10/35 UV source (also used for the work function measurements). An emission angle of ca. 45° was chosen in order maximize the intensity coming from the molecular states, which is largest for high emission angles [144]. Not being equipped with a monochromator, light other than the desired 21.22 eV (He-I_α) arrives at the sample. In particular, radiation associated with the He-I_β transition leads to spectra with an additional "echo" of the substrate d-bands shifted 1.8 eV to lower binding energy (see Fig. 2.17 in section 2.3.2). Fortunately its position does not greatly interfere with the interpretation of the spectra.

PFP and CuPc single component layers on Ag(111)

The valence band of the single component layers is shown in Fig. 5.11 together with that CuPc+PFP/Ag(111). The blue curve shows the valence band of CuPc/Ag(111).

At ca. 1.3 eV below the Fermi level we find a feature corresponding to the molecule's HOMO level, in agreement with a previous study of this system by Kröger et al. [98]. The less intense feature at ca. 2.2 eV can be identified as CuPc's HOMO-1 [98].

Comparing the Fermi region of the CuPc with that of the clean sample[1], we find that the CuPc molecule shows a significant density of states (DOS) at the Fermi level. This effect has been observed previously for this system [98; 145] as well as for other molecules on the Ag(111) substrate, such as PTCDA [128; 146], NTCDA [147] or SnPc [148] and is explained as the filling of the LUMO as it is pulled down below the Fermi level. This partly filled LUMO is sometimes referred to as former LUMO (FLUMO). The CuPc molecule shows the same effect on Cu(111), but not on the less reactive Au(111) [143]. The observation of these states by photoemission is indicative of a strong interaction and considerable charge transfer from the substrate to the molecule. In such cases it is sometimes said that the system is metallic [143]. In some systems, the LUMO can shift far enough to become completely filled, as is the case of PTCDA on Ag(110) [129] or on Cu(111) [128], turning the systems semiconducting again.

We now turn to the PFP molecule. Its valence band is shown in yellow in Fig. 5.11. No additional intensity at the Fermi level is observed, indicating a weaker interaction with the substrate than CuPc. An intense HOMO peak is found at a binding energy of about 1.8 eV, as previously reported by Duhm et al. [89] and at around 3.0 eV another peak is found, possibly the HOMO-1.

The valence band of PFP and CuPc on other substrates has been reported on in the literature. By plotting the position of the HOMO with respect to the Fermi level (i.e. the hole injection barrier Φ_{Bh}) as a function of substrate work function Φ we can obtain additional insight into the energy level alignment of the molecules with metal substrates (refer to section 1.3). We focus on the (111) surface of the noble metals Au [121; 143], Ag and Cu [105; 143]. Fig. 5.12 shows this for PFP and CuPc. The case of PFP is quite clear: the position of the HOMO varies exactly like the work function, i.e. the Fermi level shifts within the molecule's energy gap, which lacks an IDIS (induced density of interface states) to give or receive charge. This gives a slope (screening

---

[1] The intense feature in the clean spectrum (dotted grey line) at around 2.5 eV is the echo of Ag's d-bands due to the He-I$_\beta$ radiation arriving at the sample. As can be seen from the other spectra, molecular coverage completely quenches it.

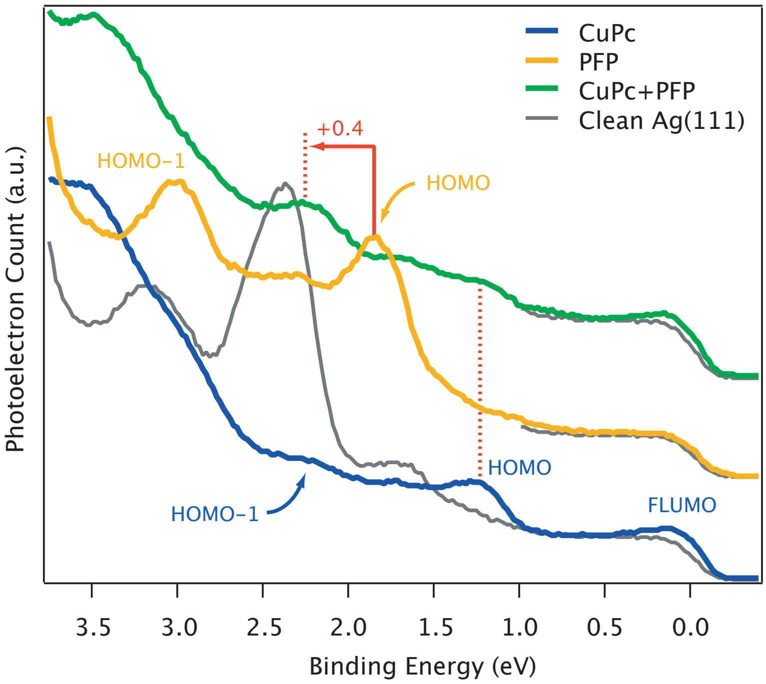

Figure 5.11: The valence band of CuPc and PFP submonolayers and their mixture on Ag(111). Photon energy was 21.22 eV and emission angle was 45°.

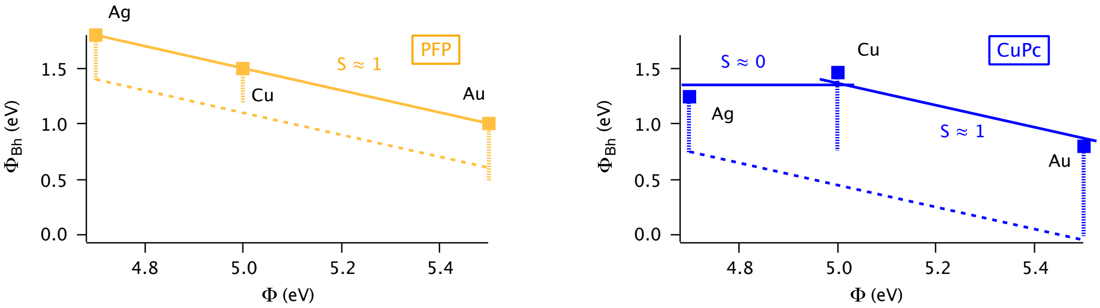

Figure 5.12: The hole injection barrier Φ_{Bh} (distance from HOMO to E_F) of PFP [89; 105; 121] and CuPc [98; 143] is plotted versus the substrate work function Φ. The slope of the solid line represents the screening parameter S and the dashed line the Schottky-Mott limit. Vertical lines represent the surface dipole.

parameter) $S = 1$. The dashed line represents the Schottky-Mott scenario,[1] and lies about 0.4 eV below the fit line. This quantity represents the dipole barrier due to the push-back effect, and agrees reasonably well with the measured values (presented in Table 5.1), which are included as vertical lines.

We now turn to CuPc. Here the three points can be fit to give a line with slope $S = 0.7$, however, we interpret the data in a different way: the considerable intensity at the Fermi level observed in the valence band of CuPc on Ag(111) (see Fig. 5.11) [98] and Cu(111) [143] but not on Au(111) [143] suggests that as the work function is reduced from that of Au, the Fermi level travels upwards in the energy gap and begins to cross into an IDIS (the molecule's broadened LUMO), finally resulting in charge transfer to the LUMO for metals with a lower work function than Au, such as Cu and Ag. Therefore, from Au to Cu a slope $S = 1$ is drawn, and from Cu to Ag—at which point an IDIS has become available for charge transfer—Fermi level pinning sets in and $S = 0$. Again, the Schottky-Mott situation is represented by a dashed line, and the measured dipole values are included as vertical lines. A smaller dipole barrier is expected for CuPc/Ag(111) with respect to the other two substrates, in agreement with the measured values. Discrepancies between the dipole barrier expected from comparison with the Schottky-Mott limit (distance from data points to dashed line) and the actual measured values (vertical lines) can in part be because we are applying our dipole values to data obtained in other experiments from the literature, where conditions (e.g. molecular coverage) may have been slightly different.

The CuPc+PFP blend on Ag(111)

We now turn to the valence band of the molecular mixture, shown in green in Fig. 5.11. Mixing both molecules yields a spectrum in which CuPc's features (HOMO, FLUMO) remain practically unchanged, while PFP's HOMO peak (and HOMO-1) is significantly shifted to higher binding energies. The shift amounts to about +0.4 eV.

These results are strongly reminiscent of those found for the core-levels (a negligible shift of CuPc core-levels to lower binding energy and a substantial shift of PFP core-levels to higher binding energy), and suggest that valence and core-levels are shifting together.

---

[1] as deduced from the molecules' ionization energies obtained from the covered Ag(111) surfaces (recall that $\Phi_{\mathrm{Bh}} = \mathrm{IE} - \Phi_{\mathrm{m}}$).

5.2.4 Near-Edge x-ray Absorption Fine-Structure

Experimental Details and Data Analysis

All NEXAFS measurements were taken at the ALOISA beamline, on the same samples as the XPS measurements. As explained in section 2.4, NEXAFS measurements consist in recording the partial electron yield as a function of excitation energy,[1] starting at an ionization edge. In our case the relevant edges are the C, N and F K-edges (excitations from an initial 1s state). As usual, the CuPc and PFP single component layers as well as their mixture were investigated.

The manipulator is mounted coaxial to the photon beam, which impinges on the surface at grazing incidence (6°). The rotation of the sample surface around the incident beam axis allows changing the surface orientation with respect to the linearly polarized x-ray electric field, while keeping a fixed grazing angle. Measurements were made in two different configurations, in order to obtain information about the molecules' orientation on the substrate: s-polarization, with the electric field parallel to the sample surface, and p-polarization, with the electric field perpendicular to the sample surface.

Due to the length of the measurements, instead of taking them on a single sample spot (as done for XPS), the data was acquired while scanning over the sample in order to avoid beam damage (see Appendix 5.2.5 for an assessment of the effects of beam damage).

As with the XPS measurements, the first thing that must be done with the data is to align the energy scale. For this, the drain current I_0 on the toroidal mirror is used as a reference. Known spectroscopical signatures in previously acquired gas phase absorption spectra, taken in real time together with I_0, allow for the precise determination of the position of certain features in the latter [133]:

- C K-edge spectra: the $C_{1s} \rightarrow \pi^*$ absorption line of CO at $h\nu = 287.40\,\text{eV}$ is used as energy reference
- N K-edge spectra: the $N_{1s} \rightarrow \pi^*$ absorption line of N_2 at $h\nu = 400.865\,\text{eV}$ is used as energy reference

---

[1] The NEXAFS absorption spectra at ALOISA are taken in partial electron yield by means of a channeltron detector with a retarding grid electrode to filter out low energy secondary electrons.

- F K-edge spectra: we lack a reference signal for the absolute photon energy calibration in this case, and simply set the Fe absorption line in the drain current I_0 to $h\nu = 706.8\,\mathrm{eV}$

Once the absolute calibration has been performed, the NEXAFS spectra must be normalized. Normalization consists of the double ratio

$$I^{\mathrm{film,norm}} = \frac{I^{\mathrm{film}}/I_0^{\mathrm{film}}}{I^{\mathrm{clean}}/I_0^{\mathrm{clean}}},$$

where I^{film} is the data for the adsorbate covered substrate and I^{clean} is that of the clean substrate. This corrects for both the beam current variations in the storage ring and the photon flux modulation due to contamination of the beamline optics (especially affecting C K-edge measurements, as carbon is the main constituent of the contaminants). A further step is required in order to be able to compare intensities between different spectra; the difference between the pre-edge and the far flat end of the spectrum can be normalized to 1, thereby eliminating the spectrum's dependence on molecular coverage. (Sometimes a final normalization is necessary to flatten the pre-edge of the spectrum.)

In order to compare the C K-edge NEXAFS of single component and mixed layers, a "simulated" mix spectrum is constructed from the weighted sum of the normalized single component spectra. The comparison of the measured mix spectrum with this simulated one will show the changes brought about by mixing the molecules.

PFP and CuPc single component layers on Ag(111)

Fig. 5.13 shows a comparison between the normalized p-polarized multilayer and monolayer spectra of CuPc. As already mentioned in the previous XPS section, in multilayer spectra the effect of the interaction wsubstrate is removed, and the comparison with the corresponding monolayer spectrum can give information on the effect of the molecule's adsorption on the metal. The comparison in the case of NEXAFS is less straightforward than in XPS, since NEXAFS spectra are additionally affected by the orientation of the molecules, which are flat in the monolayers, but typically tilted in the multilayers.

The first observation is the reduced intensity of the multilayer spectra, both on the C K-edge and N K-edge. The intensity changes are related to the loss of the flat lying geometry of the monolayer. Verification of this comes from the multilayer's s-polarization spectrum, which shows contribution from the π^* states.

Clear signs of charge transfer come from the N K-edge. We observe first a considerable shift to lower excitation energies (about 0.3 eV) of the second resonance around 400 eV (the shift of the second resonance in the C edge is less pronounced, but still appreciable), as well as the emergence of a shoulder at the onset (Fig. 5.13, inset). (The same is found when comparing CuPc/Ag(111) with CuPc/Au(111).) These effects are similar to the spectral changes found upon potassium doping (i.e. charging) of thick CuPc films [140], thereby supporting our proposed scenario of partial charge transfer from Ag(111) to CuPc based on XPS and UPS.

The new feature at the onsets of both the C and N edges, enlarged in the insets of Fig. 5.13, has been proposed [125] to correspond to the new partly occupied state appearing due to the lifting of the LUMO's degeneracy [103; 141]. This new partly filled state is visible in the NEXAFS as an added intensity at the onset, and as an intensity at the Fermi level in the valence band (section 5.2.3).

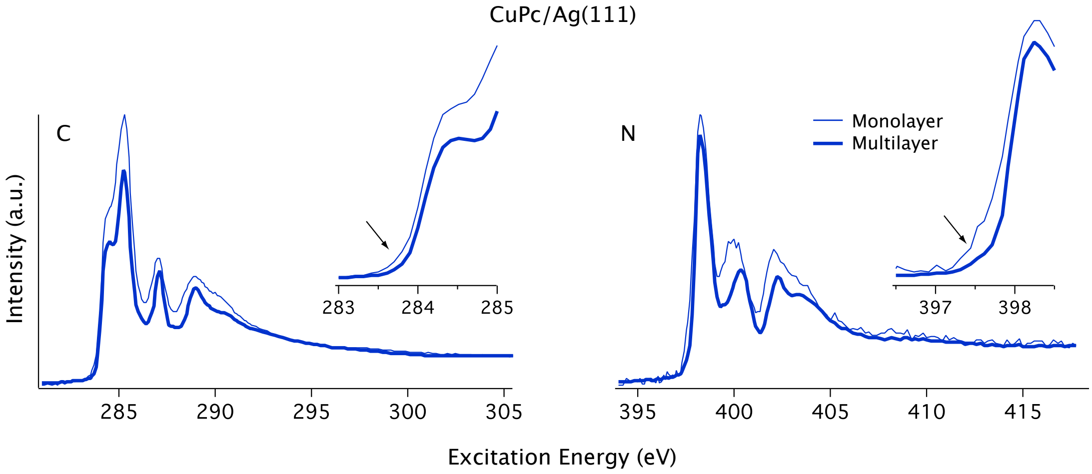

Figure 5.13: C and N K-edge p-polarized multilayer and monolayer NEXAFS of CuPc/Ag(111).

The NEXAFS spectra of about half a layer of CuPc are shown for p-polarization (continuous line) and s-polarization (dashed lines) in blue in Fig. 5.14. Both the p-polarization C and N spectra show very similar features: a large peak at the onset, followed by two smaller ones (in the case of C K-edge an additional shoulder is present

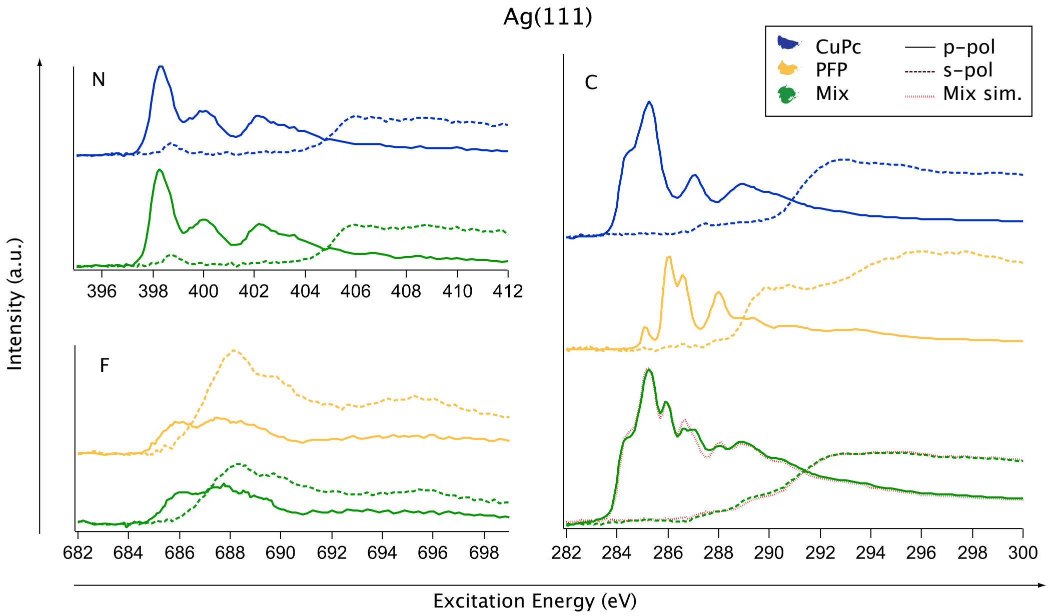

Figure 5.14: C, N and F K-edge NEXAFS spectra for single component and mixed layers of CuPc+PFP on Ag(111).

at the onset). Since N K-edge has a single level, the resonances of the N edge can be directly attributed, from lowest to highest excitation energy, to CuPc's LUMO, LUMO+1 and LUMO+2 [140]. The correspondence between the C K-edge and N K-edge spectra is due to the fact that the peaks represent excitations from these core-levels to the same final π-states, which from this is deduced to have a significant DOS on the pyrrole C (C_N) and N atoms [149]. The hump in the C K-edge— about 0.9 eV from the main peak— may be associated with an excitation to the same empty state, this time from an initial state with probability around the C_C atoms, which, from the XPS data are known to have a binding energy around 0.9 eV below that of the C_N. This is in analogy to the findings of Aristov et al. on a thick film of CuPc [149; 150]. The difference in intensity between the first main NEXAFS resonance and the smaller shoulder does not stem from the relative stoichiometry of the C_C and C_N atoms, but rather from the higher probability of a $C_N \rightarrow \pi^*$ transition that is due to the LUMO's spatial distribution [140].

The NEXAFS spectra of PFP's C and F K-edges are shown in yellow in Fig. 5.14. The first four resonances can be assigned to transitions from the C_{1s} to unoccupied π^* orbitals, whereas features after that fall above the molecule's ionization potential and are assigned to σ^* or Rydberg states [93; 151].

Conjugated organic molecules such as those studied in this work typically have π^* orbitals that are lower in energy than their σ^*. The π^* resonances of CuPc are only visible in the p-polarization spectra of C and N, while the σ^* become visible under s-polarization. This is a clear indicator of the flat-lying geometry of CuPc. It is important to note that in order to obtain reliable structural information from NEXAFS spectra, the main features of π^* and σ^* states must be well distinguishable and therefore not overlap in energy. This is the case of the C and N K-edge spectra of CuPc and the C K-edge of PFP, in which π^* resonances dominate in the first few eV of the spectrum, after which the σ^* states take over. The small feature at 398.7 eV visible in nitrogen's s-polarization spectrum is an exception, and corresponds to CuPc's single unoccupied molecular orbital (SUMO), with finite probability around the central Cu atoms and the four nearest N atoms [114; 139].

However, the F K-edge of PFP are a notable exception to this trend, and exhibit what can be described as an inverse dichroism, with σ^* states dominating the density of states already at low excitation energies. Theoretical calculations have been able to accurately reproduce this effect [152], which extends to other fluorinated molecules such as FCuPc and to other substrates like Au(111) and Cu(111).

The CuPc+PFP blend on Ag(111)

The NEXAFS spectra of the molecular mixture are shown in green in Fig. 5.14. Comparing single component and mixed layer spectra allows identifying changes brought about by mixing CuPc and PFP. The task is straightforward in the case of N and F, since these are present in only one of the two molecules. This means that any changes with respect to the single component spectra can be ascribed to the effect of mixing. Carbon on the other hand is present in both molecules, making a direct comparison more difficult. In this case, an appropriately weighted sum of the single component spectra is compared to the mixed spectrum.

Comparison shows no great changes in the onset or first few resonances. Though some changes are apparent in further resonances, the nature of the NEXAFS spectrum makes changes far into the spectrum very hard to interpret, particularly for the C edge. Here we limit analysis to the onset, which can indicate changes in the LUMO orbital.

The N K-edge spectrum is virtually identical to that of the pure CuPc layer. The F K-edge spectrum, however, shows a shift of around 0.15 eV to higher excitation energies.

PFP and CuPc single component layers on Cu(111)

We now turn to the single component layers on Cu(111). The NEXAFS spectra of CuPc and PFP are shown in Fig. 5.15 in blue and yellow, respectively. The quality of the data is somewhat worse than on the Ag(111) substrate, however, the results are similar. As with silver, we find a similarity between the C and N spectra of CuPc, as well as the inverse dichroism in the F spectra of PFP.

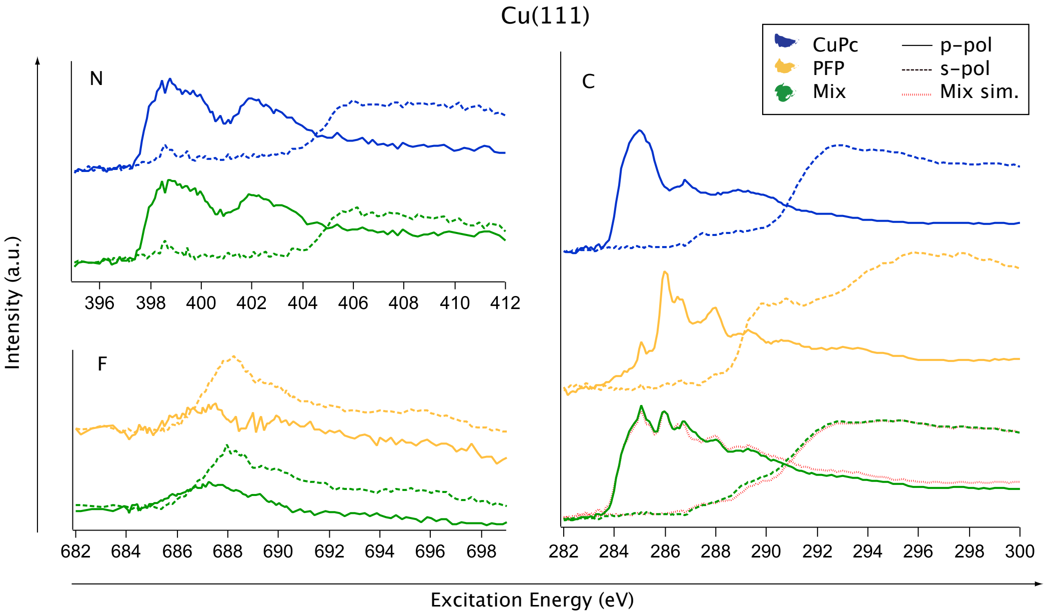

Figure 5.15: C, N and F K-edge NEXAFS spectra for single component and mixed layers of CuPc+PFP on Cu(111).

The N K-edge spectrum of CuPc/Cu(111) is the most revealing. Comparing it with those of CuPc/Ag(111) and the CuPc multilayer (see Fig. 5.16), the most obvious difference is the absence of three distinct resonances, and the significantly lower intensity of the first feature. Both these observations can be identified as the effects of charge transfer to the CuPc molecule, from the study of Calabrese et al. [140]: in this study charge transfer to the molecule is found to shift the second and third resonances to lower excitation energies and to eventually reduce the intensity of the first resonance.

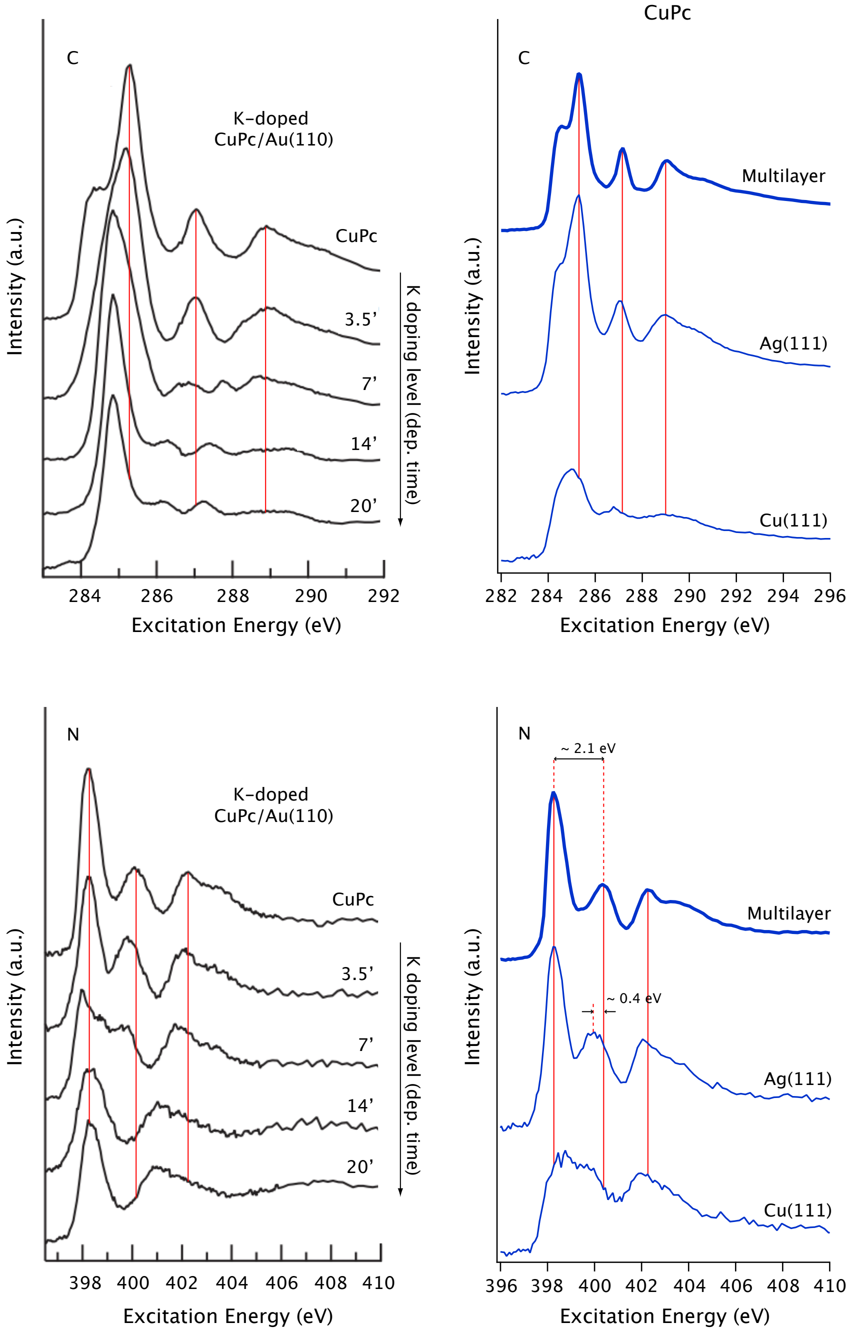

Figure 5.16: Left: C and N K-edges of a CuPc layer as a function of potassium deposition time, from the study by Calabrese et al. (figure adapted from Ref. 140). Right: Comparison of the C and N K-edges of a CuPc multilayer, and CuPc/Ag(111) and CuPc/Cu(111) monolayers.

Fig. 5.16 compares the C and N K-edges of the CuPc multilayer and the CuPc monolayer on Ag(111) and Cu(111). The data of Calabrese et al., showing the evolution of the C and N K-edges as a function of potassium deposition time, are included for reference. In the multilayer (and on Au(111) [107]) we observe the second resonance is at a distance of ca. 2.1 eV from the first. On Ag(111) we find it it to be shifted ca. 0.4 eV to lower excitation energy, whereas on Cu(111) the shift is even more pronounced and causes the second resonance to merge with a significantly quenched remnant of the first one, indicating a considerably larger amount of charge is transferred to CuPc from the Cu(111) substrate. A comparison of valence band spectra of CuPc/Ag(111) [98] and CuPc/Cu(111) [142; 143] lends support to this idea [153], since the signal of the filled LUMO is centered at considerably larger binding energies on Cu(111) (0.40 eV vs 0.15 eV). While this scenario is at odds with expectations based on the Cu(111) and Ag(111) work functions, it has also been observed for other molecules, such as PTCDA [128], and it may be related to stronger chemical interactions with the Cu(111) surface. This would be in line with the general view of the reactivity of these substrates and with the lower adsorption height of the molecules on Cu(111) [98; 154; 155]. Due to the effect of the image potential, a smaller adsorption height reduces the band-gap, leading to a lower lying LUMO level [156]. Similarly, the C K-edge shows the effects of charge transfer in the reduction of the shoulder on the first resonance [140] (Fig. 5.16).

As for PFP, the NEXAFS on Cu(111) show few changes with respect to those on the Ag(111) substrate. The C edge retains its shape, with four main resonances, attributed to $C_{1s} \rightarrow \pi^*$ transitions, while the remaining resonances correspond to transitions to states lying above the ionization potential [93; 151].

The CuPc+PFP blend on Cu(111)

Comparison between the single component and mixed layers shows no notable shifts in the spectra, indicating that the LUMO's position with respect to the core-levels remains unchanged upon molecular mixing. This is true for the three measured absorption edges level. No notable intensity changes can be made out in the measurements either.

5.2.5 Adsorption Heights

In this section we will investigate the adsorption heights of PFP and CuPc in the molecular blend. The most precise way to determine adsorption height experimentally is by means of normal incidence x-ray Standing Waves (XSW, see section 2.5). This technique has been applied to a large number of small organic molecules (such as those investigated in this work) on various surfaces [69; 89; 98; 105; 114; 154; 155; 157; 158; 159; 160].

A molecule's adsorption height generally reflects the strength of the molecule-substrate interactions. Some examples in the literature are CuPc, PTCDA and DIP, which show a clear trend of decreasing height on increasingly interactive substrates, when going from Au(111), to Ag(111) to Cu(111). This is shown in Table 5.3, taking as a reference the height of the molecular carbon backbone.

	CuPc	PTCDA	DIP
Au(111)	3.31 Å[a]	3.27 Å[c]	3.17 Å[e]
Ag(111)	3.08 Å[b]	2.86 Å[d]	3.01 Å[e]
Cu(111)	2.79 Å[a]	2.66 Å[d]	2.51 Å[e]

[a] Ref. 154; [b] Ref. 98; [c] Ref. 157; [d] Ref. 155; [e] Ref. 159;

Table 5.3: Adsorption heights of the carbon atoms of CuPc PTCDA and DIP on the Au, Ag and Cu (111) surfaces. A clear trend of smaller adsorption height for increasingly interactive substrates can be seen.

Focusing on the molecules studied in this work, another trend that can be found is that the donor molecules lie closer to the substrate than their fluorinated acceptor analogues. Table 5.4 shows the adsorption heights of the four molecules on the Au, Ag and Cu (111) surfaces. The trend is followed closely for less interactive molecules like PEN and PFP. However, CuPc and FCuPc, which interact more with the substrates, become distorted upon adsorption on Ag and Cu and these cases are therefore more difficult to assess.[1]

The XSW technique was used to determine the adsorption heights of the PFP and CuPc molecules in the 1:1 mixture. Interesting changes with respect to the single component monolayers were found.

---

[1] The fluorine atoms of FCuPc lie 0.20 Å and 0.27 Å above the carbons on Ag(111) and Cu(111) substrates respectively [69].

	FCuPc	CuPc	PFP	PEN
Au(111)	3.25 Å[a]	3.31 Å[b]	—	—
Ag(111)	3.25 Å[c]	3.08 Å[d]	3.16 Å[e]	3.12 Å[f]
Cu(111)	2.61 Å[c]	2.79 Å[b]	2.98 Å[g]	2.34 Å[g]

[a] Ref. 114; [b] Ref. 154; [c] Ref. 69; [d] Ref. 98; [e] Ref. 89; [f] Ref. 160; [g] Ref. 105.

Table 5.4: Adsorption heights of the carbon atoms of FCuPc, CuPc, PFP and PEN on the Au, Ag and Cu (111) surfaces. On Ag(111) and Cu(111) the fluorine atoms of FCuPc lie 0.20 Å and 0.27 Å above the carbons respectively [69].

Experimental Details and Data Analysis

The XSW measurements were performed at the ID32 beamline of the European Synchrotron Radiation Facility (ESRF) in Grenoble, France. The beamline is equipped with a SPECS Phoibos 225 hemispherical electron analyzer that can reach kinetic energies up to 15 keV and has an energy resolution down to $\Delta E/E = 10^{-6}$. The analyzer is mounted at 90° with respect to the incoming beam.

Before beginning with the experiment, a mapping of the reflectivity curve's full width at half maximum (FWHM) was made throughout the Cu(111) sample. During the experiment, only those points with a FWHM below 1 eV were used for measurements. Similar FWHM were obtained for the Ag(111) crystal.

Evaporation of the molecules was controlled using a quartz crystal microbalance, and the ratio between molecules was evaluated from the relative intensities of F_{1s} and N_{1s} core-levels. The PFP:CuPc molecular ratio R ranged from 1.0 to 1.6 throughout the sample.

For the measurement of CuPc, the C_{1s} and N_{1s} core-levels were probed, and for PFP, the C_{1s} and F_{1s} were probed. Three to five XSW scans were taken for each chemical species, in order to obtain a statistical average for the adsorption heights (with the exception of carbon on Ag(111), for which only one scan could be taken). Error values for the coherent fractions and positions are obtained from the standard deviation of the multiple measurements, except in the case of the C atoms on Ag(111), where only one data point was available. For the adsorption heights, an error of 0.05 Å was assigned to the C atoms on Ag(111) and when the standard deviation was below this value.

Each XSW run was taken on a different sample spot and x-ray exposure time was cut down to a minimum in order to avoid sample degradation. The effect of the beam on the molecules is assessed in the appendix.

An XSW run consisted in recording the reflectivity in a 3.4 eV energy range around the Bragg energy, followed by core-level spectra, taken in with 18 different photon energies in this same range. The intensities of the core-level lines plotted against the excitation energy give the photoelectron yield curves. The intensity of the core-levels is obtained from a fit including a Shirley background and gaussian line profiles. N_{1s} and F_{1s} core-levels were fit by a single gaussian peak. The scenario for C_{1s} is complicated by the fact that it includes contributions from both molecules: three separate peaks are resolved, as illustrated in the insets of Fig. 5.17. From highest to lowest binding energy the peaks correspond to PFP's C_F component (carbon atoms bound to fluorine, light grey filling), PFP's C_C component (carbon atoms bound solely to carbon) convolved with CuPc's C_N component (carbon atoms bound to nitrogen), and CuPc's remaining components, C_C and C_H (carbon atoms bound solely to carbon or also hydrogen, darker grey filling). In the analysis we did not consider the second, unfilled, peak, in which components belonging to both molecules overlap; we only consider C_F in PFP and $C_{C/H}$ in CuPc, which can each be fitted by a single gaussian peak and are therefore expected to give the most accurate results.

Once the yield curves have been extracted from the XSW scans, they can be fitted with the pyXSW program developed by J. Roy [161]. The program must first fit the reflectivity curve. As input the substrate element (Cu or Ag), the Bragg energy (2628.6 eV or 2970.2 eV) and the substrate reflection planes (111) are entered. The program then takes lattice parameters, structure factors, crystal susceptibilities etc of the specific element from its data base in order to simulate a theoretical reflectivity curve. In order to fit the reflectivity and photoelectron yield data, the *dare* fitting-model was used, based on the DARE analysis software developed by J. Zegenhagen.

The grand majority of measurements reported on in the literature up to date have been taken in the older geometry of the ID32 beamline at ESRF, in which electrons were detected at an angle of 45° to the incoming photon beam. In this geometry, multipolar corrections (see section 2.5.4) must be taken into account in the data analysis. The measurements presented here were taken in the new setup, in which the analyzer is mounted at 90° with respect to the incoming beam. In this geometry, the multipolar corrections can be ignored [159; 162; 163] ($S_R = S_L = 1$ and $\psi = 0$).

Adsorption height dependence on supramolecular environment

Fig. 5.17 shows some representative results. A reflectivity curve for each of the substrates (red triangles) is shown; the width of the reflectivity curves was below 1 eV. Above the reflectivity curves, photoelectron yield curves for CuPc's $\mathrm{C_C}$/H (black) and N (blue), as well as PFP's $\mathrm{C_F}$ (black) and F (purple) are plotted. From these, the coherent fraction (F^H) and coherent position (P^H) are obtained by fitting to Eq. 2.15. As explained in section 2.5, the F^H is related to the degree of vertical order in the sample, i.e. the distribution of heights of each atomic species. If all the atoms of a given species had the same height above the substrate, the coherent fraction would be equal to one. Though coherent fractions very close to unity can be measured in typical inorganic single crystals, organic layers are an entirely different matter, and coherent fractions under 0.5 are not unusual [69; 89; 105; 154]. On the other hand, the P^H is directly related to the adsorbate-substrate distance z:

$$z = d_H(n + P^H),$$

where n is a natural number and d_H is the periodicity of the standing wave (which coincides with that of the lattice planes). While z can only be determined within a multiple of d_H, d_H is sufficiently large to make all values but one unreasonable. Here we safely assume $n = 1$ in all cases.

F^H, P^H, and z values for all analyzed species are summarized in Table 5.5 and a schematic representation of the molecular heights is shown in Fig. 5.18, comparing the results for the mixed layers with the heights previously reported for single component CuPc [98; 154] and PFP [89; 105] layers.

All the measured heights show consistently lower values on Cu(111) than on Ag(111), in line with what is expected from the reactivity of the substrates. However, disregarding that difference, results on Ag(111) and Cu(111) are qualitatively similar, showing a significantly larger molecule-substrate distance for PFP than for CuPc. Analysis reveals a substantial height change in both the $\mathrm{C_F}$ and F atoms, suggesting that the entire molecule is raised ~ 0.3 Å from the surface in the mixture. On the other hand, the height of the CuPc atoms does not change substantially. In the pure CuPc layer on Au, Cu and Ag [98; 154], N remains slightly lower than the C atoms. This is expected, as they form the central cage with the Cu atom that interacts most strongly with the

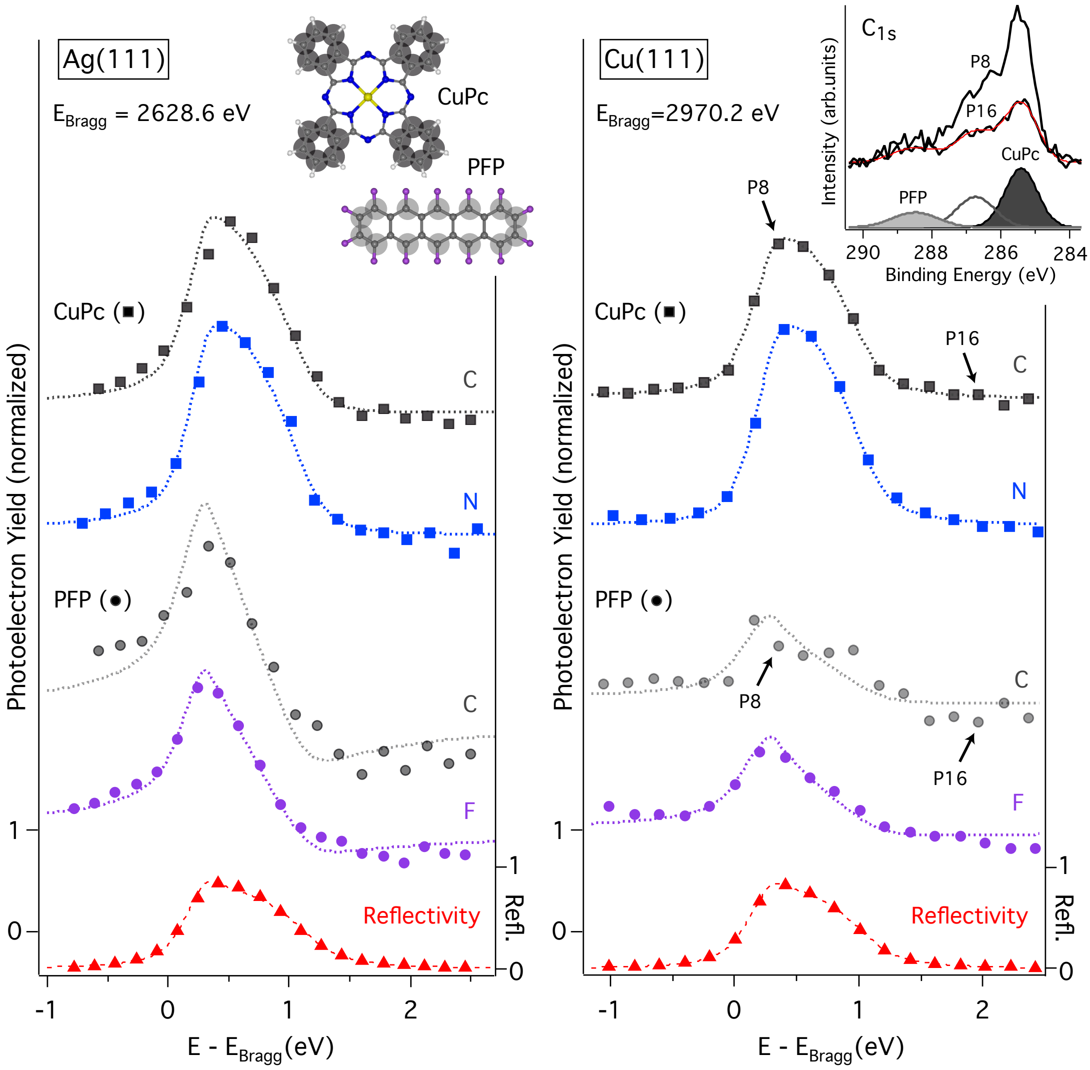

Figure 5.17: Reflectivity curve (red triangles) and C_{1s}, N_{1s} and F_{1s} photoelectron yield curves (grey, blue and purple curves; those of C and N are offset for clarity) for the molecular mixture on Ag(111) (right) and Cu(111) (left). The inset graph shows the C_{1s} photoemission intensity at the maximum (P8) and at the minimum (P16) of the photoelectron yield curve (points indicated by arrows). As shown for P16, the curves are fitted with three Gaussians, each corresponding to the different chemical environments of the carbon atoms in the molecules (see main text). The carbon atoms that were considered in the analysis are marked in grey in the molecular diagrams of the right inset (and correspondingly in the C_{1s} spectrum to the left). These are CuPc's C_H and C_C components (dark grey) and PFP's C_F component (lighter grey). The remaining carbon atoms, PFP's C_C and CuPc's C_N, are not considered.

metal substrate. In the mixture, this configuration, as well as the height of the CuPc molecules, remains practically unchanged, indicating a stronger interaction with the substrate than for PFP.

In single-component layers, CuPc lies closer to the substrate surface than PFP, both on Ag(111) and Cu(111) [89; 98; 105; 154] Upon mixing, the raising up of PFP further increases the height difference between donors and acceptors (see Fig. 5.18). The intermolecular C-F $\cdots$ H-C interactions assumed to drive the self-assembly of the highly crystalline donor-acceptor networks would be strongest in a coplanar arrangement, which would reduce the bond distance and enhance its linearity [22]. They are therefore expected to tend to level the molecular heights in the blends. However, contrary to expectations, we find that the height difference between molecules is increased in the mixed layer. The driving forces behind these surprising changes are unclear. Possible hypotheses are either substrate mediated effects or, more intuitively, halogen-π interactions between PFP's fluorines and the π-orbitals above the CuPc molecule (C-F $\cdots\pi$), which would profit from a height offset of the order of that found experimentally. As opposed to the C-F $\cdots$ H-C interactions, which would tend to level the molecular heights and are known to be amongst the weakest hydrogen bonds [21; 22; 164], C-F $\cdots\pi$ interactions have been shown to play an important role in organic crystal packing and their additional contribution to the intermolecular interactions therefore seems a plausible explanation to these findings [164].

		C_F	F	$C_{C/H}$	N
Ag(111)	F^H	0.8	0.59(8)	0.6	0.73(4)
	P^H	0.48	0.49(2)	0.34	0.301(8)
	z	3.48(5) Å	3.52(5) Å	3.16(5) Å	3.02(5) Å
Cu(111)	F^H	0.3(1)	0.32(9)	0.48(7)	0.7(1)
	P^H	0.59(4)	0.62(2)	0.30(2)	0.28(1)
	z	3.33(7) Å	3.37(5) Å	2.72(5) Å	2.66(5) Å

Table 5.5: XSW results for the CuPc+PFP mixture on Ag(111) and Cu(111). Coherent fraction (F^H), coherent position (P^H) and adsorption height z are shown.

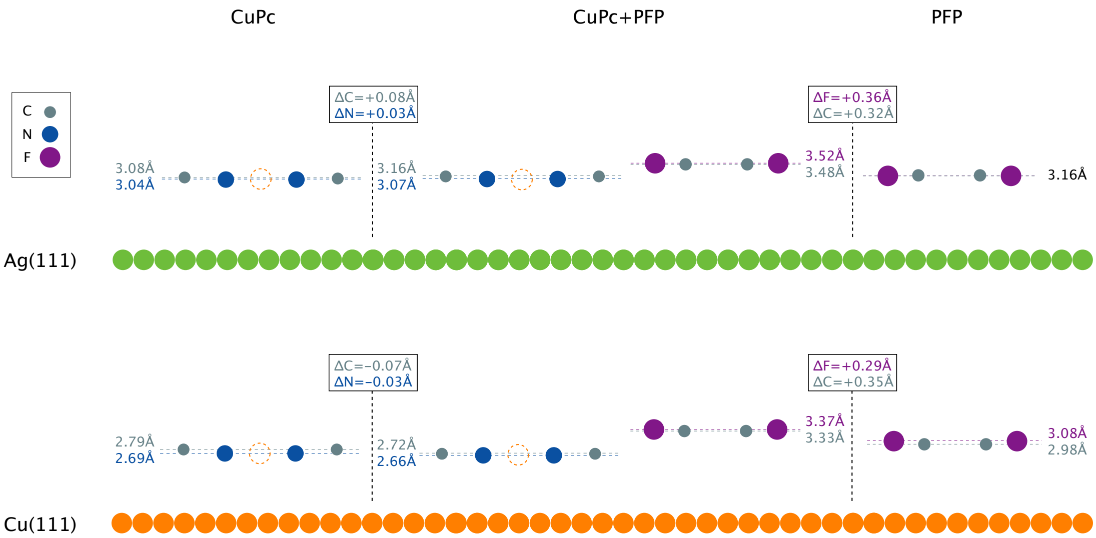

Figure 5.18: Schematic comparing the molecules' adsorption heights in single component layers (CuPc data from Refs. 98 and 154, PFP data from Refs. 89 and 105) to those in mixed layers. Distance to substrate not to scale.

Effect of adsorption height on the interface dipole

In section 5.2.1 we concluded that in a (monolayer) blend, the total work function shift is expected to be equal to the sum of the shift caused by the partial layers making up the blend (recall Eq. 5.1). However, the work function measurements presented in that section yielded a total work function shift in the blend smaller than that expected from this simple sum.

Reciprocal polarization of nearby dipoles [123; 165], i.e., depolarization of CuPc by mixing with PFP, could partially explain the reduced work function variation observed when PFP is added to the CuPc/Ag(111) interface. However, geometry changes do not affect the CuPc molecules, which strongly suggests that the CuPc dipole does not vary upon mixing. We may thus assume that only the PFP dipole changes when going from pure layers to the mixture.

The observed reduction is therefore understood in the light of the XSW results presented above, which showed that the PFP molecules raise up from the surface when mixed with CuPc. The adsorption height of PFP is larger in the CuPc+PFP mixture than it is in the PFP monolayer. Therefore, the Pauli repulsion (push-back) between the PFP and the metal's electron tail is reduced in the mix. Since geometry changes only affect the PFP molecule, it may assumed that only the PFP dipole changes when going from pure layers to the mixture. The change in the effective PFP dipole can be obtained from the experimentally determined work function changes $\Delta\phi_{\text{pure}}$ and $\Delta\phi_{\text{mix}}$ by using the Helmholtz equation [105],

$$\Delta\phi = \frac{ePn}{\epsilon\epsilon_0},$$

where P is the effective dipole moment per molecule, n is the areal density of dipoles[1], e is the elementary charge, ϵ is the relative permittivity ($\epsilon \simeq 1$ [105; 165]) and ϵ_0 is the permittivity of free space, we estimate that upon mixing, the effective dipole moment associated with PFP changes from $P_{\text{pure}} = 1.75\,\text{D}$ to $P_{\text{mix}} = 1.10\,\text{D}$ on Ag(111), and from $P_{\text{pure}} = 1.52\,\text{D}$ to $P_{\text{mix}} = 0.90\,\text{D}$ on Cu(111).[2]

Let us examine the most important effects that contribute to the interface dipole: these are (1) the Pauli repulsion between molecule's orbitals and the metal's electrons decaying into vacuum, (2) charge transfer between molecule and substrate and (3) the molecules' intrinsic electric dipole moment [28]. Option (2) is discarded as a possible explanation for the observed changes, since charge transfer values calculated on Ag(111) [122] show that this effect results in a net dipole change in the opposite direction. Option (3) is likewise ruled out as a main contributor to the reduction in P, since changes in the intrinsic dipolar moment in the mix due to modified molecular distortions lead to net dipole changes in opposite directions on Ag(111) and on Cu(111) [89; 105] (on Ag(111), when going from single component to mixed layer, the net change in intramolecular dipole points into the surface, whereas on Cu(111) it points away from it). We therefore argue that, while all contributions are present, it is mainly the Pauli repulsion (1) that is responsible for the changes in P: the increased molecule-substrate distance of PFP found in the mixture translates into a reduced Pauli repulsion, decreasing the effective interface dipole, as observed experimentally.

---

[1] $n = n_{\text{ML}} \cdot \Theta$, where Θ is the coverage of PFP and n_{ML} the dipole density for full monolayer coverage, which is $1/132\,\text{Å}^2$ for PFP/Ag(111), and $1/142\,\text{Å}^2$ for PFP/Cu(111), as determined from STM measurements in the previous chapter.

[2] $1\,\text{D} = 0.208\,e\text{Å} = 3.336\,\text{C} \cdot \text{m}$

5.2.6 CuPc+PFP - Summary and Assessment of VLP Model

Photoemission and x-ray absorption measurements of the single component layers showed that charge is transferred to the CuPc molecule from both the Ag(111) and Cu(111) substrates. NEXAFS and UPS results suggest the amount of charge transfer is larger in the case of CuPc/Cu(111). A much weaker interaction is seen to take place between the substrates and PFP. Gathering data for the position of the HOMO with respect to the substrate's Fermi level (i.e. Φ_{Bh} vs Φ) from the literature yields a picture in which PFP's levels are pinned to the vacuum level (for work functions between 4.7 and 5.5 eV), while CuPc's become pinned to the Fermi level once an IDIS becomes available (as on Ag and Cu).

The CuPc+PFP blend on Ag(111)

In this blend system photoemission measurements showed an approximately rigid shift of PFP's HOMO and core-levels 0.3-0.4 eV to higher binding energies, with the notable exception of the F_{1s} level. The CuPc levels showed practically no modification upon mixing. x-ray absorption measurements showed no notable changes in the C and N K-edges upon mixing, indicating LUMO and core-levels shift together.[1] However, a shift of about 0.15 eV to higher excitation energies of the F_{1s} onset was observed.

	CuPc, Donor					PFP, Acceptor			
	C_H	C_C	C_N	N	HOMO	C_C	C_F	F	HOMO
$\Delta\mathrm{BE}_{\mathrm{Exp}}$	−0.02	−0.02	−0.03	+0.02	0	+0.25	+0.36	+0.04	+0.4
S/S_{mix}	0.59					0.41			
σ	0.5					0.4			
$\Delta\mathrm{BE}_{\mathrm{VLP}}$	−0.04					+0.06			

Table 5.6: VLP predicted and measured molecular level shifts (ΔBE) for donor and acceptor molecules in the CuPc+PFP/Ag(111) blend. All values in eV.

Table 5.6 summarizes the experimental core-level shifts ($\Delta\mathrm{BE}_{\mathrm{exp}}$), and compares

---

[1] provided the core-hole exciton energy remains the same.

these with the values predicted by the VLP model ($\Delta \mathrm{BE}_{\mathrm{VLP}}$).[1] We find that the model cannot at all account for the large shift to higher binding energies of the acceptor molecule PFP's molecular levels. The small magnitude of $\sigma_{\mathrm{don}} - \sigma_{\mathrm{acc}}$ on Ag(111) results in predicted shifts that, though in the right direction, have very small absolute magnitudes.

For PFP, factors not taken into account by the VLP model that may contribute to the shift of the molecular levels of PFP to higher B.E. could be:

- the increased adsorption height of PFP: an increased adsorption height in the mixture means the σ_{PFP} used in the model to calculate the shifts is overestimated. A smaller σ_{PFP} would increase the predicted shift. From section 5.2.5 we know this contribution to amount to around 0.1 eV;
- the increased adsorption height also reduces the screening of the photoholes, contributing to the shift to higher binding energies of PFP's levels in the mixture;
- the actual ratio of this mix is $R \simeq 0.7$ (as estimated from XPS and Eq. 5.4), meaning that a larger PFP shift and a smaller CuPc should be expected. Correcting for this our predictions become a -0.01 eV shift of the CuPc levels to lower binding energy and a $+0.1$ eV shift of PFP to higher binding energy.

Interestingly, we find only a very small shift in PFP's $\mathrm{F_{1s}}$ levels ($+0.04$ eV), much smaller than what we find for the $\mathrm{C_{1s}}$ core-levels and the HOMO. It is not clear what this might be due to, though it goes along with another anomalous behavior of the F atoms, which is a shift of ca. $+0.15$ eV to higher excitation energies (the $\mathrm{F_{1s}}$ edge is the only one to shown any shift). What is clear is that this must be an effect specific to the interaction with Ag(111), since on Cu(111) and Au(111) [107] the $\mathrm{F_{1s}}$ level behaves in the same way as the $\mathrm{C_{1s}}$ levels.

Turning to the CuPc molecule, we find the VLP model predicts a very minor shift (even more so once the actual molecular ratio is considered), in agreement with the experimental results. In any case, another fact that should be considered is that, from PES and NEXAFS we learned that CuPc on Ag(111) has a partially filled LUMO and

---

[1] The surface area occupied by each molecule is estimated from the measured STM parameters (see the appendix for a summary of these) and gives $S_{\mathrm{don}}/S_{\mathrm{mix}} = 0.59$ and $S_{\mathrm{acc}}/S_{\mathrm{mix}} = 0.41$ for CuPc+PFP/Ag(111) and $S_{\mathrm{don}}/S_{\mathrm{mix}} = 0.55$ and $S_{\mathrm{acc}}/S_{\mathrm{mix}} = 0.45$ for CuPc+PFP/Cu(111).

a significant DOS at the Fermi energy. As a result, and as was shown in Fig. 5.12, CuPc shows signs of being pinned to the Fermi level, meaning that no shift should be expected, since any change in the vacuum level is easily compensated by an opposite interface dipole generated by partial charge transfer.

The CuPc+PFP blend on Cu(111)

The situation on Cu(111) is similar to that on Ag(111), though more in line with a rigid shift scenario: this time all of PFP's core-levels, including F_{1s}, show a shift of about +0.3 eV to higher binding energy. CuPc, on the other hand, shows a negligible shift again. Unfortunately, in this case no UPS data is available to track the molecular HOMOs in the blends, however, it seems likely that they should follow the core-levels, as in the previous system. NEXAFS shows no notable changes, indicating a shift of the LUMO with the core-levels.

As in the case of Ag(111), the data suggest a rigid shift of the acceptor's levels to higher binding energy, and no shift of the donor's levels.

The shifts predicted by the VLP model are shown in Table 5.7 along with the experimental shifts. We see that the VLP model overestimates the donor's shift, and slightly underestimates the acceptor's shift. As on Ag(111), the underestimation of the shift of PFP's levels can be explained by the increased adsorption height of this molecule in the mix, which leads to a smaller push-back effect and a reduced screening from the substrate.

	CuPc, Donor					PFP, Acceptor			
	C_H	C_C	C_N	N	HOMO	C_C	C_F	F	HOMO
Exp.	−0.01	−0.01	−0.01	0.00	—	+0.30	+0.31	+0.27	—
S/S_{mix}	0.55					0.45			
σ	0.7					0.3			
ΔBE_{VLP}	−0.18					+0.22			

Table 5.7: VLP predicted and measured molecular level shifts for donor and acceptor molecules in the CuPc+PFP/Cu(111) blend. All values in eV.

For CuPc, the overestimated shift of the donor can be explained by the fact that CuPc's levels are pinned to the substrate's Fermi level. From NEXAFS and UPS measurements we know that a large amount of charge is transferred from the Cu(111) substrate to the CuPc molecule in the single component layer, and that molecular levels become pinned to the Fermi level. Upon mixing, the vacuum level shift that occurs leads to a small amount of charge transfer that compensates this shift. It should be noted that the shift of the vacuum level is in the direction that would tend to unpin the molecule. However, from the absence of a core-level shift, we conclude that pinning is "strong" enough to withstand a shift of this magnitude (ca. $-0.2\,\mathrm{eV}$), i.e. enough charge transfer has taken place into the molecule's IDIS in the pinning process to withstand this vacuum level shift, whose direction tends to discharge (unpin) the molecule's IDIS again.[1]

---

[1] For reference, a study of PEN in which the molecule's HOMO was pinned to the Fermi level showed that a charge transfer of just $0.01\,\mathrm{e}$ was able to compensate a vacuum level shift of ca. $0.2\,\mathrm{eV}$ [166].

5.3 The PEN+FCuPc Blend on Ag(111)

5.3.1 The Interface Dipole

PEN and FCuPc single component layers on Ag(111)

The coverage dependence of the work function for PEN and FCuPc on Ag(111) is shown in Fig. 5.19. The deposition of PEN and FCuPc on the Ag(111) substrate causes a decrease in the work function as compared with that of the clean surface, just as was found for the oppositely fluorinated molecules on both Ag(111) and Cu(111). In this case the donor PEN causes a much larger change in the metal's surface dipole than FCuPc, and $|\sigma_{\text{don}} - \sigma_{\text{acc}}|$ is a substantial 0.6 eV.

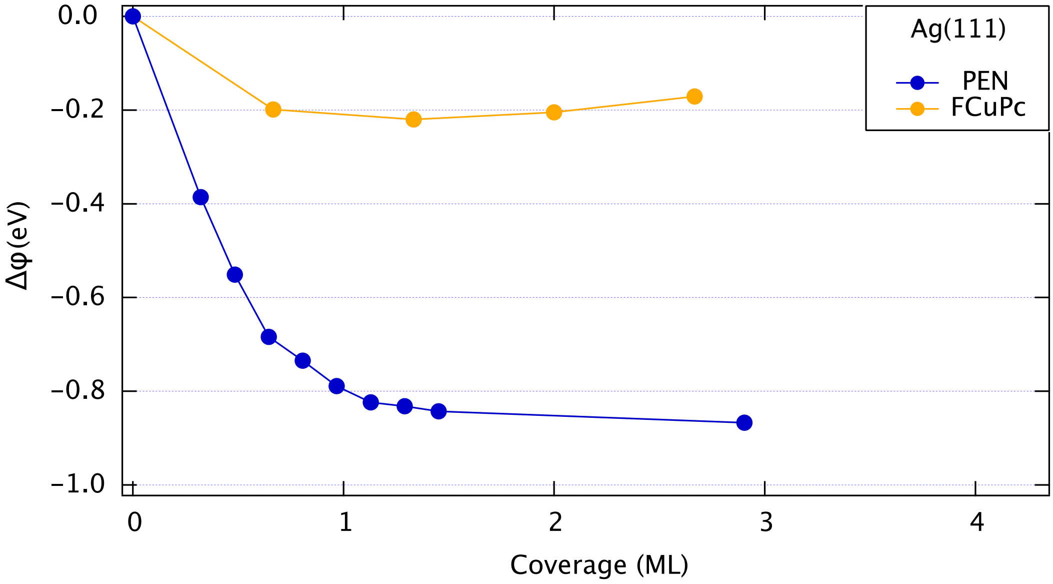

Figure 5.19: Work function change $\Delta\Phi$ as a function of molecular coverage for the PEN/Ag(111) and FCuPc/Ag(111) interfaces.

5.3.2 X-Ray Photoelectron Spectroscopy

Experimental Details and Data Analysis

The relevant experimental details and analysis procedure have mostly been presented already in section 5.2.2. However, one thing worth mentioning here is that the molecular ratio $R = N_{\text{FCuPc}}/N_{\text{PEN}}$ of the PEN+FCuPc mixture can no longer be estimated by comparing N and F intensities, as was done for the CuPc+PFP mix (recall Eq. 5.4), because in this case the N and F atoms are both located in the acceptor molecule. Instead, R can be estimated by comparing the C_F intensity of FCuPc and the C intensity of PEN (after normalizing both spectra to the substrate core-levels). The cross-sections are equal in this case, and only the different number of atoms in each case (16 and 22, respectively) must be taken into account. The molecular ratio is thus given by

$$R = \frac{N_{\mathrm{FCuPc}}}{N_{\mathrm{PEN}}} = \frac{I_{\mathrm{C_F}} \cdot N_{\mathrm{C}}}{I_{\mathrm{C}} \cdot N_{\mathrm{C_F}}} = 1.38 \cdot \frac{I_{\mathrm{C_F}}}{I_{\mathrm{C}}} \tag{5.5}$$

PEN and FCuPc single component layers on Ag(111)

The C_{1s} levels of about 0.3 ML of PEN are shown in blue in Fig. 5.20. Strictly speaking, six chemically inequivalent carbons make up the PEN molecule [167], however, in our case, a sufficiently good fit for our purposes can be obtained with a single peak centered at 284.85 eV.

The FCuPc core-levels, corresponding to a coverage of about 0.5 ML, are shown in yellow. FCuPc's C_{1s} spectrum was fitted as simply as possible, using three peaks in analogy to the phthalocyanine fits of the previous section. These are assigned (from higher to lower binding energy) to C_F, C_N and C_C and were therefore fitted in a 2:1:1 intensity ratio. FCuPc's N_{1s} and F_{1s} levels could each be fit with a single peak.

As in the case of CuPc/Ag(111), the core-levels of FCuPc/Ag(111) present broad features (especially apparent in the monolayer [125]) that can again be explained in terms of a double contribution from charged and uncharged atoms, as a consequence of the lifting of the LUMO's degeneracy [103; 141] upon charging by the substrate. (CuPc and FCuPc have a very similar electronic structure [168].)

The PEN+FCuPc blend on Ag(111)

The fit of the PEN+FCuPc mix, nominally 0.3 ML of PEN and 0.5 ML of FCuPc, is shown in green in Fig. 5.20 (green). As in the previous systems, the fit was based on the spectra of the individual components. The peak parameters were then fit, mainly the peak position, while the shapes of the peaks were kept as similar as possible to those of the individual components' spectra. Using Eq. 5.5, the molecular ratio is estimated to be $R \simeq 0.9$, very close to the desired one.

In the case of the donor molecule, PEN, we find a -0.17 eV shift to lower binding energy of its C_{1s} levels.

For FCuPc we find a shift to higher binding energy of the C_F (+0.11 eV) and F (+0.27 eV) levels, and smaller shifts to lower binding energy of the C_N (−0.04 eV) and N (−0.07 eV) levels. Due to the overlap of PEN's levels and FCuPc's C_C component, the shifts of these have a higher uncertainty, especially the less intense C_C component of FCuPc, which is buried beneath PEN's intensity. The fit was made keeping the position of the C_C component constant, and so nothing is concluded about its position.

Overall, the trend found in the model system (and in the oppositely fluorinated systems) can be discerned: the donor levels (PEN, CuPc) shift to *lower* binding energy, while the acceptor levels (FCuPc, PFP) shift to *higher* binding energy. However, a departure from this trend is found in the small shifts in the opposite direction found in the case of the of the acceptor's C_N and N levels.

5.3.3 Ultraviolet Photoelectron Spectroscopy

Experimental Details

The valence band measurements presented here were not taken using the laboratory UV source like those presented in section 5.2.3. Instead, they were taken at the ALOISA beamline of the Elettra synchtrotron, using a photon energy of 140 eV with an overall energy resolution of 200 meV. The surface was oriented with both the electric field incidence and the emission direction (detector orientation) at the "magic angle" (55°). The spectra were aligned at the Fermi level and normalized to the photon flux.

PEN and FCuPc on Ag(111)

Fig. 5.21 shows the valence spectra of ca. 0.7 ML FCuPc (yellow) and ca. 0.3 ML of PEN (blue). The FCuPc spectrum shows a large intensity at the Fermi level. As we saw in the case of CuPc/Ag(111) (section 5.2.3), this arises from a hybridization and from the lowering of the LUMO, which makes it cross the Fermi level and partially fill with charge. Farther to the left of the spectrum a prominent feature at 1.3 eV is seen, which corresponds to FCuPc's HOMO.

Turning to the PEN molecule, its spectrum (blue) shows just a hint of intensity at the Fermi level. However, its significance can be confirmed by a spectrum of higher coverage (still submonolayer), in which PEN's features are enhanced (dashed blue line). This indicates that, contrary to its fluorinated analogue PFP, PEN receives a significant

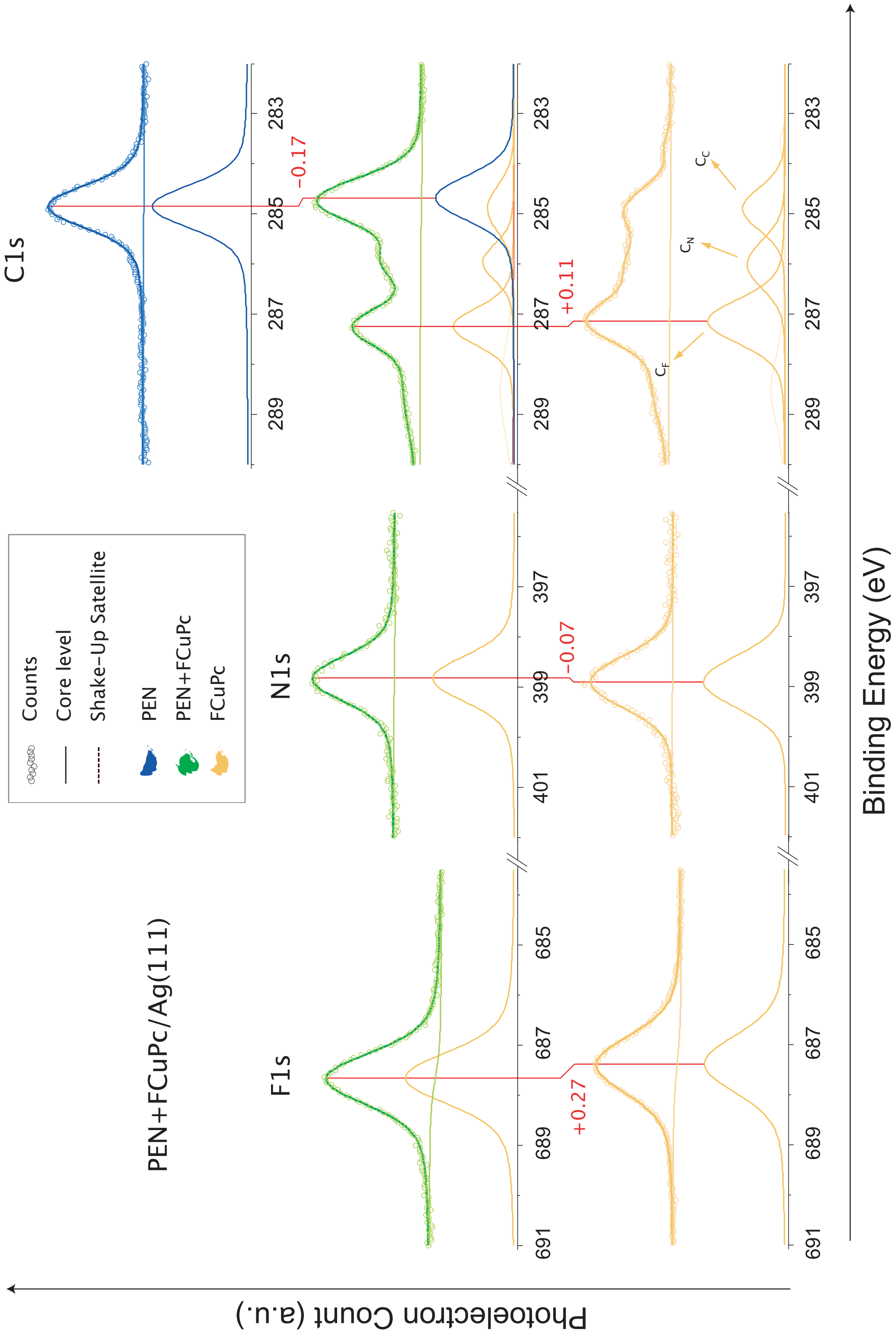

Figure 5.20: XPS spectra for single component and mixed layers of PEN+FCuPc on Ag(111).

amount of charge from the Ag(111) substrate. Though this is at odds with a previous report by Koch et al. [169], other studies based on NEXAFS have also claimed a chemisorptive PEN/Ag(111) interaction [170]. In addition, PEN's deep lying HOMO—the feature centered at 1.8 eV—makes the crossing of the low energy LUMO tail across the Fermi level plausible.

As we did for the opposite mixture in section 5.2.3, we plot the hole injection barrier Φ_{Bh} of FCuPc and PEN as a function of the substrate work function Φ. The values Φ_{Bh} on Cu(111) [105; 126] and Au(111) [113; 171] are taken from the literature. The Schottky-Mott limit (based on the Ag(111) data) is represented by a dashed line, and the vertical distance from the data to this line is associated with the interface dipole. The experimental values are drawn in as vertical lines.

For PEN, fitting the three points gives a fit with a slope 1.1. This result differs from a previous report on thicker layers by Koch et al. in which a screening parameter of 0.4 was observed [172]. Our results however, point towards a $S = 1$ behavior like that observed for PFP, i.e. PEN's molecular levels are pinned to the vacuum level. However, the valence band of PEN/Ag(111) showed an important difference with respect to PFP/Ag(111): an intensity at the Fermi level indicating charge transfer from the substrate. This suggests that the PEN molecule may have become pinned to the Fermi level via the LUMO's IDIS, and would show an $S = 0$ behavior for substrates with a lower work function than Ag.[1]

The situation of FCuPc is also very similar to CuPc, and the data is interpreted in the same way: for large substrate work functions like that of Au, the molecular levels are pinned to the vacuum level ($S = 1$), but as the work function is reduced (Cu, Ag), the Fermi level begins to cross into the LUMO's DOS, allowing charge transfer and imposing Fermi level pinning. This is consistent with the observation of an intensity at the Fermi level when FCuPc is adsorbed on Ag(111) (see Fig. 5.21) or Cu(111) [126] and the absence of this feature for FCuPc on Au(111) [113].

The PEN+FCuPc blend on Ag(111)

Shown in green in Fig. 5.21 is the molecular mixture of PEN+FCuPc in an approximately 1:1 ratio. The intensity at the Fermi level is present, and looks very similar

---

[1] The pinning of PEN's *HOMO* to the Fermi level has been studied in the absence of the push-back effect by Fukagawa et al. [166].

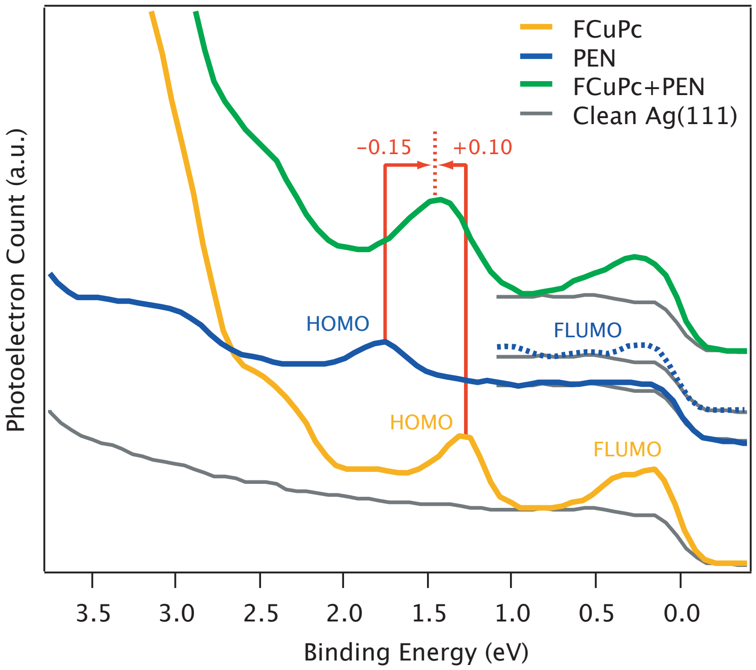

Figure 5.21: Valence band of single component and mixed layers of PEN+FCuPc on Ag(111). Photon energy was 140 eV and emission angle was 55°.

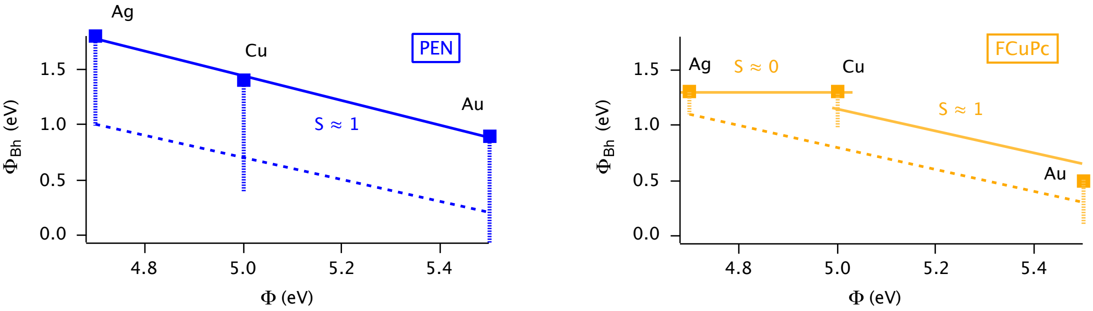

Figure 5.22: The hole injection barrier Φ_{Bh} (distance from HOMO to E_F) of PEN [105; 171] and FCuPc [113; 126] is plotted versus the substrate work function Φ. The slope of the solid line represents the screening parameter S and the dashed line the Schottky-Mott limit. The vertical lines represent the measured values of the surface dipole.

to that of the FCuPc spectrum. However, a slight shift to higher binding energies can be observed, resulting in an increased intensity in the mix. A single feature at about 1.5 eV includes the intensity of both molecules' HOMO levels. It is evident that a shift of these frontier orbitals has taken place upon mixing: FCuPc's HOMO has shifted to higher binding energy, while PEN's HOMO has shifted to lower energy. Again, as in the case of CuPc+PFP/Ag(111), we find the same tendency as was found in the core-levels in the previous section: a shift to the left of the acceptor molecule and a shift to the right of the donor molecule, suggesting the molecular electronic levels are all shifting (more or less) rigidly.

5.3.4 Near-Edge X-Ray Absorption Fine Structure

See section 5.2.4 for experimental details.

PEN and FCuPc single component layers on Ag(111)

Fig. 5.23 shows a comparison between monolayer and multilayer spectra of FCuPc. Just as in the case of CuPc, we find the N K-edge spectrum shows shifts of the second and third resonances (LUMO+1 and LUMO+2), related to the effect of charge transferring from the substrate to the molecule [140]. In addition, we see an enhanced intensity at lower excitation energies in the C and N K-edges of the monolayer, as compared to the multilayer (the same changes are found with respect to the Au(111) substrate [107]). This intensity, enlarged in the insets of Fig. 5.23, is proposed to stem, as in the case of CuPc (section 5.2.4), from the lifted degeneracy of the LUMO levels upon partial charging of the molecule [141]. This partly filled LUMO is reflected in the appearance of this shoulder in the NEXAFS spectra, to the intensity found at the Fermi level in the UPS spectrum of FCuPc/Ag(111) (Fig. 5.21) and to the splitting of the core-levels [125]. The effects of charging FCuPc are very similar to those found for CuPc, which is not surprising due to their similar electronic structures [168].

We now turn to the PEN layer. Fig. 5.24 shows a comparison between a nominally submonolayer PEN/Ag(111) spectrum (bottom) and one resulting from further deposition (total coverage of about 1 ML) directly on top of this same sample (top). The two spectra radically differ: of the three small resonances present at the onset of the bottom spectrum, the first of these completely disappears in the top spectrum, while in place of the other two we find two much larger resonances. Previous reports on the

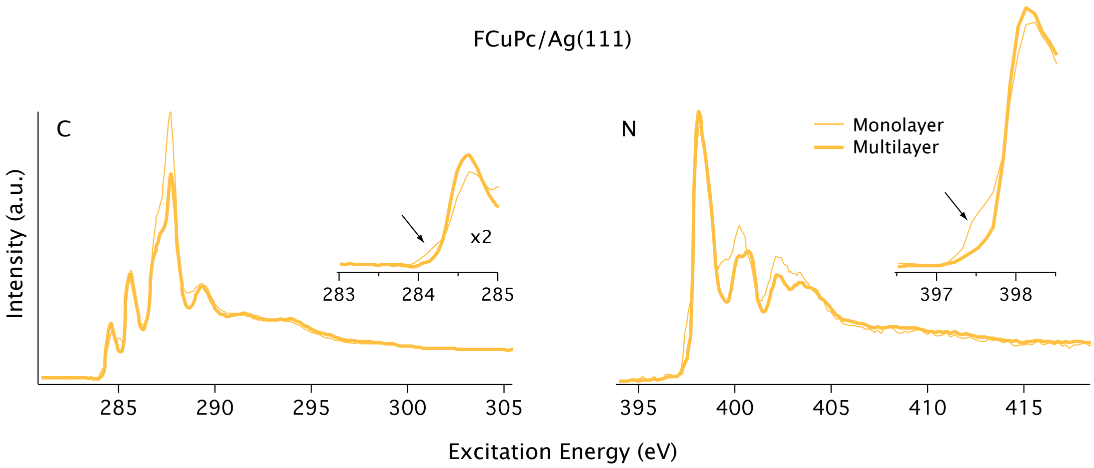

Figure 5.23: C and N K-edges of p-polarized multilayer and monolayer spectra of FCuPc/Ag(111).

PEN/Ag(111) system exist: Käfer et al. [170] and Pedio et al. [173] both record the coverage dependence of the PEN/Ag(111) C K-edge, however there are some differences regarding coverage calibration between them. In both previous reports a spectrum similar to our top spectrum is seen and is associated with the PEN monolayer. However, for lower coverages Pedio et al. report a spectrum resembling our submonolayer spectrum, while Käfer et al. report one more similar to their monolayer spectrum. In both cases the three initial resonances are recovered at multilayer coverages. Our coverage calibration, made using quartz crystal microbalance and verified by cut-off measurements, confirms that the bottom spectrum in Fig. 5.24 corresponds to a PEN submonolayer, and the top spectrum to about one monolayer, in agreement with the data of Pedio and coworkers. The radical change in the shape of the spectrum when going from submonolayer to monolayer, which effectively displaces the onset of the K-edge by ca. 0.7 eV, is likely a consequence of a structural transition as the coverage reaches the monolayer, as suggested from He atom scattering studies [174].

We now more closely examine the (sub)monolayer spectra of PEN and FCuPc. Fig. 5.25 shows the NEXAFS spectra of PEN (blue) and FCuPc (yellow) for both p-polarization (continuous line) and s-polarization (dashed line). The clear dichroism in the case of the C and N spectra of both molecules points, as was the case for the opposite molecular pair (section 5.2.4), to a flat-lying adsorption geometry. The exception to this dichroism is again the F K-edge of FCuPc, in which the s-polarization

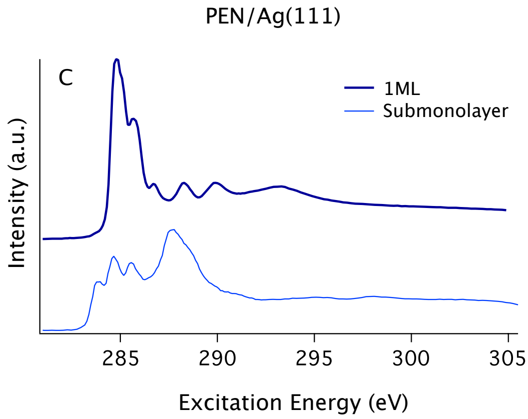

Figure 5.24: Two radically different p-polarized C K-edge spectra representing submonolayer and monolayer PEN/Ag(111).

and p-polarization have comparable intensities from the onset [152]. This is analogous to the previously presented results on PFP.

The small feature at ca. 398.6 eV in FCuPc's s-polarization spectrum corresponds, in analogy to CuPc, to the molecule's SUMO, located mainly in the central part of the molecule, at the Cu and four nearest N atoms.

The PEN+FCuPc blend on Ag(111)

The interpretation of the NEXAFS spectra can be quite complex, since it involves transitions from several levels to several unoccupied levels, and is further complicated in a molecular mixture. For this reason, we focus on the first resonance, which can be related to the lowest unoccupied state, the LUMO. The enhancement and reduction of the first resonance can be indicative of a significant amount of charge transfer occurring. An enhancement of a resonance means there are more empty states to fill, i.e. a formerly occupied state has become unoccupied or partially filled. A reduction, on the other hand, means fewer empty states are available to transition to, i.e. this final state has gained charge. Shifting or broadening/narrowing of the molecule's LUMO is one way this could be occurring: as the LUMO approaches the Fermi level, or broadens, its tail crosses it and is filled with charge; conversely, if the LUMO moves away from the Fermi level, or narrows, its tail will lose charge. Shifts in the onset of a NEXAFS spectrum indicate a shift of the LUMO *with respect to the initial state* (the core-level),

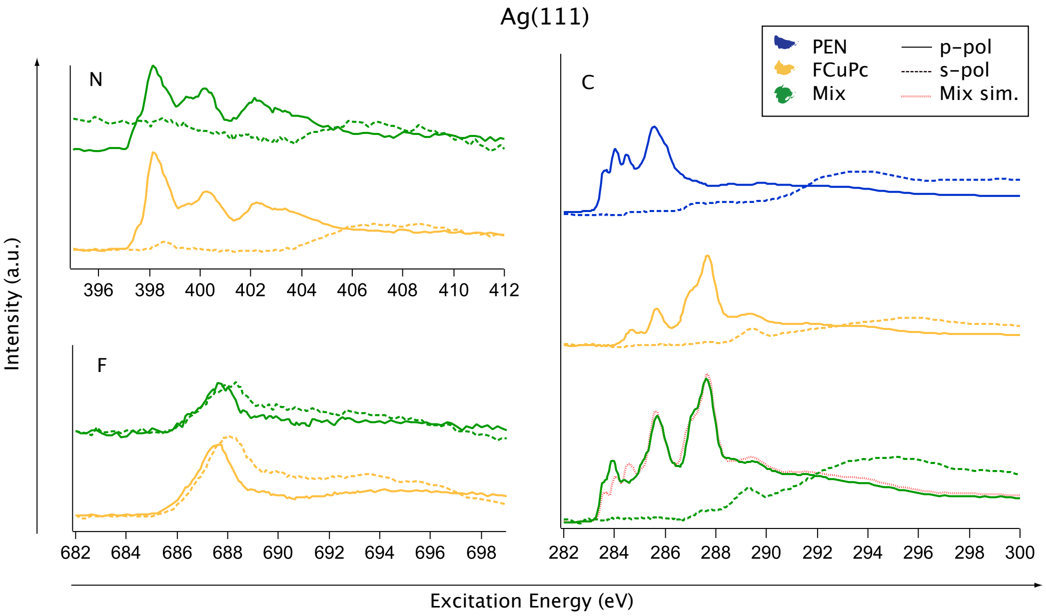

Figure 5.25: C, N and F K-edge NEXAFS spectra for single component and mixed layers of PEN+FCuPc on Ag(111). Interesting changes are observed in the mixture.

so the absence of a shift means that LUMO and the corresponding core-level are shifting together.

Contrary to the relatively unexciting NEXAFS spectra of the previous two molecular blends, we find the PEN+FCuPc/Ag(111) shows some interesting and obvious changes with respect to the single component layers. From the comparison of the C K-edge “simulated” mix spectrum (red) with the measured one (green), shown in Fig. 5.25 and enlarged in Fig. 5.26, we see that the the mix shows a clear enhancement of the first two resonances of PEN (features marked (1) and (2) in the C spectrum of Fig. 5.26), and a more ambiguous reduction of the first resonance of FCuPc (feature (3)). (Additionally, there is a shift of about $-0.1\,\text{eV}$ in the second PEN resonance.)

The lack of shift of PEN’s first resonance, combined with the ca. $-0.2\,\text{eV}$ shift to lower binding energy of the initial state (the C_{1s} core-level), suggest that the molecule’s LUMO level is shifting (together with the core-level) away from the Fermi level. In turn, the enhancement of the first resonance could be interpreted as an emptying of a partially filled LUMO as it shifts in energy. We may therefore conclude that PEN loses charge when mixed with FCuPc.

If we suppose feature (3) reflects a decrease in the first FCuPc resonance, this

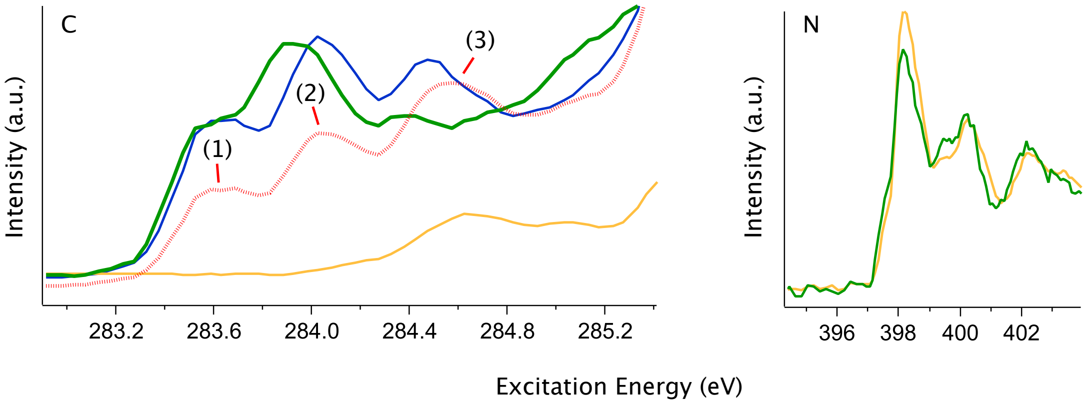

Figure 5.26: Left: A close-up of the onset of the C K-edge shown in Fig. 5.25; PEN (blue), FCuPc (yellow), Mix (green) and simulated mix (red); Right: single component FCuPc (yellow) and mixed (green) layers' N K-edge superimposed.

would mean that this molecule's LUMO fills when mixed with PEN, in line with what is expected from the lowering of the work function that is brought about by mixing. The LUMO is distributed mainly around the N and C_N atoms, with a smaller DOS on the C_C and C_F atoms [114]. The C_N and N core-levels both show a small shift to lower binding energy which could be an indication of a charge gain.

The interpretation of feature (3) is difficult due to overlapping contributions, so we look for other hints in the N K-edge spectrum, which is expected to show the most obvious signs of charge transfer. The comparison of the normalized single component (yellow) and mix (green) N K-edge spectra (see Fig. 5.26) show a reduced intensity of the first resonance in the case of the mix, as well as a small shift of the second and third resonances to lower photon energies, all indications a charge gain [140], in line with our tentative interpretation of feature (3). This picture also lends support to the observation of a growing intensity near the Fermi level for the FCuPc molecule (Fig. 5.21) observed in the UPS measurements.

In conclusion, the spectra in Fig. 5.26 suggest that, upon mixing, the acceptor molecule FCuPc is receiving charge, while the donor molecule PEN is losing it.

5.3.5 PEN+FCuPc - Summary and Assessment of VLP Model

Photoemission and x-ray absorption measurements of the single component layers showed significant charge transfer from the substrate to the molecule in the case of FCuPc/Ag(111) and a weaker interaction in the case of PEN/Ag(111). Plotting Φ_{Bh} versus substrate work function shows FCuPc and PEN to behave in the same way as CuPc and PFP, respectively: the phthalocyanines become pinned to the Fermi level on Cu and Ag, whereas are the acenes' levels are pinned to the vacuum level and interact more weakly with the metals. (PEN however begins to receive charge on the Ag(111) substrate, possibly becoming pinned to the Fermi level for lower work functions.)

Photoemission measurements of the mixed PEN+FCuPc/Ag(111) system showed a clear shift of about $-0.2\,\mathrm{eV}$ of the donor molecule's core-level and HOMO to lower binding energy. In the acceptor molecule FCuPc the shifts were not as straightforward: the $\mathrm{C_F}$, and HOMO levels showed a shift of about $+0.1\,\mathrm{eV}$ to higher binding energy and F showed a considerably larger shift of about $+0.3\,\mathrm{eV}$, whereas the core-levels of $\mathrm{C_N}$ and N showed a smaller shift in the opposite direction.

Absorption measurements showed an enhancement of the first resonance of PEN's C K-edge in the mix, and a reduction of FCuPc's first resonance and of the N K-edge spectrum, suggesting PEN loses and FCuPc gains charge when forming this mixture.

The shifts predicted by the VLP model are shown in Table 5.8. These are a large shift to lower binding energy ($+0.4\,\mathrm{eV}$) of the donor PEN's molecular levels, and a somewhat smaller shift ($-0.2\,\mathrm{eV}$) of the acceptor FCuPc's levels to higher binding energy.[1]

The experimental shift of PEN is in the same direction as that predicted by the model (to lower binding energy), but quite a bit smaller in magnitude. We propose this difference to be due to a charge loss of the PEN molecule when mixed with FCuPc, not taken into account by the VLP model. From the valence band measurements we observed that PEN in the single component layer receives charge from the Ag(111) substrate. When mixed, the PEN molecule's levels shift upward (to lower binding energies) with the vacuum level, moving the LUMO away from the Fermi level, and causing it to discharge. This charge loss tends to shift PEN's molecular levels to higher

---

[1] Recall that the surface area occupied by each molecule is estimated from the measured STM parameters (see the appendix for a summary of these) and gives $S_{\mathrm{acc}}/S_{\mathrm{mix}} = 0.67$ and $S_{\mathrm{don}}/S_{\mathrm{mix}} = 0.33$ for the FCuPc+PEN/Ag(111) system.

	PEN, Donor		FCuPc, Acceptor					
	C	HOMO	$\mathrm{C_C}$	$\mathrm{C_N}$	$\mathrm{C_F}$	N	F	HOMO
$\Delta\mathrm{BE_{Exp}}$	-0.17	-0.15	—	-0.04	$+0.11$	-0.07	$+0.27$	$+0.10$
S/S_{mix}	0.33		0.67					
σ	0.8		0.2					
$\Delta\mathrm{BE_{VLP}}$	-0.40		$+0.20$					

Table 5.8: Predicted and measured XPS shifts ΔB_{E} for donor and acceptor molecules for different blend systems. All values in eV.

binding energy, thereby partly compensating the vacuum level shift and explaining the a smaller absolute value of the experimentally observed shift.

As for the acceptor molecule, FCuPc, we find the shifts in opposite directions of the different molecular levels can again be rationalized by considering the effects of charge transfer. From NEXAFS measurements a charge gain of the acceptor molecule was concluded. Since the LUMO is mainly distributed around FCuPc's central core, i.e. the N and $\mathrm{C_N}$ atoms [114], it is these that will most strongly feel the effects of charge transfer into the molecule. Instead of exhibiting the shift to higher binding energy predicted by the VLP model, the effect of the charge gain is a (over)compensating shift in the opposite direction, which ultimately results in the small shift to lower binding energy that is measured. The core-levels $\mathrm{C_{F1s}}$ and $\mathrm{F_{1s}}$ and the HOMO on the other hand, being less affected by the charge transfer, show a shift in the expected direction. We therefore see that the behavior of the different molecular levels depends on whether they are affected by charge transfer, which in turn depends their spatial distribution. This same effect has been found when charging the CuPc by doping with Na [175].

6

Conclusions

In this work both the structure and the electronics of self-assembled layers of small π-conjugated molecules on metal surfaces are explored, using a variety of techniques: STM, XSW for structural characterization, and XPS, UPS and NEXAFS for insight into the electronic structure of the metal-organic interface.

In the first part of the thesis, Chapter 3, the dislocation network in the PFP/Ag(111) system was characterized by STM. This linear dislocation network appears at low temperature and consists in a shearing of the unit cell every six molecule rows. In order to understand the origin these dislocations, the interactions determining the assembly were broken up into intermolecular, substrate-mediated and molecule-substrate interactions and modeled by theoretical calculations based on the experimental STM parameters. We were able to conclude that

- according to the calculations, the fully commensurate structure proposed in the literature is not the most favorable, on account of the small intermolecular distance;
- an incommensurate structure based on our experimental parameters was found to be more favorable, and the introduction of dislocations for strain relief could provide a further energy gain, if these occurred every 5-7 molecules (the gain being maximal for 6).

By taking into account the different interactions in the system, this model was able to successfully explain the existence of the dislocation network at the PFP/Ag(111) interface as a strategy for stain relief within the layer.

The remainder of the thesis focuses on monolayers of molecular donor-acceptor blends. Four molecules are used throughout: PEN and CuPc (donors), and their similarly shaped fluorinated analogues PFP and FCuPc (acceptors). Mixed donor-acceptor monolayers are formed by depositing (simultaneously or sequentially) an approximately equal amount of both molecules.

In Chapter 4 several of these monolayer blends were characterized by STM: the CuPc+PFP blend on Ag(111) and Cu(111), as well as the PEN+FCuPc blend on Ag(111). From this study we concluded that

- the structure of the stoichiometric 1:1 monolayer blends is virtually identical regardless of molecular fluorination and substrate: the molecules invariably self-assemble into an ordered crystalline layer in which donor-acceptor contact is maximized;
- the driving force behind the assembly process was demonstrated to be hydrogen bonding between the hydrogen atoms of the donor and the fluorine atoms of the acceptor: when these intermolecular interactions are inhibited, as in the PEN+CuPc mixture, no ordered network forms, and the molecules instead segregate into distinct phases;
- a variety of crystalline blends of different stoichiometries exist, and can be formed by adjusting the relative amount of deposited molecules;
- combining our measurements with previous work, we may now state that both the CuPc+PFP and PEN+FCuPc blends assemble into the same 1:1 network on Au(111), Ag(111) and Cu(111). The existence of a same overlayer structure on substrates of such different reactivities tells of the leading role of the intermolecular interactions play in their formation.

In the final Chapter 5, the effects of this assembly on the vertical structure and electronics of the molecules were explored. We found that this new environment had many measurable effects of the layers:

- In both systems on which XSW measurements were performed, CuPc+PFP/Ag(111) and CuPc+PFP/Cu(111), the acceptor molecule PFP was found to raise up from the surface by a substantial amount (ca. 0.3 Å) with respect to its adsorption height in the single component layer.

- The change in adsorption height of PFP has a measurable effect on the layer's surface dipole due to a reduced push-back effect.

- In all measured blend systems shifts in the molecules' electronic levels with respect to those of the single component layers were observed by XPS and UPS.

- The direction of shifts follows a general trend—donor level's to lower binding energy, acceptor levels to higher binding energy—that is opposite to what would be expected from donor-to-acceptor charge transfer. Instead, the tendency is proposed to stem from a vacuum level pinning scenario.

The vacuum level pinning (VLP) scenario was initially put forward to explain the PEN+FCuPc/Au(111) blend system, in which molecule-substrate interactions are very weak. The blends we study in this thesis lie on the more interactive substrates Ag(111) and Cu(111), and so deviations from the VLP model are observed. These are explained in terms of phenomena such as charge transfer or conformational changes not taken into account in a simple vacuum level pinning scenario, and not present in the more weakly interacting Au(111).

Let us end with a summary of our conclusions for each system. The VLP model applied to the **CuPc+PFP/Ag(111)** system predicted a negligible shift ($-0.01\,\mathrm{eV}$) of the donor's levels to lower binding energy and an only somewhat larger one for the acceptor's levels ($+0.1\,\mathrm{eV}$). These compare in the following way with the shifts observed experimentally:

- All measured electronic levels of CuPc showed a negligible shift compatible with that predicted by the VLP-model.

- The levels of PFP showed a shift considerably larger than that predicted by the VLP-model. This is related to the larger adsorption height of PFP in the mix, since it reduces the push-back effect and the screening of the photohole.

Applying the VLP model to the **CuPc+PFP/Cu(111)** system predicted a shift of ca. $-0.18\,\mathrm{eV}$ of the donor's levels to lower binding energy and one of ca. $+0.22\,\mathrm{eV}$ of the acceptor's levels to higher binding energy. These compare in the following way with the shifts observed experimentally:

- All measured electronic levels of CuPc showed a negligible shift. This discrepancy with the VLP model is explained by the fact that CuPc's levels are pinned to the Fermi level by the molecule's LUMO, so that shifts in the vacuum level can be compensated by an opposing dipole set up by charge transfer.
- All the levels of PFP showed a shift somewhat larger (+0.3 eV) than that predicted by the VLP-model. Again, as in the case on Ag(111), we expect the larger adsorption height of PFP in the mix to contribute to a larger shift of PFP's levels to higher binding energy.

Lastly, for the **PEN+FCuPc/Ag(111)** system VLP predicted a shift of ca. −0.4 eV of the donor's levels to lower binding energy and one of ca. +0.2 eV of the acceptor's levels to higher binding energy. These compare in the following way with the shifts observed experimentally:

- The levels of PEN show a smaller shift (−0.2 eV) than that expected from VLP, due to a loss of charge brought about by mixing. This loss of charge is expected from the upward shift of the LUMO, which was seen to cross the Fermi level in the single component layer.
- The levels of FCuPc show shifts between +0.1 eV and +0.3 eV, excepting the core-levels of C_N and N, which show a small shift in the *opposite* direction. This, along with clear indications from NEXAFS, indicate a charge gain of the FCuPc molecule upon mixing, in line with the expected downward shift of the LUMO.

In conclusion, we may say that this work successfully rationalizes the shifts observed in the electronic levels of donor and acceptor molecules when these are mixed on metal substrates. This marks an important step towards understanding the energy level alignment in such systems, which is essential for achieving control over the charge injection barriers in technologically relevant metal/organic interfaces.

Appendix A

Supplementary Information

A.1 The PFP/Ag(111) Dislocation Network: Calculational Details

This appendix presents the details of the theoretical calculations on the PFP/Ag(111) system (Chapter 3), performed by J. M. García-Lastra from the group of Ángel Rubio.

For the DFT calculations it was crucial to separate the energy contributions in two terms:

i. The PFP-Ag interaction, $E_{\mathrm{PFP-Ag}}$, defined as

$$E_{\mathrm{PFP-Ag}} = E(\mathrm{PFP@Ag}) - E(\mathrm{Ag}) - E(\mathrm{PFP}),$$

where $E(\mathrm{PFP@Ag})$, $E(\mathrm{Ag})$, and $E(\mathrm{PFP})$ are total energies of an adsorbed system, a clean Ag(111) surface, and an isolated PFP molecule, respectively.

ii. The PFP-PFP nearest neighbor interaction, $E_{\mathrm{PFP-PFP}}$, defined as

$$\begin{aligned} E_{\mathrm{PFP-PFP}} &= [E(\mathrm{PFP_1 + PFP_2@Ag}) - E(\mathrm{Ag}) - 2E(\mathrm{PFP})] \\ &\quad -[E(\mathrm{PFP_1@Ag}) - E(\mathrm{Ag}) - E(\mathrm{PFP})] \\ &\quad -[E(\mathrm{PFP_2@Ag}) - E(\mathrm{Ag}) - E(\mathrm{PFP})] \\ &= E(\mathrm{PFP_1 + PFP_2@Ag}) + E(\mathrm{Ag}) \\ &\quad -E(\mathrm{PFP_1@Ag}) - E(\mathrm{PFP_2@Ag}), \end{aligned}$$

> where $E(\mathrm{PFP}_1+\mathrm{PFP}_2\mathrm{@Ag})$ and $E(\mathrm{PFP}_i\mathrm{@Ag}), (i = 1, 2)$ are the total energies of an adsorbed system with two molecules placed at sites 1 and 2, and an adsorbed system with one molecule place at site i, respectively.

In order to analyze these terms we carried out DFT calculations by means of the GPAW code [80], using periodic boundary conditions and the Local Density Approximation (LDA). $E_{\mathrm{PFP-Ag}}$ (Fig. 3.2 in Chapter 3) was mapped using the relative position of the PFP molecule center with respect to the origin of the Ag(111) surface unit cell as the coordinate. To model the metal-molecule interface we used a super-cell containing three layers of Ag(111) with 7 × 8 atoms in each layer (20.22 Å × 23.11 Å). This size ensures that the interaction between PFP replicas is negligible. The Ag(111) slab and PFP molecule structures were kept fixed. Thus the only degree of freedom was the displacement of PFP molecule over the Ag(111) surface. $E_{\mathrm{PFP-PFP}}$ was evaluated using the same super-cell, but placing two PFP molecules instead of one. The two PFP molecules were arranged in the two different configurations shown in Fig. 2a of the manuscript. Again the size of the super-cell guarantees that the interaction between a PFP pair and its replicas is insignificant.

The PFP-PFP nearest neighbor interaction was also calculated in vacuo, without the presence of the Ag(111) substrate, using the same calculation parameters. $E_{\mathrm{PFP-PFP}}$ in vacuo is simply defined as

$$E_{\mathrm{PFP-PFP}} = E(\mathrm{PFP}_1 + \mathrm{PFP}_2) - 2E(\mathrm{PFP}).$$

For both types of calculations, PFP molecules lie flat at $Z = 3.14$ Å above the surface followed by 12 Å of vacuum. We previously determined the distance $Z = 3.14$ Å, which is very close to the experimental one $Z = 3.16$ Å measured by Duhm et al. [89], by means of a geometry optimization.

The energy of formation of the bilayer with respect to the lateral displacement of the layers (Fig. 3.2b) was also mapped similarly to the $E_{\mathrm{PFP-Ag}}$ mapping. In this case we only consider two parallel PFP layers in the model, without including the Ag(111) substrate. The interlayer distance, $D = 3.46$ Å, was previously determined through a geometry optimization and kept fixed during the mapping.

A.2 Molecular Flipping

Images of both first and second PFP layers evidence a certain mobility/bistability of the pairs of molecules forming the dislocation lines. Streaks along the lines show that the molecules are moving on a time scale faster than that of STM imaging. Fig. A.1 shows the "streaking" on pairs of molecules forming the dislocation lines; these are marked on one of the lines. The fact that the streaks are only present on the dislocation lines indicates that it is only there that the molecules have some degree of freedom. A close inspection of the image reveals that the motion the pairs of PFP are undergoing is a 90° "flip" within the dislocation line: in some instances, the molecule remains in its new conformation long enough (the duration of several scan lines) to be (partly) imaged, as shown in the zooms of Fig. A.1.

Just for fun we can estimate the order of magnitude of the flipping rate. The scan speed is $v_{\text{scan}} = 150.24\,\text{nm/s}$ and the size of the image, $50 \times 50\,\text{nm}^2$; the tip travels back and forth each scan line. A simple analysis of the number of scan lines forming the streaks shows that the typical streak width is 1 scan lines, meaning that the molecule pairs, on average, remain in their flip position for $\Delta t = 2 \cdot \frac{50\,\text{nm}}{150.24\,\text{nm/s}} \simeq 0.7\,\text{s}$. The record holders in this image are the PFP pair that were able to last 5 scan lines (upper left-hand corner of Fig. A.1), meaning they remained flipped for around 3 seconds.

Of course, it is possible that faster flipping is also taking place, and goes undetected by the STM, but it is safe to say that the streaks observed along the dislocation lines arise from molecule pairs that are able to remain in their "flipped" state the order of 1 second. Fig. A.2a shows an image taken at a higher scan speed (twice that of Fig. A.1). As should be expected, the faster scanning makes it possible to image the flipped state for more scan lines. Finally, second layer images show stable flipped pairs, as shown in Fig. A.2).

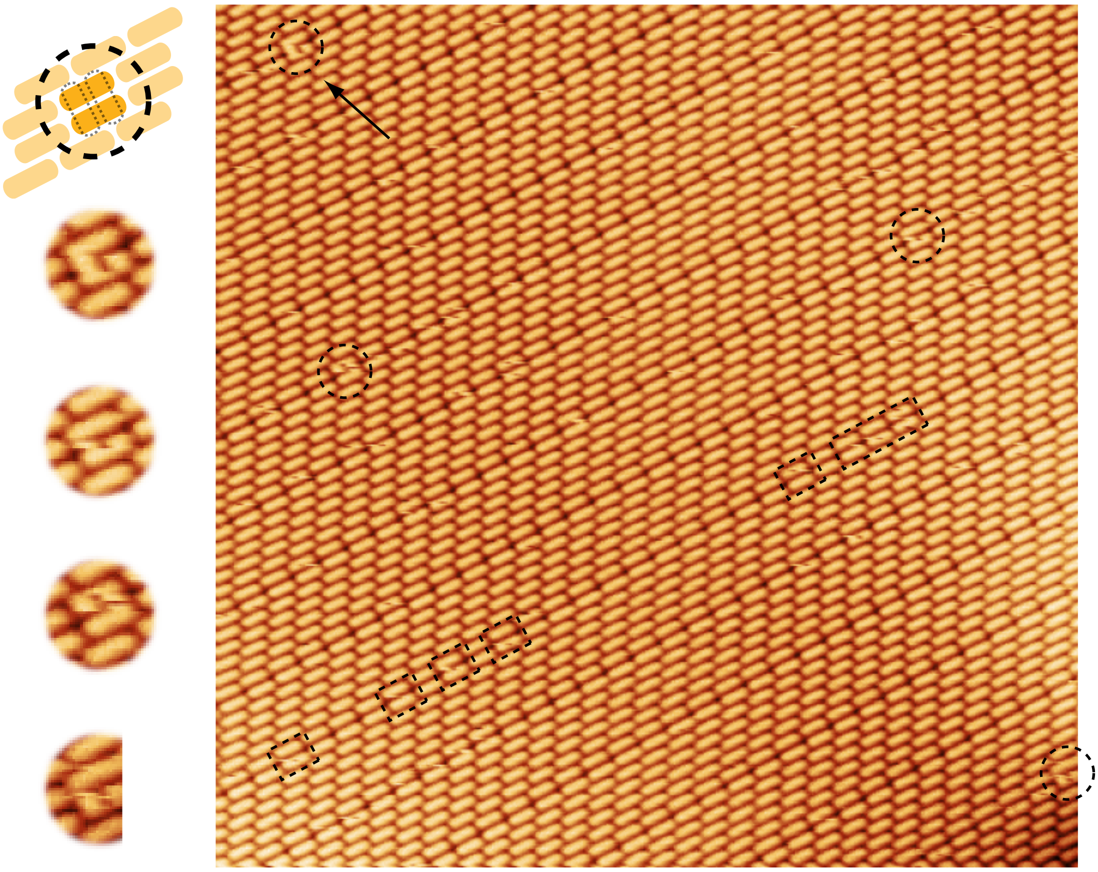

Figure A.1: Rectangles mark the PFP pairs that present streak lines, along one of the dislocation lines. Circles mark pairs that remain flipped long enough to partly image the flipped state and are shown to the left.

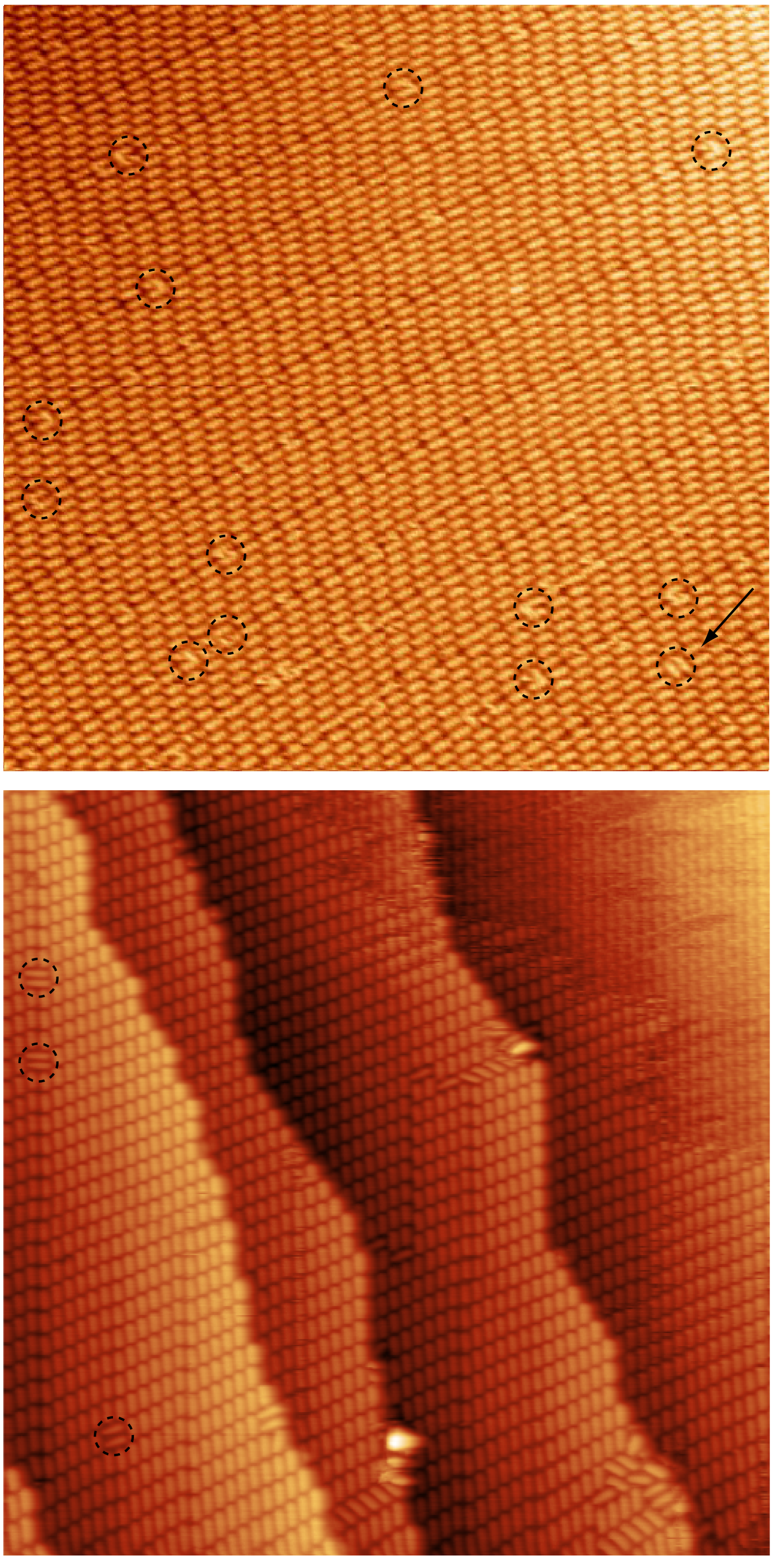

Figure A.2: An image taken at higher scan speeds allows imaging parts of the flipped state more often. The flipped conformation seems to be more stable on the second layer.

A.3 STM Gallery and Summary of Unit Cell Parameters

The experimental and modeled unit cell parameters of the different systems are summarized in Tables A.1, A.2 and A.3.

Fig. A.3 shows STM images of all the structures presented in Chapter 4.

Ag(111):	CuPc	PFP	Mix
Experiment	$a = (14.1 \pm 0.8)\,\text{Å}$ $b = (13.9 \pm 0.7)\,\text{Å}$ $\alpha = (88 \pm 4)^\circ$	$a = (8.8 \pm 0.9)\,\text{Å}$ $b = (17 \pm 1)\,\text{Å}$ $\alpha = (62 \pm 2)^\circ$	$a = (22 \pm 2)\,\text{Å}$ $b = (29.3 \pm 0.6)\,\text{Å}$ $\alpha = (89 \pm 6)^\circ$
Model	$a = 13.3\,\text{Å}$ $b = 14.5\,\text{Å}$ $\alpha = 90^\circ$	$a = 8.4\,\text{Å}$ $b = 17.3\,\text{Å}$ $\alpha = 62^\circ$	$a = 22.5\,\text{Å}$ $b = 28.9\,\text{Å}$ $\alpha = 90^\circ$
	$\begin{matrix} 5/3 & 0 \\ 0 & 8/3 \end{matrix}$	—	$\begin{matrix} 8 & 0 \\ 0 & 6 \end{matrix}$

Table A.1: Summary of results for CuPc+PFP/Ag(111). Experimental and model unit cell parameters, along with proposed epitaxy matrix (base vectors: $(\bar{1}\,1\,0)$ and $(1\,1\,\bar{2})$).

Cu(111):	CuPc	PFP	Mix
Experiment	$a = (13.2 \pm 0.6)\,\text{Å}$ $b = (13.4 \pm 0.6)\,\text{Å}$ $\alpha = (89 \pm 3)^\circ$	$a = (9.2 \pm 0.9)\,\text{Å}$ $b = (17 \pm 1)\,\text{Å}$ $\alpha = (65 \pm 7)^\circ$	$a = (21 \pm 1)\,\text{Å}$ $b = (27 \pm 2)\,\text{Å}$ $\alpha = (89 \pm 5)^\circ$
Model	$a = 13.6\,\text{Å}$ $b = 13.4\,\text{Å}$ $\alpha = 91^\circ$	$a = 9\,\text{Å}$ $b = 17.9\,\text{Å}$ $\alpha = 60^\circ$	$a = 22.2\,\text{Å}$ $b = 28.2\,\text{Å}$ $\alpha = 90^\circ$
	—	—	$\begin{matrix} 0 & 5 \\ 11 & 0 \end{matrix}$

Table A.2: Summary of results for CuPc+PFP/Cu(111). Experimental and model unit cell parameters, along with proposed epitaxy matrix (base vectors: $(\bar{1}\,1\,0)$ and $(1\,1\,\bar{2})$).

Ag(111):	FCuPc (A)	FCuPc (B)	PEN	Mix
Experiment	$a = (15 \pm 1)\,\text{Å}$; $b = (16 \pm 1)\,\text{Å}$; $\alpha = (71 \pm 4)^\circ$;	$a' = (15 \pm 1)\,\text{Å}$ $b' = (15 \pm 1)\,\text{Å}$ $\alpha' = (89 \pm 7)^\circ$	$a = (7.3 \pm 0.5)\,\text{Å}$ $b_\perp = (15.3 \pm 0.5)\,\text{Å}$	$a = (24 \pm 1)\,\text{Å}$ $b = (27 \pm 2)\,\text{Å}$ $\alpha = (92 \pm 5)^\circ$
Model	$a = 15.0\,\text{Å}$; $b = 15.3\,\text{Å}$; $\alpha = 71^\circ$;	$a' = 15.0\,\text{Å}$ $b' = 15.0\,\text{Å}$ $\alpha' = 90^\circ$	—	$a = 23.1\,\text{Å}$ $b = 30.0\,\text{Å}$ $\alpha = 90^\circ$
	$\begin{matrix} 0 & 3 \\ 5 & 1 \end{matrix}$	$\begin{matrix} 0 & 3 \\ 5 & 0 \end{matrix}$	—	$\begin{matrix} 8 & 0 \\ 0 & 6 \end{matrix}$

Table A.3: Summary of results for PEN+FCuPc/Ag(111). Experimental and model unit cell parameters, along with proposed epitaxy matrix (base vectors: $(\bar{1}\,1\,0)$ and $(1\,1\,\bar{2})$).

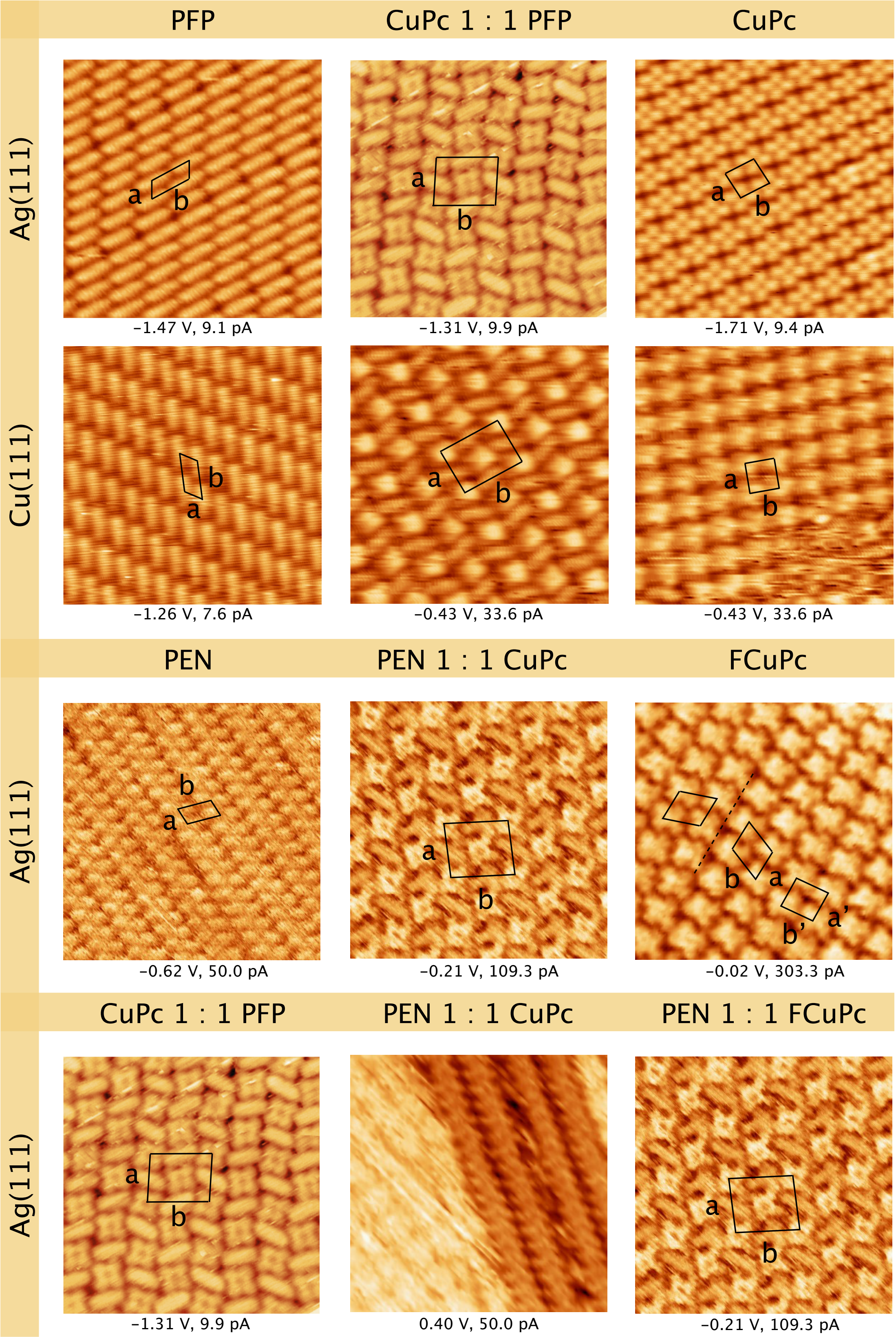

Figure A.3: 11.5 nm×11.5 nm images of pure component and 1:1 mixes on Ag(111) and Cu(111).

A.4 XPS Fit Parameters

The core-level (C.L.) binding energies obtained from the XPS fits of Chapter 5 are presented in Table. A.4.

	CuPc+PFP/Ag(111)		CuPc+PFP/Cu(111)		FCuPc+PEN/Ag(111)	
C.L.	Single	Mix	Single	Mix	Single	Mix
$C_{H/F}$	284.47	284.45	284.14	284.13	287.14	287.25
C_C	285.15	285.13	284.51	284.51	284.90	284.90
C_N	286.11	286.08	285.26	285.26	286.01	285.97
N	398.73	398.75	398.36	398.36	398.91	398.84
F	687.58	687.62	687.30	687.57	687.39	687.66
C_C	285.96	286.21	285.63	285.94	284.85	284.60
$C_{F/H}$	287.44	287.80	287.15	287.45	284.85	284.60

Table A.4: Binding energies of fitted peaks for the three systems studied in Chapter 5. All values in eV.

A.5 Beam Damage

During the XSW (also XPS) measurements, care had to be taken to avoid sample degradation. It was observed that an irradiation time of about 15 minutes already led to appreciable damage in the form of shifts of core-levels to higher binding energy and broadening. Sample degradation by ionizing radiation has already been reported on, in particular that of fluorinated compounds [151; 176; 177]. Indeed, the effects of the beam were particularly noticeable PFP's core-levels: the F_{1s} level showed the largest shifts and broadening, as well a decrease in intensity and the appearance of a new feature at lower binding energy. The C_{1s} level likewise showed large shifts, and a new feature at higher binding energy. After dividing the spectra by the standing wave field intensity (to remove the effect of the varying photon intensity), the area of the C_F peak is found to diminish. These effects can be seen in Fig. A.4.

Thermal desorption studies of PFP have shown this molecule to be a lot less stable than its unfluorinated analogue PEN [151].

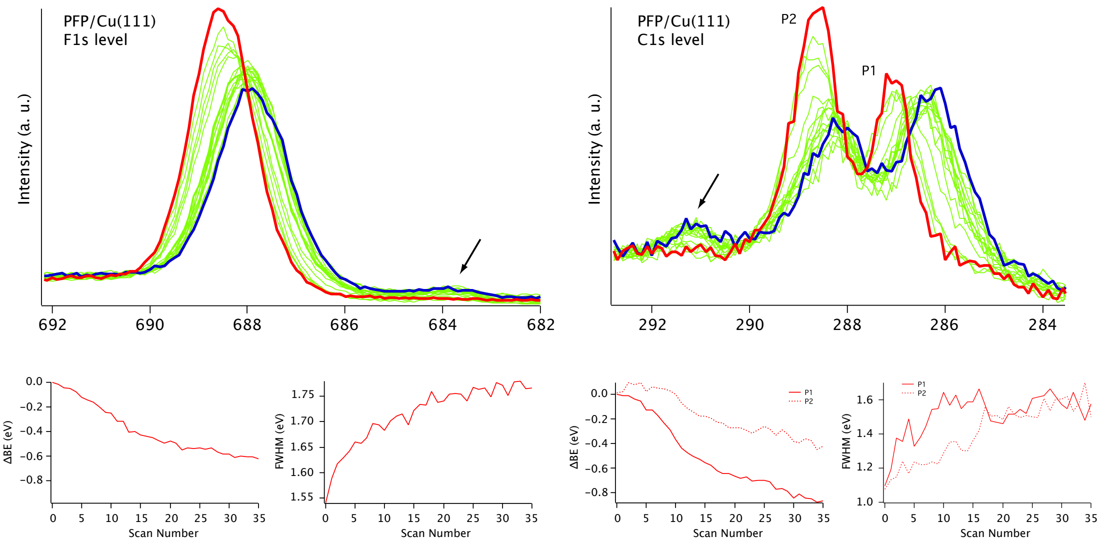

Figure A.4: 36 consecutive XPS runs on PFP/Cu(111) sample show a clear shift of the F_{1s} (left) and C_{1s} (right) levels to lower binding energy, as well as the appearance of new features (marked by arrows). The smaller graphs below show the shift in binding energy (BE) and the evolution of the FWHM.

The effect of the beam damage on the coherent position and fraction was evaluated for both molecules by taking several successive XSW measurements of F_{1s} and N_{1s} at the same position on the sample (only the first of which was used for the actual determination of the adsorption height z). As previously observed by Henze et al. [157], the coherent fraction shows a general decrease. The coherent position however, remained approximately constant in the case of CuPc (i.e. nitrogen), while it decreased as a function of exposure time in the case of PFP, further evidence of the sensitivity of this molecule. These results can be seen in Fig. A.5. Interestingly, it appears that the effect of beam damage of the molecules is much less pronounced in the case of Ag(111) (hollow markers). Though the coherent fraction shows a decrease, the coherent position remains quite unaffected by the x-ray exposure.

In the study by Henze et al. [157], the coherent position of PTCDA on Au(111) remained constant at first, but began to decrease after about 90 minutes of x-ray exposure. This suggests that longer exposure times might have eventually caused a decrease in the coherent position of CuPc as well.

A possible consequence of the beam may be de deflourination of PFP. In the study on the thermal stability of PFP by Schmidt et al. [151] defluorination is found to produce a buckling of the molecule due to a stronger bond between the deflourinated carbon atom and the metal. This buckling is a possible explanation for the decrease in coherent fraction with increasing exposure time, as well as the decreasing coherent position.

The study of Henze et al. [157] mentions that the damage observed for PTCDA on Au(111) was not observed on the Ag(111) substrate, supporting the idea that it is the photoelectron yield from the substrate (as opposed to direct x-ray exposure) that causes the degradation of the layer, as has been proposed in several studies. [151; 177; 178]. Indeed, photoelectron cross-sections for photon energies in this range (2.5 keV) are considerably larger for Au than for Ag [179].

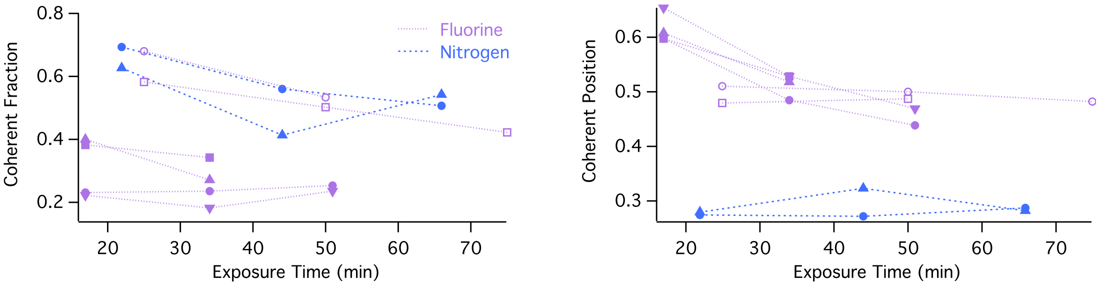

Figure A.5: Consecutive runs on the same spot on a CuPc+PFP sample a decrease of the coherent fraction and position. The differently shaped data points correspond to runs on different areas. Filled markers are for the Cu(111) sample, hollow ones are for Ag(111). The effect on Cu(111) is more pronounced than on Ag(111).

Appendix B

Abbreviations

CNL Charge neutrality level

CuPc Copper phthalocyanine

DOS Density of states

FCuPc $F_{16}CuPc$, perfluorinated copper phthalocyanine

FWHM Full width at half maximum

HOMO Highest occupied molecular orbital

IDIS Induced density of interface states

LT Low temperature

LUMO Lowest unoccupied molecular orbital

ML Monolayer

NEXAFS Near-edge x-ray absorption fine structure

PEN $C_{22}H_{14}$, pentacene

PES Photoelectron spectroscopy

PFP $C_{22}F_{14}$, perfluorinated pentacene

RT Room temperature

STM Scanning tunneling microscopy

UHV Ultra-high vacuum

UPS Ultraviolet photoelectron spectroscopy

VLP Vacuum level pinning

XPS X-ray photoelectron spectroscopy

XSW X-ray standing waves

References

[1] N. Koch. **Organic Electronic Devices and Their Functional Interfaces**. *ChemPhysChem*, **8**(10):1438, 2007.

[2] **Heliatek consolidates its technology leadership by establishing a new world record for organic solar technology with a cell efficiency of 12%**. Heliatek. Dresden, Germany (January 2013).

[3] W. Ho. **Single-Molecule chemistry**. *J. Chem. Phys.*, **117**:11033, 2002.

[4] D. G. de Oteyza, P. Gorman, Y.-C. Chen, S. Wickenburg, A. Riss, D. J. Mowbray, G. Etkin, Z. Pedramrazi, H.-Z. Tsai, A. Rubio, M. F. Crommie, and F. R. Fischer. **Direct Imaging of Covalent Bond Structure in Single-Molecule Chemical Reactions**. *Science*, **340**(6139):1434, 2013.

[5] J. V. Barth, G. Costantini, and K. Kern. **Engineering atomic and molecular nanostructures at surfaces**. *Nature*, **437**:671, 2005.

[6] J. V. Barth. **Molecular Architectonic on Metal Surfaces**. *Annu. Rev. Phys. Chem.*, **58**:375, 2007.

[7] K. W. Kolasinksi. **Surface Science: Foundation of Catalysis and Nanoscience, 2nd Ed.** Wiley & Sons Ltd., 2008.

[8] D. G. de Oteyza. **Multicomponent assembly strategies for supramolecular systems**. In N. Koch, editor, *Supramolecular Materials for Opto-Electronics.* Royal Society of Chemistry, 2014.

[9] X. Qiu, C. Wang, S. Yin, Q. Zeng, B. Xu, and C. Bai. **Self-Assembly and Immobilization of Metallophthalocyanines by Alkyl Substituents**

Observed with Scanning Tunneling Microscopy. *J. Phys. Chem. B*, **104**(15):3570, 2000.

[10] K. Autumn, M. Sitti, Y. A. Liang, A. M. Peattie, W. R. Hansen, S. Sponberg, T. W. Kenny, R. Fearing, J. N. Israelachvili, and R. J. Full. **Evidence for van der Waals adhesion in gecko setae**. *PNAS*, **99**(19):12252, 2002.

[11] M. F. Crommie, C. P. Lutz, and D. M. Eigler. **Imaging standing waves in a two-dimensional electron gas**. *Nature*, **363**:524, 1993.

[12] E. C. H. Sykes, P. Han, S. A. Kandel, K. F. Kelly, G. S. McCarty, and P. S. Weiss. **Substrate-Mediated Interactions and Intermolecular Forces between Molecules Adsorbed on Surfaces**. *Acc. Chem. Res.*, **36**(12):945, 2003.

[13] D. Wegner, R. Yamachika, Y. Wang, V. W. Brar, B. M. Bartlett, J. R. Long, and M. F. Crommie. **Single-Molecule Charge Transfer and Bonding at an Organic/Inorganic Interface: Tetracyanoethylene on Noble Metals**. *Nano Lett.*, **8**(1):131, 2008. PMID: 18069869.

[14] A. E. Baber, S. C. Jensen, and E. C. H. Sykes. **Dipole-Driven Ferroelectric Assembly of Styrene on Au(111)**. *J. Am. Chem. Soc.*, **129**(20):6368, 2007. PMID: 17472383.

[15] M. de Wild. **Novel Principle for 2D Molecular Self-Assembly: Self-Intermixed Monolayer Phases of Sub-Phthalocyanine and C60 on Ag(111)**. PhD thesis, Uni Basel, 2002.

[16] D. G. de Oteyza, E. Barrena, H. Dosch, J. E. Ortega, and Y. Wakayama. **Tunable symmetry and periodicity in binary supramolecular nanostructures**. *Phys. Chem. Chem. Phys.*, **13**:4220, 2011.

[17] K.-O. Ng and D. Vanderbilt. **Stability of periodic domain structures in a two-dimensional dipolar model**. *Phys. Rev. B*, **52**:2177, Jul 1995.

[18] M. Matena, M. Stöhr, T. Riehm, J. Björk, S. Martens, M. S. Dyer, M. Persson, J. Lobo-Checa, K. Müller, M. Enache, H. Wadepohl, J. Zegenhagen, T. A. Jung,

and L. H. Gade. **Aggregation and Contingent Metal/Surface Reactivity of 1,3,8,10-Tetraazaperopyrene (TAPP) on Cu(111)**. *Chemistry - A European Journal*, **16**(7):2079, 2010.

[19] S. Stepanow, N. Lin, D. Payer, U. Schlickum, F. Klappenberger, G. Zoppellaro, M. Ruben, H. Brune, J. V. Barth, and K. Kern. **Surface-Assisted Assembly of 2D Metal-Organic Networks That Exhibit Unusual Threefold Coordination Symmetry**. *Angew. Chem. Int. Ed.*, **46**(5):710, 2007.

[20] A. Langner, S. L. Tait, N. Lin, C. Rajadurai, M. Ruben, and K. Kern. **Self-recognition and self-selection in multicomponent supramolecular coordination networks on surfaces**. *PNAS*, **104**:17927, 2007.

[21] G. R. Desiraju. **Hydrogen Bridges in Crystal Engineering: Interactions without Borders**. *Acc. Chem. Res.*, **35**(7):565, 2002. PMID: 12118996.

[22] T. Steiner. **The Hydrogen Bond in the Solid State**. *Angew. Chem. Int. Ed.*, **41**(5036):48, 2002.

[23] G. Pawin, K. L. Wong, K.-Y. Kwon, and L. Bartels. **A Homomolecular Porous Network at a Cu(111) Surface**. *Science*, **313**(5789):961, 2006.

[24] L. M. A. Perdigao, N. R. Champness, and P. H. Beton. **Surface self-assembly of the cyanuric acid-melamine hydrogen bonded network**. *Chem. Commun.*, pages 538–540, 2006.

[25] Y. L. Huang, W. Chen, H. L., J. Ma, J. Pflaum, and A. T. S. Wee. **Tunable Two-Dimensional Binary Molecular Networks**. *Small*, **6**(37):70, 2010.

[26] J. A. Theobald, N. S. Oxtoby, M. A. Phillips, N. R. Champness, and P. H. Beton. **Controlling molecular deposition and layer structure with supramolecular surface assemblies**. *Nature*, **424**:1029, 2003.

[27] D. E. Hooks, T. Fritz, and M. D. Ward. **Epitaxy and Molecular Organization on Solid Substrates**. *Adv. Mater.*, **13**(4):227, 2001.

[28] H. Ishii, K. Sugiyama, E. Ito, and K. Seki. **Energy Level Alignment and Interfacial Electronic Structures at Organic/Metal and Organic/Organic Interfaces**. *Adv. Mater.*, **11(8)**:605, 1999.

[29] H. Vázquez, Y. J. Dappe, J. Ortega, and F. Flores. **Energy level alignment at metal/organic semiconductor interfaces: Pillow effect, induced density of interface states, and charge neutrality level**. *J. Chem. Phys.*, **126**:144703, 2007.

[30] M. G. Betti, A. Kanjilal, C. Mariani, H. Vázquez, Y. J. Dappe, J. Ortega, and F. Flores. **Barrier Formation at Organic Interfaces in a Cu(100)-benzenethiolate-pentacene Heterostructure**. *Phys. Rev. Lett.*, **100**:027601, Jan 2008.

[31] J. Hwang, A. Wan, and A. Kahn. **Energetics of metal-organic interfaces: New experiments and assessment of the fields**. *Mat. Sci. Eng. R*, **64**:1, 2009.

[32] I. G. Hill, A. Rajagopal, A. Kahn, and Y. Hu. **Molecular level alignment at organic semiconductor-metal interfaces**. *Appl. Phys. Lett.*, **73**:662, 1998.

[33] F. Babudri, G. M. Farinola, F. Naso, and R. Ragnia. **Fluorinated organic materials for electronic and optoelectronic applications: the role of the fluorine atom**. *Chem. Commun.*, **10**:1003, 2006.

[34] G. Löbbert. **Phthalocyanines**. In *Ullmann's Encyclopedia of Industrial Chemistry*. Wiley-VCH Verlag GmbH & Co. KGaA, 2002.

[35] Z. Bao, A. J. Lovinger, and A. Dodabalapur. **Organic field-effect transistors with high mobility based on copper phthalocyanine**. *Appl. Phys. Lett.*, **69**:3066, 1996.

[36] L. Zou, V. Savvateev, J. Booher, C.-H. Kim, and J. Shinar. **Combinatorial fabrication and studies of intense efficient ultraviolet-violet organic light-emitting device arrays**. *Appl. Phys. Lett.*, **79**:2282, 2001.

[37] C. Zhang, S. W. Tong, C. Jiang, E. T. Kang, D. S. H. Chan, and C. Zhu. **Efficient multilayer organic solar cells using the optical interference peak**. *Appl. Phys. Lett.*, **93**:043307, 2008.

[38] W. H. Mills and M. Mills. **CCXXX.-The synthetical production of derivatives of dinaphthanthracene**. *J. Chem. Soc., Trans.*, **101**:2194, 1912.

[39] C. D. Dimitrakopoulos, I. Kymissis, S. Purushothaman, D. A. Neumayer, P. R. Duncombe, and R. B. Laibowitz. **Low-Voltage, High-Mobility Pentacene Transistors with Solution-Processed High Dielectric Constant Insulators**. *Adv. Mater.*, **11**(16):1372, 2009.

[40] M. C. Ruiz Delgado, K. R. Pigg, D. A. da Silva Filho, N. E. Gruhn, Y. Sakamoto, T. Suzuki, R. M. Osuna, J. Casado, V. Hernández, J. T. L. Navarrete, N. G. Martinelli, J. Cornil, R. S. Sánchez-Carrera, V. Coropceanu, and J.-L. Brédas. **Impact of Perfluorination on the Charge-Transport Parameters of Oligoacene Crystals**. *J. Am. Chem. Soc.*, **131**(4):1502, 2009.

[41] Y. Sakamoto, T. Suzuki, M. K., Y. Gao, Y. Fukai, Y. Inoue, F. Sato, and S. Tokito. **Perfluoropentacene: High-Performance p-n Junctions and Complementary Circuits with Pentacene**. *J. Am. Chem. Soc.*, **126**(26):8138, 2004.

[42] C. Klauber. **UHV Basics**. In D. J. O'Connor, B. A. Sexton, and R. S. C. Smart, editors, *Surface Analysis Methods in Materials Science*. Springer, 2003.

[43] C. J. Chen. **Introduction to Scanning Tunneling Microscopy**. Oxford University Press, 1993.

[44] C. Bai. **Scanning Tunneling Microscopy and Its Applications**. Springer, 2000.

[45] J. Bardeen. **Tunnelling from a Many-Particle Point of View**. *Phys. Rev. Lett.*, **6**(2):57, 1961.

[46] A. Gottlieb and L. Wesoloski. **Bardeen's tunnelling theory as applied to scanning tunnelling microscopy: a technical guide to the traditional interpretation**. *Nanotechnology*, **17**(8):R57, 2006.

[47] C. J. Chen. **Origin of atomic resolution on metal surfaces in scanning tunneling microscopy**. *Phys. Rev. Lett.*, **65**(4):448, 1990.

[48] J. Tersoff and D. R. Hamann. **Theory and Application for the Scanning Tunneling Microscope**. *Phys. Rev. Lett.*, **50**(25):1998, 1983.

[49] A. Baratoff. **Theory of scanning tunneling microscopy – methods and approximations**. *Physica B+C*, **127**(1-3):143, 1984. Proceedings of the 4th General Conference of the Condensed Matter Division of the EPS.

[50] S. Ohnishi and M. Tsukada. **Molecular Orbital Theory for Scanning Tunneling Microscopy**. *Solid State Commun.*, **71**:391, 1989.

[51] N. D. Lang. **Theory of Single-Atom Imaging in the Scanning Tunneling Microscope**. *Phys. Rev. Lett.*, **56**(11):1164, 1986.

[52] P. Sautet. **Atomic adsorbate identification with the STM: a theoretical approach**. *Surf. Sci.*, **374**(1-3):406, 1997.

[53] J. Wintterlin, R. Schuster, and G. Ertl. **Existence of a 'Hot' Atom Mechanism for the Dissociation of O_2 on Pt(111)**. *Phys. Rev. Lett.*, **77**(1):123, 1996.

[54] M. O. Pedersen, L. Österlund, J. J. Mortensen, M. Mavrikakis, L. B. Hansen, I. Stensgaard, E. Lægsgaard, J. K. Nørskov, and F. Besenbacher. **Diffusion of N Adatoms on the Fe(100) Surface**. *Phys. Rev. Lett.*, **84**(21):4898, 2000.

[55] R. Wiesendanger. **Scanning Probe Microscopy and Spectroscopy: Methods and Applications**. Cambridge University Press, 1994.

[56] C. J. Villagomez, T. Zambelli, S. Gauthier, A.Gourdon, S. Stojkovic, and C. Joachim. **STM images of a large organic molecule adsorbed on a bare metal substrate or on a thin insulating layer: Visualization of HOMO and LUMO**. *Surf. Sci.*, **603**(10-12):1526, 2009.

[57] K. Oura, M. Katayama, A. V. Zotov, V. G. Lifshits, and A. A. Saranin. **Surface Science: An Introduction**. Springer, 2003.

[58] J. J. Yeh. **Atomic Calculation of Photoionization Cross-Sections and Asymmetry Parameters**. Gordon and Breach Science Publishers, Langhorne, PE (USA), 1993.

[59] S. Hüfner. **Photoelectron Spectroscopy - Principles and Applications**. Springer, 2003.

[60] F. Himpsel. **Angle-resolved measurements of the photoemission of electrons in the study of solids**. *Advances in Physics*, **32**(1):1, 1983.

[61] K. Wandelt, editor. **Surface and Interface Science: Vol 1 Concepts and Methods**. Wiley-VCH Verlag GmbH & Co. KGaA, 2012.

[62] G. Hähner. **Near edge X-ray absorption fine structure spectroscopy as a tool to probe electronic and structural properties of thin organic films and liquids**. *Chem. Soc. Rev.*, **35**:1244, 2006.

[63] A. Authier. **Dynamical Theory of X-Ray Diffraction**. Oxford University Press, 2004.

[64] J. Zegenhagen. **Surface structure determination with X-ray standing waves**. *Surf. Sci. Rep.*, **18**(7-8):202, 1993.

[65] D. P. Woodruff. **Surface structure determination using x-ray standing waves**. *Rep. Prog. Phys.*, **68**(4):743, 2005.

[66] J. A. Golovchenko, B. W. Batterman, and W. L. Brown. **Observation of internal x-ray wave fields during Bragg diffraction with an application to impurity lattice location**. *Phys. Rev. B*, **10**:4239, Nov 1974.

[67] P. L. Cowan, J. A. Golovchenko, and M. F. Robbins. **X-Ray Standing Waves at Crystal Surfaces**. *Phys. Rev. Lett.*, **44**:1680, Jun 1980.

[68] D. P. Woodruff. **Normal incidence X-ray standing wave determination of adsorbate structures**. *Prog. Surf. Sci.*, **57**:1, 1998.

[69] A. Gerlach, F. Schreiber, S. Sellner, H. Dosch, I. A. Vartanyants, B. C. C. Cowie, T.-L. Lee, and J. Zegenhagen. **Adsorption-induced distortion of F_{16}CuPc on Cu(111) and Ag(111): An x-ray standing wave study**. *Phys. Rev. B*, **71**:205425, 2005.

[70] J. P. Rabe and S. Buchholz. **Commensurability and Mobility in Two-Dimensional Molecular Patterns on Graphite**. *Science*, **253**(5018):424, 1991.

[71] R. Strohmaier, L. C., J. Petersen, B. Gompf, and E. W. **STM investigations of C_6Br_6 on HOPG and MoS_2**. *Scuface Science Letters*, **318**:L1181, 1994.

[72] J. A. hlund, J. Schnadt, K. Nilson, E. Göthelid, J. Schiessling, F. Besenbacher, N. M. rtensson, and C. Puglia. **The adsorption of iron phthalocyanine on graphite: A scanning tunnelling microscopy study**. *Surface Science*, **601**(17):3661 , 2007.

[73] B. Ilan, G. M. Florio, M. S. Hybertsen, B. J. Berne, and G. W. Flynn. **Scanning Tunneling Microscopy Images of Alkane Derivatives on Graphite: Role of Electronic Effects**. *Nano Letters*, **8**(10):3160, 2008. PMID: 18798685.

[74] V. Oison, M. Koudia, M. Abel, and L. Porte. **Influence of stress on hydrogen-bond formation in a halogenated phthalocyanine network**. *Phys. Rev. B*, **75**(3):035428, 2007.

[75] Y. Wei and J. Robey, S.W.AND Reutt-Robey. **TiOPc Molecular Dislocation Networks as Nanotemplates for C_60 Cluster Arrays**. *J. Am. Chem. Soc.*, **131**:12026, 2009.

[76] T.-C. Tseng, C. Urban, Y. Wang, R. Otero, S. L. Tait, M. Alcamí, D. Écija, M. Trelka, J. M. Gallego, N. Lin, M. Konuma, U. Starke, A. Nefedov, L. Alexander, C. Wöll, M. A. Herranz, F. Martín, N. Martín, K. Kern, and R. Miranda. **Charge-transfer-induced structural rearrangements at both sides oforganic/metal interfaces**. *Nature Chemistry*, **2**:374, 2010.

[77] J. Götzen, C. H. Schwalb, C. Schmidt, G. Mette, M. Marks, U. Höfer, and G. Witte. **Structural Evolution of Perfluoro-Pentacene Films on Ag(111): Transition from 2D to 3D Growth**. *Langmuir*, **27(3)**:993, 2011.

[78] E. Goiri, J. M. García-Lastra, M. Corso, Z. M. Adb El-Fattah, J. E. Ortega, and D. G. de Oteyza. **Understanding Periodic Dislocations in 2D Supramolecular Crystals: The PFP/Ag(111) Interface**. *J. Phys. Chem. Lett.*, **3**(7):848, 2012.

[79] S. L. Wong, H. Huang, Y. L. Huang, Y. Z. Wang, X. Y. Gao, T. Suzuki, W. Chen, and A. T. S. Wee. **Effect of Fluorination on the Molecular Packing of**

Perfluoropentace and Pentacene Ultrathin Films on Ag(111). *J. Phys. Chem. C*, **114**:9356, 2010.

[80] J. Enkovaara, C. Rostgaard, J. J. Mortensen, J. Chen, M. Dułak, L. Ferrighi, J. Gavnholt, C. Glinsvad, V. Haikola, H. A. Hansen, H. H. Kristoffersen, M. Kuisma, A. H. Larsen, L. Lehtovaara, M. Ljungberg, O. López-Acevedo, P. G. Moses, J. Ojanen, T. Olsen, V. Petzold, N. A. Romero, J. Stausholm-Møller, M. Strange, G. A. Tritsaris, M. Vanin, M. Walter, B. Hammer, H. Häkkinen, G. K. H. Madsen, R. M. Nieminen, J. K. Nørskov, M. Puska, T. T. Rantala, J. Schiøtz, K. S. Thygesen, and K. W. Jacobsen. **Electronic structure calculations with GPAW: a real-space implementation of the projector augmented-wave methods**. *J. Phys.: Condens. Matter*, **22**:253202, 2010.

[81] J. P. Perdew and A. Zunger. **Self-interaction correction to density-functional approximations for many-electron systems**. *Phys. Rev. B*, **23**:5048, May 1981.

[82] J. P. Perdew, K. Burke, and M. Ernzerhof. **Generalized Gradient Approximation Made Simple**. *Phys. Rev. Lett.*, **77**:3865, Oct 1996.

[83] M. Dion, H. Rydberg, E. Schröder, D. C. Langreth, and B. I. Lundqvist. **Van der Waals Density Functional for General Geometries**. *Phys. Rev. Lett.*, **92**:246401, Jun 2004.

[84] S. Grimme. **Semiempirical GGA-type density functional constructed with a long-range dispersion correction**. *J. Comput. Chem.*, **27**(15):1787, 2006.

[85] K. Toyoda, I. Hamada, K. Lee, S. Yanagisawa, and Y. Morikawa. **Density functional theoretical study of pentacene/noble metal interfaces with van der Waals corrections: Vacuum level shifts and electronic structures**. *J. Chem. Phys.*, **132**(13):134703, 2010.

[86] K. Toyoda, I. Hamada, K. Lee, S. Yanagisawa, and Y. Morikawa. **Density Functional Theoretical Study of Perfluoropentacene/Noble Metal Interfaces with van der Waals Corrections: Adsorption States and Vacuum Level Shifts**. *J. Phys. Chem. C*, **115**(13):5767, 2011.

[87] M. Vanin, J. J. Mortensen, A. K. Kelkkanen, J. M. García-Lastra, K. S. Thygesen, and K. W. Jacobsen. **Graphene on metals: A van der Waals density functional study**. *Phys. Rev. B*, **81**:081408, Feb 2010.

[88] J. Wellendorff, A. Kelkkanen, J. J. Mortensen, B. I. Lundqvist, and T. Bligaard. **RPBE-vdW Description of Benzene Adsorption on Au(111)**. *Top. Catal.*, **53**:378, 2010.

[89] S. Duhm, S. Hosoumi, I. Salzmann, A. Gerlach, M. Oehzelt, B. Wedl, T.-L. Lee, F. Schreiber, N. Koch, N. Ueno, and S. Kera. **Influence of intramolecular polar bonds on interface energetics in perfluoro-pentacene on Ag(111)**. *Phys. Rev. B*, **81**(4):045418, Jan 2010.

[90] C. B. France, P. G. Schroeder, J. C. Forsythe, and B. A. Parkinson. **Scanning Tunneling Microscopy Study of the Coverage-Dependent Structures of Pentacene on Au(111)**. *Langmuir*, **19**(4):1274, 2003.

[91] E. C. H. Sykes, B. A. Mantooth, P. Han, Z. J. Donhauser, and P. S. Weiss. **Substrate-Mediated Intermolecular Interactions: A Quantitative Single Molecule Analysis**. *J. Am. Chem. S.*, **127**(19):7255, 2005. PMID: 15884967.

[92] D. Syomin, J. Kim, B. E. Koel, and G. B. Ellison. **Identification of Adsorbed Phenyl (C_6H_5) Groups on Metal Surfaces: Electron-Induced Dissociation of Benzene on Au(111)**. *J. Phys. Chem. B*, **105**(35):8387, 2001.

[93] M. Marks, C. Schmidt, C. H. Schwalb, T. Breuer, G. Witte, and U. Höfer. **Temperature Dependent Structural Phase Transition at the Perfluoropentacene/Ag(111) Interface**. *J. Phys. Chem. C*, **116**(2):1904, 2012.

[94] I. Horcas, R. Fernández, J. M. Gómez-Rodríguez, J. Colchero, J. Gómez-Herrero, and A. M. Baro. **WSXM: A software for scanning probe microscopy and a tool for nanotechnology**. *Rev. Sci. Instrum.*, **78**(1):013705, 2007.

[95] D. Nečas and P. Klapetek. **Gwyddion: an open-source software for SPM data analysis**. *Cent. Eur. J. Phys.*, **10**:181, 2012.

[96] K. Manandhar, T. Ellis, K. Park, T. Cai, Z. Song, and J. Hrbek. **A scanning tunneling microscopy study on the effect of post-deposition annealing of copper phthalocyanine thin films**. *Surf. Sci.*, **601**(17):3623, 2007.

[97] J.-Y. Grand, T. Kunstmann, D. Hoffmann, A. Haas, J. S. M. Dietsche, and R. Möller. **Epitaxial growth of copper phthalocyanine monolayers on Ag(111)**. *Surf. Sci.*, **366**:403, 1996.

[98] I. Kröger, B. Stadtmüller, C. Stadler, J. Ziroff, M. Kochler, A. Stahl, F. Pollinger, T.-L. Lee, J. Zegenhagen, F. Reinert, and C. Kumpf. **Submonolayer growth of copper-phthalocyanine on Ag(111)**. *New J. Phys.*, **12**:083038, 2010.

[99] M. Lackinger and M. Hietschold. **Determining adsorption geometry of individual tinphthalocyanine molecules on Ag(111)a STM study at submonolayer coverage**. *Surf. Sci.*, **520**(1-2):L619, 2002.

[100] I. Chizhov, G. Scoles, and A. Kahn. **The Influence of Steps on the Orientation of Copper Phthalocyanine Monolayers on Au(111)**. *Langmuir*, **16**(9):4358, 2000.

[101] Y. Wakayama. **Assembly Process and Epitaxy of the F_{16}CuPc Monolayer on Cu(111)**. *J. Phys. Chem. C*, **111**:2675, 2007.

[102] H. Huang, W. Chen, and A. T. S. Wee. **Low-Temperature Scanning Tunneling Microscopy Investigation of Epitaxial Growth of F_{16}CuPc Thin Films on Ag(111)**. *J. Phys. Chem. C*, **112**(38):14913, 2008.

[103] H. Karacuban, M. Lange, J. Schaffert, O. Weingart, T. Wagner, and R. Müller. **Substrate-induced symmetry reduction of CuPc on Cu(111): A LT-STM study**. *Surf. Sci.*, **603**(5):L39, 2009.

[104] J. C. Buchholz and G. A. Somorjai. **The surface structures of phthalocyanine monolayers and vapor-grown films: A low-energy electron diffraction study**. *J. Chem. Phys.*, **66**(2):573, 1977.

[105] N. Koch, A. Gerlach, S. Duhm, H. Glowatzki, G. Heimel, A. Vollmer, Y. Sakamoto, T. Suzuki, J. Zegenhagen, J. P. Rabe, and F. Schreiber.

Adsorption-induced intramolecular dipole: Correlating molecular conformation and interface electronic structures. *J. Am. Chem. Soc.*, **130**(23):7300, 2008.

[106] H. Glowatzki, G. Heimel, A. Vollmer, S. L. Wong, H. Huang, W. Chen, A. T. S. Wee, J. P. Rabe, and N. Koch. **Impact of Fluorination on Initial Growth and Stability of Pentacene on Cu(111)**. *J. Phys. Chem. C*, **116**(14):7726, 2012.

[107] A. El-Sayed. **Structure-Dependent Electronic Properties in Donor-Acceptor Assemblies on Metal Surfaces**. PhD thesis, University of the Basque Country (UPV-EHU), 2013.

[108] Y. Wakayama, D. G. de Oteyza, J. M. García-Lastra, and D. J. Mowbray. **Solid-State Reactions in Binary Molecular Assemblies of F_{16}CuPc and Pentacene**. *ACS Nano*, **5**(1):581, 2011.

[109] E. Barrena, D. G. de Oteyza, H. Dosch, and Y. Wakayama. **2D Supramolecular Self-Assembly of Binary Organic Monolayers**. *ChemPhysChem*, **8**(15):1915, 2007.

[110] G. A. Jeffrey. **An Introduction to Hydrogen Bonding**. Oxford University Press, 1997.

[111] A. El-Sayed, P. Borghetti, E. Goiri, C. Rogero, L. Floreano, G. Lovat, D. J. Mowbray, J. L. Cabellos, Y. Wakayama, A. Rubio, J. E. Ortega, and D. G. de Oteyza. **Understanding Energy-Level Alignment in Donor-Acceptor/Metal Interfaces from Core-Level Shifts**. *ACS Nano*, **7**(8):6914, 2013.

[112] Y. L. Huang, H. Li, J. Ma, H. Huang, W. Chen, and A. T. S. Wee. **Scanning Tunneling Microscopy Investigation of Self-Assembled CuPc/F_{16}CuPc Binary Superstructures on Graphite**. *Langmuir*, **26**(5):3329, 2010.

[113] A. El-Sayed, D. J. Mowbray, J. M. García-Lastra, C. Rogero, E. Goiri, P. Borghetti, A. Turak, B. P. Doyle, M. Dell'Angela, L. Floreano, Y. Wakayama, A. Rubio, J. E. Ortega, and D. G. de Oteyza. **Supramolecular Environment-Dependent Electronic Properties of Metal-Organic Interfaces.** *J. Phys. Chem. C*, **116**(7):4780, 2012.

[114] D. G. de Oteyza, A. El-Sayed, J. M. García-Lastra, E. Goiri, T. N. Krauss, A. Turak, E. Barrena, H. Dosch, J. Zegenhagen, A. Rubio, Y. Wakayama, and J. E. Ortega. **Copper-phthalocyanine based metal-organic interfaces: The effect of fluorination, the substrate, and its symmetry**. *J. Chem. Phys.*, **133**:214703, 2010.

[115] M. Eremtchenko, R. Temirov, D. Bauer, J. A. Schaefer, and F. S. Tautz. **Formation of molecular order on a disordered interface layer: Pentacene/Ag(111)**. *Phys. Rev. B*, **72**:115430, Sep 2005.

[116] D. B. Dougherty, W. Jin, W. G. Cullen, J. E. Reutt-Robey, and S. W. Robey. **Variable Temperature Scanning Tunneling Microscopy of Pentacene Monolayer and Bilayer Phases on Ag(111)**. *J. Phys. Chem. C*, **112**(51):20334, 2008.

[117] J. A. Smerdon, M. Bode, N. P. Guisinger, and J. R. Guest. **Monolayer and bilayer pentacene on Cu(111)**. *Phys. Rev. B*, **84**:165436, Oct 2011.

[118] O. McDonald, A. Cafolla, D. Carty, G. Sheerin, and G. Hughes. **Photoemission, NEXAFS and STM studies of pentacene thin films on Au(100)**. *Surface Science*, **600**(16):3217 , 2006.

[119] D. Vanderbilt. **Phase segregation and work-function variations on metal surfaces: spontaneous formation of periodic domain structures**. *Surf. Sci.*, **268**(1-3):L300 , 1992.

[120] A. Opitz, M. Bronner, W. Brütting, M. Himmerlich, J. A. Schaefer, and S. Krischok. **Electronic properties of organic semiconductor blends: Ambipolar mixtures of phthalocyanine and fullerene**. *Appl. Phys. Lett.*, **90**:212112, 2007.

[121] N. Koch, A. Vollmer, S. Duhm, Y. Sakamoto, and T. Suzuki. **The Effect of Fluorination on Pentacene/Gold Interface Energetics and Charge Reorganization Energy**. *Adv. Mater.*, **19**:112, 2007.

[122] J. L. Cabellos, D. J. Mowbray, E. Goiri, A. El-Sayed, L. Floreano, D. G. de Oteyza, C. Rogero, J. E. Ortega, and A. Rubio. **Understanding Charge**

Transfer in Donor–Acceptor/Metal Systems: A Combined Theoretical and Experimental Study. *J. Phys. Chem. C*, **116**(34):17991, 2012.

[123] H. Fukagawa, H. Yamane, S. Kera, K. K. Okudaira, and N. Ueno. **Experimental estimation of the electric dipole moment and polarizability of titanyl phthalocyanine using ultraviolet photoelectron spectroscopy**. *Phys. Rev. B.*, **73**:041302, 2006.

[124] N. J. Watkins, L. Yan, and Y. Gao. **Electronic structure symmetry of interfaces between pentacene and metals**. *Appl. Phys. Lett.*, **80**(23):4384, 2002.

[125] P. Borghetti. *(in preparation)*.

[126] A. El-Sayed, E. Goiri, P. Borghetti, C. Rogero, L. Floreano, Y. Wakayama, J. E. Ortega, and D. G. Oteyza. **Tuning Charge Transfer in Organic Blends on Metal Surfaces**. *(in preparation)*.

[127] A. W. Dweydari and C. H. B. Mee. **Work function measurements on (100) and (110) surfaces of silver**. *phys. stat. sol. (a)*, **27**(1):223, 1975.

[128] S. Duhm, A. Gerlach, I. Salzmann, B. Bröker, R. Johnson, F. Schreiber, and N. Koch. **PTCDA on Au(111), Ag(111) and Cu(111): Correlation of interface charge transfer to bonding distance Original Research Article**. *Organic Electronics*, **9**:111, 2008.

[129] Y. Zou, L. Kilian, A. Schöll, T. Schmidt, R. Fink, and E. Umbach. **Chemical bonding of PTCDA on Ag surfaces and the formation of interface states**. *Surf. Sci.*, **600**(6):1240, 2006.

[130] Y. Y. Tomashpolsky. *Solid Surface Physics. Springer Tracts in Modern Physics. Vol. 85* **edited by G. Höhler**. *Acta Crystallogr. Sec. A*, **35**(6):1088, Nov 1979.

[131] H. B. Michaelson. **The work function of the elements and its periodicity**. *J. Appl. Phys.*, **48**(11):4729, 1977.

[132] E. Goiri, M. Matena, A. El-Sayed, J. Lobo-Checa, P. Borghetti, C. Rogero, B. Detlefs, J. Duvernay, J. E. Ortega, and D. G. de Oteyza. **Self-assembly**

of bicomponent molecular monolayers: adsorption height changes and their consequences. *(submitted)*, 2014.

[133] L. Floreano, G. Naletto, D. Cvetko, R. Gotter, M. Malvezzi, L. Marassi, A. Morgante, A. Santaniello, A. Verdini, F. Tommasini, and G. Tondello. **Performance of the grating-crystal monochromator of the ALOISA beamline at the Elettra Synchrotron**. *Rev. Sci. Instrum.*, **70**(10):3855, 1999.

[134] J. J. Olivero and R. L. Longbothum. **Empirical fits to the Voigt line width: A brief review**. *J. Quant. Spectrosc. Radiat. Transfer*, **17**(2):233236, 1977.

[135] T. Schwieger, H. Peisert, M. S. Golden, M. Knupfer, and J. Fink. **Electronic structure of the organic semiconductor copper phthalocyanine and K-CuPc studied using photoemission spectroscopy**. *Phys. Rev. B*, **66**:155207, Oct 2002.

[136] S. Duhm, I. Salzmann, G. Heimel, M. Oehzelt, A. Haase, R. L. Johnson, J. P. Rabe, and N. Koch. **Controlling energy level offsets in organic/organic heterostructures using intramolecular polar bonds**. *Appl. Phys. Lett.*, **94**(3):033304, 2009.

[137] H. C. Potter and J. M. Blakely. **LEED, Auger spectroscopy, and contact potential studies of copper - gold alloy single crystal surfaces**. *J. Vac. Sci. and Technol.*, **12**(2):635, 1975.

[138] B. Bröker, R.-P. Blum, J. Frisch, A. Vollmer, O. T. Hofmann, R. Rieger, K. Müllen, J. P. Rabe, E. Zojer, and N. Koch. **Gold work function reduction by 2.2 eV with an air-stable molecular donor layer**. *Appl. Phys. Lett.*, **93**:24330, 2008.

[139] F. Evangelista, V. Carravetta, G. Stefani, B. Jansik, M. Alagia, S. Stranges, and A. Ruocco. **Electronic structure of copper phthalocyanine: An experimental and theoretical study of occupied and unoccupied levels**. *J. Chem. Phys.*, **126**:124709, 2007.

[140] A. Calabrese, L. Floreano, A. Verdini, C. Mariani, and M. G. Betti. **Filling empty states in a CuPc single layer on the Au(110) surface via electron injection**. *Phys. Rev. B*, **79**(11):115446, Mar 2009.

[141] C. Uhlmann, I. Swart, and J. Repp. **Controlling the Orbital Sequence in Individual Cu-Phthalocyanine Molecules**. *Nano Lett.*, **13**(2):777, 2013.

[142] J. Schaffert, M. C. Cottin, A. Sonntag, H. Karacuban, C. A. Bobisch, N. Lorente, J.-P. Gauyacq, and R. Möller. **Imaging the dynamics of individually adsorbed molecules**. *Nature Mater.*, **12**((3)):223, 2012.

[143] B. Stadtmüller, I. Kröger, F. Reinert, and C. Kumpf. **Submonolayer growth of CuPc on noble metal surfaces**. *Phys. Rev. B*, **83**(8):085416, Feb 2011.

[144] J. Ziroff, F. Forster, A. Schöll, P. Puschnig, and F. Reinert. **Hybridization of Organic Molecular Orbitals with Substrate States at Interfaces: PTCDA on Silver**. *Phys. Rev. Lett.*, **104**:233004, Jun 2010.

[145] J. Ziroff, S. Hame, M. Kochler, A. Bendounan, A. Schöll, and F. Reinert. **Low-energy scale excitations in the spectral function of organic monolayer systems**. *Phys. Rev. B*, **85**:161404, Apr 2012.

[146] M. Jung, U. Baston, G. Schnitzler, M. Kaiser, J. Papst, T. Porwol, H. Freund, and E. Umbach. **The electronic structure of adsorbed aromatic molecules: Perylene and PTCDA on Si(111) and Ag(111)**. *Journal of Molecular Structure*, **293**(0):239 , 1993.

[147] A. Bendounan, F. Forster, A. Schöll, D. Batchelor, J. Ziroff, E. Umbach, and F. Reinert. **Electronic structure of 1ML NTCDA/Ag(111) studied by photoemission spectroscopy**. *Surf. Sci.*, **601**(18):4013, 2007.

[148] M. Häming, C. Scheuermann, A. Schöll, F. Reinert, and E. Umbach. **Coverage dependent organic-metal interaction studied by high-resolution core level spectroscopy: SnPc (sub)monolayers on Ag(111)**. *J. Electron. Spectrosc. Relat. Phenom.*, **174**(1-3):59, 2009.

[149] V. Aristov, O. Molodtsova, V. Maslyuk, D. Vyalikh, V. Zhilin, Y. Ossipyan, T. Bredow, I. Mertig, and M. Knupfer. **Electronic structure of pristine CuPc: Experiment and calculations**. *Appl. Surf. Sci.*, **254**(1):20, 2007. Proceedings of the 13th International Conference on Solid Films and Surfaces - ICSFS 13.

[150] O. V. Molodtsova, M. Knupfer, V. V. Maslyuk, D. V. Vyalikh, V. M. Zhilin, Y. A. Ossipyan, T. Bredow, I. Mertig, and V. Y. Aristov. **Unoccupied electronic states in an organic semiconductor probed with x-ray spectroscopy and first-principles calculations**. *J. Chem. Phys.*, **129**(15):, 2008.

[151] C. Schmidt, T. Breuer, S. Wippermann, W. G. Schmidt, and G. Witte. **Substrate Induced Thermal Decomposition of Perfluoro-Pentacene Thin Films on the Coinage Metals**. *J. Phys. Chem. C*, **116**(45):24098, 2012.

[152] D. G. de Oteyza, A. Sakko, A. El-Sayed, E. Goiri, L. Floreano, A. Cossaro, J. M. García-Lastra, A. Rubio, and J. E. Ortega. **Inversed linear dichroism in F K-edge NEXAFS spectra of fluorinated planar aromatic molecules**. *Phys. Rev. B*, **86**:075469, Aug 2012.

[153] I. Kröger. **Adsorption von Phthalocyaninen auf Edelmetalloberflächen**. PhD thesis, Universität Würzburg, 2011.

[154] I. Kröger, B. Stadtmüller, C. Kleimann, P. Rajput, and C. Kumpf. **Normal-incidence x-ray standing-wave study of copper phthalocyanine submonolayers on Cu(111) and Au(111)**. *Phys. Rev. B*, **83**(19):195414, May 2011.

[155] A. Gerlach, S. Sellner, F. Schreiber, N. Koch, and J. Zegenhagen. **Substrate-dependent bonding distances of PTCDA: A comparative x-ray standing-wave study on Cu(111) and Ag(111)**. *Phys. Rev. B*, **75**:045401, Jan 2007.

[156] F. Flores and J. Ortega. **Basic Theory of the Molecule-Metal Interface**. In N. Koch, N. Ueno, and A. Wee, editors, *The Molecule-Metal Interface*. Wiley-VCH Verlag GmbH & Co. KGaA, 2013.

[157] S. Henze, O. Bauer, T.-L. Lee, M. Sokolowski, and F. Tautz. **Vertical bonding distances of PTCDA on Au(111) and Ag(111): Relation to the bonding type**. *Surf. Sci.*, **601**(6):1566, 2007.

[158] C. Stadler, S. Hansen, I. Kröger, C. Kumpf, and E. Umbach. **Tuning intermolecular interaction in long-range-ordered submonolayer organic films**. *Nature Phys.*, **5**:153, 2009.

[159] C. Bürker, N. Ferri, A. Tkatchenko, A. Gerlach, J. Niederhausen, T. Hosokai, S. Duhm, J. Zegenhagen, N. Koch, and F. Schreiber. **Exploring the bonding of large hydrocarbons on noble metals: Diindoperylene on Cu(111), Ag(111), and Au(111)**. *Phys. Rev. B*, **87**:165443, Apr 2013.

[160] S. Duhm, C. Bürker, J. Niederhausen, I. Salzmann, T. Hosokai, J. Duvernay, S. Kera, F. Schreiber, N. Koch, N. Ueno, and A. Gerlach. **Pentacene on Ag(111): Correlation of Bonding Distance with Intermolecular Interaction and Order**. *ACS Appl. Mater. Interfaces*, **5**(10):9377, 2013.

[161] J. Roy. **pyXSW Documentation, Release 1.1rc1**, 2012.

[162] I. A. Vartanyants and J. Zegenhagen. **Photoelectric scattering from an X-ray interference field**. *Solid State Commun.*, **113**(6):299, 2000.

[163] F. Schreiber, K. Ritley, I. Vartanyants, H. Dosch, J. Zegenhagen, and B. Cowie. **Non-dipolar contributions in XPS detection of X-ray standing waves**. *Surface Science*, **486**(3):L519 , 2001.

[164] M. Prasanna and T. Guru Row. **C-halogen$\cdots\pi$ interactions and their influence on molecular conformation and crystal packing: a database study**. *Crystal Engineering*, **3**(2):135 , 2000.

[165] H. Fukagawa, S. Hosoumi, H. Yamane, S. Kera, and N. Ueno. **Dielectric properties of polar-phthalocyanine monolayer systems with repulsive dipole interaction**. *Phys. Rev. B*, **83**:085304, Feb 2011.

[166] H. Fukagawa, S. Kera, T. Kataoka, S. Hosoumi, Y. Watanabe, K. Kudo, and N. Ueno. **The Role of the Ionization Potential in Vacuum-Level Alignment at Organic Semiconductor Interfaces**. *Adv. Mater.*, **19**(5):665, 2007.

[167] C. Baldacchini, F. Allegretti, R. Gunnella, and M. G. Betti. **Molecule-metal interaction of pentacene on copper vicinal surfaces**. *Surf. Sci.*, **601**:2603, 2007.

[168] W. Wu, L. A. Rochford, S. Felton, Z. Wu, J. L. Yang, S. Heutz, G. Aeppli, T. S. Jones, N. M. Harrison, and A. J. Fisher. **Magnetic properties of copper**

hexadecaphthalocyanine (F_{16}CuPc) thin films and powders. *J. Appl. Phys.*, **113**(1):013914, 2013.

[169] N. Koch, I. Salzmann, R. Johnson, J. Pflaum, R. Friedlein, and J. Rabe. **Molecular orientation dependent energy levels at interfaces with pentacene and pentacenequinone**. *Organic Electronics*, **7**(6):537 , 2006.

[170] D. Käfer and G. Witte. **Evolution of pentacene films on Ag(111): Growth beyond the first monolayer**. *Chem. Phys. Lett.*, **442**(4-6):376, 2007.

[171] N. Koch. **Energy levels at interfaces between metals and conjugated organic molecules**. *J. Phys.: Condens. Matter*, **20**(18):184008, 2008.

[172] N. Koch, A. Elschner, J. Rabe, and R. Johnson. **Work Function Independent Hole-Injection Barriers Between Pentacene and Conducting Polymers**. *Advanced Materials*, **17**(3):330, 2005.

[173] M. Pedio, B. Doyle, N. Mahne, A. Giglia, F. Borgatti, S. Nannarone, S. Henze, R. Temirov, F. Tautz, L. Casalis, R. Hudej, M. Danisman, and B. Nickel. **Growth of pentacene on Ag(111) surface: A NEXAFS study**. *Appl. Surf. Sci.*, **254**(1):103 , 2007.

[174] M. F. Danışman, L. Casalis, and G. Scoles. **Supersonic molecular beam deposition of pentacene thin films on two Ag(111) surfaces with different step densities**. *Phys. Rev. B*, **72**:085404, Aug 2005.

[175] H. Ding, K. Park, K. Green, and Y. Gao. **Electronic structure modification of copper phthalocyanine (CuPc) induced by intensive Na doping**. *Chem. Phys. Lett.*, **454**(4-6):229 , 2008.

[176] A. J. Wagner, C. D. Vecitis, and D. H. Fairbrother. **$CF_2(CF_2)_7(CH_2)_2SH$ Self-Assembled on Au and Subsequent Degradation Under the Influence of Ionizing Radiation as Measured by XPS**. *Surf. Sci. Spectra*, **8**(1):32, 2001.

[177] M. Sato, H. Watanabe, T. Furusawa, and N. Suzuki. **The Degradation of Perfluorinated Organic Thin Film During XPS Measurement**. *J. Surf. Anal.*, **12**, 2005.

[178] R. L. Graham, C. D. Bain, H. A. Biebuyck, P. E. Laibinis, and G. M. Whitesides. **Damage to trifluoroacetamido-terminated organic self-assembled monolayers (SAMs) on aluminum, titanium, copper and gold by aluminum K.alpha. x-rays is due principally to electrons**. *J. Phys. Chem.*, **97**(37):9456, 1993.

[179] J. H. Scofield. **Theoretical Photoionization Cross-Sections from 1 to 1500 keV**. 1973.


CFM

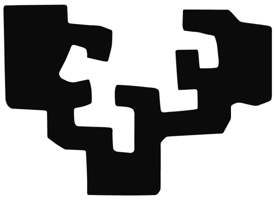


dipc